Recent ice dynamics of outlet glaciers in Enderby Land, Kemp Land and Dronning Maud Land, East Antarctica, and their links to ocean-climate forcings between 1960s and 2024

SHARMA, ANWESHA

Recent ice dynamics of outlet glaciers in Enderby Land, Kemp Land and Dronning Maud Land, East Antarctica, and their links to ocean-climate forcings between 1960s and 2024

Anwesha Sharma

A thesis presented for the degree of

Doctor of Philosophy

in the

Department of Geography

Durham University, United Kingdom

August 2025

Abstract

The East Antarctic Ice Sheet (EAIS) holds the largest potential contribution to global sea-level rise—approximately $\sim$ 53 m—yet its outlet glaciers display pronounced regional heterogeneity in both past behaviour and future vulnerability. Observations and numerical models alike have shown that while some sectors of the EAIS are losing mass, others remain stable or even gain mass, raising questions about which regions may be most susceptible to continued warming.

To address this, the present thesis combines multi-decadal (1960s–2023) satellite remote sensing with statistical analysis to examine terminus behaviour across 44 marine-terminating glaciers in Enderby Land, Kemp Land, and Dronning Maud Land (DML). The regional assessment across Enderby and Kemp Land revealed that between the 1970s and 1988, reduced sea-ice cover drove widespread retreat; this pattern reversed from 1988 to 2000 as cooler ocean conditions and higher sea-ice concentrations—associated with a positive phase of the Southern Annular Mode—promoted glacier advance. Since 2000, however, the fraction of advancing glaciers has declined modestly. Furthermore, the terminus behaviour across individual glaciers was asynchronous, underscoring the influence of local, glacier-specific controls alongside ocean-climatic drivers.

Statistical correlations between terminus-position change and ocean–climate drivers further underscore this heterogeneity. Across the study regions, higher seasonal sea-ice concentrations are generally associated with glacier advance—that is, terminus positions tend to advance when sea-ice cover increases (positive correlation coefficients, typically ranging from +0.3 to +0.7). In contrast, elevated subsurface ocean temperatures correlate with glacier retreat (negative correlation coefficients, often between –0.2 and –0.6). Nevertheless, the precise strength and direction of these relationships differ substantially among individual glaciers. While some glaciers exhibited positive moderate correlations with sea-ice conditions, others exhibited negative mdoerate correlations with ocean warming. This variability highlighted

the critical role of local factors—such as fjord geometry, ice-shelf thickness, and grounding-line depth—in modulating each glacier's ocean-climatic response.

To examine some of these processes in more detail, two case studies focussed on Wilma–Robert–Downer (WRD) system in Kemp Land and Jutulstraumen in DML. These illustrate contrasting calving dynamics mediated by rift propagation. At WRD, rifts repeatedly nucleate in the same sector, advance with the ice tongue, and spawned major calving events in 1991 and 2003 (and a smaller event in 2014); persistent sea-ice and mélange within rift cavities have, however, mitigated calving severity and facilitated subsequent advance. By contrast, Jutulstraumen's floating tongue has hosted long-lived, slowly propagating rifts since the 1960s, enabling uninterrupted advance since its last major calving in 1967—stabilised by topographic pinning and cold waters, though recent warm-water incursions suggest rising vulnerability.

In contrast to the persistent mass losses of Greenland, West Antarctica and parts of the EAIS, majority of these EAIS outlet glaciers demonstrate net stability or advance on annual to decadal timescales, punctuated by episodic retreat. Local geomorphological and oceanic factors—fjord geometry, ice-shelf buttressing, and pinning points—emerge as critical stabilising influences, highlighting the non-uniform sensitivity of EAIS glaciers to both regional climate variability and site-specific controls.

Declaration

The work in this thesis is based on research carried out at the Department of Geography, Durham University, United Kingdom. No part of this thesis has been submitted elsewhere for any other degree or qualification and it is all my own work unless referenced to the contrary in the text.

Acknowledgements

I am profoundly grateful to my supervisors, Prof. Chris R. Stokes and Prof. Stewart S.R. Jamieson, for their expert guidance, insightful critiques, and unwavering support at every stage of this research. Their encouragement and constructive feedback have been invaluable in shaping both my scientific approach and the final thesis.

I gratefully acknowledge Durham University for supporting this project through a Durham Doctoral Studentship and for funding my attendance at key scientific conferences—opportunities that have been instrumental in my growth as a researcher. I would also like to thank the scientists from other institutions who reviewed my paper. Thank you to the community in the Department of Geography at Durham University, including many chats in the Manley Room.

My heartfelt thanks go to my parents for their endless encouragement and steadfast belief in me—especially my mother, who patiently nodded through every intricate explanation, and to my father, whose quiet confidence and gentle humour sustained me. And to my partner, thank you for the endless cups of tea and coffee, the pep talks, and the laughter that kept me grounded when the data simply refused to cooperate.

Contents

List of Figures

List of Tables

List of Abbreviations

AABW	Antarctic Bottom Water
AIS	Antarctic Ice Sheet
ASB	Aurora Subglacial Basin
ASC	Antarctic Slope Current
DML	Dronning Maud Land
DMSP	Defense Meteorological Satellite Program
DSW	Dense Shelf Water
EAIS	East Antarctic Ice Sheet
ERA	Reanalysis from European Centre for Medium-Range Weather Forecasts
ETM+	Enhanced Thematic Mapper Plus
FIS	Filchner Ice Shelf
GEEDiT	Google Earth Engine Digitisation Tool
GL	Grounding Line

GMSL	Global Mean Sea Level
GrIS	Greenland Ice Sheet
ITS_LIVE	Inter-mission Time Series of Land Ice Velocity and Elevation
LGM	Last Glacial Maximum
mCDW	modified Circumpolar Deep Water
MEaSUREs	Making Earth System Data Records for Use in Research Environments
MISI	Marine Ice Sheet Instability
MODIS	MODerate-resolution Imaging Spectroradiometer
OT	Ocean Temperature
PDD	Positive Degree Days
QML	Queen Maud Land
SAM	Southern Annular Mode
SIC	Sea Ice Concentration
SIE	Sea Ice Extent
SLE	Sea-level Equivalent
SMB	Surface Mass Balance
SMMR	Scanning Multichannel Microwave Radiometer
SSM/I	Special Sensor Microwave Imager
SSMIS	Special Sensor Microwave Imager/Sounder
SST	Sea Surface Temperature
WAIS	West Antarctic Ice Sheet
WDW	Warm Deep Water

WRD	Wilma-Robert-Downer
WSB	Wilkes Subglacial Basin

CHAPTER 1

Introduction

1.1 Rationale

The potential impact of melting ice sheets on Global Mean Sea Level (GMSL) rise is significant. Together, the Greenland Ice Sheet (GrIS) and the Antarctic Ice Sheet (AIS) hold enough frozen water to raise the GMSL by approximately 65.3 m (Otosaka et al., 2023). The GrIS contains ice that could contribute 7.42 m to sea-level rise (Morlighem et al., 2017), while the AIS contains 57.9 m of sea-level equivalent (SLE) (Morlighem et al., 2020). Over the past three decades, ice losses from both AIS and GrIS have accelerated 6-fold (IMBIE Team, 2018, 2020). This rapid melting has led to measurable increases in global sea levels (WCRP Global Sea Level Budget Group, 2018) and has heightened the risk of coastal flooding around the world (Kulp and Strauss, 2019; Vitousek et al., 2017; Hanson et al., 2011). Understanding the mechanisms driving this mass loss is crucial for projecting future sea-level rise and developing effective mitigation and adaptation strategies. For instance, the GrIS has been losing mass at an accelerated rate of -169 ± 16 Gt yr^{-1} between 1992 and 2020 (IMBIE Team, 2023). This loss is primarily driven by rising air temperatures (Hanna et al., 2021; Hofer et al., 2017) resulting in intensified summertime surface melting (Leeson et al., 2015; Tedesco and Fettweis, 2020) and increased runoff (Trusel et al., 2018; Slater et al., 2021). Additionally, ocean warming has led to the acceleration (Rignot and Kanagaratnam, 2006) and retreat (King et al., 2020) of outlet glaciers (Straneo and Heimbach, 2013). Unlike the GrIS, the AIS's mass loss is predominantly due to ocean-induced melting of ice shelves and their thinning. This, in turn, accelerates ice flow from the interior of the ice sheet as a result of reduced buttressing which further destabilises, particularly, marine-terminating glaciers (Hogg et al., 2017; Selley et al., 2021; Rignot et al.,2019).

Of note is that the AIS has been highly sensitive to climate variations in the past. Palaeoclimate records (DeConto & Pollard, 2016; Noble et al., 2020) and ice sheet models (Nowicki et al., 2013; Payne et al., 2021; Seroussi et al., 2020) have highlighted the sensitivity of the AIS to past warm periods, serving as an analogue for potential mass loss under future atmospheric warming projections (Fogwill et al.,

2014). Reconstructions of GMSL during the Last Interglacial (LIG, ∼129 to 116 ka) suggested that the AIS was a major contributor to sea level rise of around 6-8 m higher than present, driven by atmospheric and oceanic forcings (DeConto & Pollard, 2016). Model simulations for the mid-Pliocene warm period (3.3–3.0 Ma), characterised by global mean temperatures around ∼2-4°C warmer-than-present and CO_2 levels similar to current concentrations (approximately 400-450 ppm) (Pagani et al. 2010; Bartoli et al., 2011; Haywood et al., 2016; de la Vega et al., 2020; Burton et al. 2023), indicated a GMSL 10-25 m higher than present (Oppenheimer et al., 2019), with approximately +17 m thought to originate from the AIS alone (Pollard et al., 2015). Moreover, future coupled ice sheet and climate models predict that, under a high emission scenario, the AIS could contribute more than a metre of sea level rise by 2100 and possibly exceed 15 metres by 2500 (DeConto & Pollard, 2016).

The AIS is typically divided into three regions: the East Antarctic Ice Sheet (EAIS), which constitutes the majority of the AIS with approximately 53 m of SLE; the West Antarctic Ice Sheet (WAIS), containing about 5.3 m of SLE (Morlighem et al., 2020); and the Antarctic Peninsula Ice Sheet (APIS), consisting of around 0.24 m of SLE (Pritchard and Vaughan, 2007). Numerous studies have indicated that ice loss is predominantly concentrated in the WAIS (Bamber et al., 2009; Joughin & Alley, 2011; Pattyn & Morlighem, 2020; IMBIE Team, 2023), with -82 ± 9 Gt yr^{-1} of mass loss between 1992 and 2020 (IMBIE Team, 2023), primarily due to the intrusion of warm modified Circumpolar Deep Water (mCDW) onto the continental shelves. This influx accelerates basal melting of ice shelves (Adusumilli et al., 2020; Paolo et al., 2015) and leads to their subsequent retreat and/or thinning (Jacobs et al. 2011; Dutrieux et al. 2014; Alley et al. 2015; Jenkins et al. 2016, 2018; Nakayama et al. 2019). Given that most sections of the WAIS are grounded below sea level, they are vulnerable to Marine Ice Sheet Instability (MISI) (Rignot et al., 2013; Favier et al., 2014; Joughin et al., 2014; Schmidtko et al., 2014; Christianson et al., 2016; Yu et al., 2018), potentially resulting in rapid increases in ice discharge rates.

In contrast, the EAIS has remained largely stable (Shepherd et al., 2012; King et al., 2012; Shepherd et al. 2019; Rignot et al. 2019; Schröder and others, 2019; Smith and others, 2020), resulting in a net mass balance of $+3 \pm 15$ Gt yr^{-1} between 1992 and 2020 (The IMBIE Team, 2023). However, this overall stability masks significant regional variations. For example, Dronning Maud Land (DML) has been gaining mass at $+13.3 \pm 3.4$ Gt yr^{-1} between 1992 and 2017 (Shepherd and others, 2019), largely due to substantial snowfall events. Conversely, Wilkes Land has been losing mass (Khazendar and others, 2013; Greenbaum and others, 2015; Li and others, 2016; Rignot and others, 2019; Brancato and others, 2020; Zwally & Giovinetto, 2011; Shepherd and others, 2012; Medley and others, 2018; Smith and others, 2020; Stokes and others, 2022; The IMBIE team, 2023) at -8.2 ± 2 Gt yr^{-1} between 1992 and 2017 (Shepherd et al., 2019) due to intrusion of warm mCDW into the deep troughs connecting the glacier cavities to the ocean and resulting in enhanced basal melt rates (King et al, 2012; Greenbaum et al. 2015; Miles et al. 2016; Rintoul et al. 2016; Shepherd and others, 2019; Rignot et al. 2019; Ribeiro et al. 2021; Arthur et al. 2022). These regional variations highlight the complexity of the EAIS's response to climate change, which can differ significantly from basin to basin (Stokes et al., 2022) and even at individual glacier scale.

Despite the perceived stability of the EAIS, recent studies have raised concerns about its potential vulnerability to future climate change (see review in Stokes et al., 2022). For example, an increase in basal melt at Fimbulisen in DML has been observed between 2009 and 2019 at the rate of 0.61 m yr^{-1}. This has been attributed to the influx of Warm Deep Water (WDW) (Lauber et al., 2023) into the ice shelf cavities. A further increase in WDW influx beneath Fimbulisen could potentially enhance ice discharge, leading to greater mass loss in the future. In addition, models also predict that major subglacial basins within the EAIS are susceptible to sustained ocean warming, leading to significant mass loss under high-emission future warming scenarios (Golledge et al., 2015, 2017; DeConto et al., 2021). For instance, Recovery basin catchment is vulnerable to increasing ocean temperatures similar to the basins

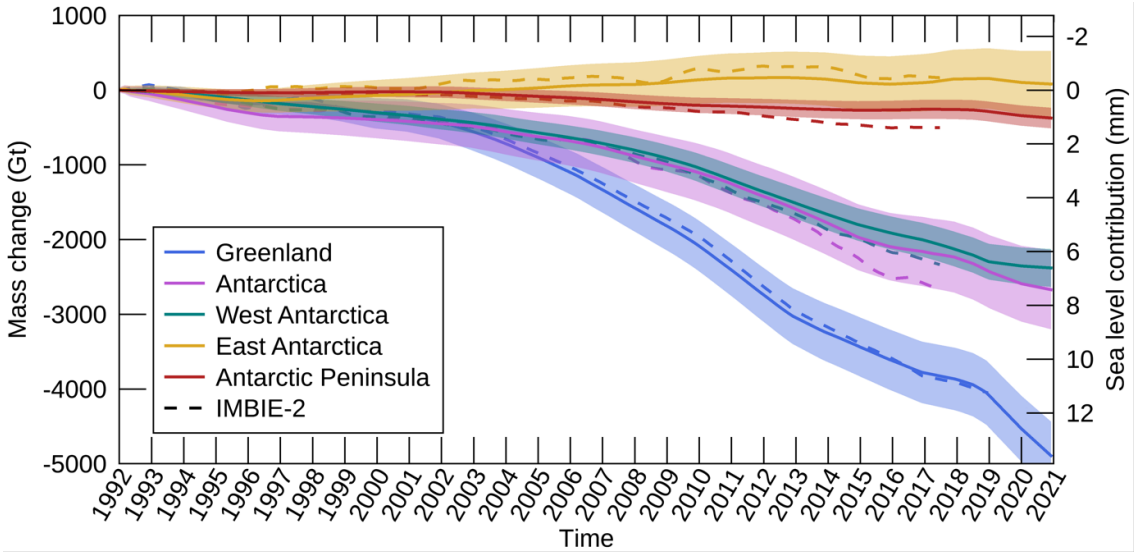

Figure 1.1: *Cumulative ice sheet mass balance for each ice sheet (The IMBIE Team, 2023). The shaded regions represent 1σ uncertainty of cumulative change. The dashed lines show results from previous assessments.*

in WAIS under future high emission scenarios (Golledge et al., 2015; Golledge et al., 2017). However, these model simulations carry significant uncertainties regarding the precise factors that drive such glacier behaviour. They are largely dependent on the inclusion of various physical processes and forcings under different Representative Concentration Pathways (RCPs) (Seroussi et al., 2020). The variability of these processes and forcings across the EAIS adds further complexity to model simulations. Therefore, the drivers of ice dynamics that might lead to future mass loss in the EAIS remain poorly understood.

In recent years, research in the EAIS has significantly advanced (e.g. Miles et al. 2016, 2021, 2022; Nakamura et al. 2016; Golledge et al. 2017; Stokes et al., 2022; Walker et al. 2024), yet large portions of the EAIS, particularly concerning the behaviour and underlying drivers of its outlet glaciers remain understudied. Until recently, much of the existing research has concentrated on Wilkes Land in the EAIS (e.g. Miles et al., 2016, 2017; Shen et al., 2018; Pelle et al., 2020, 2021; Arthur et al., 2021; Jordan et al., 2023; Iizuka et al., 2023) given its substantial mass loss, leaving other regions comparatively unexplored. In particular, Kemp Land, Enderby Land, and parts of DML (see Fig. 1.2) remained poorly understood in terms of outlet glacier dynamics and their potential drivers. As shown in Figure

1.2, between 2003 and 2019, these regions have experienced mass gain inland of the grounding line, while mass loss was particularly evident along the ice shelves fringing the coast of DML (Smith et al. 2020). This includes the floating tongue of the Jutulstraumen Glacier, the largest glacier in the region, which drains into the Fimbulisen (Fig. 1.2). In addition, limited research exists on the mass loss or gain of glaciers in Enderby and Kemp Land, where the glaciers are relatively smaller than in DML and are either unconstrained or constrained within fjord-like settings. These differing geographical and geomorphological settings imply that glacier-ocean-climate interactions may vary considerably within as well as across these regions. As a result, it remains unclear how glacier behaviour differs under these contrasting settings. This underscores the need for further investigation into the spatial variability of glacier behaviour across the EAIS.

Therefore, to address these issues and reduce the uncertainties in model simulations, this thesis aims to provide regional and local analyses of recent changes in marine-terminating glaciers in underexplored regions and identify the drivers behind these changes.

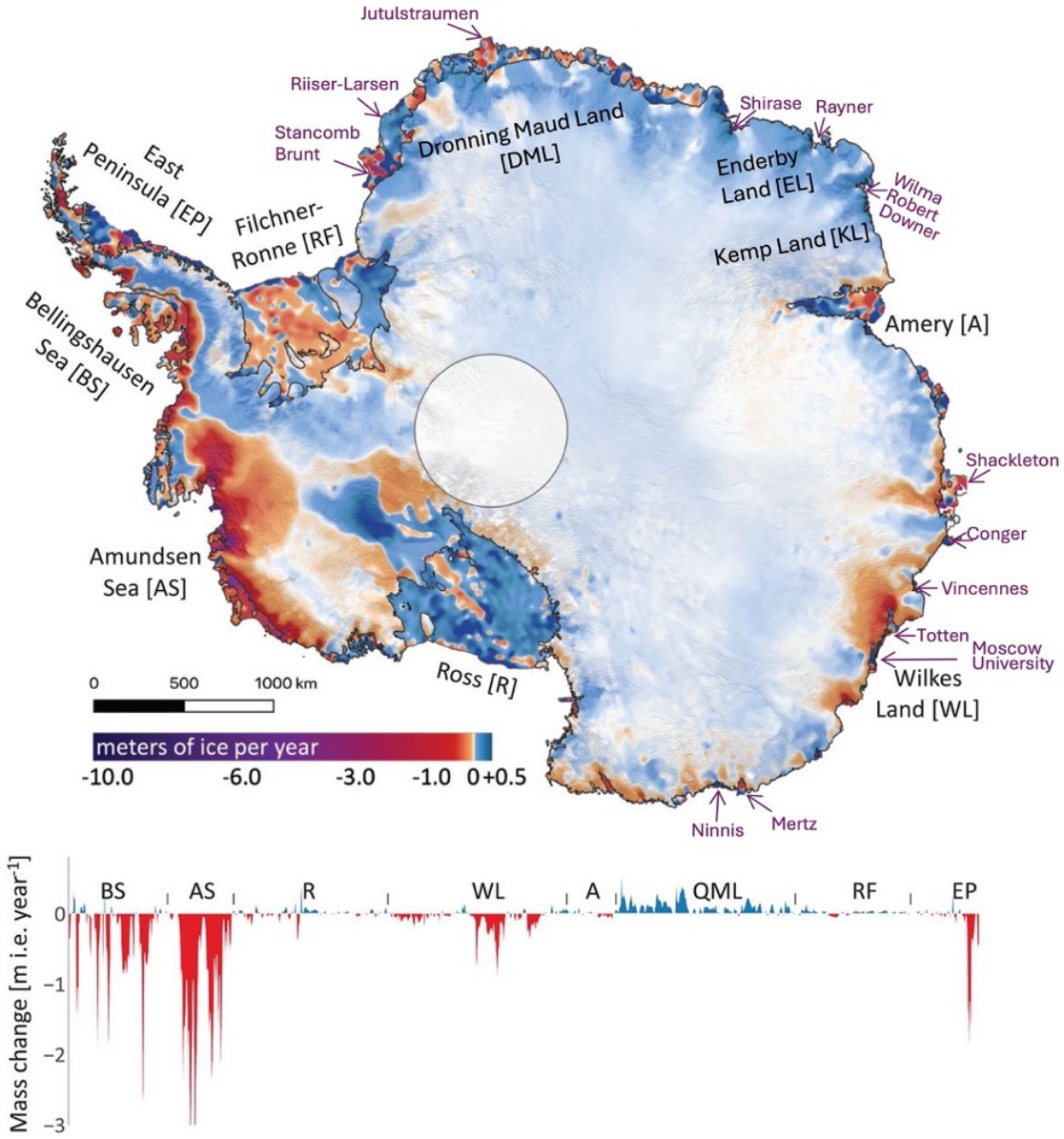

Figure 1.2: *Mass change for Antarctica between 2003 and 2019 from Smith et al. (2020).*

1.2 Research aims and objectives

The overall aim of this thesis is to investigate and explore the sensitivity of major outlet glaciers in the regions of DML, Enderby Land and Kemp Land to climatic and non-climatic drivers from 1960s to present. Given the lack of studies in these regions, the work will address the following key research gaps/questions:

RQ1: How do marine-terminating glaciers in Enderby and Kemp Land vary in terminus behaviour over decadal and interannual timescales?

(a) Map and quantify glacier terminus position change for 44 marine-terminating glaciers from the 1970s–2023, and identify multi-decadal trends of advance and retreat.

(b) Assess temporal heterogeneity in glacier behaviour across epochs and evaluate whether glaciers respond synchronously or asynchronously at regional and individual-glacier scales.

RQ2: Is there a regional pattern in glacier behaviour across the neighbouring regions of Enderby and Kemp Land?

(a) Compare glacier behaviour between Enderby Land and Kemp Land and assess how regional contrasts evolve across different time periods.

(b) Investigate intra-regional variability in terminus position by examining differences in behaviour between individual neighbouring glaciers.

RQ3: What are the primary factors influencing the terminus behaviour of marine-terminating glaciers in these regions?

(a) Analyse temporal variability in environmental drivers such as sea-ice concentration and extent, subsurface ocean temperatures and air temperature, and compare these with phases of glacier advance and retreat.

(b) Compute lagged correlation relationships at regional and glacier-specific

scales to assess the strength and consistency of links between environmental forcing and glacier behaviour.

(c) Determine whether glacier change is most strongly associated with sea-ice buttressing, ocean thermal forcing, atmospheric variability, or a combination of these influences.

RQ4: How do the dynamics and structural characteristics of glaciers evolve over time, what impact do these changes have on their overall behaviour?

(a) Analyse ice dynamic changes by examining ice velocity, grounding-line position and surface elevation.

(b) Map and assess the evolution of rifts to understand the structural evolution of glaciers.

(c) Assess whether structural and dynamic adjustments precede or follow changes in terminus behaviour, and what this implies for future glacier stability.

1.3 Thesis structure

The thesis is organised into eight chapters. Following this introductory chapter, Chapter 2 provides a review of key literature on historical, recent, and projected responses of marine-terminating glaciers across the EAIS to ocean-climate change, emphasising the region's vulnerability to warming, the variability in glacier responses, and the potential drivers shaping their behaviour. Chapter 3 outlines the study area, providing an overview of its geographical setting, glaciological features, and relevance to the research objectives. Chapters 4 to 6 present the findings from specific study regions, addressing the research questions outlined above and written up as stand-alone manuscripts, the latter of which has already been published (Sharma et al., 2025). Since the methods are specific to each study, they are included within the relevant chapters rather than as a separate section. Chapter 7 offers a broader discussion of the collective results, highlighting the interplay of ocean-climatic and non-climatic factors influencing glacier dynamics. The chapter 7 also addresses the

limitations and explores opportunities for future research. Chapter 8 draws conclusions by summarising the key findings.

CHAPTER 2

Literature Review

2.1 Understanding the East Antarctic Ice Sheet

The EAIS is the largest ice sheet in the world, containing enough ice to raise GMSL by ∼53 m, whereas the WAIS and APIS contain only 5.3 m and 0.24 m, respectively (Rignot et al., 2019). Despite its size, the modern patterns of EAIS change have historically received less attention, likely because the ice sheet has been observed to be gaining mass or maintaining near equilibrium in recent decades, primarily due to increased snow accumulation which, on an ice sheet scale, is sufficient to offset much of the dynamic ice loss that happens more locally (Otosaka et al., 2023; Rignot et al., 2019; Medley et al., 2018; Shepherd et al., 2012; Smith et al., 2020; Zwally & Giovinetto, 2011). However, with improvement in remote sensing data, numerical modelling and field techniques, the amount of research focused on the EAIS has increased in the last few years. This growing body of research has revealed that the EAIS may be more sensitive to ongoing climate and ocean change than previously thought (Stokes et al., 2022). While uncertainties persist, modelling studies indicate that the EAIS could contribute to sea-level rise on decadal to centennial timescales (Gwyther et al., 2014; Golledge et al., 2015, 2017; DeConto & Pollard, 2016; Pelle et al., 2020; DeConto et al., 2021).

Unlike the relatively smaller GrIS, where ice sheet response to climate change tends to exhibit more regional consistency (Black & Joughin, 2022), the EAIS exhibits a more variable response to climate change, both locally and regionally, and across different timescales (Miles et al., 2016). In the EAIS, while some areas continue to gain mass (e.g. the Dronning Maud Land), others have experienced significant mass loss (e.g. the Wilkes Land) over the past few decades (Rignot et al., 2019). This heterogeneous response shows that the nature of climate and ocean impacts on the EAIS are complex and localised, underscoring the need for more targeted studies to understand and predict future changes. In addition, increased attention was drawn recently to several ice shelves and outlet glaciers which have been historically understudied but now have exhibited substantial changes. Yet, the drivers of these changes have often remained unclear. For example, the 2022 disintegration of the

Conger-Glenzer Ice Shelf appeared abrupt but further analyses revealed that this ice shelf may have been predisposed to disintegration since the 1990s (Walker et al., 2024; Alley et al., 2024). It is still uncertain whether this ice shelf loss has had any measurable impact on the flow of the upstream glaciers. Such findings highlight the importance of studying individual glacier catchments and the mechanisms driving their ice loss.

Generally, glaciers in the EAIS are buttressed by extensive ice shelves and floating ice tongues that help regulate their flow (Bindschadler et al., 2011). However, compared to the West Antarctic Ice Sheet (WAIS), these ice shelves are typically shorter, less extensive, and often less confined by topography, potentially limiting their buttressing capacity (Dupont and Alley, 2005; Rignot et al., 2019; Morlighem et al., 2020). Losing these ice shelves or floating ice tongues can trigger enhanced ice discharge from the inland of the ice sheet (Fürst et al., 2016; Miles et al., 2022). Indeed, previous research has shown such increases in ice discharge following thinning or collapse of ice shelves or floating ice tongues in the WAIS and APIS (De Angelis and Skvarca, 2003; Scambos et al., 2004; Joughin et al., 2012; Andreason et al., 2023; Davison et al., 2024), typically driven by climate change.

This chapter aims to integrate the existing knowledge regarding the sensitivity of the EAIS in response to past, present, and future climate change and understand the variable responses of the marine basins to climate change. Section 2.2 explores the historical behaviour of the EAIS, followed by a review of recent changes observed across the EAIS in Section 2.3. Section 2.4 examines the drivers of ice dynamic changes in marine basins to date, while Section 2.5 discusses predictions of the EAIS's future contributions to sea-level rise.

2.2 Tracing the Past: Understanding Historical Changes in the East Antarctic Ice Sheet

The AIS as a whole has been highlighted to be highly sensitive to past warm periods as evidenced by palaeoclimate records (Noble et al., 2020) and ice sheet models

(Nowicki et al., 2013; Payne et al., 2021; Seroussi et al., 2020). These responses to warm periods can be used as an analogue for mass loss with respect to future atmospheric warming projections (Fogwill et al., 2014). In fact, the EAIS has experienced substantial mass loss during these warm periods. Specifically, the EAIS witnessed its most significant volume reduction during the Mid-Miocene Climatic Optimum (17.0-14.8 million years ago), a period when atmospheric CO_2 levels were around 600-800 ppm (Rae et al., 2021) During this Mid-Miocene period, sea surface temperatures (SSTs) were significantly higher, ranging from 6-10°C in the Ross Sea (Levy et al., 2016) to around 11–17 °C off the Adélie Coast (Sangiori et al., 2018).

During the Mid-Pliocene warming (3.3-3.0 million years ago), the global temperatures were 2-4°C warmer than present (Haywood et al., 2016), and sea levels were 10-25 m higher (Raymo et al., 2011; Miller et al., 2012; Oppenheimer et al., 2019). Given that the complete melting of the GrIS and WAISwould contribute only about 12 m to sea-level rise (Bamber et al., 2013; Fretwell et al., 2013), this implies that a significant contribution from the EAIS is necessary to account for the higher sea levels observed. Additionally, geological data (Cook et al., 2013; Patterson et al., 2014; Reinardy et al., 2015) and ice sheet model simulations (Austermann et al., 2015; DeConto and Pollard, 2016) indicate that marine-based sectors in the EAIS were unstable during these Pliocene warm intervals. For example, model simulations estimated a +11.26 m contribution to sea level rise from the EAIS under mid-Pliocene warming (Fig. 2.1, DeConto and Pollard, 2016), with mass loss predominantly from the Aurora, Wilkes and Recovery subglacial basins, with beds well below sea level (Gasson et al., 2016; Golledge et al., 2017). Indeed, geochemical evidence from sediments also points to substantial erosion of underlying bedrock during the Pliocene warming in the Wilkes Subglacial Basin (WSB) (Cook et al., 2013). This mass loss has been linked to the ice margin retreating by hundreds of kilometres inland during this period, contributing to 3-10 m of sea level rise (Cook et al., 2013). Similarly, Williams et al. (2010) found evidence of large quantities of ice-rafted debris (IRD) in Prydz Bay, which has been traced to have originated from bedrock sources in the Wilkes Land and Adélie Land. These findings point to episodes during the Pliocene when glaciers in these areas discharged large numbers of icebergs into the Southern

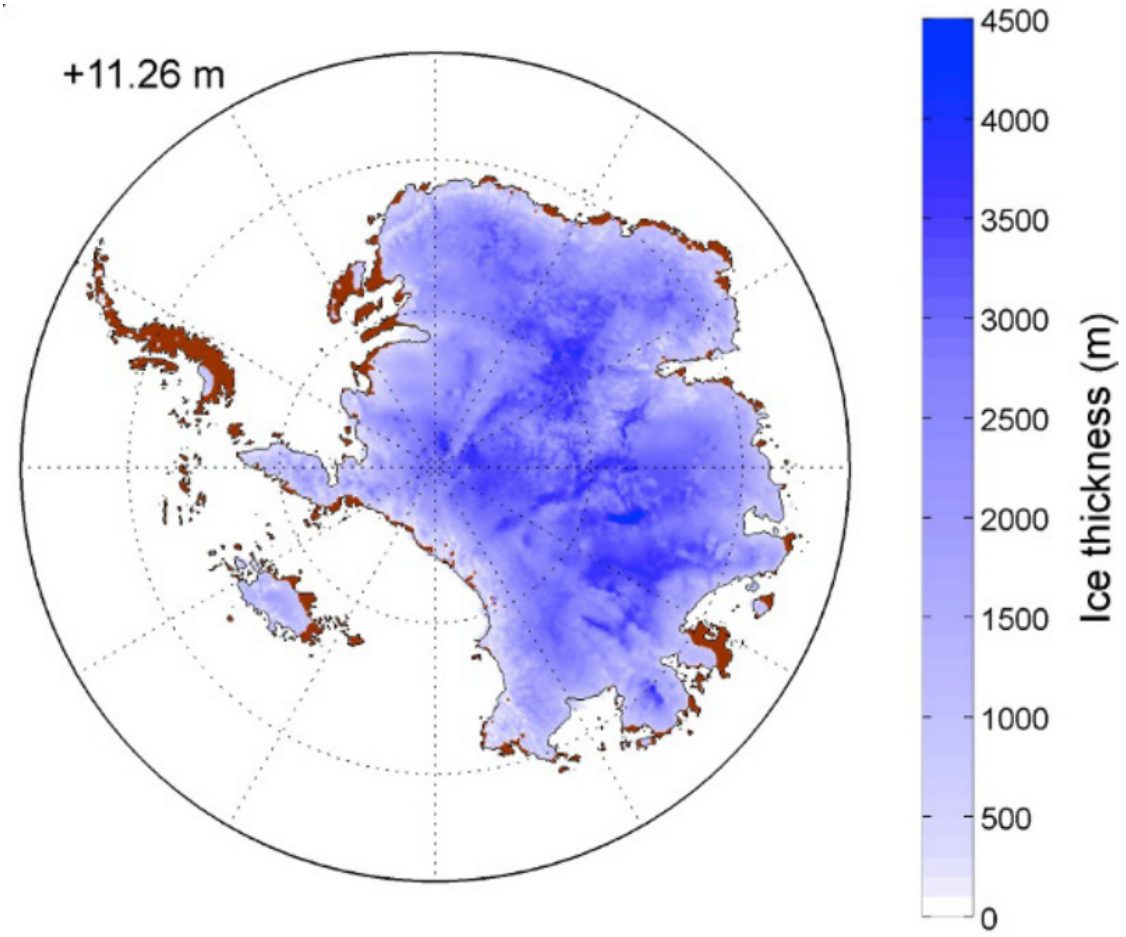

Figure 2.1: *Simulated Pliocene ice sheet configuration (DeConto and Pollard, 2016)*

Ocean. These IRD events are interpreted as evidence of rapid ice stream destabilisation and ice margin retreat, particularly near the marine-based sectors of Wilkes and Aurora Subglacial Basins (ASB) during Pliocene warming.

Furthermore, during the Last Interglacial (LIG) period—approximately 129,000 to 116,000 years ago—global temperatures were similar or only slightly warmer than today, likely around 1–1.5°C. During this time, the AIS contributed significantly to GMSL, with estimates indicating a sea level equivalent (SLE) contribution ranging from 1 to 7 m above pre-industrial levels (Hutchinson et al., 2024). The GMSL was 6-9 m higher compared to pre-industrial levels possibly driven by small increase in global mean temperatures and polar amplification (Dutton et al., 2015).

While much attention has been on the WAIS, emerging evidence and climate model simulations indicated that the EAIS also exhibited sensitivity to warming during

the LIG. Indeed, model simulations by DeConto & Pollard (2016) suggested that a partial ice loss from the AIS led to significant changes in surface elevation, which weakened southerly offshore winds (DeConto and Pollard, 2016). This atmospheric shift caused surface air temperatures over the EAIS to rise by 2-4 °C, with SSTs in the Weddell and Ross Seas increasing by up to 2 °C (DeConto and Pollard, 2016). Model simulations reveal that meltwater input during the LIG had a significant impact on ocean dynamics, leading to approximately 1 °C of subsurface warming along the EAIS coast (DeConto and Pollard, 2016), with an increase by around 2 °C in the Ross Sea. The combined effects of partial AIS removal and enhanced meltwater input in the model simulations resulted in greater subsurface warming and amplified Antarctic warming compared to either perturbation alone (Hutchinson et al., 2024). Interestingly, while these deeper ocean layers warmed, the same simulations show that high-latitude surface waters experienced a slight cooling effect (DeConto and Pollard, 2016). This subsurface warming could initiate a positive feedback mechanism for ice sheet disintegration through marine ice sheet instability (MISI) on reverse-sloping bedrock, which is present in the WSB and ASB of the EAIS (Fig. 2.2; Adhikari et al., 2014; Morlighem et al., 2020). Therefore, these regions could be particularly vulnerable to destabilisation. It is also worth noting that, ASB and WSB are among the largest and deepest regions with reverse-bed topography in the EAIS. Numerous other individual outlet glaciers across the EAIS also rest on reverse-sloping beds, for example, Ninnis, Recovery and Jutulstraumen (Fig. 2.2; DeConto & Pollard, 2016; Morlighem et al., 2020). Although these outlet glaciers may not be as wide or deep as the WSB and ASB, their underlying geometry still makes them susceptible to MISI-driven retreat. This highlights the importance of including both major basins and smaller outlet systems in assessments of modern and future ice sheet vulnerability.

Moreover, other model simulations estimated a sea-level contribution of 0.12 m to 1.14 m from the region spanning 120°E–180°E, which includes the Wilkes Subglacial Basin (WSB), under two different ice sheet retreat scenarios during the Last Interglacial (Hutchinson et al., 2024). These include SL4.1, which simulates the removal of 4.1 m sea level-equivalent ice using the RCP4.5–1900 CE climate anomaly, and

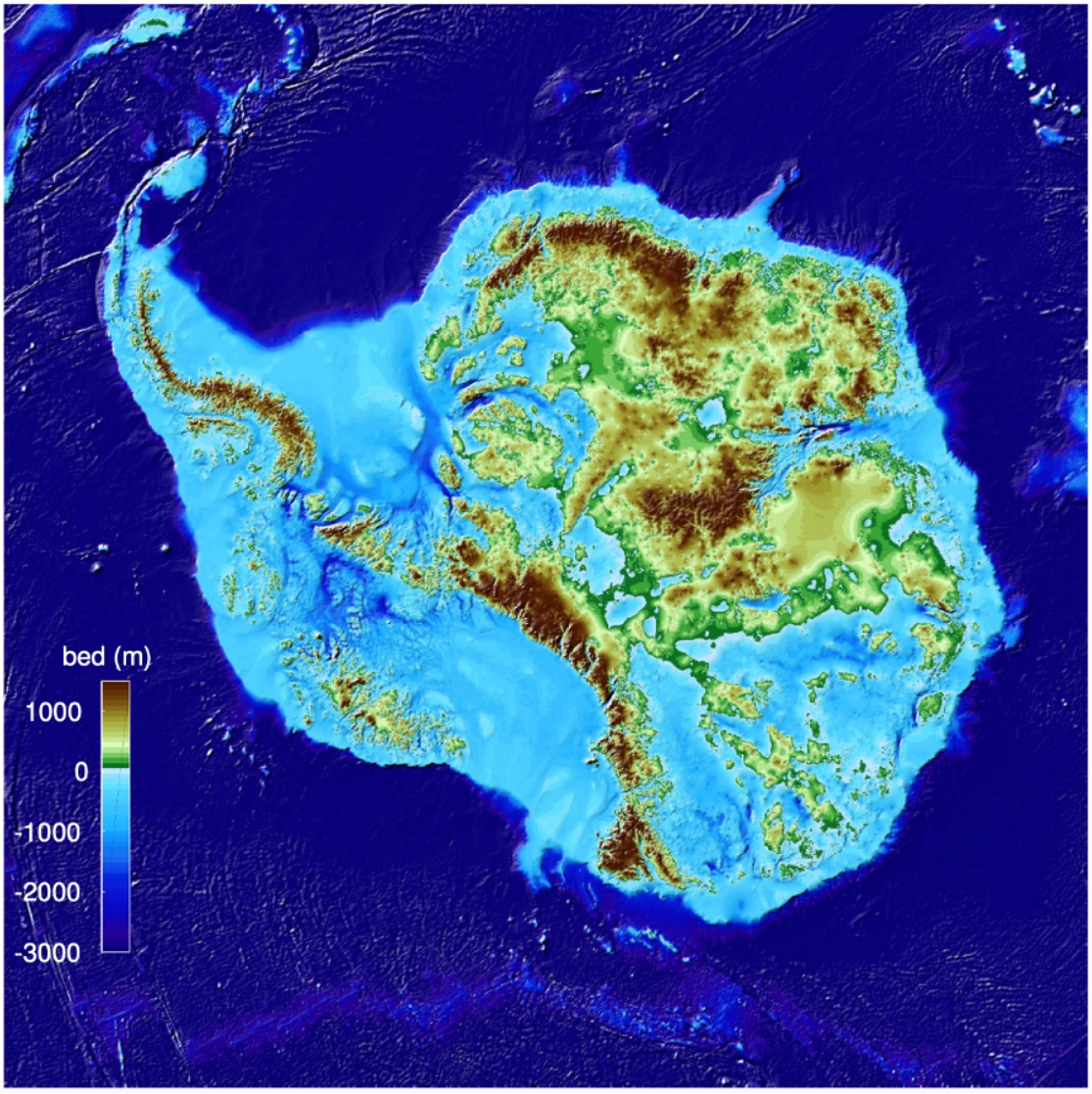

Figure 2.2: *Bed elevation of Antarctic Ice Sheet from Morlighem et al.,(2020). The White lines represent the basins (Rignot et al.,2019).*

SL7.1, which assumes the removal of 7.1 m sea level-equivalent ice using the absolute ice surface elevation from the RCP4.5 scenario (Golledge et al., 2015). These findings broadly align with earlier studies, which estimated a 0.4-0.8 m SLE contribution from the WSB during the LIG (Sutter et al., 2020). However, sedimentological and geochemical records also indicated significant retreat during the LIG from the WSB, which holds 3-4 m of SLE in marine-based ice (Wilson et al., 2018). This suggests that during LIG, WSB and ASB were the most vulnerable regions and may have experienced extensive retreat.

During the Last Glacial Maximum (LGM), approximately 27 ka to 20 ka years ago, the EAIS expanded significantly, with its marine-based sectors advancing nearly to the continental shelf edge (Bentley et al., 2014; Mackintosh et al., 2014). Deglaciation began around 19 ka to 18 ka and, by around 15 ka, grounding lines in the Ross Sea sector had retreated to the mid-continental shelf, marking the initial stages of ice sheet retreat from its maximum extent (Mackintosh et al., 2014; Livingstone et al., 2012; Anderson et al., 2014). In the Weddell Sea sector, grounding lines exhibited oscillating positions on the outer continental shelf until about 12 ka, indicating a more complex and fluctuating retreat pattern compared to other areas (Hillenbrand et al., 2014; Arndt et al., 2020). Bed topography played a crucial role in these dynamics with over deepened basins such as the Mertz Trough and western Ross Sea experiencing accelerated grounding-line retreat, while elevated bedrock in other regions slowed the retreat process (Mackintosh et al., 2014; Livingstone et al., 2012; Halberstadt et al., 2016; McKay et al., 2016; Jones et al., 2021). Additionally, positive feedback mechanisms, including the freshening of surface ocean waters and the intrusion of warm mCDW, further influenced grounding line retreat by facilitating continued ice loss (Mackintosh et al., 2014; Golledge et al., 2014; Lowry et al., 2019; Jones et al., 2021).

Ice-sheet models of the last deglaciation highlight that the most substantial ice losses occurred in major marine embayments like the Ross Sea, Weddell Sea and Prydz Bay, driven by a combination of oceanic warming, atmospheric temperature increases, and sea-level changes (Mackintosh et al., 2011; Whitehouse et al., 2012; Golledge et al., 2014; Noble et al., 2020). This historical behaviour emphasises that regions of the EAIS which underwent significant mass loss in the past may be similarly susceptible to present and projected temperature increases, highlighting the critical need for continued monitoring and research. In addition, several regions containing smaller outlet glaciers with reverse-sloping beds that terminate in the ocean—such as those in Enderby and Kemp Land as well as in Dronning Maud Land—remain poorly studied and are often absent from palaeoclimate investigations. In summary, both palaeoclimate evidence and numerical ice sheet models demonstrate that marine-based sectors of the EAIS have been sensitive to past episodes of climatic warming,

some of which were comparable to or exceeded current warming trends (Stokes et al., 2022). This highlights the importance of incorporating both major and smaller, less-studied basins into future vulnerability assessments.

2.3 Recent changes in the East Antarctic Ice Sheet and possible drivers

Over the past 3 decades, the APIS and the WAIS have been losing mass at a rate of -13 ± 5 Gt yr^{-1} and -82 ± 9 Gt yr^{-1}, respectively (The IMBIE Team, 2023). In WAIS, particularly in the Amundsen and Bellingshausen Sea sectors, widespread mass loss is observed inland of the grounding line as well as on the ice shelves across the WAIS (Fig. 1.2). In contrast, the EAIS has been estimated to have an overall mass budget of $+3 \pm 15$ Gt yr^{-1} between 1992 and 2020, with large spatial variability. Some basins have been gaining mass, while others experiencing mass loss. For example, as shown in Figure 2.3a, areas such as Queen Maud Land (QML), also known as Dronning Maud Land (DML) along with Enderby and Kemp Land exhibit mass gain inland of the grounding line. However, Wilkes, Oates and George V Land exhibited substantial mass loss. The mass loss in the WSB has been estimated at -8.2 ± 2.0 Gt yr^{-1} between 1992 and 2017 (Shepherd et al., 2019), with Totten Glacier alone contributing approximately -236 Gt of mass loss (~ -6.2 Gt yr^{-1}) between 1979 and 2017 (Rignot et al., 2019). In contrast, the mass gain in DML has been estimated at $+13.3 \pm 3.4$ Gt yr^{-1} between 1992 and 2017 (Shepherd et al., 2019), where the Shirase Glacier catchment and Jutulstraumen Glacier contributed approximately +46 Gt and +33 Gt to this mass gain between 1979 and 2017, respectively (Rignot et al., 2019). Note that, despite inland mass gain in regions such as DML, localised mass loss is still observed on its ice shelves, highlighting the complex spatial heterogeneity across the EAIS (Fig. 1.2).

Furthermore, Baumhoer et al. (2021) highlighted regional variations in outlet glacier terminus and ice shelf changes across the EAIS between 1997 and 2018 (Fig. 2.3). While some glaciers and ice shelves advanced, others retreated during each decade.

For example, during the first decade (1997–2008), Dronning Maud Land (DML), Coates Land, and Queen Mary Land experienced the highest advances at rates of 249 ± 14.9 km^2 yr^{-1} (A–Ap), 306 ± 7.8 km^2 yr^{-1} (K–A), and 380 ± 7.7 km^2 yr^{-1} (C–Cp), respectively. However, during the same period, the greatest loss occurred at the Ross East Ice Shelf, at approximately 400 km^2 yr^{-1} (Fig. 2.3). In contrast, the second decade (2009–2018) showed a much smaller total retreat across the EAIS, with losses primarily concentrated in Wilkes (Cp–D), Victoria (Dp–E), and Oates and George V Land (D–Dp), at rates of -97 ± 4.1 km^2 yr^{-1}, -81 ± 8.3 km^2 yr^{-1}, and -317 ± 4.3 km^2 yr^{-1}, respectively (Baumhoer et al., 2021).

This substantial variability in terminus position changes across the EAIS has also been reported by Miles et al. (2016) between 1970s and 2012. They observed the maximum retreat across the EAIS between 1974 and 1990 (Fig. 2.4a). During this period, the highest median retreat rates were estimated over DML (DB 5/6) at approximately -50 to -100 m yr^{-1}, followed by Enderby Land (DB7), Wilkes Land (DB13) and George V Land (DB 14) which retreated at a median rate of around -25 to -50 m yr^{-1}. This trend reversed in 1990–2000, when the majority of outlet glaciers advanced (Fig. 2.4b). Median advance rates reached approximately +100-200 m yr^{-1} in DML and about +50-100 m yr^{-1} in Wilkes Land. However, between 2000 and 2012, outlet glaciers continued to advance in most basins across the EAIS such as DML (DB5/6), Enderby Land (DB7) and Kemp Land (DB8), with the notable exception of Wilkes Land, where glaciers experienced continued retreat at median rates of ~ -50 to -100 m yr^{-1} (Fig. 2.4c). This underscores that the EAIS's response to climate change is highly variable over different timescales.

The mass balance across the EAIS is generally driven by a complex interplay of climatic and oceanic factors which exhibit significant spatial and temporal variability along with non-climatic factors. For instance, Miles et al. (2016) suggested that the anomalous retreat in Wilkes Land, where 74% glaciers retreated between 2000-2012 (Fig. 2.4c), could be attributed due to extreme reduction of number of sea ice days. They observed a reduction of approximately 11.5 sea ice days per year,

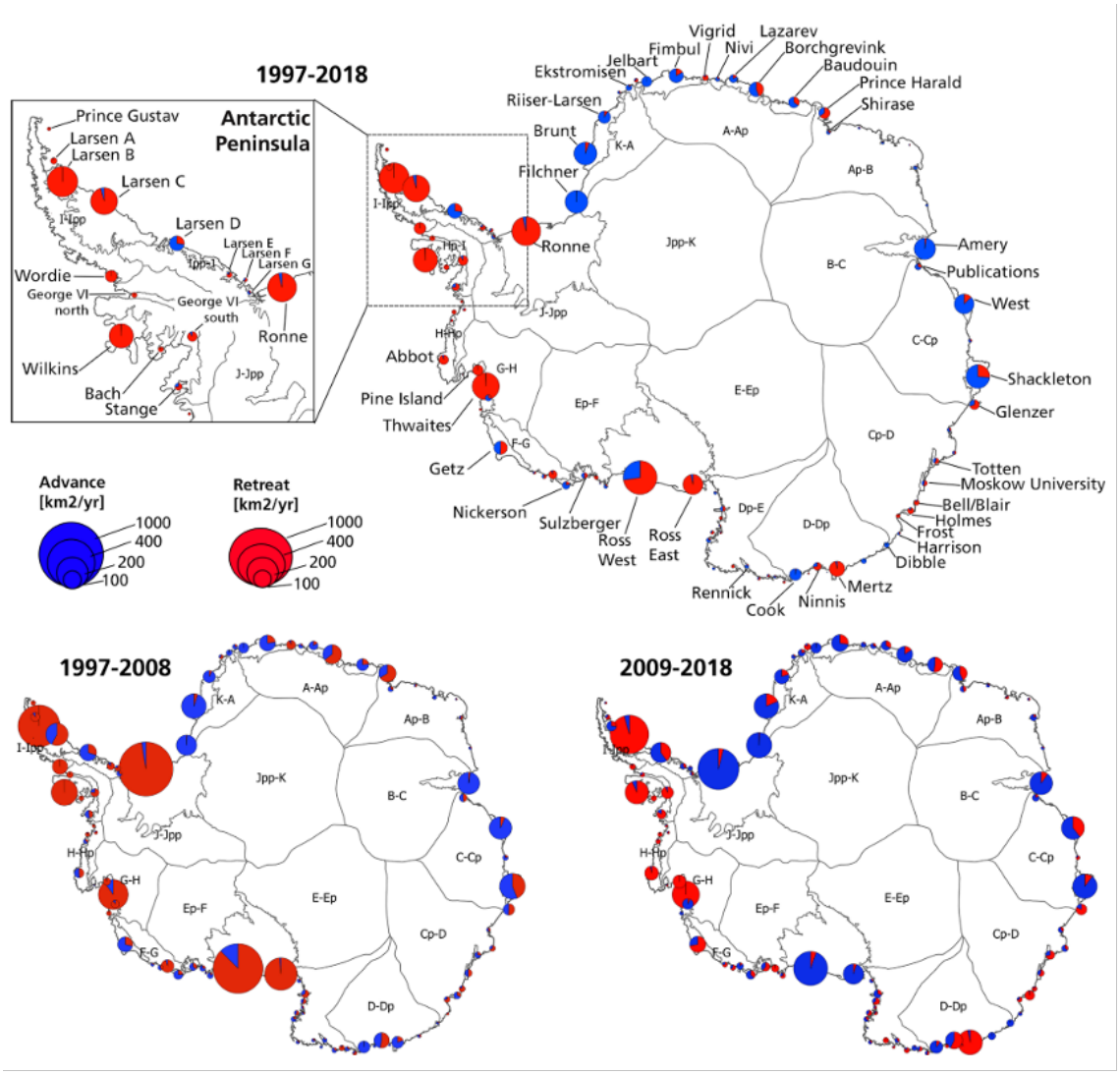

Figure 2.3: *Glacier and ice shelf extent changes for major glaciers and ice shelves over the last two decades. Circles indicate the rate of retreat or advance (Baumhoer et al., 2021).*

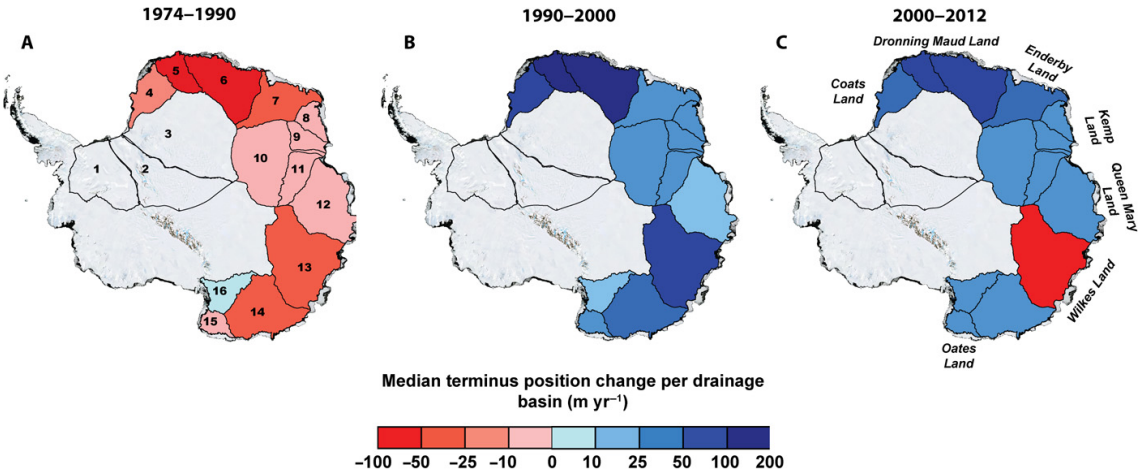

Figure 2.4: *Median terminus position change in each basin in the EAIS over three periods (a) 1974-1990, (B) 1990-2000 and (C) 2000-2012. Here, blue denotes advance and red denotes retreat (Miles et al., 2016).*

with maximum reduction of ∼27 days per year. However, between 2009-2018 when majority of glaciers in the Wilkes Land retreated, Baumhoer et al. (2021) could not find a link between glacier and ice shelf retreat and decrease in sea ice days. They suggested that this link could not be established here possibly because the decrease in number of sea ice days was minor, with only about 5 days below the long-term average. In comparison, Miles et al. (2016) reported a more pronounced decline of ∼34 sea ice days below average between 2000 and 2012. Therefore, Baumhoer et al. (2021) suggested that sea ice impacts glacier retreat primarily under extreme conditions, specifically when there is a drastic reduction in the number of sea ice days. Whilst for the retreat between 2009-2018, other factors could be in play such as upwelling of warm Circumpolar Deep Water (CDW), which could have led to increased basal melting and contributed to the observed glacier retreat.

On the other hand, non-climatic drivers could also play a crucial role in influencing mass balance, often interacting with climatic factors or amplifying their effects. These non-climatic influences include topography, geographical setting, pinning points and the presence or absence of ice shelves. For instance, WSB is located in a deep marine-based setting, with depths reaching 2000 m below sea level (Fretwell et al., 2013; Pritchard et al., 2025), with two deep troughs extending towards Cook and Ninnis ice shelves which discharges ice directly into the ocean (Rignot et al.,

2019; Wang et al., 2024). This topographic setting makes WSB sensitive to ocean forcing, where intrusion of warm mCDW into its troughs could significantly increase basal melt rates (Rignot et al., 2019). On the other hand, the presence of ice shelves provides buttressing to the outlet glaciers suppressing calving events and acceleration of ice discharge (Fürst et al., 2016). For example, the Larsen B Ice Shelf collapse in 2002 in the APIS led to a threefold increase in the flow speed of tributary glaciers in the Antarctic Peninsula (Rignot et al., 2004). In addition, the presence of pinning points—areas where ice shelves are grounded on topographic highs or islands provide critical resistance to ice flow. They provide buttressing and stabilises the flow of upstream ice. The loss of such pinning points due to enhanced basal melting or ice shelf thinning could lead to accelerated ice flow and mass loss. For example, on Thwaites Glacier, WAIS, loss of contact with its pinning points is projected to trigger irreversible retreat (Scambos et al., 2017). Therefore, understanding these factors is crucial for future climate models.

2.3.1. The role of atmospheric and oceanic forces in influencing changes across the EAIS

The mass gain, primarily localised in DML, is driven by enhanced snowfall (Davis et al., 2005; Shepherd et al., 2012). A notable snowfall event in May 2009 and February 2011 (Lenaerts et al., 2013; 2019; Gorodetskaya et al., 2014) resulted in the deposition of approximately +200 Gt of snow, which constituted a substantial fraction of the total mass gain observed in the EAIS throughout the satellite observational era (Shepherd et al., 2012). In addition, there was another significant snowfall event that occurred in February 2003, which was linked to a persistent blocking high that directed moisture into the region (Schlosser et al., 2010). Nevertheless, the specific climatic conditions that led to this anomalous snowfall event remain unclear, prompting questions about whether the anomaly was caused by atmospheric warming or fell within the range of natural variability.

Simon et al. (2024) highlighted that extreme precipitation events in DML are driven by a combination of atmospheric rivers, orographic effects, wind patterns, synoptic conditions, and inter-annual variability, all of which interact to create the

extreme precipitation observed in this region. Such extreme precipitation events arise from north-easterly to easterly winds, atmospheric rivers channelling moist air from subtropical regions, coupled with a dynamic east-west configuration of a mid-tropospheric ridge alongside a low-pressure centre directing these air masses (Schlosser et al., 2010; Baiman et al., 2023). On the other hand, the mass gain at Shirase Glacier catchment that began around 2000 (Schröder and others, 2019; Smith and others, 2020), has been attributed to a thickening of the floating ice tongue (Schröder and others, 2019; Smith and others, 2020) due to strengthening of alongshore winds. These winds reduce the intrusion of warm mCDW onto the continental shelf, which lowers basal melt rates under the ice tongue. This reduced melting allows the ice tongue to thicken dynamically. Additionally, this thickening enhances the buttressing effect near the grounding line, which contributes to a slowdown in ice discharge and grounding line advance (Miles et al., 2023). Furthermore, Miles et al., (2013) previously found that between the Ross and Shackleton Ice Shelves, 63% of floating glaciers retreated from 1974 to 1990, followed by 72% advancing from 1990 to 2000, and 58% continuing to advance through 2010. These changes were most evident along the warmer South Pacific coast, where glacier retreat was closely linked to rising summer air temperatures and a shift to the positive phase of the Southern Annular Mode (SAM) in the 1990s, likely driven by ozone depletion. In contrast, glaciers in the colder Ross Sea region showed little change, remaining largely stable.

Furthermore, since 2016 the AIS has experienced a substantial reduction in sea ice extent (Fig. 2.5; Parkinson et al., 2019; Fogt et al., 2022).In February 2022, Antarctic sea ice reached a new record low (Raphael & Handcock, 2022), followed by another record-low sea-ice extent in February 2023, with unusually low levels persisting through to June 2023 (Fig. 2.5; Josey et al., 2024). Most strikingly, an exceptional reduction in sea ice coverage was also observed during the winter months of 2023 (June–July) relative to the 1990–2015 baseline. In June alone, the sea ice extent anomaly measured 2.33 million square kilometres below the 1979–2022 mean for that month—marking the most negative anomaly in the entire satellite observation record (Purich & Doddrich, 2023). This decline was especially pronounced in

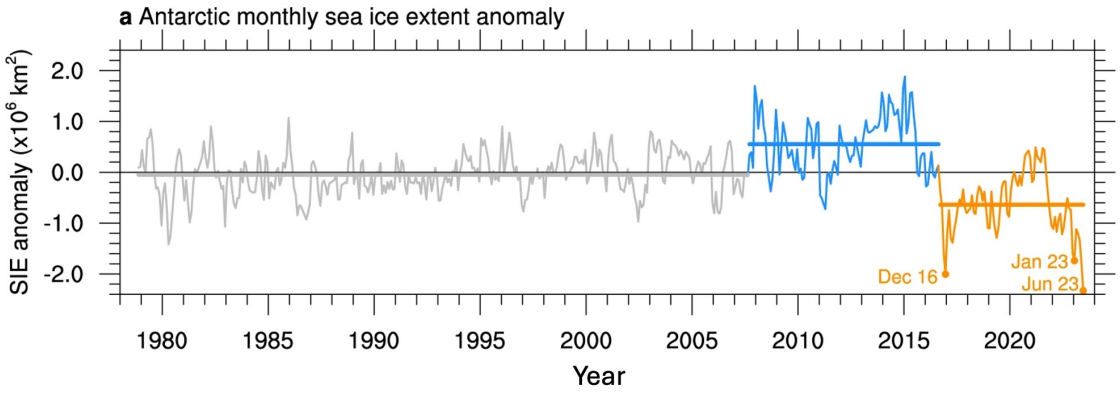

Figure 2.5: *Monthly Antarctic sea ice extent (SIE) anomaly time series from November 1978 to June 2023, derived from satellite observations provided by the National Snow and Ice Data Center (NSIDC). Anomalies were computed relative to the 1979–2022 climatological baseline. Two statistically significant change points divide the time series into three periods: November 1978 to August 2007 (grey), September 2007 to August 2016 (blue), and September 2016 to June 2023 (orange). The mean anomaly for each period is indicated by horizontal lines (Purich & Doddrich, 2023).*

three key sectors: the Weddell Sea, Ross Sea, and Bellingshausen Sea, where 80% reduction in sea ice was observed. Additionally, Enderby Land experienced a 50% decrease in winter sea ice relative to the long-term average (Purich & Doddrich, 2023). Moreover, this period was characterised by an unprecedented doubling of mid-winter oceanic heat loss, indicating a significant perturbation in the coupled ocean–ice system (Josey et al., 2024).

Previous studies have highlighted that presence of sea ice provides buttressing to the ice shelves and floating ice tongues, delaying calving events (Massom et al., 2010). Disintegration of the Porpoise Bay has been associated with formation of meltwater ponding on multi-year landfast sea ice, driven by atmospheric anomalies which further leads to weakening and fracturing of the landfast sea ice, which ultimately reduces buttressing and triggers disintegration (Miles et al., 2016). Similarly, the complete disintegration of the Parker Ice Tongue in Victoria Land in March 2020 was triggered by the breakup of summer fast ice (Gomez-Fell et al., 2022). Conversely, the mechanical coupling of multi-year sea ice with the Mertz floating ice tongue delayed its calving (Massom et al., 2010). Thus, long-term decline in sea ice

coverage could lead to collapse of ice shelves and floating ice tongues, primarily due to their prolonged exposure to ocean swells and increased wave-induced stress. For example, Miles et al. (2016) observed a strong link between extreme reduction in number of sea ice days and glacier retreat in Wilkes Land.

2.3.2. The role of ice shelves in glacier retreat

Ice shelves fringe approximately three-quarters of the Antarctic coastline, playing a critical role in stabilising the ice sheet. A recent study by Andreason et al. (2023) found that between 2009 and 2019, the AIS experienced a modest net gain of ice shelf area, increasing by about 0.4% (5,305 km^2). This overall gain was primarily driven by two largest ice shelves: Ronne–Filchner and the Ross Ice Shelf, which grew by 14,028 km^2 (1.5%) and an additional gain of 3,532 km^2 (1.3%) in the EAIS. These increases offset significant ice shelf ice losses in the APIS ($-6,692.5$ km^2) and WAIS ($-5,563$ km^2), relative to their 2009 areas. In the EAIS, most ice shelves exhibited gains, although a few—namely Baudouin, Totten, Mertz, and Nansen—experienced mass losses of -5, -4, -50, and -2 Gt yr^{-1}, respectively (Fig. 2.6). Despite these localised losses, the region as a whole gained approximately 51 Gt yr^{-1} of ice over the 2009–2019 period.

These ice shelves serve as a "safety band" by restraining the flow of grounded ice and reducing mass loss through their buttressing of inland ice flow (Fig. 2.7; Bindschadler et al., 2011; Fürst et al., 2016). These floating extensions transmit buttressing forces to upstream regions through shear at lateral confinements and grounded pinning points, such as ice rises and rumples, which anchor the shelves to the seafloor (Miles et al., 2024). The stability provided by these ice shelves helps regulate ice discharge across grounding lines, where ice transitions from grounded to floating. For example, the Fimbulisen, which consists of multiple pinning points, has been thickening at $+0.3 \pm 0.15$ m yr^{-1} between 1992 and 2017 (Hogg et al., 2021). These pinning points has been contributing to the stabilisation of the ice shelf and reducing the flow of grounded ice into the ocean.

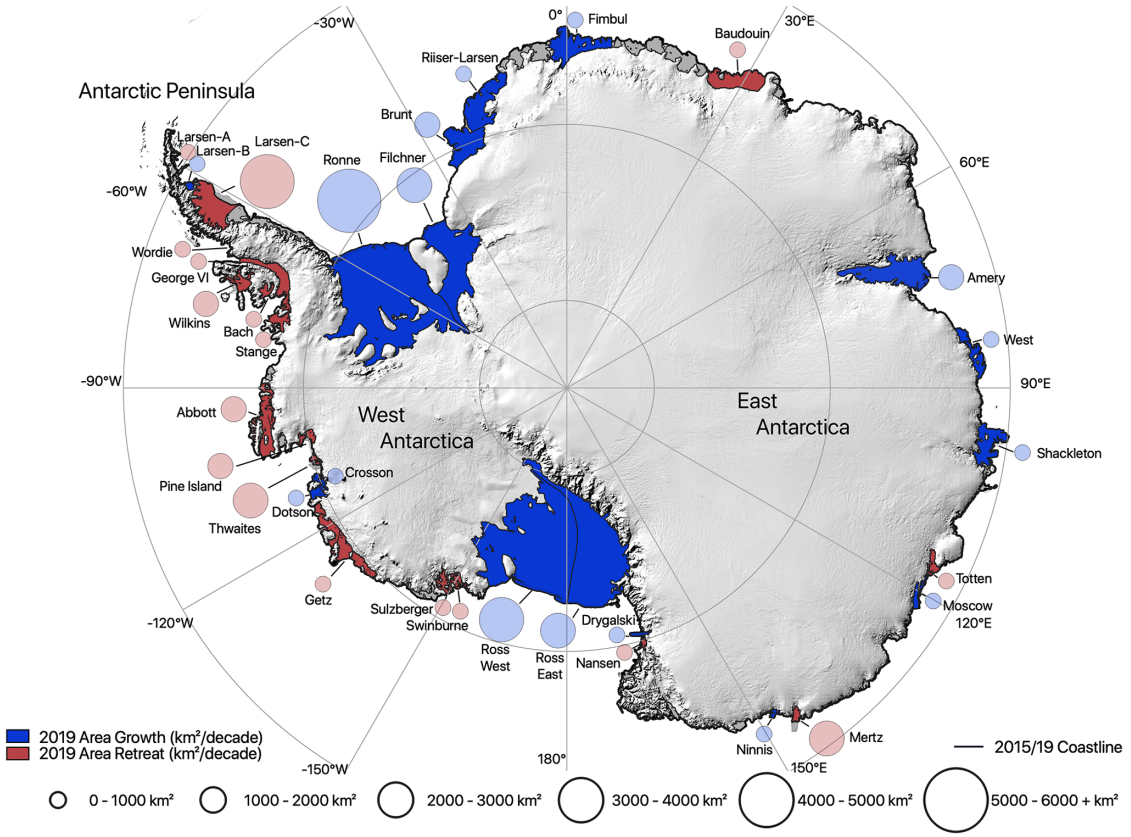

Figure 2.6: *Map of Antarctic ice shelf area changes from 2009 to 2019, overlaid on the Bedmap2 surface of Antarctica with labeled ice shelf names. Circle sizes indicate the total area of ice shelves lost (red) or gained (blue) in square kilometers. The bold black line represents the Antarctic coastline, based on combined data from 2015 and 2019 (Andreason et al., 2023).*

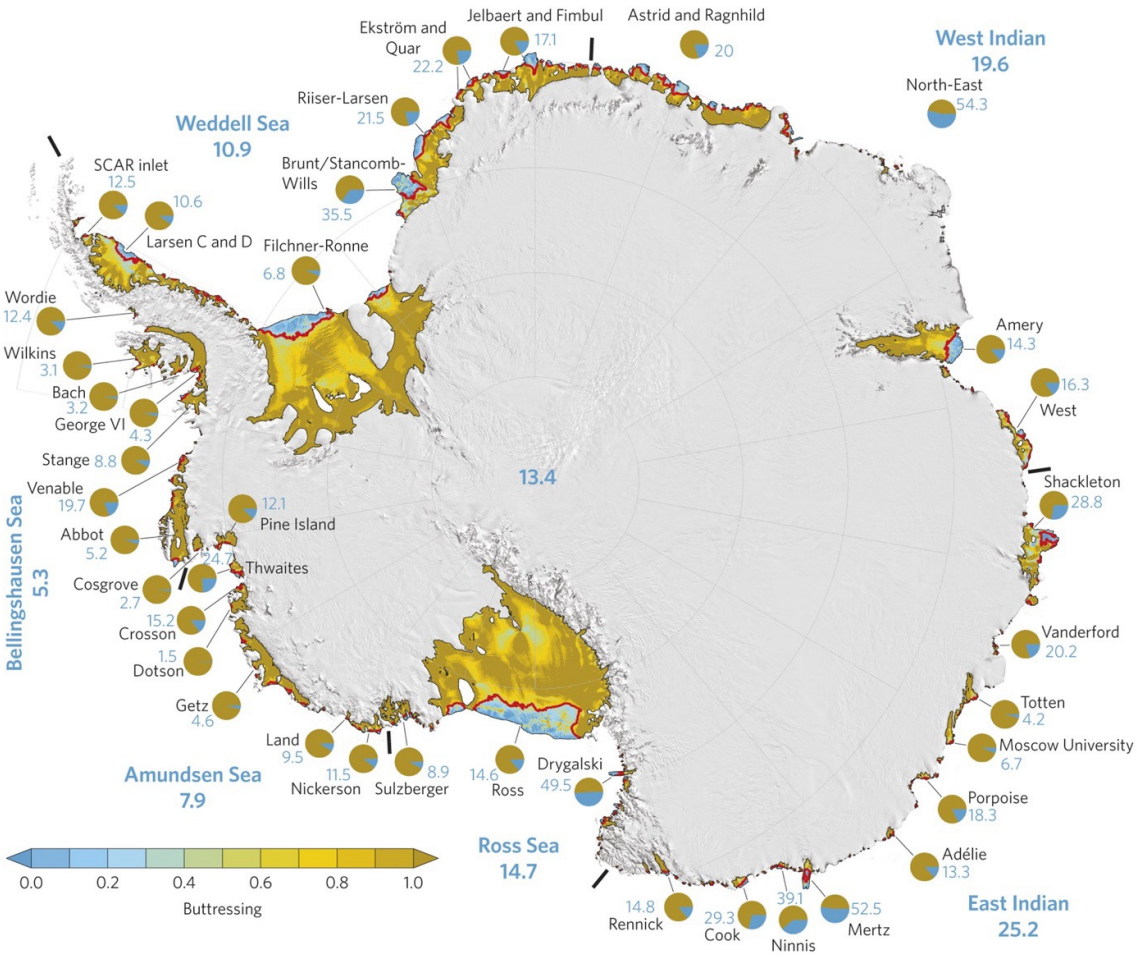

Figure 2.7: *Maximum buttressing of Antarctic ice shelves, with the relative proportion of passive ice recorded for each ice shelf (Furst et al., 2016).*

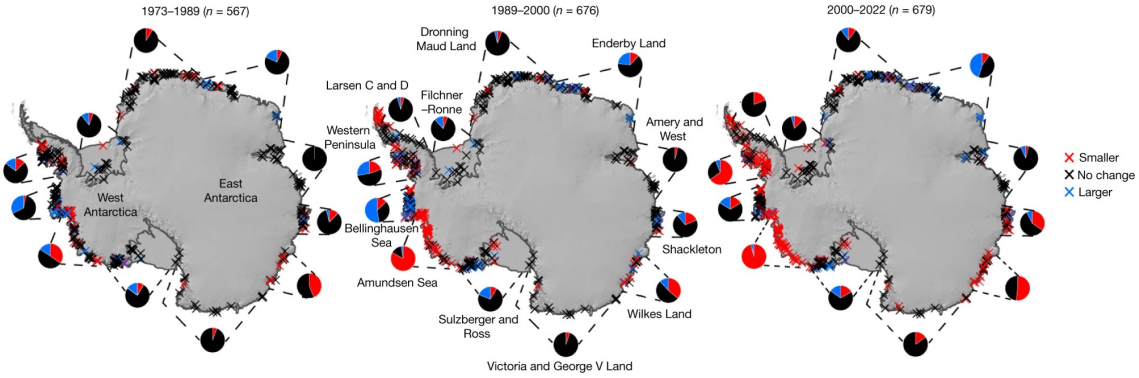

Figure 2.8: *Proportion of change in pinning point area over three time periods: 1973-1989, 1989-2000 and 2000-2022 from Miles et al. (2024).*

However, recent findings by Miles et al. (2024) highlights that the spatial extent of these pinning points have declined in the past few decades. Between 1973 and 1989, 15% decline in pinning point extent was observed, which increased to 25% during the 1990s and further to 37% between 2000 and 2022 (Fig. 2.8). This 25% decrease in the extent of pinning points during the 1990s coincides with a period of rapidly ice shelf thinning across Antarctica during the 1990s and 2000s. This progressive loss of pinning point extents could weaken the buttressing provided by the ice shelves and contribute to enhanced glacier flow and upstream mass loss.

The loss of buttressing as a result of disintegration or collapse of ice shelves, such as Larsen A in 1995 (Royston & Gudmundsson, 2016) and Larsen B in 2002 (Rack and Rott, 2004) leads to accelerated flow of its tributary glaciers into the ocean, with some glaciers experiencing up to an eightfold increase in velocity (Rignot et al., 2004; Scambos et al., 2004). In the EAIS, the weakening of the buttressing effect of ice shelves is primarily caused by the influx of warm mCDW into ice shelf cavities driven by a poleward shift in ocean currents (Herráiz-Borreguero et al., 2015; Turner et al., 2022). This is particularly observed in Wilkes Land, where mass loss is most pronounced (Pritchard et al., 2009; Flament & Remy, 2012; Li et al., 2015, 2016; Rintoul et al., 2016; Shen et al., 2017; Xia et al., 2023). The persistent presence of warm mCDW is particularly concerning, as it melts ice shelves from below, reducing their thickness and structural integrity, destabilizes the ice sheet, ultimately leading to debuttressing and increased glacier discharge (Rintoul et al.,

2016; Rignot et al., 2019; Stokes et al., 2022). In fact, the Totten Ice Shelf (TIS) in Wilkes Land experienced basal melt rates averaging $\sim 9.1 \pm 4.6$ m yr^{-1} (Xia et al., 2023), resulting in significant thinning, grounding line retreat, and increased ice flow into the ocean (Greene et al., 2017; Achter et al., 2022). Furthermore, recent studies reveal that subglacial freshwater drainage from the interior of the ice sheet to the coast (Wright et al., 2012; Young et al., 2016) can also enhance basal melting, further accelerating glacier retreat (Pelle, 2024; Gwyther et al., 2023). The presence of dynamic subglacial water systems exacerbates ice flow and mass loss, underscoring the complex interplay between subglacial hydrology and ice dynamics (Pelle, 2023). For example, the thinning of the Roi Baudouin Ice Shelf has been linked to changes in subglacial hydrology and oceanic conditions, which reduce the ice shelf's ability to buttress grounded ice (Drews et al., 2017). Areas where warm water enters ice shelf cavities experience the highest thinning rates, significantly compromising the stability of both the ice shelf and the grounded ice it supports (Herráiz-Borreguero et al., 2015).

Furthermore, the melting of ice shelves has broader implications on ocean circulation patterns. As ice shelves melt, they release freshwater into the ocean, disrupting salinity and density-driven circulation, slowing deep water formation, and altering heat transport. These disruptions can trigger cascading effects throughout the global climate system, highlighting the essential link between ice shelf dynamics and ocean circulation (Adusumilli et al., 2020; Hirano et al., 2020). Additionally, as ice shelves thin and retreat, feedback mechanisms may intensify the EAIS's response to climate change, potentially accelerating future mass loss (Greene et al., 2017). Pattyn et al. (2017) used a fast Elementary Thermomechanical Ice Sheet (f.ETISh) model on multi-centennial timescales and found that complete removal of ice shelves in the model simulation could result in collapse of the WAIS and significant mass loss in certain parts of the EAIS, particularly marine basins. After 500 years, this could lead to a sea-level rise of about 5 metres when using a power-law basal sliding condition, and up to 16 metres when using a Coulomb friction condition at the grounding line. This suggests that ice shelves play a crucial role in stabilising the AIS, and their loss could lead to substantial ice mass loss across the continent. In addition, the melting

underneath the floating ice shelves, and especially by the basal conditions at the grounding line plays the biggest role in how much ice is lost. These interconnected processes emphasise the role of ice shelves in regulating regional ice dynamics and contributing to global sea-level changes.

2.4 Anticipating the Future: Predicting the EAIS's Impact on Sea Levels

Recent modelling studies indicate that if global warming is limited to 2°C or less, Antarctic ice loss is expected to proceed at rates similar to current levels throughout the 21st century (Pattyn et al., 2018). However, scenarios aligned with current policies, allowing for up to 3°C of warming, predict a significant acceleration in ice loss starting around 2060 (Golledge et al., 2017; DeConto et al., 2021; Stokes et al., 2022;). Moreover, Stokes et al. (2025) suggests that +1.5 °C of warming is already too high for Antarctic ice sheets, even current forcing (+1.2 °C above pre-industrial) is likely sufficient to commit the WAIS to irreversible retreat. Under more aggressive, fossil-fuel-intensive scenarios, this acceleration could be even greater. Ice-sheet retreat, driven by the thinning and loss of buttressing ice shelves, is projected to persist for centuries, leading to irreversible sea-level rise of up to 3.5 meters if key glaciers collapse (Greene et al., 2017; Hirano, 2023). Projections by DeConto et al. (2021) emphasise the potential of the AIS to contribute significantly to future sea-level rise, ranging from 0.5 to 2.5 meters by 2100 under varying emission scenarios. A critical driver of this contribution is the interaction between warming ocean waters and ice shelves, especially in marine-based sectors.

Some modelling studies suggest that interaction between warm ocean conditions and ice shelves could trigger Marine Ice Cliff Instability (MICI), a mechanism where retreating ice shelves expose tall cliffs that structurally fail and are prone to collapse, thereby accelerating ice discharge. For example, Bronsealer et al. (2018) projected that EAIS could contribute up to 1 m by 2100 if MICI is triggered under high emission scenarios (RCP8.5). However, the inclusion of MICI in models has been largely

based on a single, simplified parameterization and with lack of direct observational support. Recently, Morlighem et al. (2024) tested the vulnerability of Thwaites Glacier in the WAIS to MICI using three independent ice sheet models. They found that even under high emission scenarios the models did not exhibit ice cliff collapse this century. Instead, they suggested that dynamic feedback such as rapid ice flow acceleration and thinning resulted in stabilising the ice front. They concluded that MICI was unlikely to initiate under expected 21st-century conditions. Moreover, other studies (e.g. Bassis et al., 2021) indicated that significant retreat could occur through Marine Ice Sheet Instability (MISI) alone, without invoking MICI, particularly where grounding lines retreat on retrograde slopes. In fact, DeConto et al. (2021) suggested that MISI and MICI do not play a key role until 2100 but could have influence after 2100.

Until recently, much of such research has been focused on the WAIS due to its inherently unstable marine-based sectors, with retrograde bed slopes and bedrock sitting at 100-1000 m below sea level (Fig. 2.2; Fretwell et al., 2013; DeConto & Pollard, 2016; Morlighem et al., 2020). However, parts of the EAIS, once considered more stable, are now acknowledged as vulnerable to future climate change and recognised for its potential impact on sea level rise (Golledge et al., 2016; 2017; DeConto & Pollard, 2016). The EAIS also contains deep subglacial basins with retrograde bed slopes including troughs with ∼1500 m depth at some glaciers (Fig. 2.2; Fretwell et al., 2013; DeConto & Pollard, 2016; Morlighem et al., 2020). Recent studies have also drawn parallels between WAIS and EAIS, as the EAIS is increasingly exposed to warm mCDW intrusions, grounding line retreat, and loss of ice shelf buttressing at certain regions. However, the EAIS contributions to sea-level rise are projected to occur over a longer timescale (Turner et al., 2017; Padman et al., 2018; Noble et al., 2020).

A modelling study by DeConto et al. (2021) used a coupled ice sheet and climate dynamics model which incorporated key processes such as surface melt induced hydrofracturing, MISI and MICI. They found that significant ice loss from the EAIS is unlikely unless global warming exceeds 2°C above pre-industrial levels, underscor-

ing a relatively higher resilience compared to the WAIS under moderate-emission scenarios. Under RCP 2.6, the EAIS remains largely stable with no net ice loss projected before 2100 and only a small 20 cm contribution to sea-level rise by 2500 (Fig. 2.7a). However, under RCP 4.5 scenarios, two major marine-based subglacial basins, WSB and ASB, particularly the Totten Glacier and Law Dome region emerge as key contributors (Fig. 2.7b). These areas could contribute a 5 m GMSL rise by the year 2500, if sustained warming persists. In the RCP 8.5 scenarios, rapidly increasing summer air temperatures are projected to drive extensive surface meltwater production and hydrofracturing of ice shelves by the mid-21st century. While WAIS glaciers could undergo substantial retreat within 250 years, the EAIS response is more gradual due to thicker ice and only a few marine-based sectors. Nevertheless, EAIS is projected to contribute substantially to long-term sea-level rise, especially in vulnerable regions such as WSB, ASB and Recovery Subglacial Basin (RSB) (Fig. 2.9c). Simulations show that the WSB and ASB undergo a more gradual retreat, with ice thickness above flotation exceeding 2,000 m. Despite this gradual response, these regions are projected to contribute over 4 cm per year to sea-level rise in the following century, surpassing the rate of the RSB, which is expected to contribute around 3 cm per year (Fig. 2.10). This highlights that while the WAIS responds more rapidly to atmospheric warming, the gradual retreat of the WSB and ASB is triggered by prolonged warming over a longer timescale.

Earlier work by DeConto and Pollard (2016) demonstrated that ocean warming also plays a key role in influencing the behaviour of individual outlet glaciers during the early stages of their simulations. However, their findings emphasise that atmospheric warming is the primary driver of long-term sea-level rise under RCP 4.5 and RCP 8.5 scenarios, as it triggers widespread surface meltwater production. In addition, DeConto and Pollard (2015) argued that, without atmospheric warming, the levels of ocean warming projected under RCP 8.5 are insufficient to cause substantial retreat of the WAIS or EAIS basins. This contrasts with earlier studies (e.g., Golledge et al., 2015; Winkelmann et al., 2015; Feldmann et al., 2015), which placed greater emphasis on ocean warming as the dominant factor in driving ice sheet retreat.

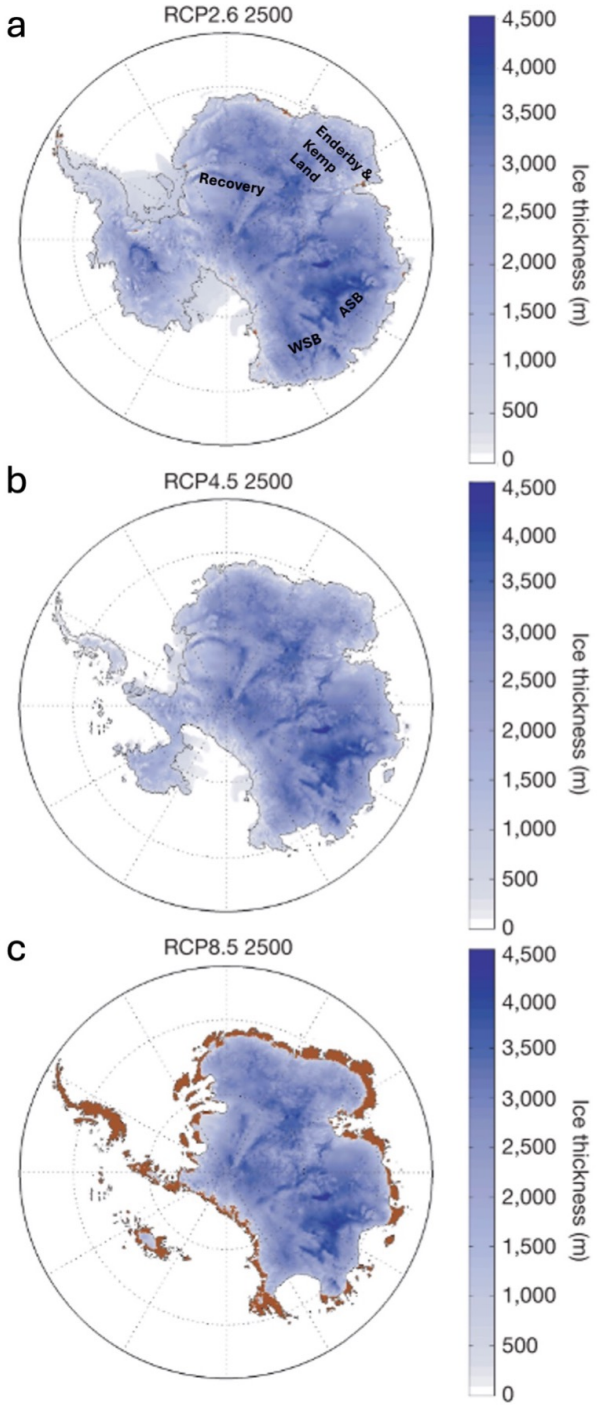

Figure 2.9: *Simulated ice-sheet configurations for the year 2500 under different emission scenarios: (a) RCP 2.5, (b) RCP 4.5, (c) RCP 8.5. Ice-free land surfaces are depicted in brown (DeConto and Pollard, 2016). Notable are the significant retreats observed in the Aurora (ASB), Recovery, and Wilkes Subglacial Basins (WSB) under RCP 4.5 (b) and RCP 8.5 (c) scenarios.*

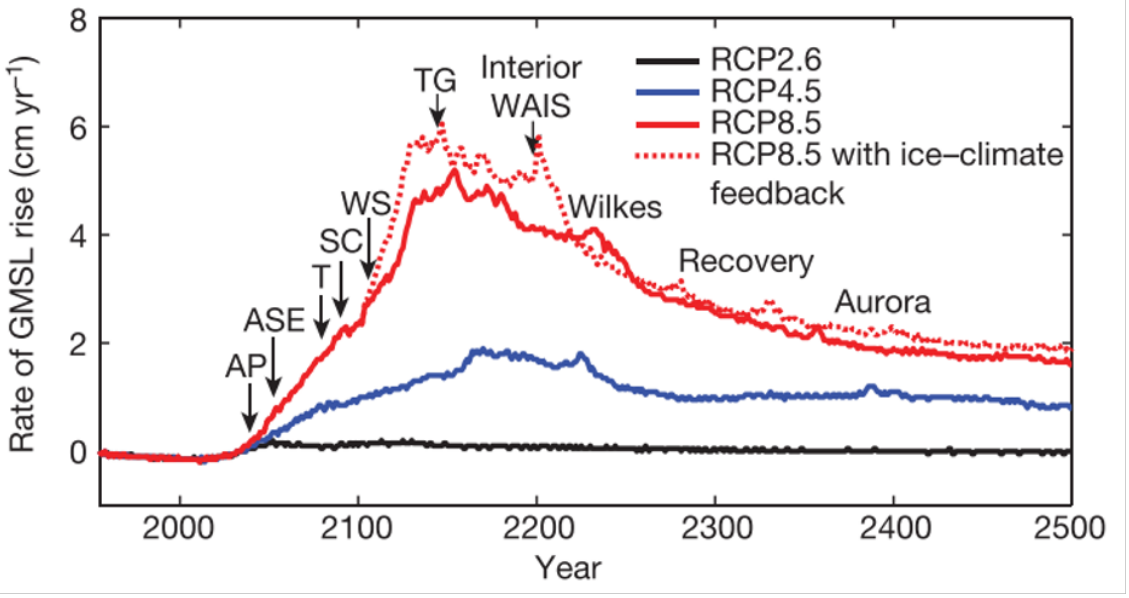

Figure 2.10: *Rate of sea-level rise and approximate timing of major retreat and thinning (DeConto & Pollard, 2016).*

More recently, Seroussi et al. (2024) used an ensemble of 16 ice-flow models and forcing from global climate models to provide a projection of the Antarctic ice sheet contribution to sea level rise until 2300. Under SSP2-4.5 scenario, the EAIS begins to exhibit a more pronounced response, particularly in its marine-based sectors such as the Totten Glacier region of the ASB and the WSB. These areas are especially susceptibility to ocean-driven basal melting and ice shelf collapse, resulting in projected EAIS contributions of up to 0.6 meters by 2300. The most substantial changes are projected under high emission, SSP5-8.5 scenario, when contribution to GMSL from the EAIS increases markedly. By 2100, EAIS is projected to either gains mass or experience minimal changes (Fig. 2.11a). However, by 2200, the mass loss rapidly increases and EAIS is projected to contribute between -0.2 and 0.2 m SLE (Fig. 2.11b). By 2300, the sea level contribution from the EAIS is projected to further increase. While the CCSM4 climate model projects that EAIS contributes to small changes, the other three climate models project larger contribution of 0.3–0.6 m SLE (Fig. 2.11c). By this time (2300), widespread thinning is projected across much of Wilkes Land and Queen Maud Land, with slight thinning also projected along the coastal margins of regions such as Enderby and Kemp Land (Fig. 2.12c). In addition, large grounding line retreat is particularly projected in Totten, Moscow

University, Cook, and Ninnis glaciers (Fig. 2.13c). Moreover, regions such as DML and Kemp Land were also projected to undergo slight grounding line retreat by 2300. Enderby Land, however, remains largely grounded until 2300 (Fig. 2.13a-c). These rates of grounding line retreat in areas of retrograde bed slopes are largely attributed to the bedrock topography (Jones et al., 2021; Seroussi et al., 2017). Under the high emission scenarios, several models project GMSL contributions from the EAIS exceeding 1 m by 2300, primarily driven by the retreat of marine-based sectors, intensified surface melting, and dynamic ice loss from major glaciers such as Totten and Denman (Seroussi et al., 2024).

Golledge et al. (2017) also explored the EAIS response to future warming scenarios using use an ensemble of idealised climates to drive ice-sheet simulations, emphasising the significance of regional and basin-specific factors in modulating ice sheet dynamics (Fig. 2.14). Their findings reveal that the Recovery catchment in the eastern Weddell Sea is particularly sensitive to ocean warming whilst the WSB and ASB are more sensitive to atmospheric warming at longer timescales. The study attributes these differences to variations in basin topography. In the Recovery basin catchment, the grounding line is situated below sea level and terminates in a floating ice shelf, making it highly vulnerable to ocean-driven thermal erosion. In contrast, the WSB and ASB are stabilised by topographic high points at their seaward margins, preventing significant grounding-line retreat unless atmospheric warming exceeds a threshold of 4°C. Above this threshold, ice loss in these basins increases linearly with rising atmospheric temperatures, driven primarily by surface melt and ice surface lowering. This is interesting because despite similar climate forcings, the glaciological response depends on ice geometries which will provide heterogeneous responses across EAIS basins to future warming scenarios. However, each model has its own limitations. For instance, the coarse resolution (20 km) may fail to capture narrow subglacial troughs that facilitate the intrusion of warm mCDW, leading to increased basal melting. Additionally, DeConto and Pollard (2015, 2016) include MICI in their model, which results in more extensive and rapid ice margin retreat compared to this model.

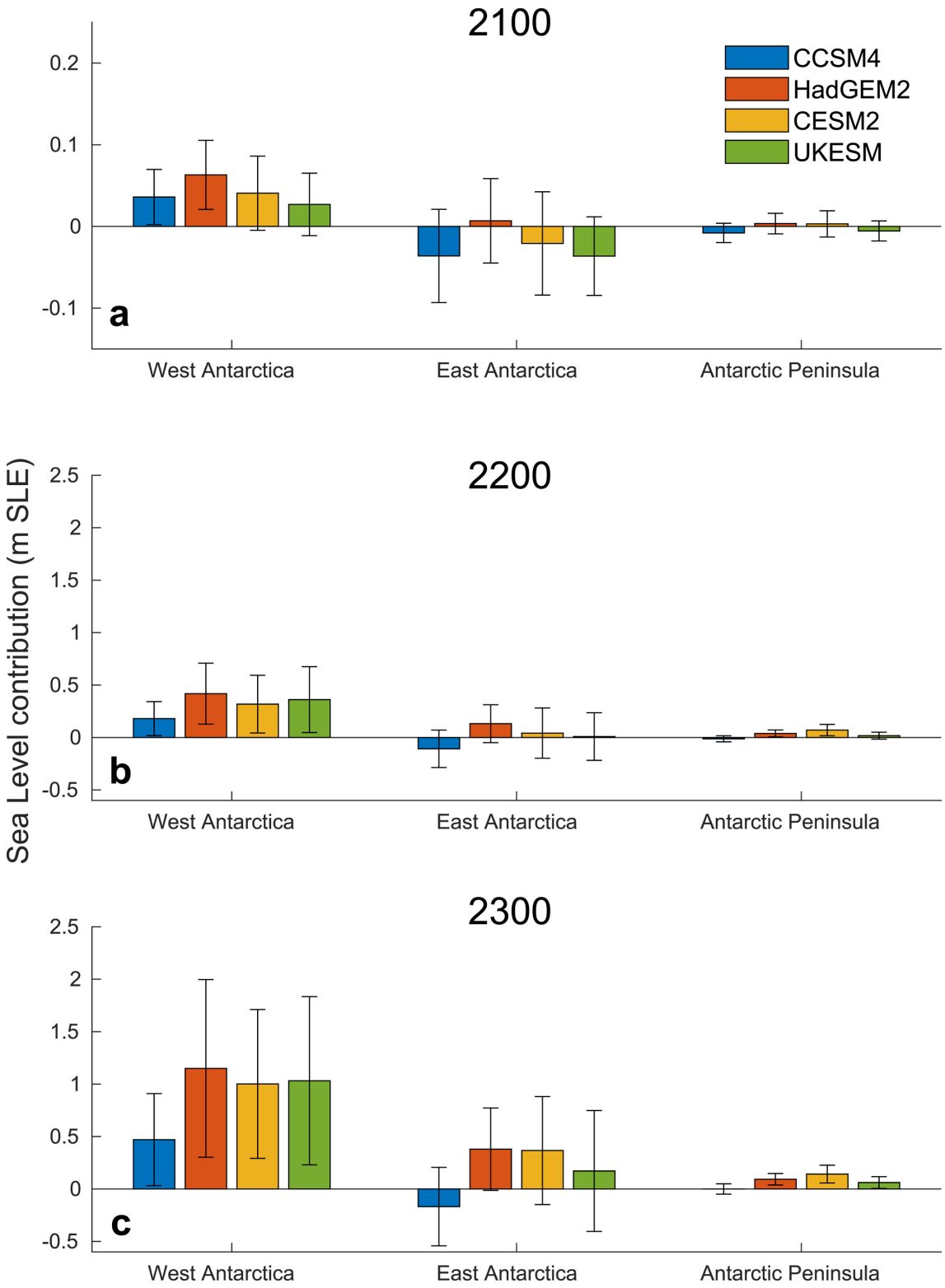

Figure 2.11: *Changes in modelled sea level contributions at years 2100, 2200, and 2300 under high emission climate forcings for WAIS, EAIS and APIS (Seroussi et al., 2024).*

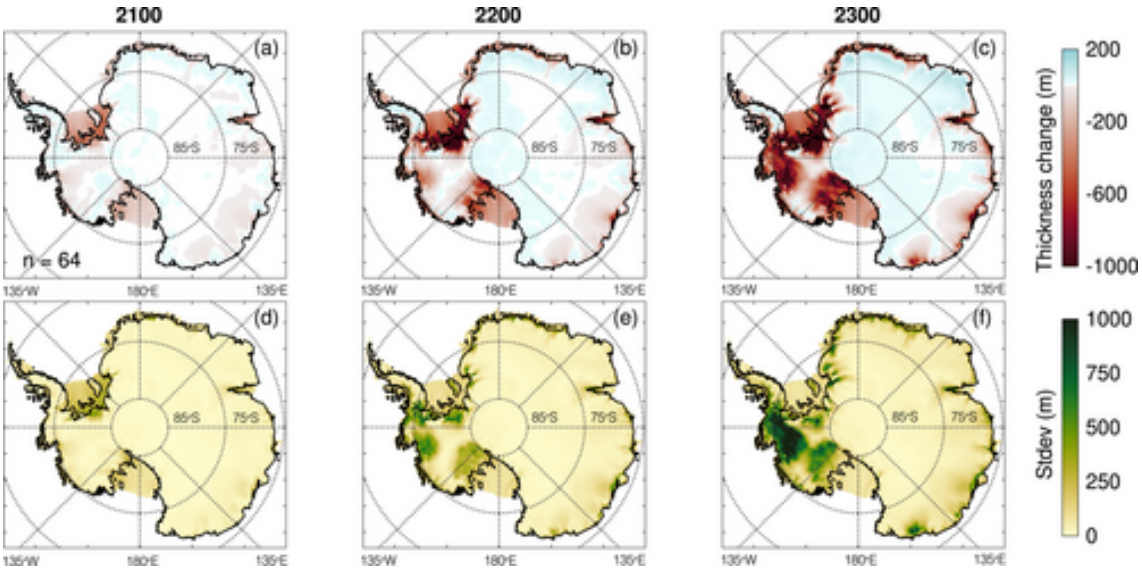

Figure 2.12: *The ensemble mean and variability in projected ice thickness for the years 2100, 2200, and 2300 under a high-emission scenario (experiments expAE02 to expAE05) are shown for 64 primary ice sheet model simulations. Panels (a–c) display the average ice thickness changes for each respective year, while panels (d–f) illustrate the corresponding standard deviations. Areas of ice loss are highlighted in red, indicating thinning, whereas regions of ice gain appear in blue, reflecting thickening. For reference, the current grounding line—based on the BedMachine Antarctica v2 dataset (Morlighem et al., 2020)—is superimposed in black on all panels (Seroussi et al., 2024).*

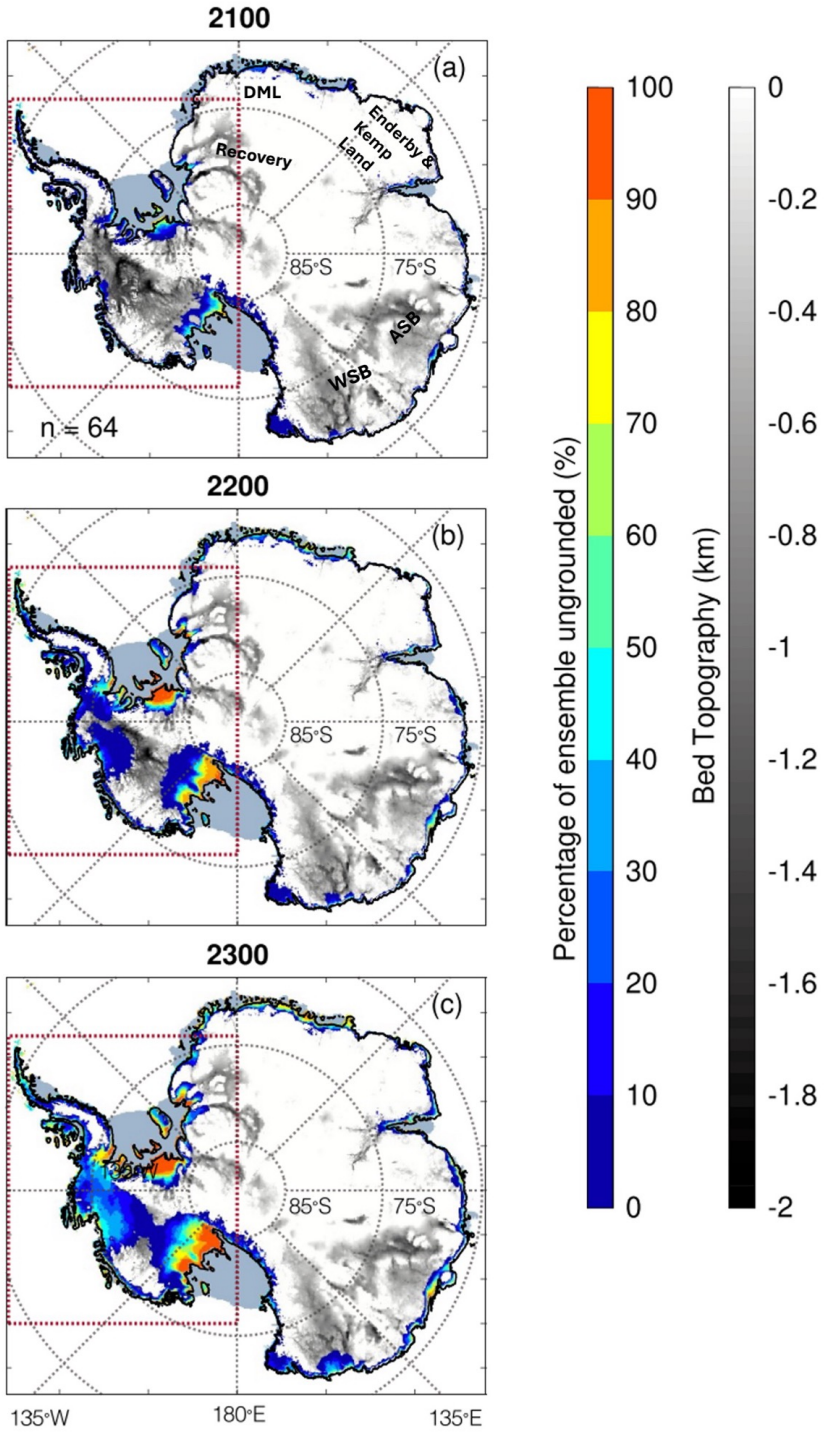

Figure 2.13: *The maps illustrate the proportion of ice sheet models—out of 64 simulations under high-emission forcing scenarios extending to the year 2300 (experiments expAE02 to expAE05)—that project ungrounding of areas currently grounded by (a) 2100, (b)2200, and (c) 2300. The baseline configuration of the AIS is based on the BedMachine Antarctica v2 dataset (Morlighem et al., 2020). In each panel, regions corresponding to present-day floating ice shelves are indicated in muted blue tones for reference (Seroussi et al., 2024).*

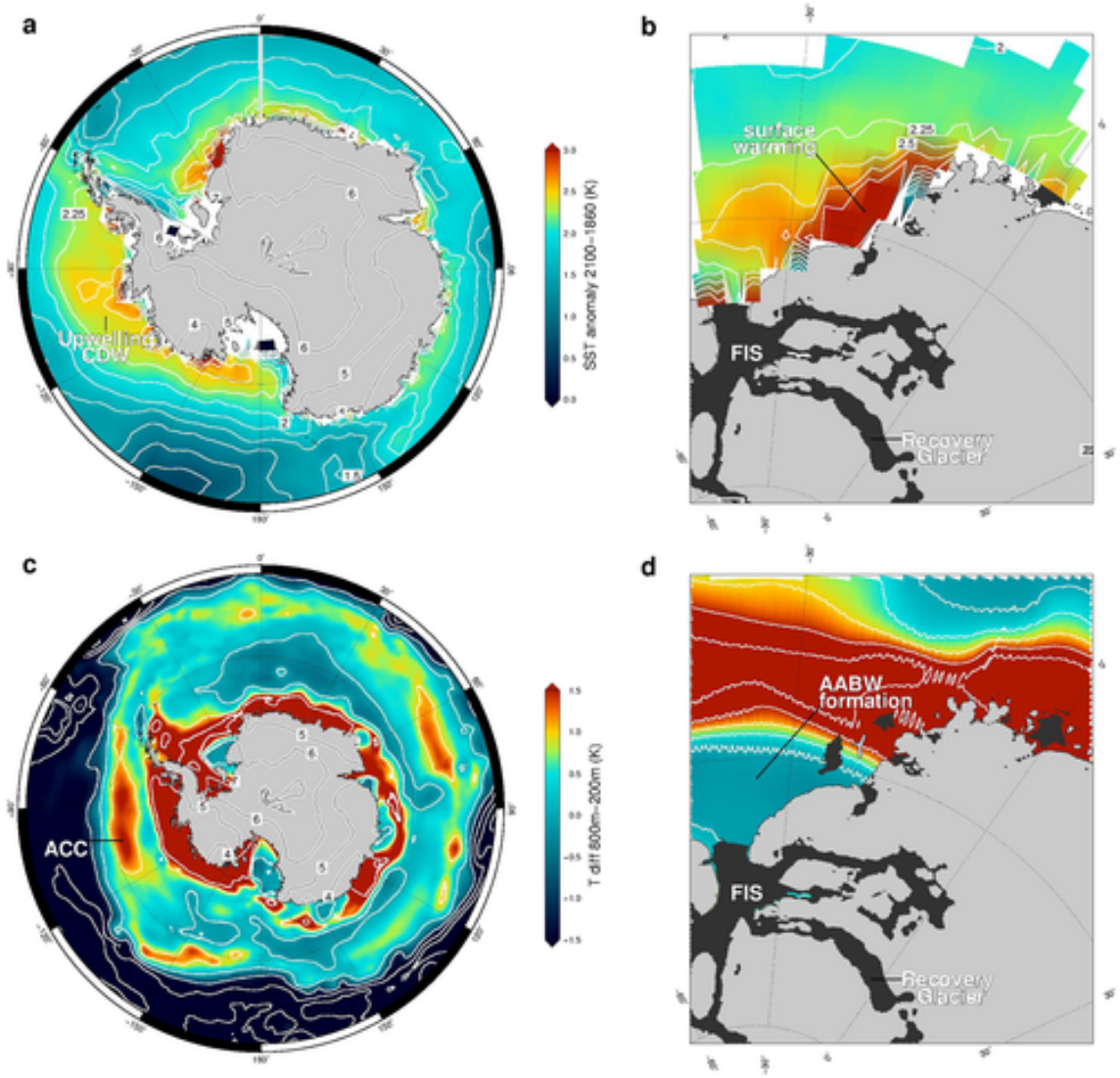

Figure 2.14: *(a) CMIP5 ensemble mean sea-surface temperature anomalies at 2100 CE, showing coastal warming around West Antarctica from CDW upwelling. (b) Peak warming near the Filchner Ice Shelf in the eastern Weddell Sea. (c) Vertical ocean temperature gradients from WOCE data, highlighting the Antarctic Circumpolar Current and areas of Antarctic Bottom Water formation. (d) Eastern Weddell Sea bathymetry below 500 m shown in dark gray. Air temperature anomalies over land are indicated by contours (Golledge et al., 2017).*

Jordan et al. (2023) used an ice sheet model and simulated the effects of both current ocean regime as well as an ocean regime dominated by mCDW intrusions combined with moderate RCP 4.5 and RCP 8.5 high emission scenarios. They projected that under current cooler Shelf Water conditions ($\sim -1.5°C$), the EAIS may experience net mass gain over the next two centuries, with -33 mm SLE under RCP 4.5 and -74 mm SLE under RCP 8.5 emission scenarios. This was attributed to increased atmospheric warming leading to enhanced precipitation outweighing the ice discharge from ice shelf melting. The only vulnerable region under RCP 4.5 under current cooler Shelf Water conditions is basin D-D which constitutes the George V Land and estimates a mass balance of -14 Gt a^{-1} over the 200 years. However, a shift to a warmer ocean regime, marked by intrusion of warm modified Circumpolar Deep Waters (mCDW) is projected to result in significant mass loss in the EAIS. Under RCP 4.5 moderate emission scenario, EAIS is projected to contribute +48 mm SLE over the next 200 years. This represents the most negative mass balance due to sustained increase in ice discharge, up to 335 Gt a^{-1}, driven by extensive grounding line retreat and thinning, surpassing precipitation gains throughout the simulation. Interestingly, higher negative mass balances were projected under RCP4.5 moderate emission scenarios in comparison to high emission scenarios (RCP8.5). For instance, basin D–D (including Cook and Ninnis Glaciers) contributes -103 mm SLE under RCP4.5 mCDW, compared to -82 mm SLE under RCP8.5 mCDW. Similarly, basin A–A contributes -44 mm and -32mm SLE under RCP4.5 and RCP8.5 mCDW, respectively (Fig. 2.15). This was linked to relative increase in ice discharge outweighing precipitation gains. Under RCP8.5 mCDW, the EAIS initially experiences a modest mass gain (+45 Gt a^{-1}) in the first century, followed by a reversal and net loss of $-1,398$ Gt VAF in the second century—equivalent to a +4 mm SLE contribution. The delayed response to warm mCDW highlights the temporal lag between peak oceanic warming and maximum ice discharge. This study finds that the basin D-D which includes Cook and Ninnis Glacier is most vulnerable to both current ocean regime as well as warmer ocean regime with warm mCDW intrusion. This is supported by previous studies that this region is susceptible to past (Crotti et al., 2022; Blackburn et al., 2022) and future climate change (Mengel et al., 2014;

Jordan et al., 2022).

Thus, regional variability in the EAIS response is prominent. While central regions, grounded above sea level, are less sensitive to ocean warming, marine-based sectors like the RSB, WSB and ASB are highly vulnerable (Gwyther et al., 2014; Golledge et al., 2015; DeConto & Pollard, 2016; Rintoul et al., 2016; Pelle et al., 2020; Pan et al., 2021; Gwyther et al., 2023; Pelle et al. 2024; Wang et al., 2024) and observations have already documented mass loss in glaciers draining into the WSB and ASB (Pelle et al., 2021; Roberts et al., 2018; Smith et al., 2020; Sun et al., 2016). Models suggest that if fully melted, the combined ice volume in the WSB and ASB could raise global sea levels by approximately 12 meters (Sutter et al., 2020). The WSB is especially vulnerable, with projections indicating a tipping point for significant ice mass loss between 2200 and 2300, potentially contributing 0.23 to 0.34 m to global sea levels by 2500 (Berends et al., 2023). Additionally, the RSB, with its deep subglacial trough extending 800 km inland, is also at risk from warm ocean waters reaching its grounding line, potentially contributing several meters to sea-level rise, similar to vulnerable basins in WAIS (Golledge et al., 2015; Golledge et al., 2017; Diez et al., 2018; 2019). The intrusion of warm mCDW into sub-ice shelf cavities, such as beneath the Filchner Ice Shelf, is also expected to cause ice shelf thinning and reduce the buttressing effect on inflowing glaciers (Diez et al., 2018; Daae et al., 2020), thereby accelerating ice flow into the ocean and contributing further to ice loss and eventually sea-level rise. Projections extending beyond 2100 show that EAIS dynamics will continue to influence sea levels for centuries and millennia, even after global temperatures stabilise. Uncertainties in basal melt rates, subglacial hydrology, and feedback mechanisms create a wide range of possible outcomes, with potential contributions to sea-level rise ranging from 0.2 to 1.4 meters by 2150 depending on emission pathways (Klose et al., 2024).

Historically, many climate models underestimated the influence of meltwater from the AIS and its ice shelves, leading to biases in IPCC assessments (IPCC, 2019; 2021; Bamber et al., 2019; DeConto & Pollard, 2016). The incorporation of meltwater effects has significantly altered projections, delaying the timing at which key

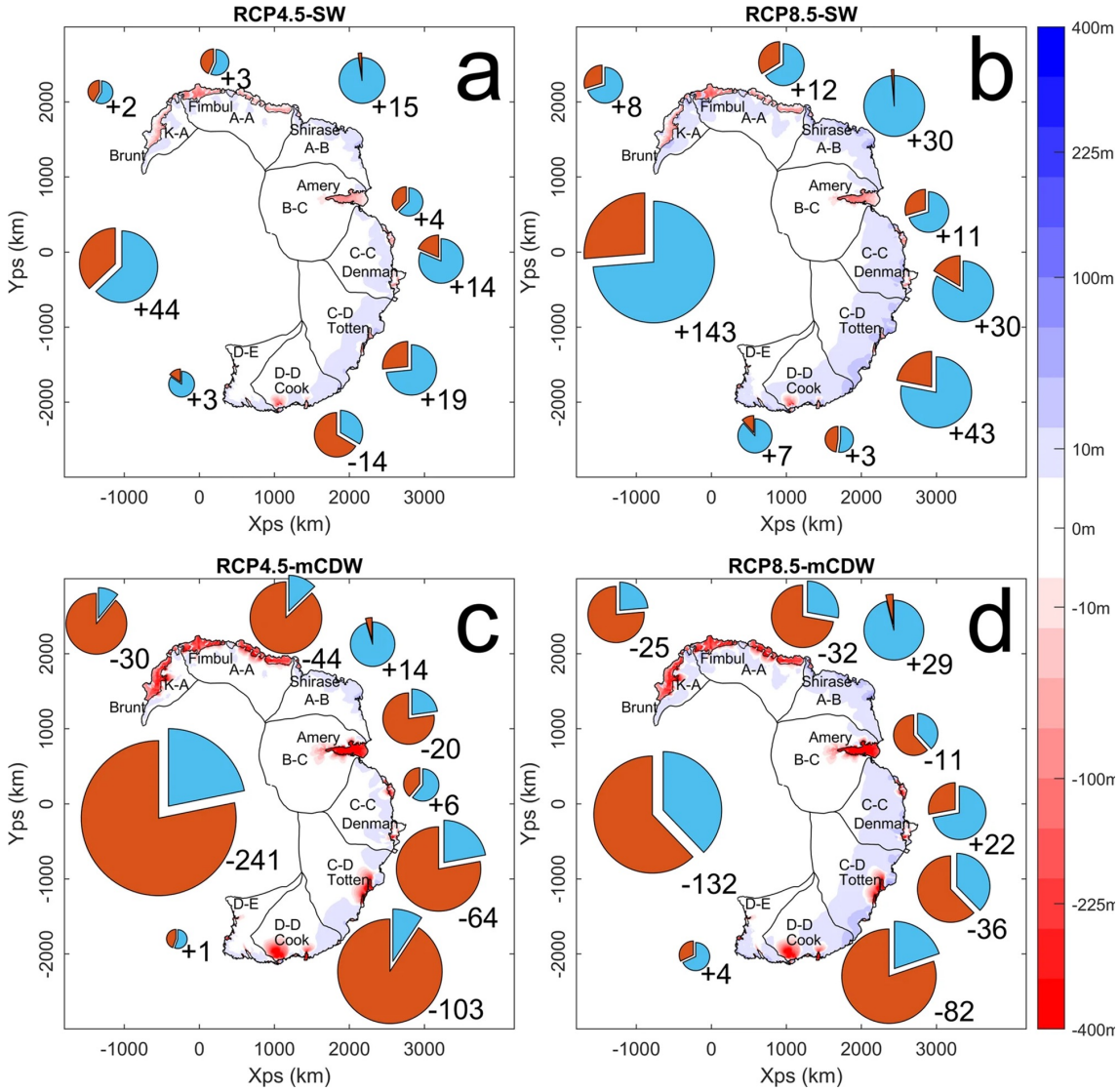

Figure 2.15: *Total mass balance (Gt yr^{-1}) for eight basins (Zwally et al., 2012). The pie charts represent area proportional to the net mass balance with ice discharge (orange) and precipitation (blue). Ice thickness change is represented by the colour bar from blue (thickening) to red (thinning) after 200 years relative to the unforced scenario for (a) RCP4.5-SW, (b) RCP8.5-SW, (c) RCP4.5-mCDW and (d) RC8.5-mCDW climate scenarios, where SW refers to current cold Shelf Water conditions and mCDW refers to warm ocean regime with warm mCDW intrusions (Jordan et al., 2023).*

global warming thresholds are reached, modifying precipitation patterns, increasing Antarctic sea ice formation, and warming the subsurface ocean around Antarctica (Bronselaer et al., 2018). This subsurface warming exacerbates ice sheet and ice-shelf melting through positive feedback mechanisms, highlighting the urgent need to account for meltwater effects in future climate models. Feedback processes such as ice-albedo interactions and ocean-ice dynamics add further complexity. For instance, the ice-albedo feedback accelerates surface melting, while intrusions of warm mCDW under high-emission scenarios melt ice shelves, weakening their stabilising role. Additionally, inclusion of MICI in model simulations amplifies ice loss by causing tall, unstable ice cliffs, exposed as ice shelves to retreat and collapse.

Although advanced modelling techniques, including deep learning, have improved the accuracy of parameters such as basal melt rates beneath Antarctic ice shelves (Bouissou et al., 2022), predicting the future behaviour of these ice sheets remains highly uncertain. The response of ice sheets depends on complex interactions, nonlinear processes, and feedback mechanisms within the Earth System, operating across diverse timescales. These interactions, coupled with the inherent inertia of ice sheets, could initiate ice loss in the near term, with effects persisting and evolving over centuries to millennia (Klose et al., 2024).

Uncertainties surrounding the timing and magnitude of future sea-level contributions from the EAIS remain significant. While oceanic warming is expected to dominate mass loss in the short term, atmospheric warming is projected to become the primary driver over longer timescales (Golledge et al., 2017). However, many of the mechanisms driving glacier changes remain poorly understood, with substantial gaps in observational data, particularly in EAIS, which has received less attention compared to other regions. Numerical model predictions rely heavily on observational data for calibration, yet uncertainties in parameters such as ice shelf melt rates and climate forcing continue to challenge projections. Despite these limitations, models consistently emphasize the need for ambitious mitigation efforts to prevent catastrophic sea-level rise. Enhancing model accuracy by incorporating meltwater dynamics, improving ice-sheet simulations, and addressing data gaps is essential for producing

more reliable predictions. As modelling techniques advance and our understanding of ice-sheet behaviour deepens, policymakers and scientists will be better equipped to assess risks and devise strategies to mitigate and adapt to the impacts of sea-level rise on global communities.

2.5 Summary

While considerable progress has been made in understanding the EAIS, there remain gaps in literature about past, present and future responses to climate change. Palaeo-climate records and ice sheet models have highlighted that the EAIS has undergone substantial mass loss during the warm periods such as Pliocene warming (and possibly the Last Interglacial), yet the spatial extent of mass loss and their drivers has remained poorly understood due to limited access to geological and sedimentary data. With the recent advances in remote sensing technology, the understanding of the EAIS since the 1970s has improved over time, yet there remains gap in understanding regional and local variations in outlet glacier behaviour and their potential drivers.

Furthermore, large portions of the EAIS, including smaller outlet glaciers and ice shelves remain understudied due to limited field observations and challenging access. This arises from observational biases that tend to focus on areas where mass loss has been detected, e.g. the ASB. These regions such as the ASB have experienced mass loss in the past and are projected to lose mass in the future under moderate and high emission scenarios. However, the behaviour of other smaller outlet glaciers across regions such as Enderby and Kemp Land have remained underexplored. Recent observations indicate that sea ice extent near Enderby Land has declined by at least 50% in recent years, raising concerns about changing oceanic conditions. Despite this, there is limited knowledge on whether these environmental shifts have had any measurable influence on the dynamics and stability of outlet glaciers in these areas. Moreover, although large portions of the EAIS rest on predominantly prograde bed slopes, providing a degree of protection against MISI, many other areas within the EAIS still exhibit retrograde bed slopes, beyond the well-known vulnerable regions

such as the WSB, ASB, and RSB. Although these retrograde slopes are generally narrower and less extensive compared to the broader, deeper basins in WAIS and key EAIS basins, they still present a location of potential vulnerability. Even modest retrograde sections could be susceptible to the intrusion of warm mCDW, potentially initiating localized instability and contributing to future mass loss.

Future projections, although increasingly sophisticated, are hindered by model resolution limitations, incomplete representation of key processes and uncertainties. While some models project mass gain under current cooler shelf water regimes, others suggest that even moderate climatic perturbations, especially involving mCDW intrusions, could lead to substantial regional mass loss. However, the timing, extent, and spatial variability of such oceanic transitions remain poorly constrained. Under moderate emission scenarios (e.g., RCP 4.5), in particular, model divergence is large, with some projecting substantial retreat due to warm mCDW intrusions, while others indicate relative stability. The role of temporal lags between climatic forcing and glaciological response also poses a challenge for prediction. These knowledge gaps—particularly those concerning the stability of underexplored marine-based basins such as Enderby Land, Kemp Land, and parts of DML, along with the poorly understood roles of atmospheric and oceanic forcings—form the central rationale for this thesis. The research aims to better constrain the regional sensitivity of these sectors of the EAIS to changing climatic and oceanographic conditions through satellite remote sensing (Section 1.2).

CHAPTER 3

Study Area

This thesis investigates the Fimbulisen region of central Dronning Maud Land (cDML) in the eastern Weddell Sea sector and alongside the areas of Enderby and Kemp Land in the West Indian Ocean sector (Fig. 3.1). These three regions are particularly interesting and important because they have been gaining mass in the past few decades (Rignot et al. 2019) and surrounded by cold ocean waters (Lowther et al. 2022), resulting in limited research. They encompass four major drainage basins DB5, 6, 7 and 8 (Zwally et al. 2012).

DB 5 and 6, which span the DML region between 20° W and 45° E, comprise approximately ten major ice shelves (Fig. 3.1) extending 50-200 km from the grounding zone (Matsuoka et al. 2015) and around twenty outlet glaciers (Miles et al., 2016). Both basins discharge into extensive ice shelves, which provide critical buttressing to the glaciers (Høydal, 1996). Fimbulisen is one of the largest ice shelves in DML and Jutulstraumen, the largest glacier in the region feeds into it. In the grounded portion of the two basins, near the mountain range in DML, 170-200 named and unnamed glaciers also exist.

In contrast, DB 7 and 8, covering Enderby and Kemp Lands (45°E to 60°E), are characterised by the absence of such major ice shelves. These two basins together drain approximately 50 relatively smaller glaciers directly into the ocean. Compared to DML, there is a smaller mountain range in the region as well. The following sections will examine in greater detail the glaciological, topographical, climatic, and oceanographic contexts of these regions.

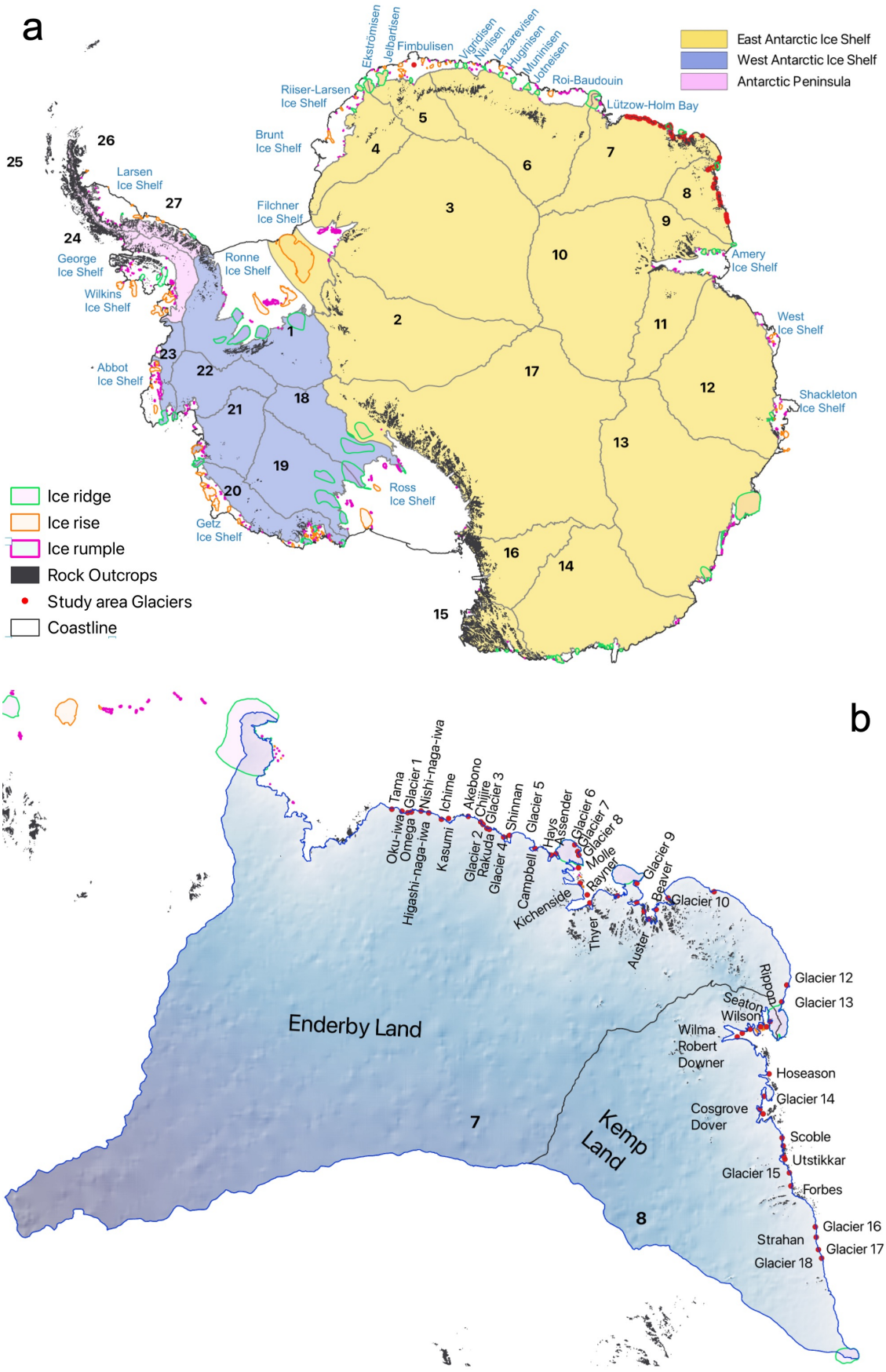
a
East Antarctic Ice Shelf
West Antarctic Ice Shelf
Antarctic Peninsula
Ekströmisen
Jelbartisen
Fimbulisen
Vigridisen
Wivilisen
Lazarevisen
Hughmisen
Muninisen
Jotneisen
Roi-Baudouin
Lützow-Holm Bay
Riiser-Larsen Ice Shelf
Brunt Ice Shelf
Filchner Ice Shelf
Ronne Ice Shelf
Larsen Ice Shelf
George Ice Shelf
Wilkins Ice Shelf
Abbot Ice Shelf
Getz Ice Shelf
Ross Ice Shelf
Amery Ice Shelf
West Ice Shelf
Shackleton Ice Shelf
1
2
3
4
5
6
7
8
9
10
11
12
13
14
15
16
17
18
19
20
21
22
23
24
25
26
27
Ice ridge
Ice rise
Ice rumple
Rock Outcrops
Study area Glaciers
Coastline
b
Tama
Glacier 1
Nishi-naga-iwa
Ichime
Akebono
Chijire
Glacier 3
Shinman
Glacier 5
Hays
Lassender
Glacier 6
Glacier 7
Glacier 8
Oku-iwa
Omega
Higashi-naga-iwa
Kasumi
Glacier 2
Rakuda
Glacier 4
Campbell
Kichenside
Molle
Rayner
Glacier 9
Beaver
Glacier 10
Thyer
Auster
Rippon
Glacier 12
Glacier 13
Seaton
Wilson
Wilma
Robert
Downer
Hoseason
Glacier 14
Cosgrove
Dover
Scoble
Utstikkar
Glacier 15
Forbes
Glacier 16
Glacier 17
Strahan
Glacier 18
Enderby Land
Kemp Land
7
8

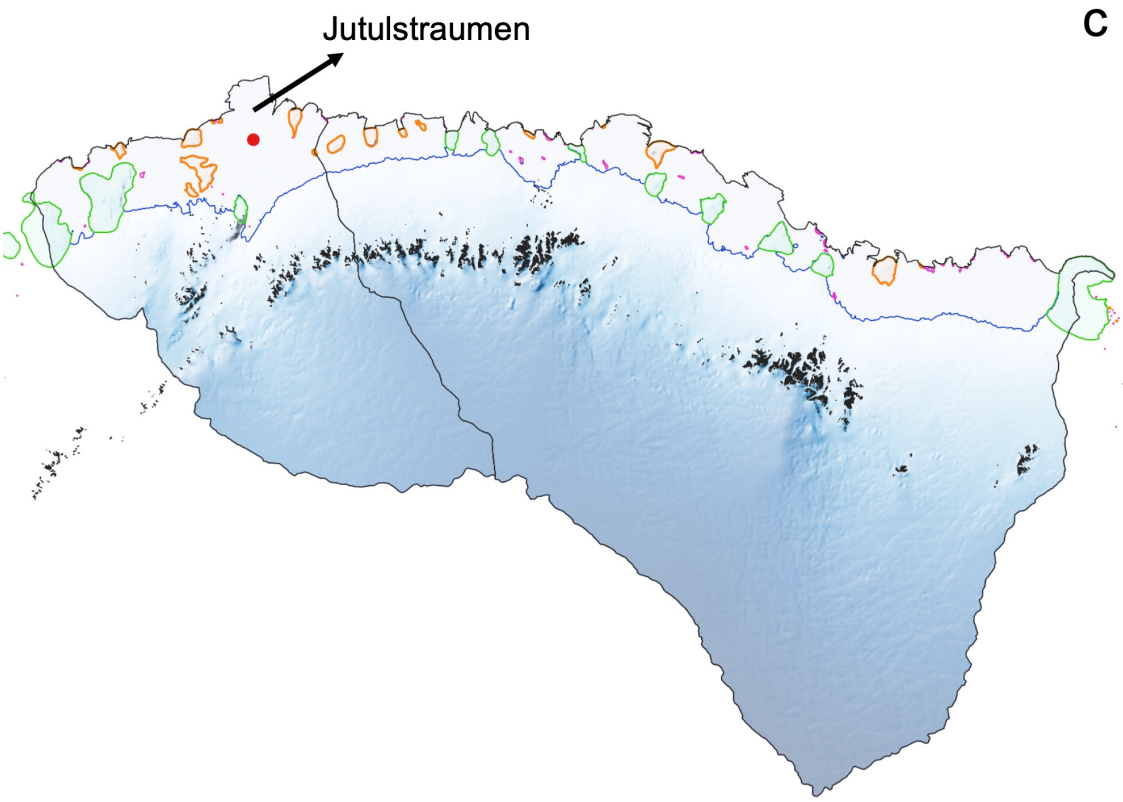

Figure 3.1: *(a) Map of Antarctica showing drainage basins (Zwally et al., 2012) overlaid with surface features from Quantarctica. Pink region represents the region of East Antarctica, blue represents West Antarctica, and yellow shows the Antarctic Peninsula. Two blue boxes outline the thesis study areas, and red symbols mark the glaciers analysed. (b) Zoomed-in view of the region examined in Chapters 4 and 5. (c) Zoomed-in view of Drainage basins 5 and 6 encompassing DML, examined in Chapter 6, with glacier names labeled. Antarctic outlines were sourced from SCAR's Antarctic Digital Database (ADD) through Quantarctica (Matsuoka et al., 2021).*

3.1 Glaciological setting

DML (consisting of DB5 and 6), one of the largest sectors of the EAIS, has exhibited consistently positive mass balances across multiple time periods. Shepherd et al. (2020) reported a gain of $+13.3 \pm 3.4$ Gt yr^{-1} over 1992–2017, while King et al. (2012) estimated $+10 \pm 4$ Gt yr^{-1} for the interval 2002–2010. More recently, Kim et al. (2024) quantified a mass gain of $+12.9 \pm 2.4$ Gt yr^{-1} between 2003 and 2020, corroborating earlier findings. Although these studies employ differing methodologies and time spans, their results consistently indicate a net accumulation of approxi-

mately 10-13 Gt yr^{-1} in DML. This sector is characterised by relatively small ice shelves compared to those in the WAIS (Fig. 3.2). Typically, these ice shelves extend $\sim$ 50-200 km from the grounding zone (averaging $\sim$ 110 km) and exhibit widths ranging from roughly 50 to 400 km (mean $\sim$ 170 km), thereby providing essential buttressing to the inland ice (Goel et al. 2020). The ice shelves of DML cover a total area of $\sim 221,000$ km^2, accounting for around 14% of all Antarctic ice shelves (Lowther et al., 2022). The thickness of these ice shelves varies from a few hundred meters to approximately one kilometre, with the greatest thickness observed near the grounding lines of major ice streams and outlet glaciers (Fretwell et al., 2013; Morlighem et al., 2020).

Within DML, Fimbulisen is the largest ice shelf, extending from 7°W to 8°E in cDML. Its central region is predominantly fed by Jutulstraumen, the largest outlet glacier in the area. The ice front of Jutulstraumen, illustrated in light blue in Fig. 3.2, is composed of Passive Shelf Ice (PSI), meaning that if these parts of it were to be lost, there would be no change in the level of buttressing the Fimbulisen provides to Jutulstraumen. As a consequence, calving events such as the 1963 loss of the ice tongue known as 'Trolltunga', did not significantly affect the buttressing of the inland ice. In addition, between 2009 and 2019, Fimbulisen is known to have experienced a net area gain of 1.2% ($\sim$ 43 km^2 per year) as well (Fig. 3.3b; Andreason et al. 2023).

In contrast to DML, the mass balance of Enderby (DB7) and Kemp Land (DB8) has remained largely stable between 1992 and 2017 with some spatial variability within the two regions (Shepherd et al. 2020; Rignot et al. 2019; Kallenberg et al. 2017). For example, the two largest outlet glaciers in the region display markedly contrasting behaviours. While the Wilma-Robert-Downer Glacier remains close to equilibrium, Rayner Glacier has experienced a mass loss of -0.7 Gt yr^{-1} between 1992 and 2017 (Rignot et al. 2019). Moreover, unlike DML, the coastal region of Enderby and Kemp Land lack ice shelves, resulting in glaciers directly discharging into the ocean (Fürst et al., 2016; Fig. 3.2c, 3.3c). In the absence of such extensive ice shelves in this region (Fig. 3.1c), any buttressing of inland ice is likely governed

by the topography—particularly where large outlet glaciers, such as Rayner Glacier or Wilma-Robert-Downer Glacier, descend through deep glacial troughs or fjords. These topographic confinements could provide lateral support, effectively stabilising the glacier flow and partially compensating for the lack of ice shelf-derived buttressing (see Section 3.2). However, the outlet glaciers in Enderby and Kemp Land are considerably smaller than those in DML, with widths between only 2-12 km. Given the contrasting glaciological conditions and processes operating between these regions, a deeper investigation into the mechanisms regulating ice mass and stability is needed.

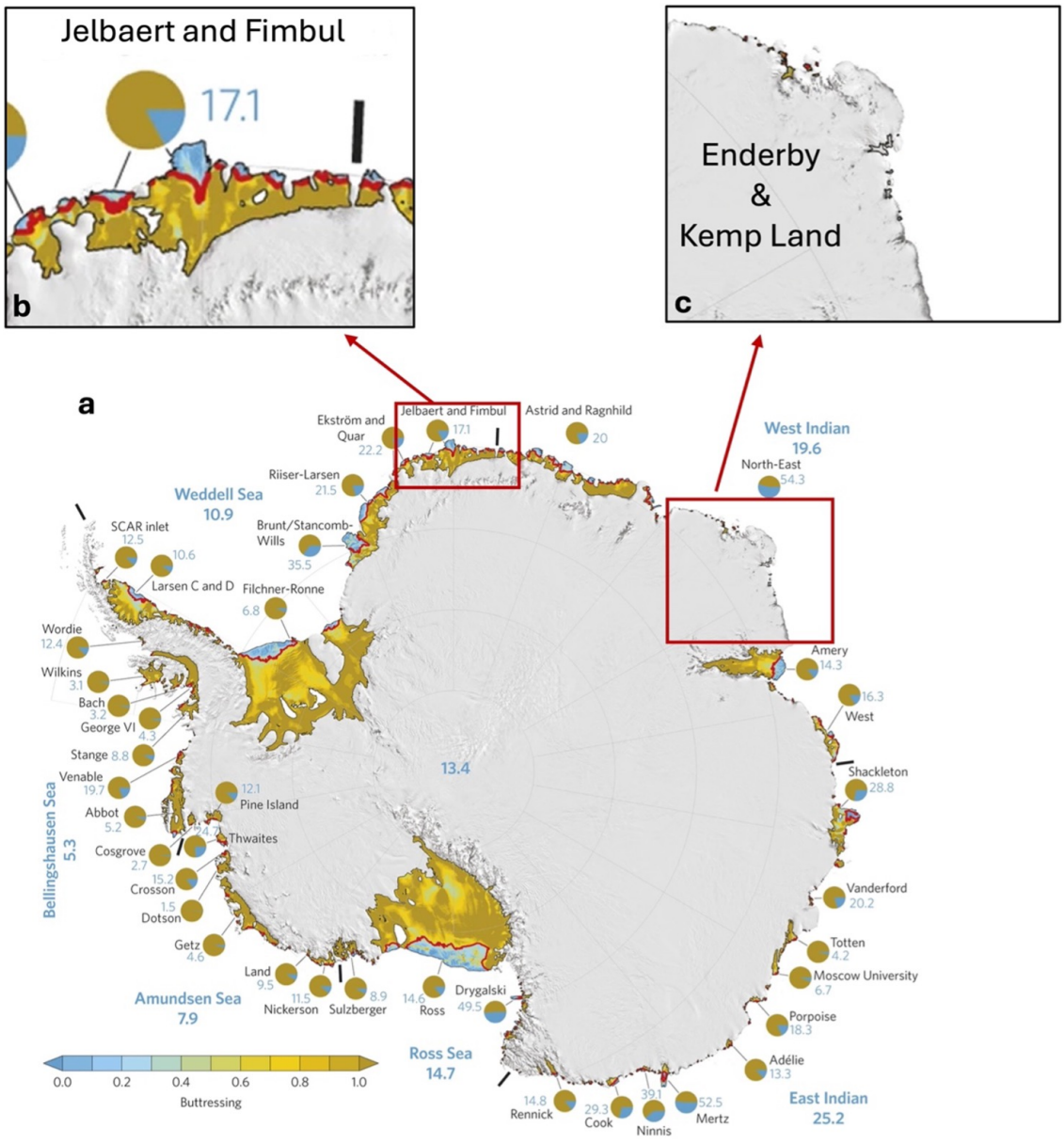

Figure 3.2: *(a) The safety band of Antarctica from Fürst et al. (2016) showing the buttressing provided by the ice shelves. (b–c) Zoomed-in views of the Fimbulisen region, as well as the Enderby and Kemp Land areas, providing a closer look at the study regions.*

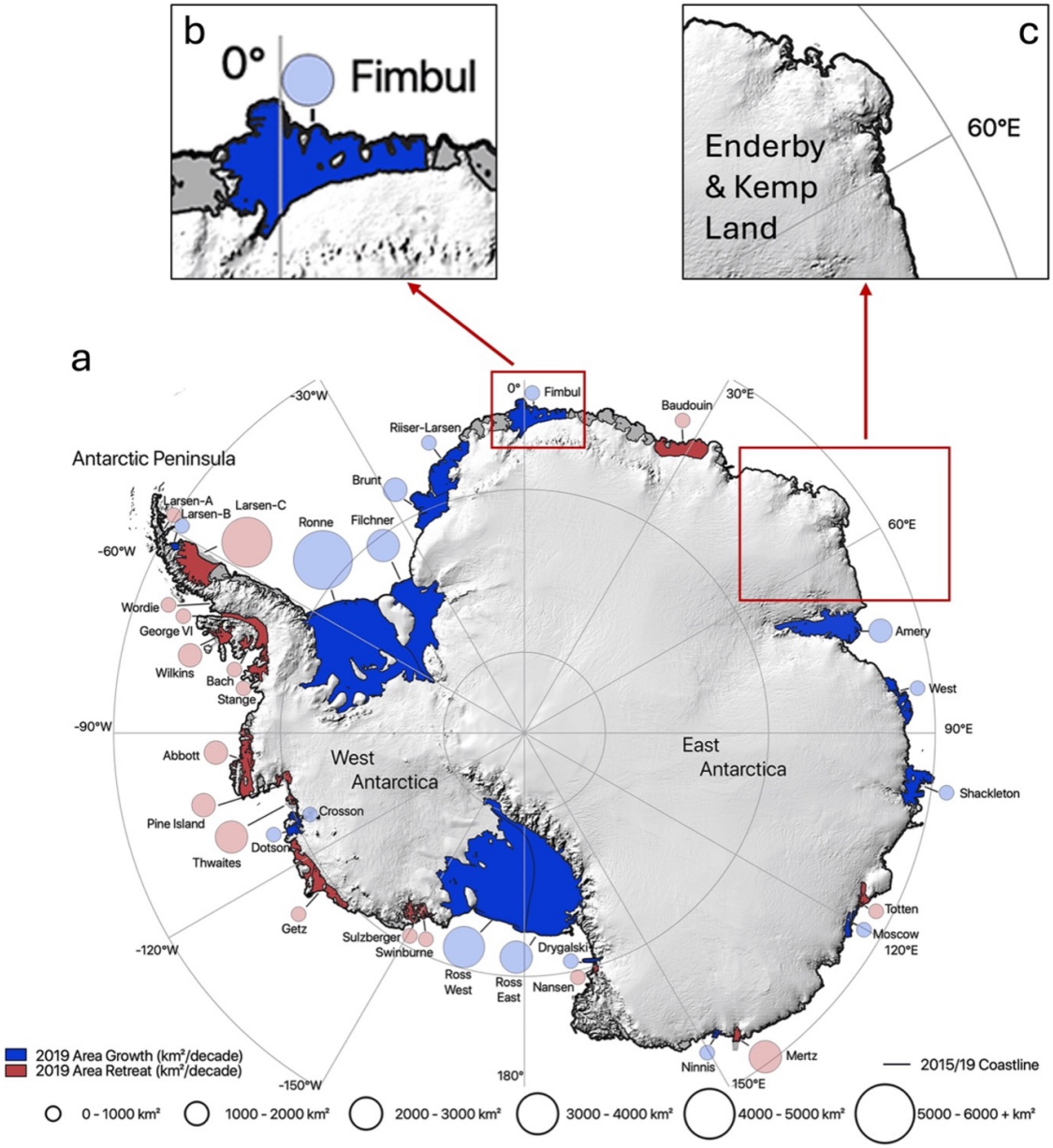

Figure 3.3: *(a) Map of Antarctic ice shelf area changes between 2009 and 2019 taken from Andreasen et al. (2023), showing ice shelf names overlaid on the Bedmap2 ice surface of Antarctica. Coloured circles indicate the total ice shelf area (in km^2) either lost (red) or gained (blue). The bold black line marks the Antarctic coastline, based on combined data from 2015 and 2019. (b–c) Zoomed-in views of the Fimbulisen region, as well as the Enderby and Kemp Land areas, providing a closer look at the study regions.*

The geographic setting of glaciers in Enderby and Kemp Land, which lack major ice shelves, is more similar to those of Greenlandic glaciers that typically terminate in fjords. In these two regions, the glaciers can be divided into three distinct terminus groups according to the standard classification in the GLIMS Illustrated Glacier Classification Manual (Rau et al., 2005; Lovell et al. 2016), and in doing so, this may reflect differences in likely processes operating to control these types of glaciers. The first group is characterised by a constrained terminus configuration, where ice flow is channelled by valleys, basins, or surrounding topographic features. These glaciers are typically bordered by exposed bedrock and terminate within embayments or fjord-like environments. These are called floating constrained glaciers (FC), for instance Rayner Glacier, which flows into Casey Bay, and Wilma-Robert-Downer Glacier, which flows into Edward Gulf (see Fig. 3.4b, c). The second group features unconstrained glaciers with a floating, unconstrained tongue (FU) that spread outward largely independent of local geography and extends out of a fjord directly into the ocean. In such glaciers, at times, the ice front retreats to positions very close to the grounding line and then advances again to its furthest extent. Examples include Nishi-naga-iwa, Higashi-naga-iwa, Utstikkar (see Fig. 3.4c, d). The third group comprises of grounded glaciers (G), which do not have a floating tongue, for example, Glacier 15 and Glacier 18 (Fig. 3.4e, f).

Table 3.1: *Summary of Glacier types in Enderby and Kemp Land. See also Fig.3.3.*

Glacier types	**Enderby Land**	**Kemp Land**
Floating Constricted (FC)	12	12
Floating Unconstricted (FU)	20	3
Grounded (G)	5	5

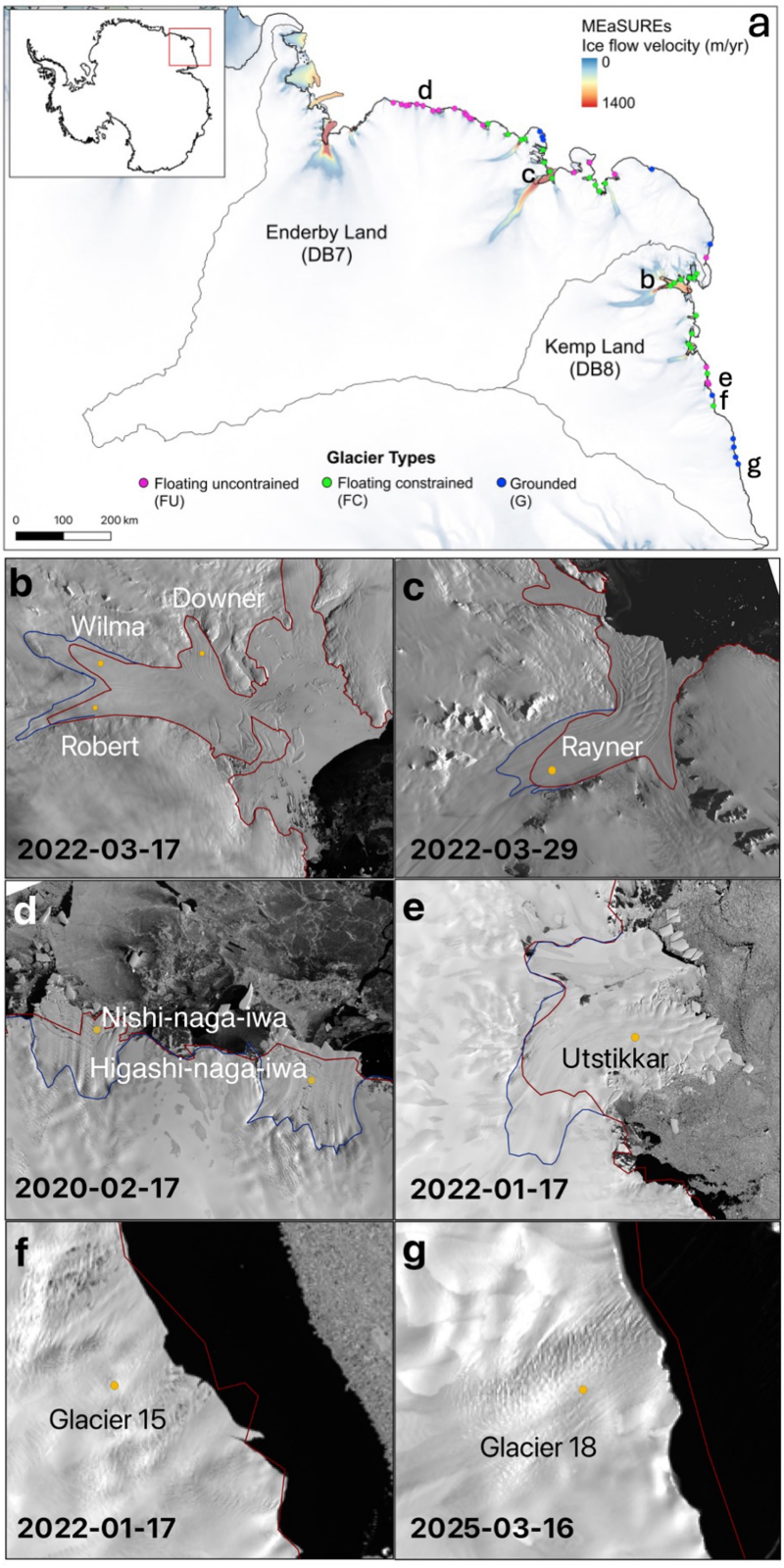

Figure 3.4: *Examples of (b-c) floating constrained (FC) glaciers (Background image: Landsat-9), (d-e) floating unconstrained (FU) glaciers (Background image: Landsat-8) and (f-g) grounded (G) glaciers with no floating tongues. Red lines represent the MEaSUREs grounding line and blue lines represent the grounding lines mapped in this study.*

Furthermore, ice front changes in the Fimbulisen, Enderby, and Kemp Land regions remain relatively understudied compared to other parts of Antarctica, probably because they do not drain one of the major deep marine basins of East Antarctica. One of the few long-term analyses in Fimbulisen, Enderby, and Kemp Land, conducted by Miles et al. (2016), found that glaciers exhibited alternating phases of advance and retreat over the decades between 1970s and 2010 (Fig. 2.4). Notably, a pronounced and widespread retreat (∼53% glaciers) occurred between the 1974 and 1990, followed by a predominant trend of glacier advance during the subsequent two decades, spanning 1990–2000 and 2000–2010. Miles et al. (2016) suggested that this initial retreat between 1974 and 1990 was due to reduction in sea ice concentration, where a mean reduction of 7 days per year was observed between DB4 and DB7. Goel et al. (2020) reported that approximately 95% of ice fronts in DML advanced between 2009 and 2014, indicating a regional tendency toward frontal growth during this period. More recently, Baumhoer et al. (2021) also identified a dominant trend of ice front advance across these regions between 1997 and 2018 (Fig. 3.5). This advance is thought to result from the fact that environmental conditions at DML and Enderby and Kemp Lands remained largely unchanged following the sea-ice decline between 1979 and 1990. Furthermore, the presence of ice rises and ice rumples in these areas confer additional stability to glacier flow. These surface features exert a pronounced influence on ice-shelf dynamics by perturbing, diverting, and constraining flow trajectories. Interestingly, the only significant known calving event in Fimbulisen remains the loss of the Trolltunga ice tongue, which detached in the early 1960s (Swithinbank et al., 1969; Vinje et al., 1977). This event stands out as a major calving episode in an otherwise relatively stable ice front history of Fimbulisen.

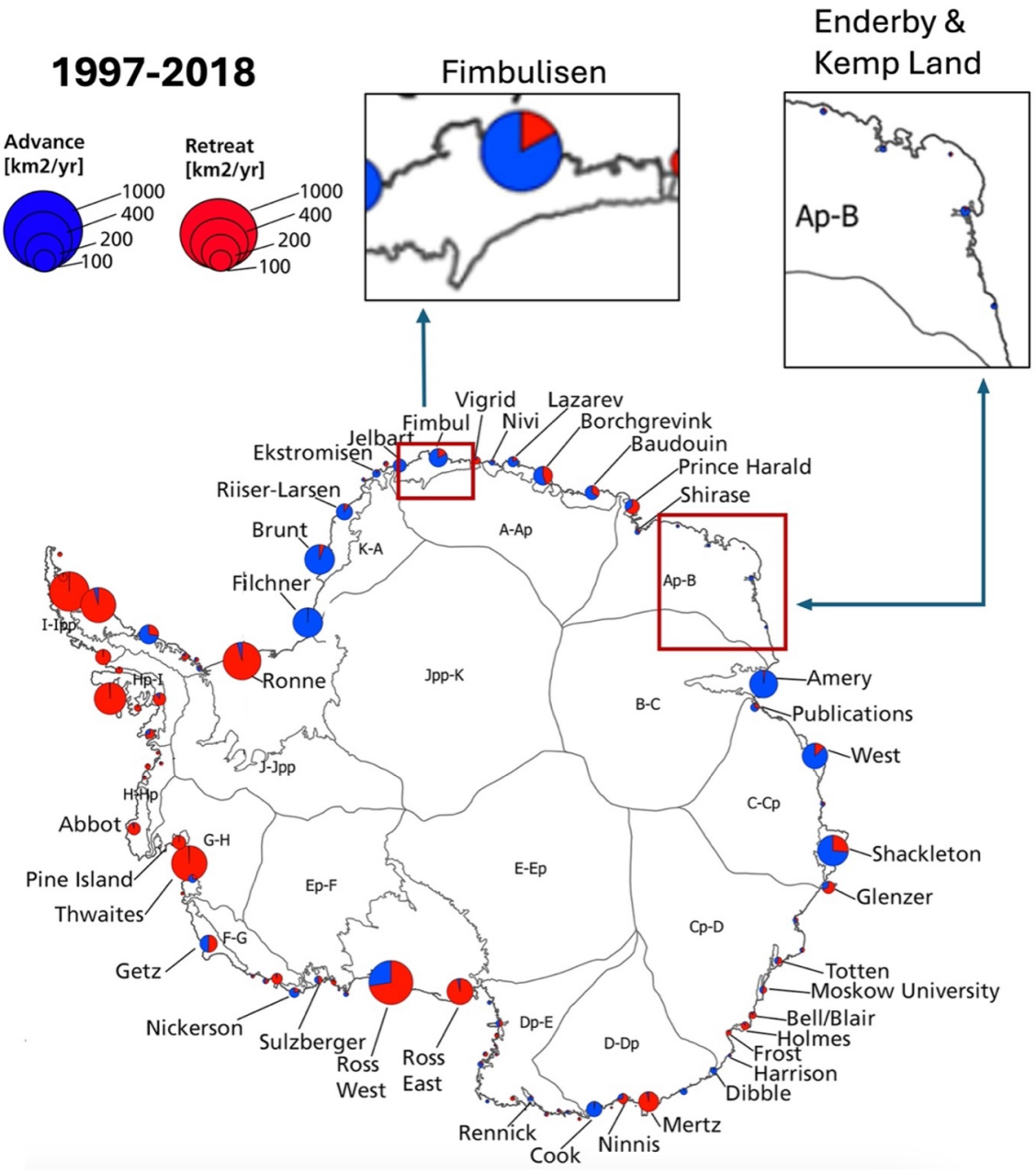

Figure 3.5: *Ice front changes across Antarctica between 1997 and 2018 with the panels zooming into Fimbulisen and Enderby and Kemp Land from Baumhoer et al. (2021).*

The ice rises and rumples that are present along the coast of DML, Enderby and Kemp Land (Wolmarans and Kent, 1982) exerts a significant buttressing effect that modulates the flow of ice toward the ocean (Fig. 3.6; Favier and Pattyn, 2015; Barletta et al., 2018; Reese et al., 2018; Still et al., 2019; Still and Hulbe, 2021; Schannwell et al., 2020). They also influence the position and migration of the continental grounding line, acting as pinning points and playing a crucial role in the stability of ice shelves (Favier et al., 2012; Bindschadler et al., 1990, 2005; Barletta et al., 2018; Kingslake et al., 2018; Wearing and Kingslake, 2019). Infact, at Fimbulisen, Humbert and Steinhage (2011) noted that they induce intense shearing and fracturing within the surrounding regions and along the ice shelf margins, often resulting in extensive crevassing and rifting.

Recently, Miles et al. (2024) identified numerous key ice rises and rumples across Antarctica (Fig. 3.4a), reporting a general decline in their areal extent. This trend has important implications, as the reduction in such pinning points may facilitate the unpinning of ice shelves and ice tongues, potentially accelerating ice loss. Notably, between 1963 and 1997, a 6.8% reduction in ice shelf area within DML occurred predominantly in sectors lacking ice rises and rumples proximal to the calving front (Kim et al., 2001). Despite this broader trend, most ice rises and rumples within Fimbulisen have remained relatively stable according to Miles et al. (2024). For instance, of the 27 identified ice rises and rumples within the Fimbulisen, 25 remained unchanged over this period. Notably, one ice rise on the western side of Jutulstraumen has shown a decrease in area, which may compromise glacier stability in the future. In contrast, another ice rise farther east is expanding, potentially contributing to increased local stability (blue in Fig. 3.6b). Moreover, among the largest ice rises in Fimbulisen, Bløskimen Island (BI), Kupol Moskovskij (KM), and Kupol Ciolkovskogo (KC), no change in area was also observed between 1973 and 2022. However, Goel et al. (2024) reported that Kupol Moskovskij (KM) and Kupol Ciolkovskogo (KC) on the eastern side of Jutulstraumen (Fig. 3.6d), have been gaining mass. In Kemp Land, only 11 ice rises and rumples were identified, of which, most of them exhibited increase in area between 1973 and 2022 which could contribute to future stability.

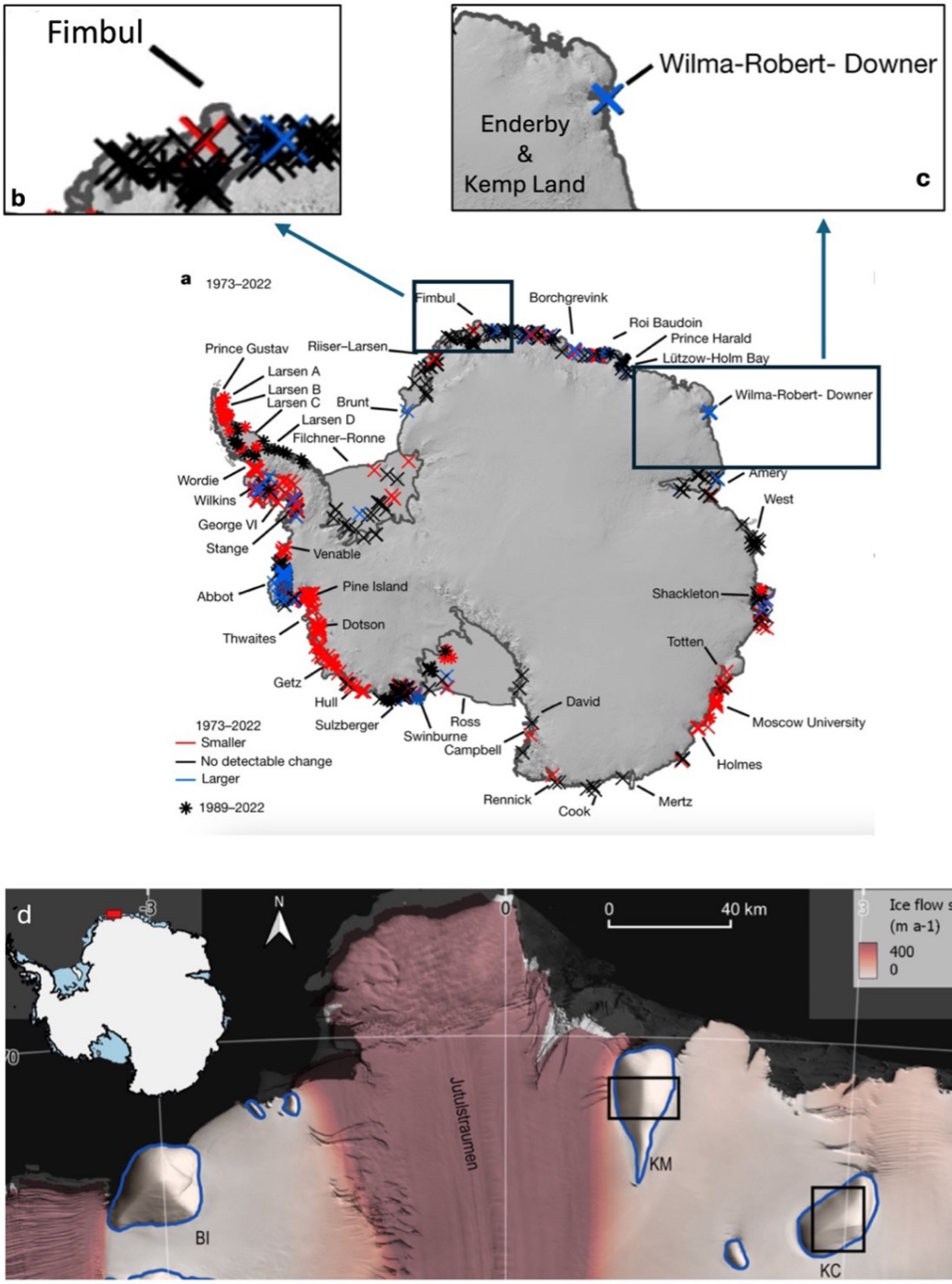

Figure 3.6: *(a) Mapped change in ice rises and rumples between 1973 to 2022 overlain on the REMA mosaic of Antarctica (Miles et al. 2024) with zoomed in subsets (b) Fimbulisen (c) Enderby and Kemp Land. (d) Ice rises and field data in the Fimbul Ice Shelf, Dronning Maud Land where KM is Kupol Moskovskij ice rise and KC is Kupol Ciolkovskogo ice rise (Goel et al. 2024).*

3.2 Topographic setting

The topography of DML, with Fimbulisen in its central region, is defined by four primary features: major ice shelves (e.g. Riiser-Larsenisen, Ekströmisen, and Fimbulisen), lower inland ice regions (Ritscherflya and Hellehallet), a high-altitude plateau namely the Wegener Inlandeis, composed of Amundsenisen and Wegenerisen, with elevations exceeding 2500 m a.s.l. and nunatak areas associated with the Heimefrontfjella, Kirwanveggen, and Mühlig-Hofmann-Gebirge mountain ranges, with heights of about 2700 m a.s.l. and lie approximately 200–250 km inland from the grounding line (Fig. 3.7a; Rotschky et al. 2007; Elevold et al., 2024). The mountain range (in Fig. 3.7a) exhibits an extensive passive margin escarpment morphology that likely developed due to Jurassic uplift following the rifting and subsequent break-up of Gondwana (Sirevaag et al., 2021). This mountain range serves as a topographic barrier to the inland ice, generating a pronounced feature on the ice-sheet surface, with the polar plateau rising above 2500 m and a steep slope down to the coastal region which is largely below 1500 m above sea level (Van den Broeke et al., 1999). In contrast, Enderby and Kemp Land are underlain by two tectonic zones, the Napier Complex and the Rayner Complex (Kamenev, 1972). The Napier Complex is made up of ancient, highly metamorphosed rocks and igneous intrusions from the Archean, offering a record of early Earth processes and continental formation. The Rayner Complex, formed later, has its own distinct metamorphic and magmatic characteristics (Sheraton et al. 1987; Harley et al. 2019; Król et al. 2022). Together, these regions have not responded to Gondwanan rifting to the same extent as DML and only a few mountain ranges are present (e.g. Napier mountains, Tula Mountains) in comparison to DML and in these there is only a limited area of exposed rock (Fig. 3.7b). The Enderby Land peninsula exhibits high bedrock relief, featuring numerous bedrock rises between 1500 and 2000 m. Moreover, two bedrock rises along Wilma, situated between 500 and 1000 m in altitude, could influence its flow velocity (Allison et al., 1982).

Topography could exert a fundamental control on glacier behaviour, influencing ice dynamics at both large and small scales. Large-scale topographic features such as deep troughs or reverse-sloping beds can channelise ice flow, enhance grounding line retreat, or increase vulnerability to marine ice sheet instability. At smaller scales, bedrock rises, ridges, or undulations can serve as pinning points that stabilise ice shelves. These local variations in bed geometry could affect stress distributions within the ice, modulate flow velocity, and influence basal sliding and melting.

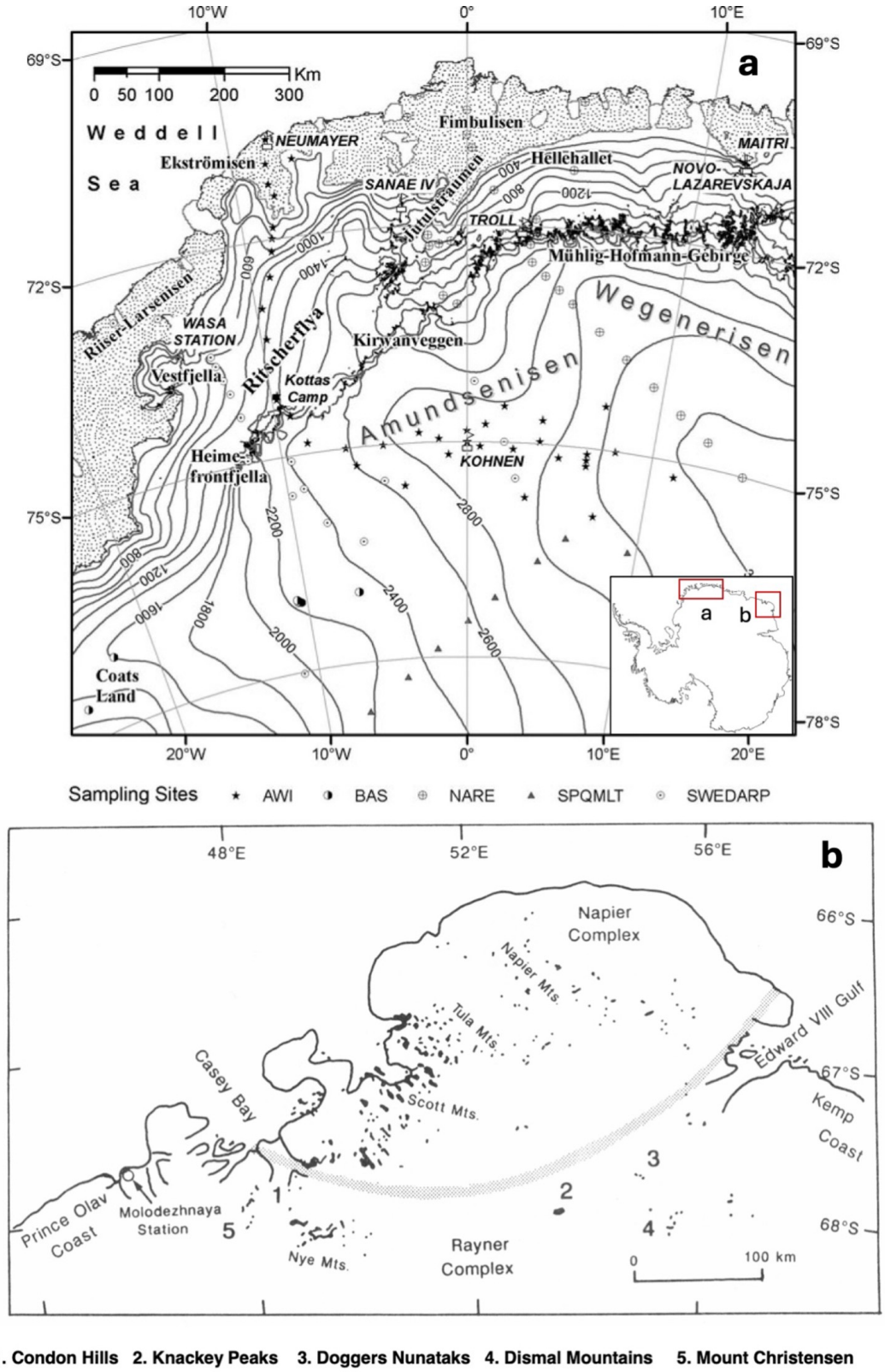

Figure 3.7: *a) Morphology of DML with elevation contours in 200 m intervals (solid black lines). Black features shows the mountain range with exposed rocks (Rotschky et al. 2007) b) Topography of Enderby and western Kemp Land (Golynsky et al. 1996).*

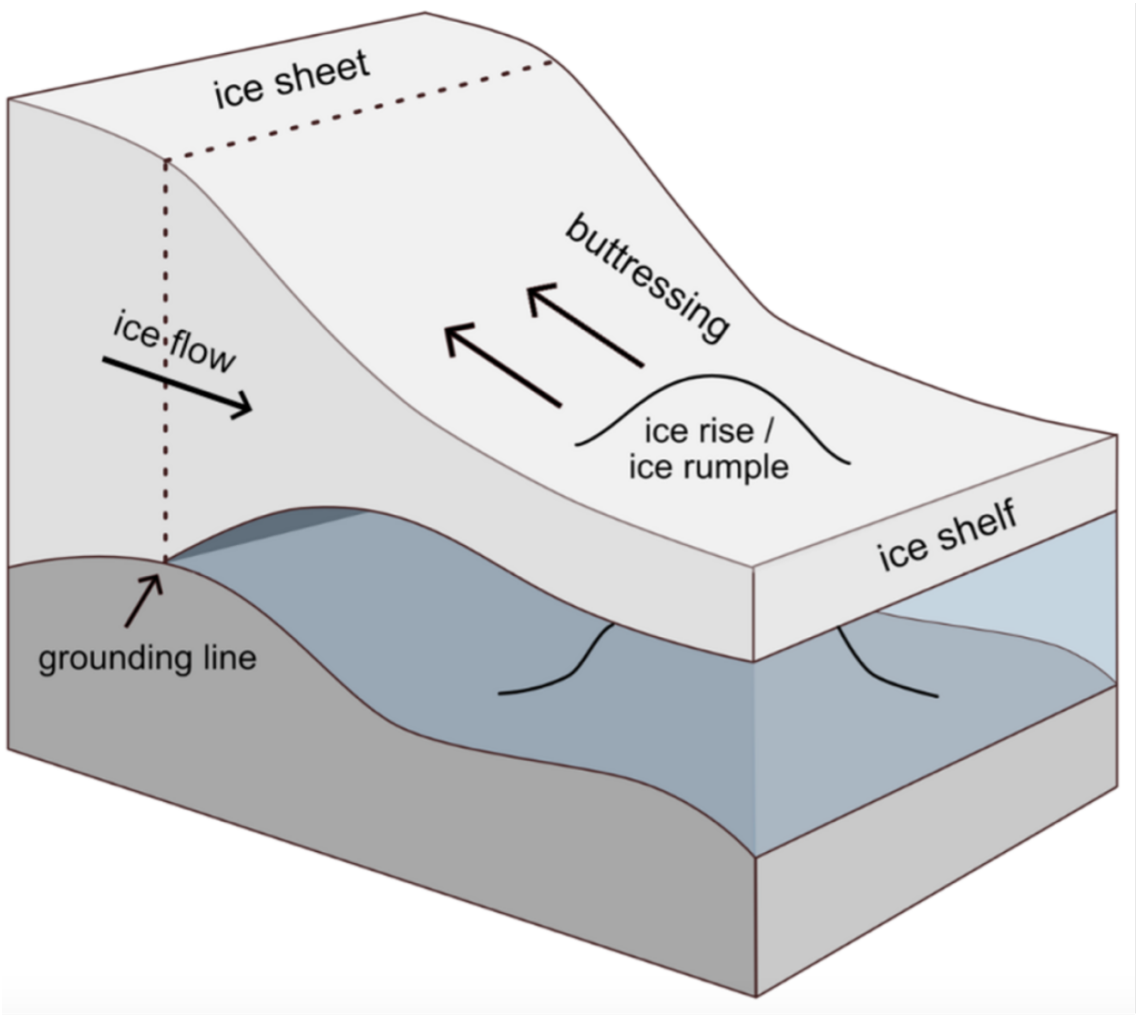

Figure 3.8: *Schematic of ice rises and ice rumple providing buttressing to the inland ice from Clara et al. (2022).*

The sub-ice shelf bathymetry in Fimbulisen identified deep troughs separated by bathymetric highs that likely reflect intense past glacial erosion (Fig. 3.9a; Eisermann et al. 2020). The central trough beneath Fimbulisen has three clear depth peaks at 1300, 1250, and 1150 m. Similarly, the nearby ice shelves, like Ekström and Jelbart, also have uniform troughs running parallel to their main flow, with Ekström's trough reaching about 1100 m and Jelbart's ranging from 1000 to 1200 m (Eisermann et al., 2020; Chang et al., 2015). Although the Fimbulisen is in direct contact with near-freezing ocean water and is classified as a cold-cavity system (Rignot et al., 2013) these deep, topographic structures can serve as conduits for warm circumpolar deep water if the protective shallow sills near the calving fronts are compromised. For instance, ocean warming or a shallower thermocline could let warmer water enter these cavities, increasing basal melting at the ice front and causing increased thinning, rifting and crevassing. This, in turn, could weaken the ice stream, promote calving beyond the passive ice and accelerate ice flow. Notably, in this region the troughs gradually vanish in shallower waters near the calving fronts, where the ice shelves rest on sills with depth maxima of 550 to 600 m. These sills effectively limit the entry of Warm Deep Waters (WDW), which are warm, salty, and dense layer of ocean water originating from the mid-latitudes and flowing southward onto the Antarctic continental shelf, into the ice shelf cavities. This is because the thermocline is typically around 600 m deep in 1000 m deep water (Schröder & Fahrbach, 1999; Hattermann, 2018).

In the Fimbulisen, Jutulstraumen is characterised by the deepest troughs reaching depths of around 1500 m, rendering it especially vulnerable to the incursion of warm waters, a slight but notable sign of which has already been observed (Fig.3.9a, b, Lindbäck et al. 2025). Lauber et al. (2024) noted that WDW has begun to infiltrate the Fimbulisen beneath Jutulstraumen, causing a modest increase in basal melting between 2016 and 2019. These warm water intrusions have been mostly observed from January to March and from September to November during this period (Lauber et al. 2024). The presence of a deep trough of 1500 m depth and shallower sills near the calving front at Jutulstraumenp may allow warm ocean waters or a rising thermocline to influence basal melting in the future.

On the other hand, the bathymetry of Enderby and Kemp Land remains poorly studied, with limited information available on subglacial topography on the continental shelf due to inaccessibility and its remote nature. The bedrock map (Fig. 3.9c) reveals a deep trench connecting Amundsen Bay to Edward VIII Gulf, which effectively separates northern Enderby Land (including the Napier and Tula mountains) from the main continental mass and the ends of this trench are now occupied by the Beaver and Wilma glaciers. Additionally, another major trench extends southward from Edward VIII Gulf along the course of the Robert Glacier.

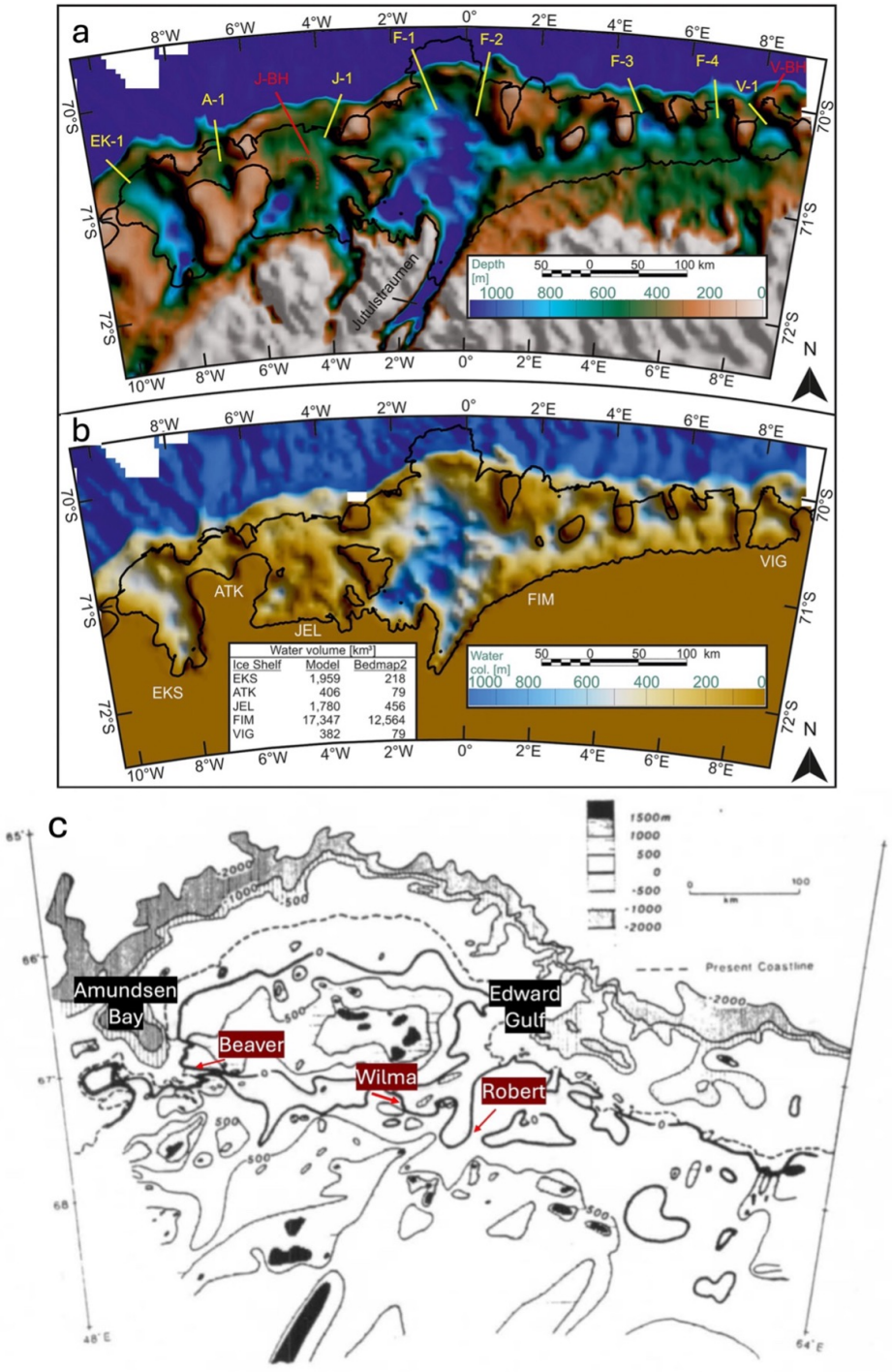

Figure 3.9: *(a) Subglacial bathymetry and water column thickness beneath ice shelves of western DML from Eisermann et al. (2020). Bathymetry, relative to WGS84, shows secluded shelf ice cavities with distinct gateways marked for each ice shelf (yellow). The red labels show bathymetric highs and former possible pinning points in Jelbart (J-BH) and Vigrid Ice Shelf (V-BH). (b) Water column thickness inferred from newly generated bathymetries and ice draft (Riedel et al., 2012) (c) The bedrock elevation with 500 m contour interval (Allison et al. 1982).*

In summary, topography influences DML, Enderby Land and Kemp Lands glaciers in different ways. Importantly, topography also provides the link between the terrestrial and grounded ice and its interaction with climate, as well as the link between the grounded ice and the surrounding ocean, whose changing conditions may influence the ice behaviour. The climatic and oceanic setting of the study areas are now briefly discussed.

3.3 Climatic setting

DML, along with Enderby and Kemp Land, is characterised by an extremely cold and windy climate, with precipitation occurring primarily as snowfall. Over recent decades, DML has experienced episodic extreme precipitation events that have significantly influenced the regional SMB. Average annual snow accumulation on the ice shelves of DML typically ranges between 0.2 and 0.6 m water equivalent (w.e.) (Sinisalo et al., 2013; Pratap et al., 2022), though these rates exhibit substantial spatial variability. Enhanced accumulation often occurs around ice rises due to orographic uplift, whereas wind-driven erosion can reduce deposition locally (Lenaerts et al., 2014; Kausch et al., 2020).

Between 2009 and 2011, DML experienced one of the most pronounced snowfall anomalies on record, resulting in an estimated mass gain of 350 Gt over a three-year period (Boening et al., 2012; Gorodetskaya et al., 2013). This event was driven by anomalous large-scale atmospheric circulation patterns that intensified the poleward transport of moisture (Lanaert et al., 2013). Snow accumulation in DML also exhibits pronounced interannual and spatial variability (Van den Broeke et al., 2004; Pattyn et al., 2010; Takahashi et al., 1994, 2003), largely influenced by the region's high frequency of cyclonic activity (Jones and Simmonds, 1993; Simmonds and Keay, 2000). This region is highly sensitive to changes in midlatitude atmospheric circulation patterns as most precipitation originates from extratropical cyclones (Noone et al., 1999).

Atmospheric rivers (ARs) play a pivotal role in shaping the precipitation dynamics

of East Antarctica, particularly in DML, Enderby and Kemp Land. In DML, ARs contribute significantly to extreme snowfall events, leading to short-lived but intense accumulation episodes that can substantially impact the surface mass balance (SMB) (Baiman et al., 2023). These episodes are often linked to amplified Rossby wave activity and persistent blocking high-pressure systems, which create pathways for the advection of warm, moisture-laden air from lower latitudes (Schlosser et al., 2010). While such events offer short-term gains in SMB, their occurrence remains highly sensitive to variability in midlatitude atmospheric circulation (Massom et al., 2004).

Between 1980 and 2018, notable increases in annual snowfall were observed in both DML and Enderby Land, regions where AR activity is particularly influential (Fig. 3.10; Wille et al., 2021). These snowfall trends are closely aligned with a statistically significant rise in AR frequency over the same period. In fact, a large proportion of the positive snowfall trends in these regions can be directly attributed to increased AR-related precipitation. This is especially evident when analysing the percentage of snowfall trends explained by AR events, underscoring ARs as a dominant driver of recent precipitation variability and accumulation in DML and Enderby Land (Wille et al., 2021).

Furthermore, the DML region encompasses blue-ice areas, where the rate of annual snow sublimation and erosion exceeds that of snowfall accumulation (Bintanja, 1999; Winther et al., 2001; Van den Broeke et al., 2006).

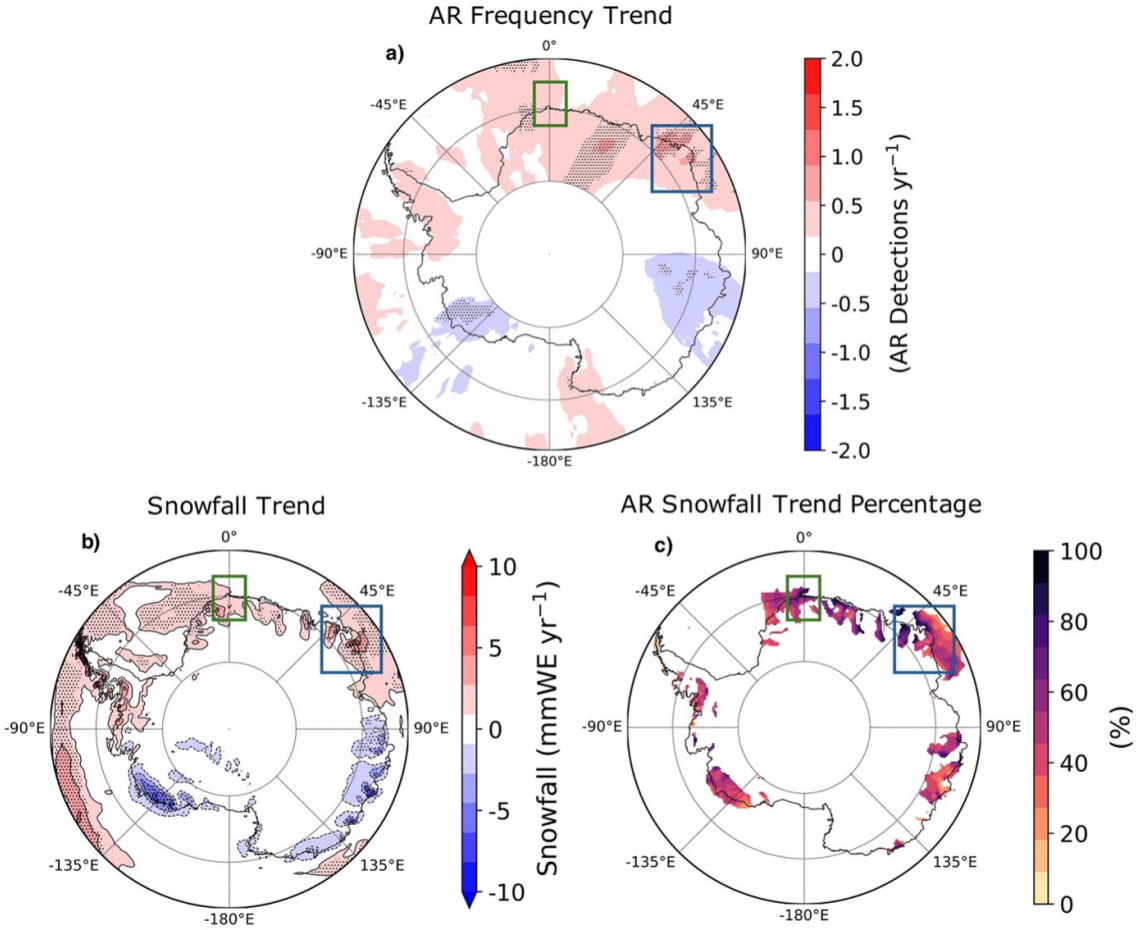

Figure 3.10: *(a) Trends from 1980 to 2018 from Wille et al. (2021) in (a) annual atmospheric river (AR) frequency, (b) annual snowfall simulated by MAR, and (c) the percentage of annual snowfall attributed to AR-related events in regions where absolute snowfall trends exceed 0.5 mm WE yr^{-1}. Black circles indicate areas with statistically significant trends (p-value $<$ 0.025). Refer to Figure 3 in Wille et al. (2021) for AR-related snowfall totals.*

3.4 Oceanic setting

3.4.1 Ocean temperatures

Ocean conditions along the East Antarctic margin, including the DML, Enderby and Kemp Land sectors, are primarily governed by the Antarctic Slope Current (ASC), a westward-flowing current that follows the continental slope (Jacobs, 1991). This current plays a critical role in controlling the distribution and movement of water masses along the Antarctic coastline, influencing both heat transport and ice-ocean interactions. The structure and variability of the ASC significantly affect oceanic processes along the Antarctic margin, particularly the cross-slope transport of heat, which plays a role in ice shelf melting and water mass formation (Heywood et al., 2014; Schmidtko et al., 2014; Cook & Vaughan, 2010; Paolo et al., 2015; Pritchard et al., 2012).

In the DML region, shelf waters are primarily composed of cold, low-salinity Fresh Shelf Water (Fig. 3.11a, c, e). Persistent easterly winds drive surface waters towards the coast, resulting in elevated sea surface height near the shore and strengthening the ASC (Thompson et al., 2018). This circulation regime limits the onshore intrusion of warm, saline CDW by creating tilted isopycnals that act as a barrier along the continental slope. As a result, CDW must move across different density layers to reach the continental shelf. This process, called diapycnal mixing, changes the temperature and salinity of the CDW. This altering of thermohaline properties help keep shelf waters relatively cold and limit the amount basal melting of ice shelves. Interaction between the ASC and the southern limb of the Weddell Gyre, a large, wind-driven current guided by topographic steering, also contributes to regional circulation patterns (Fig. 3.12a; Fahrbach et al., 1992; Heywood et al., 2013). The Weddell Gyre transports CDW westward, where it is gradually transformed into WDW through mixing and surface heat loss. Although the ASC generally restricts WDW from accessing the shelf, episodic intrusions driven by wind anomalies, tides, or mesoscale eddies have been observed, notably beneath central Fimbulisen since 2016 (Lauber et al. 2023). These intrusions have been associated with sub-ice tem-

peratures exceeding -1.5°C and occasional peaks up to 0.2°C, resulting in basal melt rates of 0.62 m yr^{-1} and ice mass loss of 15.5 Gt yr^{-1} between 2016 and 2019 (Fig. 3.12b; Lauber et al., 2023).

In contrast, the Enderby and Kemp Land regions are characterised by Dense Shelf Water (DSW) (Fig. 3.11b, d, e), formed through brine rejection during sea ice production (Thompson et al. 2018). These high-salinity, high-density waters contribute to deep ocean ventilation processes and are a key component of Antarctic Bottom Water (AABW) formation and global deep ocean circulation which subsequently flows downslope across the continental shelf break (Gill, 1973; Baines, 2009; Thompson et al., 2018). The hydrodynamic regime in these regions differs from that of DML, as DSW is capable of descending the continental slope and interacting more directly with CDW near the shelf break. The interaction between the descending DSW and the ASC forms a distinct V-shaped frontal structure, which accommodates both offshore downslope export of DSW and limited onshore transport of CDW. Unlike in Fresh Shelf Water region, CDW in this regime can shoal near the shelf break, allowing for a greater range of density classes to access the continental shelf without direct contact with the ocean surface or seafloor (Thompson et al. 2018).

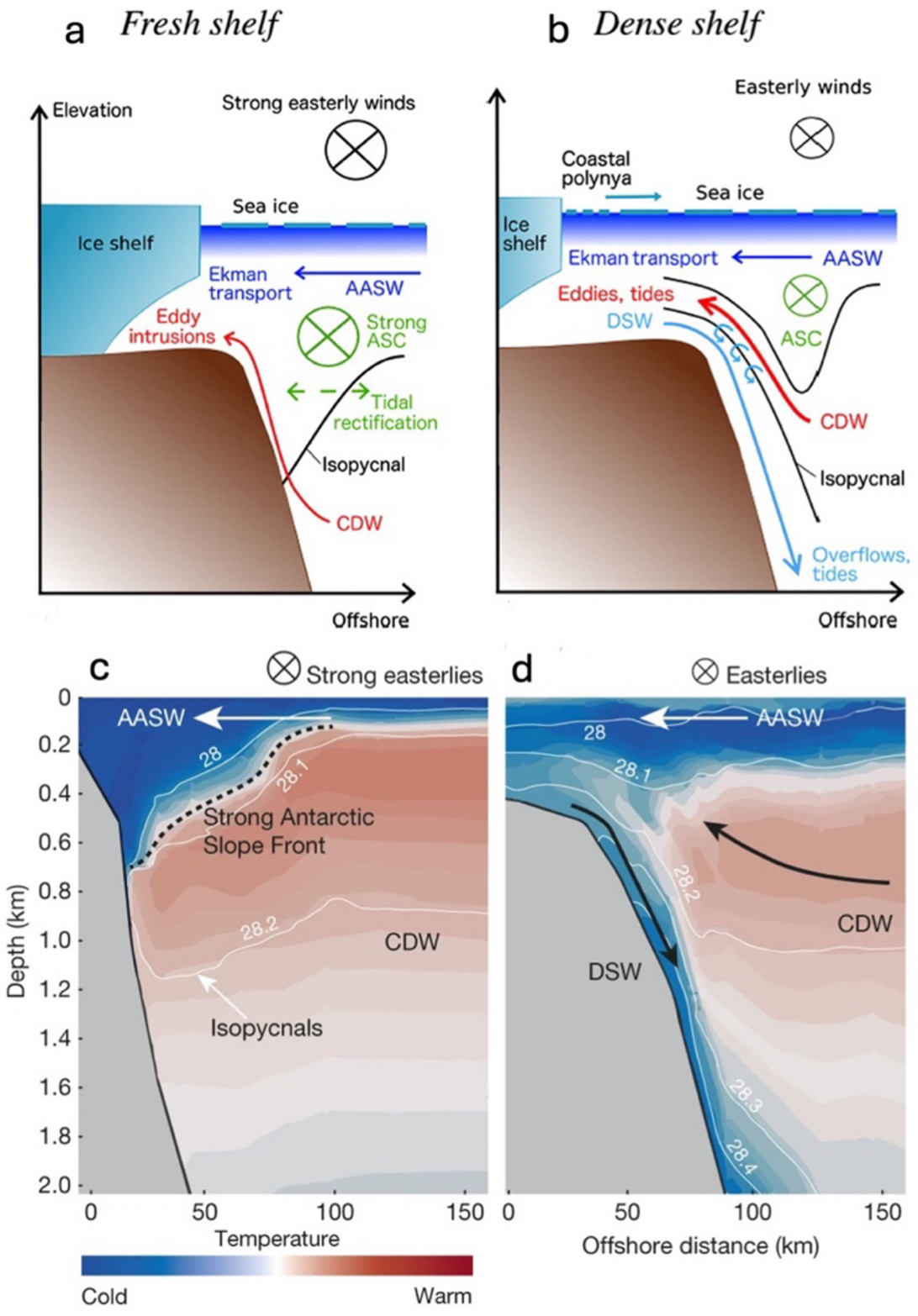
a Fresh shelf
Elevation
Strong easterly winds
Sea ice
Ice shelf
Ekman transport
AASW
Eddy intrusions
Strong ASC
Tidal rectification
Isopycnal
CDW
Offshore
b Dense shelf
Easterly winds
Coastal polynya
Sea ice
Ice shelf
Ekman transport
AASW
Eddies, tides
DSW
ASC
CDW
Isopycnal
Overflows, tides
Offshore
c
Strong easterlies
AASW
28
28.1
Strong Antarctic Slope Front
28.2
CDW
Isopycnals
Depth (km)
0
0.2
0.4
0.6
0.8
1.0
1.2
1.4
1.6
1.8
2.0
0
50
100
150
Temperature
Cold
Warm
d
Easterlies
AASW
28
28.1
28.2
CDW
DSW
28.3
28.4
0
50
100
150
Offshore distance (km)

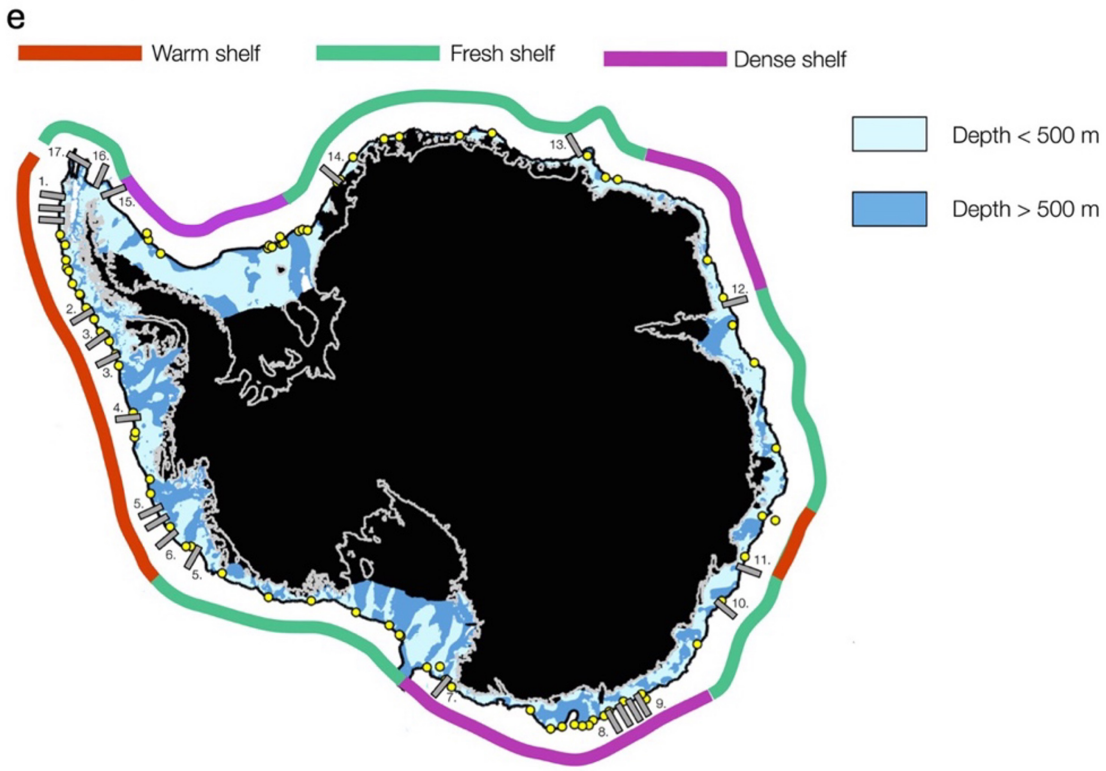

Figure 3.11: *(a) Schematic representation of the Fresh Shelf and Dense Shelf regimes of the Antarctic Slope Current (ASC), illustrating two key water masses, along- and across-slope flows, and the mechanisms that sustain them. (c) and (d) show latitude–depth transects of these regimes, depicting typical wind patterns, subsurface ocean circulation, temperature, and density structures (Stokes et al., 2022; Thompson et al., 2018). The coloured bar represents the spatial distribution of the three ASC classifications shown in (a) and (b). The black contour line marks the 1,000-meter isobath, indicating the shelf break, while shaded regions illustrate continental shelf bathymetry and depth variations.*

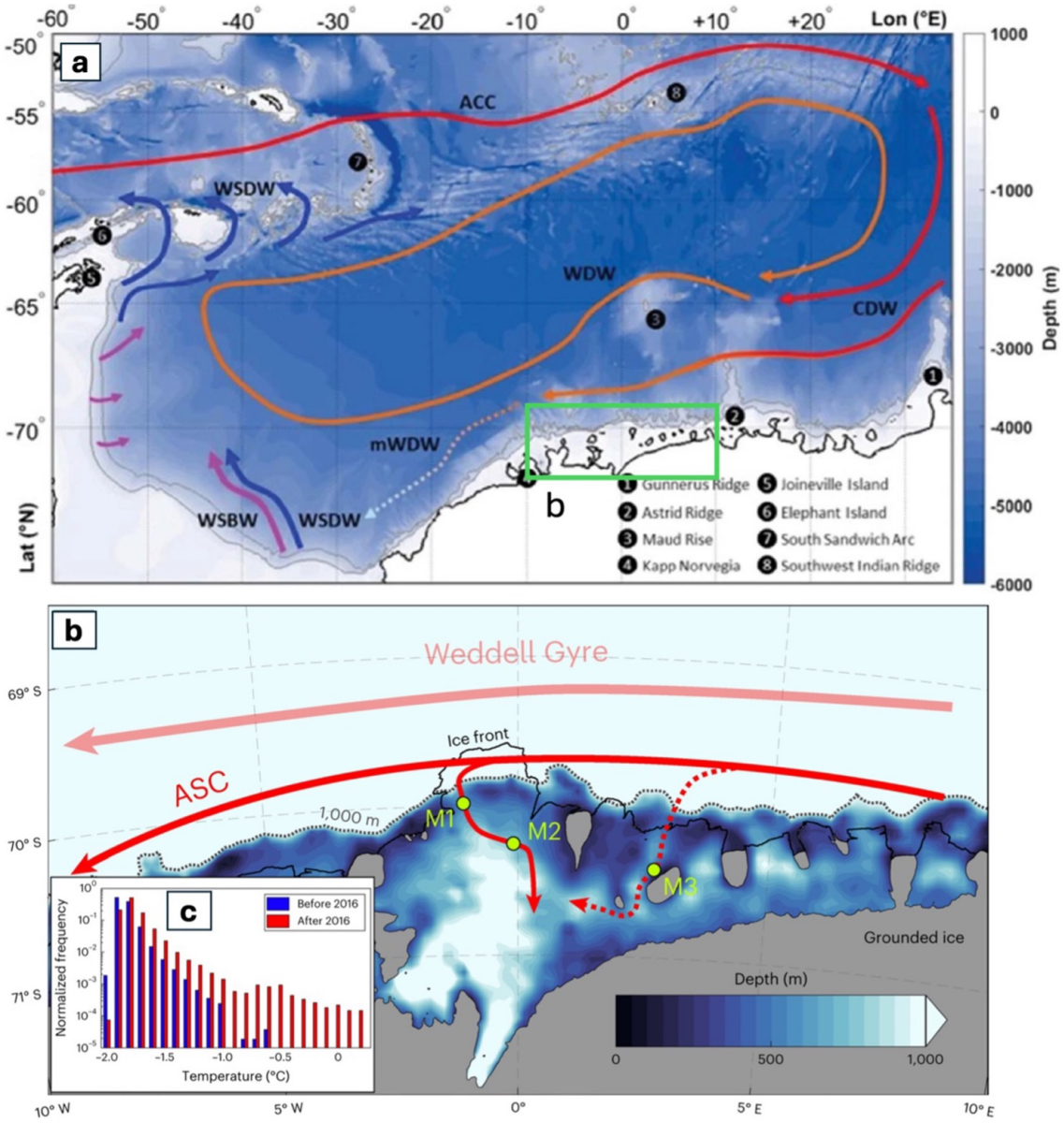

Figure 3.12: *(a) The general circulation and pathways of water masses in the Weddell Gyre off the Dronning Maud Land coast (from Reeve et al. 2019), where ACC: Antarctic Circumpolar Current, CDW: Circumpolar Deep Water, WDW: Warm Deep Waters, WSDW: Weddell Sea Deep Water, WSBW: Weddell Sea Bottom Water (Lowther et al. 2022) (b) Map of the Filchner Ice Shelf (FIS) displaying bathymetry in colour. Green dots indicate the locations of three sub-ice-shelf moorings (M1–M3). Red arrows represent the Weddell Gyre and the ASC, along with the primary (solid) and secondary (dashed) pathways of mWDW follows the trough of Jutulstraumen. (c) A histogram comparing the occurrence of M1 lower-layer temperatures before and after (including) 2016. The y-axis represents the fraction of time each temperature bin was observed in the respective period, illustrating changes in temperature distribution over time (Lauber et al. 2023).*

3.4.2 Sea ice conditions

Sea ice conditions in the coastal region of DML are characterised by a relatively limited and short-lived presence of landfast ice compared to other parts of the Antarctic margin (Fraser et al., 2020). Fast ice refers to sea ice that remains stationary because it is anchored to coastal features such as shorelines, glacier tongues, ice shelves, grounded icebergs, or shallow seabeds (World Meteorological Organization 1970; Massom et al. 2001; Fraser et al. 2012). Fast ice coverage in this area varies seasonally between approximately 10,000 and 70,000 km^2. During summer, fast ice accounts for around 30% of the regional sea ice area, declining to about 1% in winter, indicating significant seasonal variability (Fraser et al., 2020). This reduced extent and persistence is likely related to the region's deep bathymetry, which limits the presence of grounded icebergs that typically anchor fast ice (Fraser et al., 2021). Within DML, the Fimbulisen area is particularly notable for its fragmented and ephemeral fast ice cover. In contrast, the Enderby and Kemp Land regions, within the western Indian Ocean sector, maintain some of the most extensive and persistent fast ice along the EAIS. These areas contribute substantially to the overall continental fast ice distribution, with persistence ranging from approximately 70% to 100%, compared to 50% in the Fimbulisen area (Fig. 3.13). The timing of seasonal minimum fast ice extent also varies across regions: in Enderby Land, it typically occurs in April, while further east along the Mawson Coast of Kemp Land, the minimum generally occurs between February and March (Fraser et al., 2021). These regional differences reflect the influence of localised oceanographic and atmospheric conditions on fast ice dynamics.

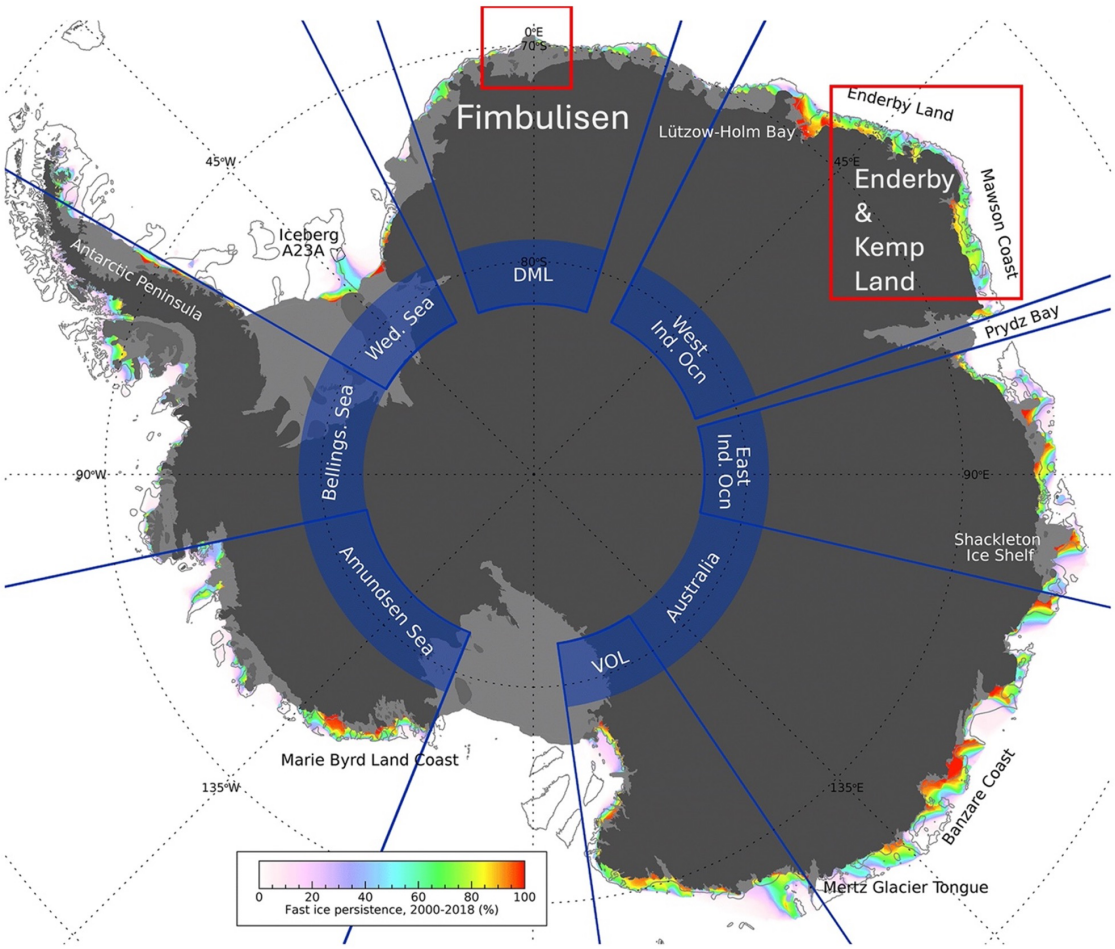

Figure 3.13: *(a) Trends from 1980 to 2018 from Wille et al. (2021) in (a) annual atmospheric river (AR) frequency, (b) annual snowfall simulated by MAR, and (c) the percentage of annual snowfall attributed to AR-related events in regions where absolute snowfall trends exceed 0.5 mm WE* yr^{-1}*. Black circles indicate areas with statistically significant trends (p-value* < 0.025*). Refer to Figure 3 in Wille et al. (2021) for AR-related snowfall totals.*

In the Enderby Land sector, this landfast sea ice is predominantly older than 12 months, with notable spatial variation. At the western margin, fast ice often reaches ages of approximately 24 months, indicating a stable and persistent ice regime. Eastward toward 45°E, typical fast ice ages decrease to around 12 months. Between 45°E and the inland plateau, ice is generally younger, with ages typically below 12 months. In Kemp Land, a persistent fast ice regime is observed offshore of the Wilma–Robert–Downer Glacier system, where ice can also attain ages of up to 24 months. East of this area, fast ice ages decline, with $\sim$ 12-month-old ice prevalent in western Kemp Land and sub-12-month ice dominating the eastern portion. Across both Enderby and Kemp Land, offshore fast ice is generally the youngest, typically between 0 and 10 months in age. In contrast, the Fimbulisen region supports only limited and short-duration fast ice, usually less than six months old. This spatial variability in fast ice age is primarily governed by coastal geometry, bathymetric features, and regional ocean–atmosphere interactions (Fraser et al., 2021).

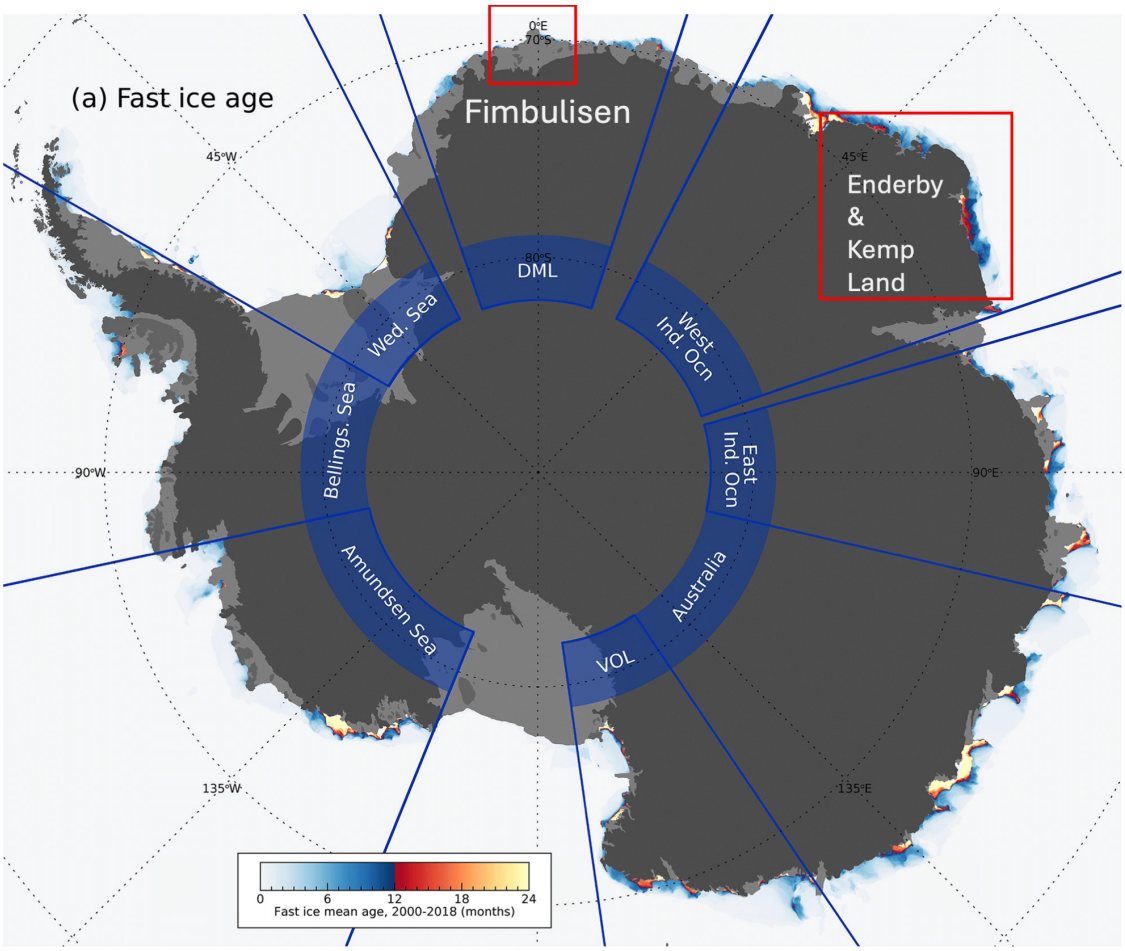

Figure 3.14: *The mean age of landfast sea ice over the 18-year study period reveals distinct spatial patterns in fast ice persistence. Areas shaded from white to blue represent regions characterised by seasonal fast ice, typically forming and melting within a single annual cycle. A deliberate colour transition at the 12-month threshold—from blue to warmer hues (yellow to red)—is employed to clearly demarcate zones of multi-year fast ice. These red-yellow regions indicate areas where fast ice remains stable and persists for more than one year, highlighting locations of enhanced longevity and structural resilience within the broader fast ice regime (Fraser et al. 2021).*

The long-term trends in SIC reveal regional and temporal variability. In the DML sector, which includes the Fimbulisen region (red box in Fig. 3.15a, b), SIC increased between 1979 and 2015, followed by a marked decline from 2015 to 2018 (Fig. 3.15, Eayrs et al. 2021). In contrast, within the Western Indian Ocean sector, where Enderby and Kemp Lands are located (purple box in Fig. 3.15a, b), SIC exhibited a slight decrease west of 45°E and a slight increase to the east during the 1979–2015 period (purple box in Fig. 3.15a, Eayrs et al. 2021). Subsequently, between 2015 and 2018, there was an increase in SIC over the entire Enderby and Kemp Land region (purple box in Fig. 3.15b, Eayrs et al. 2021).

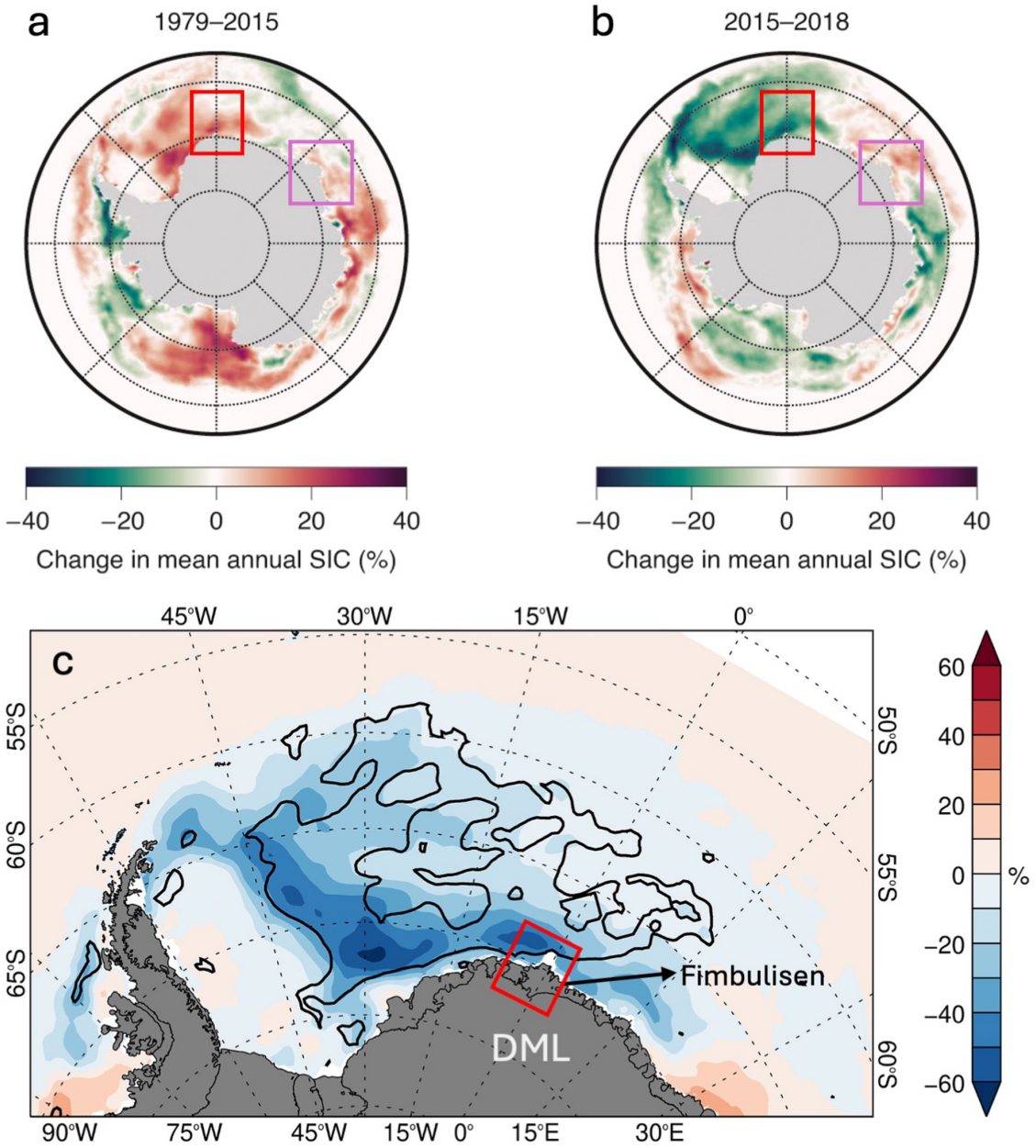

Figure 3.15: *Mean annual SIC changes from (a) 1979 to 2015 (b) 2015 to 2018 (Eayrs et al. 2021). The red box shows the location of Fimbulisen and the purple box shows Enderby and Kemp Land. (c) The difference of summer SIC between 2013/2015 and 2016/2018. Red box shows the location of Fimbulisen (Turner et al. 2020).*

Additionally, Turner et al. (2020) reported a substantial decrease in summer SIC between 2013/2015 and 2016/2018 across the Weddell Sea and DML sector (see Fig. 3.13 for the location of DML). This decline was particularly extensive in the Weddell Sea sector, but within DML, the Fimbulisen region experienced the most pronounced losses, especially west of the Jutulstraumen Glacier, where SIC fell by approximately 40% (Fig. 3.15). In contrast, no notable change was observed directly in front of the Jutulstraumen terminus (Fig. 3.15).

Fraser et al. (2021) observed that between 1979 and 2015, mean annual SIC in the DML region increased by approximately 20–30%, consistent with the overall growth in sea ice during this period (Fig. 3.15a). This positive trend was also pronounced in the Fimbulisen area (Fig. 3.15a). However, following 2015, this trajectory reversed sharply, with SIC in the wider Weddell Sea sector, DML and in the Fimbulisen region, declining by roughly 20–30% between 2015 and 2018 (Fig. 3.15b, 3.16). This recent decline is further corroborated by fast ice anomaly data. These anomalies indicate a marked reduction in fast ice extent after 2015 across both DML and the Enderby and Kemp Land regions (Fig. 3.16b, d).

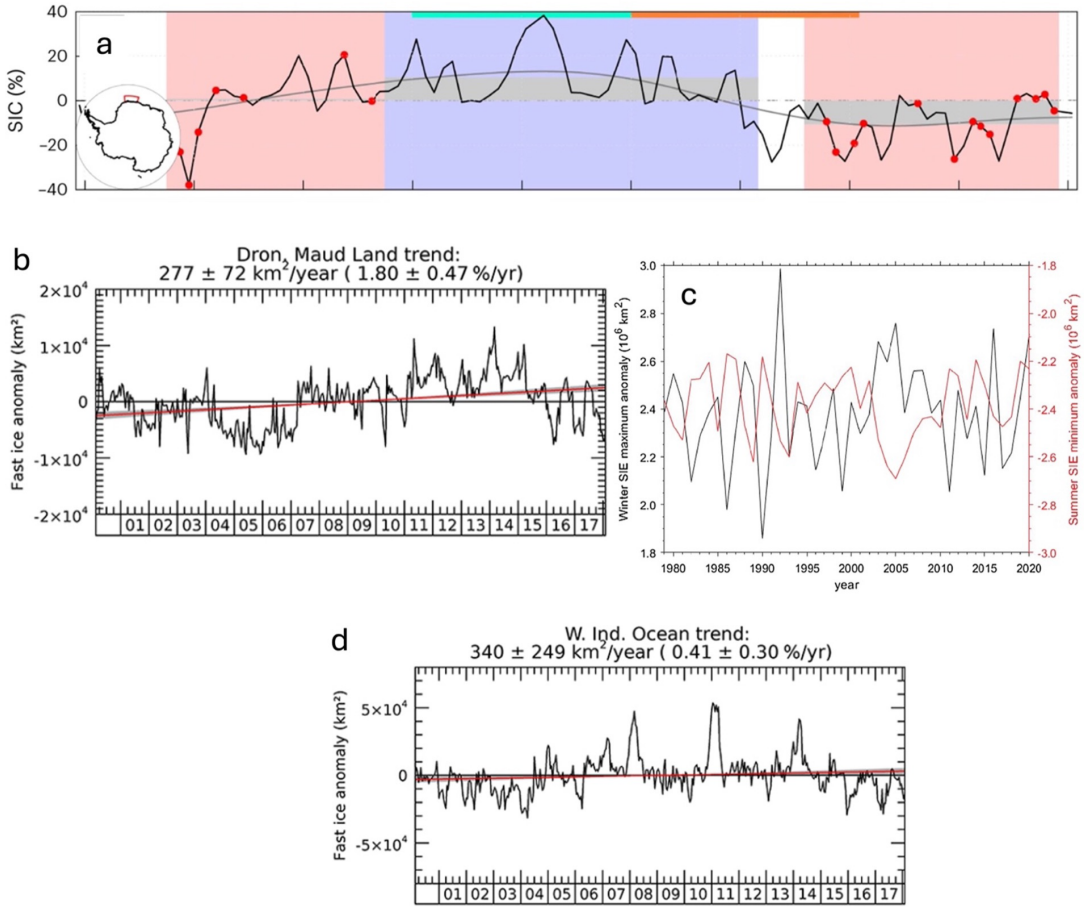

Figure 3.16: *(a) Time series of sea ice concentration (SIC) from Lauber et al. (2024), with grey lines representing the 48-month filtered data. (b) Anomalies in fast-ice extent for Dronning Maud Land (black line), with corresponding linear trends shown in red. The trend magnitude and bootstrapped 95% confidence intervals are provided in the subplot titles (Fraser et al. 2021). (c) Anomalies in sea ice extent (SIE) for the winter maximum and summer minimum in the Dronning Maud Land sector of the Southern Ocean, based on monthly mean SIC derived from Special Sensor Microwave/Imager data (Lowther et al., 2022) (d) Anomalies in fast-ice extent for Western Indian Ocean (black line), with corresponding linear trends shown in red (Fraser et al. 2021).*

The prolonged sea ice loss in Weddell Sea and the DML sector is potentially attributed to several factors. Firstly, a large and long-lasting polynya over Maud Rise (Fig. 3.17) began forming in summer 2015 and became the most extensive since the 1970s (Carsey, 1980). This area of open water allowed early summer shortwave radiation to warm the ocean surface, delaying sea ice formation in the seasons that followed. As a result, a reduction in the SIC in both these sectors were observed between 2013/2015 and 2016/2018 (Fig. 3.15b, c). In addition, SIE between 2017 and 2019 remained well below the 2013–2015 average throughout the year in the Weddell Sea sector (Turner et al., 2020). Secondly, the region was impacted by two extremely deep cyclones in September 2016 and 2017, marked by record low sea level pressures (Wang et al., 2019). Thirdly, a strong negative phase of the SAM contributed to unusual ocean surface warming (Thompson & Wallace, 2000; Stuecker et al., 2017). In addition, strong westerly winds in September 2016 pushed sea ice away from the northwestern Weddell Sea (Turner et al., 2020). However, in Enderby Land and Kemp Land, the reasons for the change in sea ice conditions is understudied and is therefore not well understood.

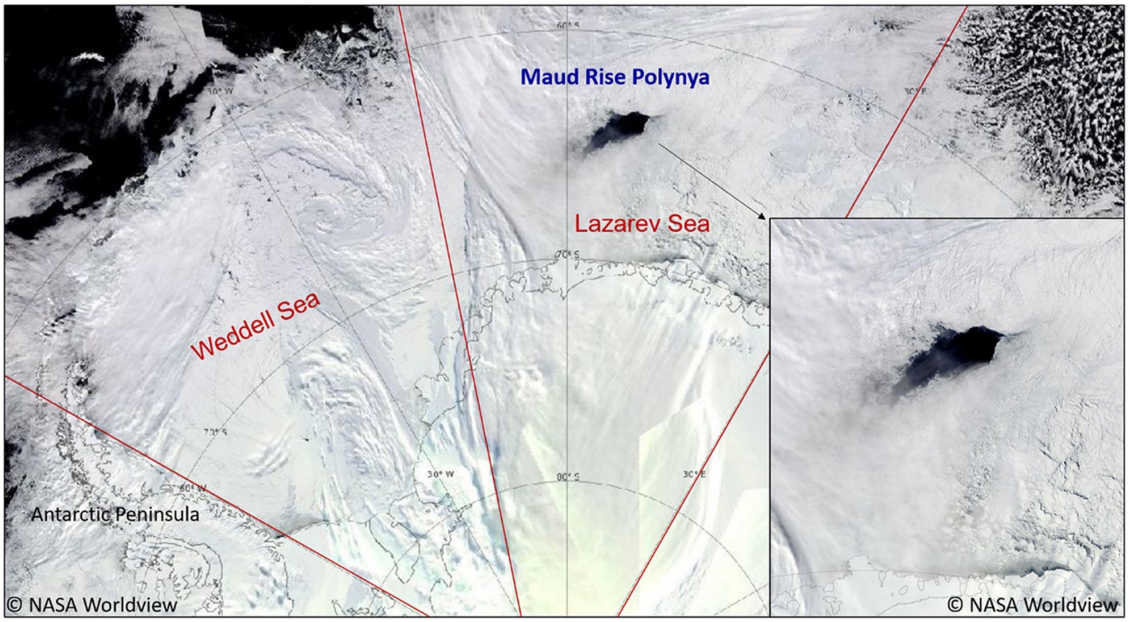

Figure 3.17: *MODIS visible satellite imagery illustrating the location of the Maud Rise polynya in the Lazarev Sea, situated to the east of the Weddell Sea and the Antarctic Peninsula. Satellite imagery is sourced from NASA Worldview (https://worldview.earthdata.nasa.gov/) and has been adapted by the authors from Francis et al. (2019).*

3.5 Summary

The Fimbulisen, Enderby, and Kemp Land regions represent uniquely important yet understudied sectors of East Antarctica. Their contrasting glaciological, topographic, climatic and oceanographic settings, ranging from buttressed ice shelves in DML to fjord-like glacier systems in Enderby and Kemp Land, offer the potential to investigate a wide range of mechanisms governing ice sheet stability. Despite recent mass gains or near-equilibrium conditions, these regions are not immune to change, as evidenced by evolving sea ice dynamics, atmospheric variability, and emerging signs of ocean-driven basal melting. Their sensitivity to climatic and oceanic forcing, coupled with structural and topographic complexity, makes them ideal natural laboratories for investigating the processes that may dictate the future behaviour of the EAIS. Understanding these processes is critical for improving projections of regional and continental ice mass balance in a warming climate. The first step required to achieve this understanding, is to systematically measure any glacier changes that

have occurred in this region taking special care to observe glaciological details (e.g. terminus change, glacier structure, sea ice conditions) at individual glacier scales that have tended to be ignored in studies that look solely at ice sheet mass balance at a catchment to regional scale.

CHAPTER 4

Influence of climate variables on glacier terminus behaviour in Enderby Land and Kemp Land, East Antarctica (1970s-2023)

Sharma, A., Stokes, C. R., & Jamieson, S. S. R. (2025). Influence of climate variables on glacier terminus behaviour in Enderby Land and Kemp Land, East Antarctica (1970s-2023) [To be submitted]

4.1 Abstract

This study presents an analysis of glacier terminus position changes in Enderby Land and Kemp Land, East Antarctica, from the 1970s to 2023. A total of 44 marine-terminating outlet glaciers are examined using satellite imagery, analysing their behaviour with key oceanic and atmospheric climate drivers. The study reveals that glacier terminus positions have shown significant temporal and spatial variability, with phases of both retreat and advance. From 1970 to 1988, 61% of glaciers retreated, followed by a period (1988–2000) when 68% of glaciers advanced. In the subsequent two periods (2000–2010 and 2010–2023), 64% of glaciers exhibited advance during the former, whereas 57% underwent retreat in the latter. At the regional scale, terminus retreat phases were moderately correlated with lower sea-ice concentrations at a two-year lag, implying that reduced sea-ice cover may precede glacier retreat or reduce buttressing at the ice front. A strong negative correlation was also found between glacier terminus change and subsurface ocean temperatures at a five-year lag, particularly in the upper ocean layer (5–109 m), indicating that prolonged exposure to warmer waters can drive retreat through increased frontal and basal melting. However, the prevalence of glacier advance—particularly after 2000—coincided with a multi-decadal cooling trend in subsurface ocean temperatures, along with sustained or increasing sea-ice concentration in most parts of the study area. Across individual glaciers, responses to ocean–climate forcings were asynchronous. While some glaciers showed sensitivity to sea-ice variability, others were more strongly influenced by ocean thermal conditions. Subsurface ocean temperatures at 5–109 m exhibited a strong, statistically significant negative correlation with terminus behaviour, suggesting that higher temperatures tend to precede retreat, whereas colder waters are associated with stability or advance. Sea-ice concentration, in contrast, showed a moderate positive correlation with terminus position at a two-year lag, but only for a subset of glaciers. This indicates that high sea-ice cover may exert a localised buttressing effect by suppressing ocean swell and limiting warm water access to glacier fronts. Taken together, these findings highlight that the recent dominance of glacier advance in Enderby and Kemp Lands is likely linked

to the persistence of cold ocean conditions and relatively high sea-ice concentration in these regions over the past few decades. This contrasts with other sectors of the Antarctic margin where dynamic thinning and retreat are more common, underscoring the importance of regional ocean-climate conditions in modulating glacier response.

4.2 Introduction

Numerous studies have shown that the Greenland Ice Sheet (GrIS) and Antarctic Ice Sheet (AIS) have experienced substantial mass loss over the past several decades, with the drivers of mass loss varying significantly between the two ice sheets. In GrIS, increased ice discharge coupled with a negative surface mass balance drives mass loss in approximately equal proportions (van den Broeke et al., 2016; Enderlin et al., 2014; IMBIE, 2022). In contrast, the AIS's increased ice discharge predominantly arises from processes such as iceberg calving and ocean-induced thinning of ice shelves in the West Antarctic Ice Sheet (WAIS), which can destabilise marine-terminating glaciers by reducing buttressing effect (Bindschadler et al., 2011).

Typically, it has been observed that, in the EAIS, prolonged atmospheric and oceanic preconditioning weakens ice shelves, ultimately leading to calving or disintegration events. For example, the 2022 collapse of the Conger-Glenzer Ice Shelf in the EAIS offers an example of how long-term precursor processes can compromise ice shelf stability (Baumhoer et al., 2021; Walker et al., 2024). This disintegration event occurred primarily as a result of around 90 m of thinning over 25 years and sustained basal melting which weakened the ice shelf over time making it even more vulnerable to external forcings. In 2011, retreat from a pinning point marked a key threshold, after which thinning and basal melt persisted, and fracturing became more intensified around 2017. Accelerated thinning and the propagation of large rifts eventually led to unpinning from Bowman Island, triggering the complete collapse of the ice shelf in 2022. Therefore, recognising long-term oceanic and structural precursors—such as sustained thinning, loss of pinning points, and rift propagation—is crucial for understanding how floating ice tongues become destabilised and how glaciers and

ice shelves may be preconditioned for eventual collapse.The disintegration of the Porpoise Bay and Voyeykov ice shelves in 2007 (Miles et al., 2016; Arthur et al., 2022) and the Parker Ice Tongue in 2020 (Gomez-Fell et al., 2022) also highlight the importance of oceanic and atmospheric conditions in preconditioning ice shelves and ice tongues for collapse. In Porpoise Bay, the 2007 breakup followed the loss of multi-year landfast sea ice that had previously buttressed the glacier fronts (Miles et al., 2016). This loss was linked to unusual atmospheric conditions in the summer of 2005/2006, including strong easterly winds, weakened westerlies, and elevated sea surface temperatures, which likely triggered sea ice fractures after December 2005 (Miles et al., 2016). Similarly, the Voyeykov Ice Shelf disintegrated following several years of reduced landfast sea ice and warmer-than-normal air temperatures, alongside a decline in the stabilizing effect of the local latent heat polynya (Stammerjohn et al., 2011; Khazendar et al., 2013). The Parker Ice Tongue collapse in 2020 followed multiple seasons of complete fast-ice loss. This loss removed a key stabilising force, exposing the tongue to ocean swell and currents. Fast-ice had previously helped maintain the tongue's structural integrity, but after its removal, rifting began in 2017 and culminated in the full detachment in 2020. This underscores how the progressive weakening or removal of frontal buttressing, particularly through sea ice loss can act as a precursor to major calving or collapse events.

Moreover, the calving of a major iceberg from Mertz Glacier in 2010 was the outcome of several interacting external processes (Massom et al., 2015). Between 2002 and 2004, the glacier's ice tongue experienced two abrupt changes in flow direction after grounding on shallow shoals, which led to rotational strain, increased internal stress, and the development of rifts (Massom et al., 2015). The second grounding event caused extensive fracturing and deformation in the northwestern section of the tongue, while the eastern margin remained relatively intact, enabling the formation of a rift that eventually cut across the tongue (Massom et al., 2015). Additionally, a large tabular iceberg (C08), which calved from the Ninnis Glacier tongue between 1980 and 1982 (Frezzotti et al., 1998), collided with the northeastern corner of the Mertz Glacier Tongue in early 2002. This event may have intensified contact with the first shoal, enhancing the eastward deflection (Massom et al., 2015). However,

the calving from two conjoined through-cutting rifts on the Mertz floating tongue was delayed from 2002 to 2010 due to mechanical coupling provided by multiyear fast-ice (Massom et al., 2015). Its removal that year coincided with the final calving event, which was likely triggered by the drift of iceberg B09B, further destabilising the already weakened ice tongue (Massom et al., 2015). Similarly, a thick consolidated ice mélange played an important role in holding disparate parts of the Brunt/Stancomb-Wills Ice shelf together (Khazender et al., 2009). In addition, the presence of landfast sea ice in the summer of 2006 in front of the Wilkins Ice Shelf buttressed the weakened outer margins of the ice shelf, maintaining the structural integrity and suppressing calving (Massom et al., 2018). Together, these examples emphasize the stabilizing role of sea ice, fast ice, and ice mélange in maintaining the structural integrity of floating ice shelves and tongues in the EAIS.

In addition to sea ice conditions, ocean temperatures play a key role in controlling the glacier behaviour due to enhanced basal melt by ocean heat flux and ice shelf thinning (Pritchard et al., 2012; Paolo et al., 2015; Rignot et al., 2014). For example, in Wilkes Land, the glacier termini retreat observed between 2000 and 2012 was largely attributed to an exceptionally low number of sea ice days. However, the subsequent retreat from 2009 to 2018 occurred without similar extreme sea ice anomalies (Miles et al., 2016). In this case, Baumhoer et al. (2021) proposed that the retreat was driven by the upwelling of CDW, which likely enhanced basal melting and contributed to glacier weakening. This upwelling was linked to a marked positive trend in zonal wind speeds—reaching up to +0.44 m/s above the reference mean—which would have intensified ocean-driven melt (Baumhoer et al., 2021).

Importantly, existing studies collectively highlight that ice shelf and glacier disintegration is rarely the result of a single, abrupt event. Rather, it reflects the cumulative impact of multiyear external stressors, including atmospheric anomalies, declining sea ice concentrations, and a range of pre-conditioning processes such as prolonged thinning, structural weakening, interactions with shoals, fracture development, and loss of buttressing (Scambos et al., 2000; Pollard et al., 2015; Wouters et al., 2015; Cook et al., 2016; Scambos et al., 2017; Kopp et al., 2017; Alley et al., 2018; Leeson

et al., 2020; Francis et al., 2022; Wallis et al., 2023; Miles et al., 2016; Arthur et al., 2022). These drivers of calving and disintegration also exhibit considerable spatial variability across the Antarctic Ice Sheet (AIS). This raises a key question: to what extent are these pre-conditioning processes consistent across different regions of the EAIS? Addressing this question requires a deeper understanding of the interactions between glacier dynamics and both localized and regional atmospheric–oceanic forcing, especially in under-studied regions such as Enderby Land and Kemp Land (Chapter 3).

As noted earlier in the thesis, research in Enderby and Kemp Lands remains limited. Rignot et al. (2019) reported that Enderby Land and Kemp Land were broadly in mass balance between 1979 and 2017. However, detailed long-term investigations of individual glacier termini have been scarce. One of the most comprehensive studies was conducted by Miles et al. (2016), who analysed changes in glacier termini from the 1970s to 2010. Their results showed alternating decadal phases of retreat and advance, with widespread retreat between the 1970s and 1990s associated with declining sea ice concentrations, followed by advance from 1990 to 2000 linked to increased sea ice coverage. The decade from 2000 to 2010 was characterised by continued glacier advance but the study ended in 2010.

More recently, Baumhoer et al. (2021) investigated decadal-scale changes in a subset of glaciers in Enderby and Kemp Land between 1997 and 2018. Their study reported that outlet glaciers and ice shelves advanced at a rate of 62 ± 4.8 km^2 yr^{-1} and retreated at a rate of 89 ± 5.6 km^2 yr^{-1} during the first decade (1997–2008). In the subsequent decade (2009–2018), the trend shifted, with advance rates increasing to 80 ± 8.9 km^2 yr^{-1} and retreat rates declining to 53 ± 4.2 km^2 yr^{-1}. Overall, across the entire region of Enderby and Kemp Land very little net change was found, with comparable mean rates of advance (34 ± 3.8 km^2 yr^{-1}) and retreat (36 ± 2.1 km^2 yr^{-1}) from 1997 to 2018. Notably, spatial variability was evident—Rayner–Thyer Glacier advanced between 1997 and 2008 while the Wilma–Robert–Downer Glacier system retreated, with this trend reversing in the following decade (2009–2018). Despite these spatial differences within Enderby and Kemp Lands, Baumhoer et al. (2021)

did not explore in detail the environmental drivers responsible for the contrasting behaviours of individual glaciers, nor did they include the majority of glaciers within this region, leaving critical gaps in our understanding of glacier dynamics in this region.

This study builds on the insights of Miles et al. (2016) and Baumhoer et al. (2021), it differs in several important ways. First, this study includes extended temporal coverage by more than a decade to include glacier behaviour up to 2023. Second, the dataset includes a larger and more comprehensive sample of glaciers—with 44 glaciers from both Enderby and Kemp Land, compared to a smaller subset analysed by Miles et al. (2016) and Baumhoer et al. (2021) in the same region. Finally, this study integrates statistical correlation analyses between glacier terminus change and multiple ocean–climate variables, enabling a more direct and quantitative assessment of environmental drivers for this particular region.

Therefore, this chapter addresses the following research questions, and the associated objectives are mentioned below:

• What is the long-term behaviour of glacier termini in Enderby and Kemp Lands between the 1970s and 2023 and is there any spatial relationship between glacier termini behaviour across the two regions?

- To address this question, the terminus position of 44 glaciers were mapped and quantified from 1973 to 2024 using a combination of satellite imagery at approximately decadal resolution.

• What external factors influence the glacier termini behaviour in these regions?

- Environmental drivers—including sea-ice concentration, sea ice extent, subsurface ocean temperatures, and air temperatures—were analysed to determine if there were any correlations with the patterns in terminus change.

• Does a statistical relationship exist between ocean–climate forcings and glacier terminus behaviour, and do adjacent glaciers exhibit similar responses?

- Correlation coefficients were computed for both regional groupings and individual glaciers in relation to the environmental drivers.

4.3 Study area

Enderby Land (DB 7) and Kemp Land (DB 8) are situated along the eastern coast of Antarctica, between 45°E and 65°E. Enderby Land lies to the west of Kemp Land, with both areas featuring outlet glaciers draining the EAIS into the Southern Ocean. These specific regions were selected for the study due to several compelling factors (see Section 1.1). Firstly, these regions have historically been underrepresented in glaciological research, making them relatively understudied sectors compared to other parts of the EAIS. Secondly, earlier assessments have suggested that these regions are in a state of near mass balance (Rignot et al. 2019). Their relative stability makes them ideal case studies to understand the reason behind the stability and for detecting the onset of change due to ocean-climatic forcings. Thirdly, these regions are particularly intriguing because of their morphology and topographic setting of their outlet glaciers which are very similar to glaciers in the Greenland Ice Sheet (GrIS) where substantial terminus retreat has been observed in the past few decades (Black & Joughin, 2022). In this chapter, a total of 44 marine-terminating glaciers are studied, with velocities $> 100\,\mathrm{m\,yr^{-1}}$. These glaciers were chosen because satellite imagery showed that these glaciers are different in their topographic settings, shapes and sizes. The topographic settings of these glaciers' mirrors that of tidewater glaciers in the GrIS were discussed in detail in Chapter 3. Figure 4.1 shows the location and names of all the glaciers studied in this chapter.

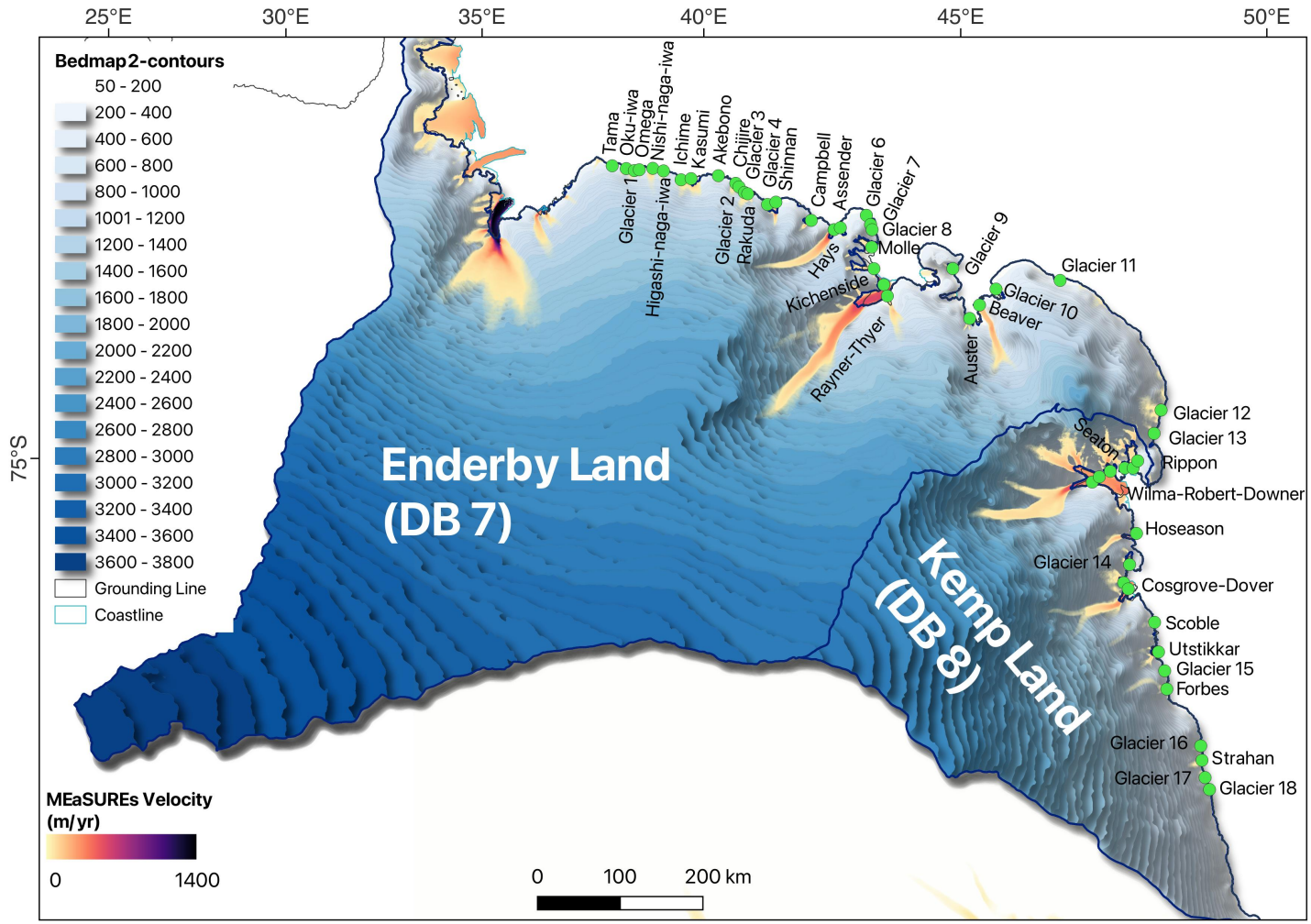

Figure 4.1: *Location of the study area showing the individual glacier locations that were measured and the location of the Enderby Land (DB 7) and Kemp Land (DB 8) drainage basins and the sea ice sampling areas. The contour lines represent the ice surface elevations derived from BedMap 2. Basemaps: Bedmap 2 and MEaSUREs ice flow velocity. The dark blue lines separate the basins DB7 and DB8 (Zwally et al. 2012).*

4.4 Data and Methods

To investigate the behaviour of marine-terminating glaciers in Enderby and Kemp Lands, a comprehensive framework grounded in remote sensing techniques was employed. Satellite imagery facilitated the mapping of glacier terminus position changes over time, enabling the identification of both retreat and advance periods. Atmospheric and oceanic datasets were analysed to compute annual and decadal means, providing insight into the environmental drivers that may influence glacier dynamics. Additionally, statistical approaches—particularly correlation analyses—were applied to examine the relationships between terminus changes and atmospheric and oceanic variables across both temporal scales.

4.4.1 Ice front mapping

In this study, terminus positions were manually digitised for a total of 44 glaciers in Enderby Land and Kemp Land with velocities greater than 100 m yr^{-1}. The digitisation was performed using the Google Earth Engine Digitisation Tool (GEEDiT) v2.03 (Lea et al. 2018) which included satellite images from Landsat 1 MSS (1973-1974), Landsat TM 4 and 5 (1989-1991), Landsat 7 ETM+ (1999-2013), Landsat 8 OLI/TIRS (2013-2022), and Landsat 9 (2021-2023). Images with cloud cover less than 40% were selected to ensure optimal visibility and accuracy in terminus delineation. As the images were already georeferenced, associated error is derived from manual digitisation of the ice front estimated at 0.5 pixels (Miles et al., 2013, 2016, 2018, 2021; Black and Joughin, 2022) and ranges between ±15 to ±70 m.

A major challenge was distinguishing glacier ice fronts from sea ice. This was addressed primarily through visual interpretation. Glacier termini typically exhibit a rough, crevassed texture and appear brighter in optical imagery, whereas sea ice is generally smoother and has a more greyish tone. However, landfast sea ice can also appear bright, making the distinction more difficult. In such cases, glacier termini were identified by their more jagged outlines, which contrast to more uniform and smooth edges of landfast sea ice. Additionally, subtle shadowing cast by the slightly

elevated glacier tongue relative to the adjacent sea ice provided a further visual differentiation.

The glacier area changes were calculated over time using the box method, which accounts for uneven changes along the ice front (Moon & Joughin, 2008). A 50-year time series of glacier terminus positions was generated, estimating relative length changes by dividing the area changes between each measurement and the reference year by the individual box width. Note that there were gaps in satellite imagery between 1970-1980s and 1990-2000s.

To investigate glacier terminus change over time, specific epochs were selected based on the availability, quality, and consistency of satellite imagery across the study region. The analysis was divided into four unequal epochs—1970s–1988, 1988–2000, 2000–2010, and 2010–2023. These intervals reflect variations in data availability and quality, as well as significant advancements in satellite observation capabilities over the study period. The 1970s–1988 period represents the earliest available Landsat imagery and provides a long-term baseline despite sparse temporal coverage. The 1988–2000 interval corresponds to a transitional period with variable image availability, preceding the operational use of Landsat 7, with particularly gap between 1990 and 2000. From 2000 onwards, data availability significantly improved with the launch of Landsat 7 (1999), and later Landsat 8 OLI/TIRS (2013), and Landsat 9 (2021), enabling more consistent decadal interval (2000–2010 and 2010–2023).

To compare glacier behaviour across the two regions, the percentage area change relative to each glacier's initial area within each box were calculated. To further standardise comparisons, normalised glacier terminus position changes were derived by linearly scaling each glacier's area change, such that the minimum observed area was set to 0 and the maximum to 1, following the approach outlined by Baumhoer et al. (2021) and Black and Joughin (2022). The average of the normalised glacier areas were then computed to identify potential synchronicity in glacier terminus position changes across the regions over the study period and calculated the standard deviation of these changes to quantify variability. This method allowed for the

consistent examination of the terminus position changes from 1970 to 2023, focusing on the months between December and March. During this period seasonal cloud cover is minimal, allowing for greater image availability and accuracy in terminus delineation.

4.4.2 Sea ice concentrations

The Sea Ice Index Version 3.0 was used to estimate long-term trends in sea ice extent (SIE). These data are derived from Nimbus-7 Scanning Multichannel Microwave Radiometer (SMMR); and, since August 1987, from a series of Special Sensor Microwave Imager (SSM/I) and Special Sensor Microwave Imager/Sounder (SSMIS) instruments on Defense Meteorological Satellite Program (DMSP) satellites. This dataset provides SIE as daily and monthly polygon shapefiles, generated using a 15% sea ice concentration threshold. For this study, monthly shapefiles were downloaded, and analysis was conducted at regional scale by clipping these shapefiles using a bounding box over each region (see Fig. 4.2). The areas of the resulting polygons were then calculated to estimate regional SIE in km^2. This approach enabled a consistent and spatially constrained analysis of regional variability and long-term trends in SIE. Note that SIE data is available from 1979 onwards.

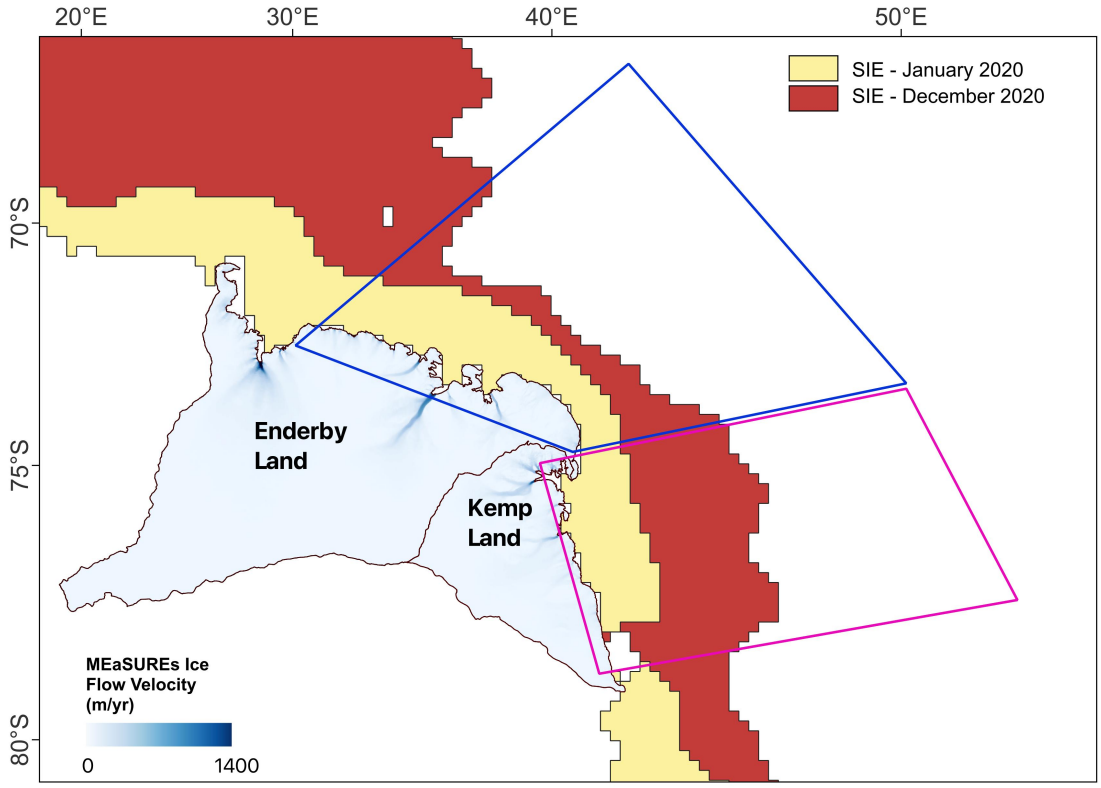

Figure 4.2: *The two polygons represent the region from where sea ice extent (SIE) was extracted.*

Note that, SIE analysis is limited to the regional scale. This is because this approach results in a coarser, less detailed representation of ice distribution, making it unsuitable for capturing fine-scale variability in SIE in front of the glacier, with spatial resolution of 25×25 km. Thus, in this study SIE data is used solely for assessing broader regional patterns to understand whether the extent of sea ice has decreased or increased over the years. Therefore, we also analyse sea ice concentration data at both local and regional scales. Although both products are based on passive microwave data with 25×25 km spatial resolution, sea ice concentration provides a continuous measure of the percentage of sea ice within each grid cell. This allows us to detect variations in sea ice conditions directly in front of glacier termini, where changes in concentration can influence glacier dynamics.

Sea ice concentrations (SIC) were estimated at monthly scale from SMMR, SSM/I and SSMIS passive microwave instruments carried on the Nimbus-7 satellite between 1979 and 2023 acquired from https://nsidc.org/data/nsidc-0051/versions/2. The

spatial resolution of the dataset is 25 km. To assess the influence of sea ice conditions on glacier terminus change, SIC data were extracted at two spatial scales. For each region, an approximately 100 km wide polygon offshore along the coastline was defined (Fig. 4.3). Every SIC grid cells within this polygon were averaged for the summer months (December to March). This allowed us to capture the broader sea ice conditions surrounding each coastal sector and assess how regional-scale variability in sea ice coverage may influence to average glacier termini changes.

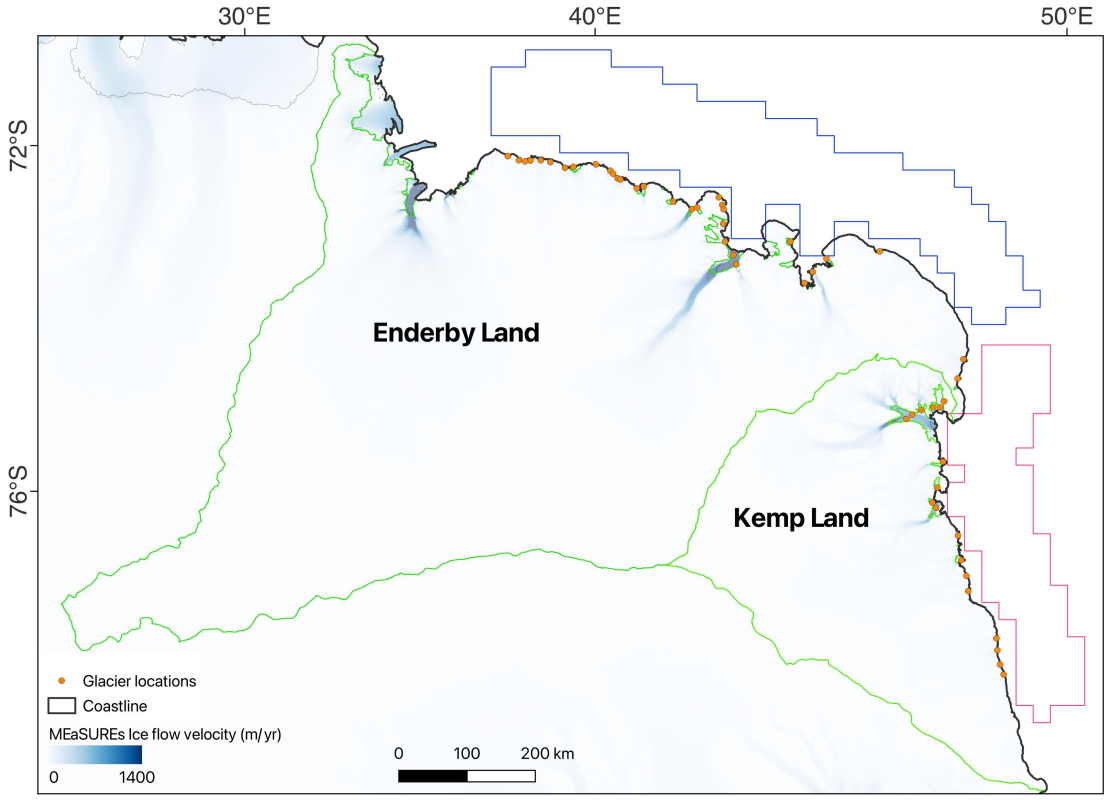

Figure 4.3: *The two polygons represent the region from where sea ice extent (SIE) was extracted.*

In addition, to assess local-scale effects, the SIC values from a single 25 × 25 km grid cell located directly offshore from the terminus of each glacier were extracted. For example, Figure 4.4 how how the SIC value for Higashi-naga-iwa Glacier was extracted from the grid cell highlighted by the red box, which is directly in front of the glacier. Similarly, for Tama Glacier and Omega Glacier, SIC values were extracted from the grid cells denoted by the cyan and dark blue boxes, respectively.

In examples where the ice front intersected two grid cells equally, the SIC values from both cells were averaged to better represent conditions at the terminus. For example, at Nishi-naga-iwa Glacier, where the ice front overlaps two adjacent grid cells, the SIC was calculated as the average of the two cells within the yellow box. Similarly, for Oku-iwa and Glacier 1, which are also positioned between two grid cells, the mean SIC from the green box was used. This extraction method ensures that the SIC value assigned to each glacier is geographically representative of the immediate offshore conditions. By doing so, it provides a focused assessment of the potential influence of sea ice on individual glacier termini.

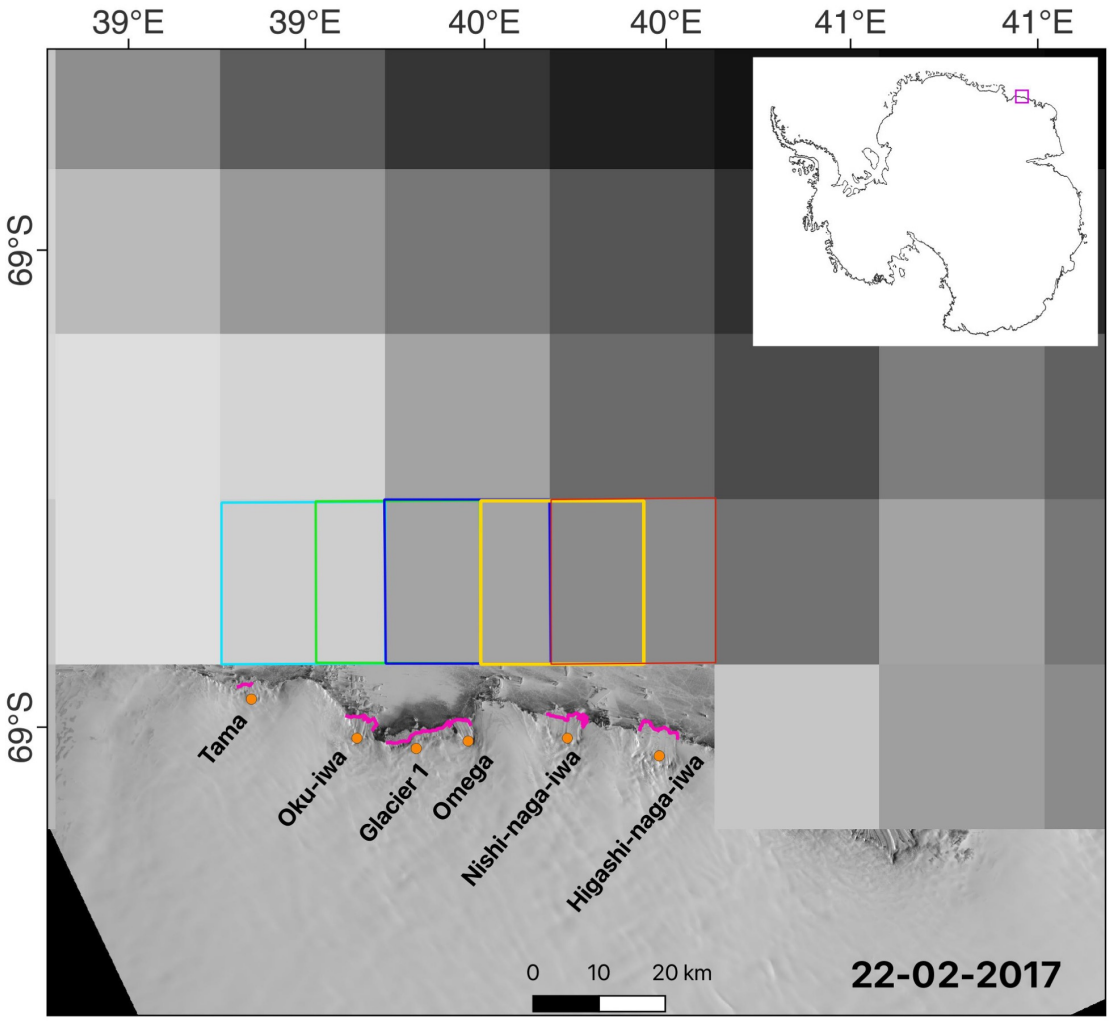

Figure 4.4: *Monthly sea ice concentration (SIC) values from the NSIDC dataset are shown as gridded cells. Orange markers indicate the locations of selected glaciers in Enderby Land (EL). The pink lines represent the ice front position as of 22 February 2017, overlaid on a Landsat-8 background image.*

While the austral summer is conventionally defined as spanning December to February, sea ice extent and sea ice concentration typically continues to decline into March, often reaching its seasonal minimum during this month. Capturing this late-summer reduction in sea ice is crucial for assessing its potential influence on glacier terminus change and so 'summer' in this study for SIC and SIE refers to December to March. For both datasets, summer mean SIC and SIE were calculated for each year along with decadal summer mean. Summer mean monthly anomalies for both SIE and SIC were also computed relative to the long-term summer averages.

4.4.3 Subsurface ocean temperature

Previous studies have suggested that ocean temperatures are an important control on terminus behaviour of marine-terminating glaciers, particularly at Wilkes Land (Miles et al. 2016; Greenbaum et al. 2015) and recent studies found evidence of Warm Deep Waters (WDW) underneath Fimbulisen increasing its basal melt rate (Lauber et al. 2024). However, direct ocean temperature observations are extremely scarce. Nonetheless, examining ocean temperature data is essential for gaining insight into oceanic conditions, especially in these underexplored regions. Therefore, the EN4.0.2 subsurface ocean temperature objective analysis dataset, acquired from the UK Meteorological Office Hadley Centre (`https://www.metoffice.gov.uk/hadobs/en4/download-en4-0-2.html`) was used. This dataset has a spatial resolution of $1^{\circ} \times 1^{\circ}$, with data obtained from the WOD09, GTSPP, Argo, and ASBO collections (Good et al. 2013). To assess the reliability of the EN4 ocean temperature data in the study region, the accompanying 'observation influence' fields were used as proxies for observation weights (Good et al., 2013). These indicate the degree to which the objective analyses were constrained by actual in situ measurements (e.g., from Argo, GTSPP, WOD09). The observation weight values close to one suggest strong observational constraint, while values near zero indicate reliance on background climatology and interpolation. This allowed us to qualitatively assess data coverage and uncertainty across the Enderby and Kemp Land regions. In these two regions, these values ranged between 0.6 to 0.8, exhibiting a higher influence of observations in constructing the data. Although the

influence of observations is higher in these regions, there still remains uncertainty associated with some values that have been derived from climatology and interpolation in the dataset. The associated uncertainties provided with the dataset range between 0.05°C and 0.3°C.

The dataset consists of 28 ocean depth layers, and the ocean temperatures for depths between 5-109 m, 109-446 m and 446-967 m were averaged, similar to approaches used in Miles et al. (2016). These depth layers were chosen for the analysis because at 5-109 m depth layer captures the near-surface ocean conditions that could influence the glacier frontal melting. The 109-446 m depth layer reflects the region which could drive basal melting of floating ice tongues and the 446-967 m depth layer represents the potential deeper intrusion of warm waters (mCDW) which could influence melting near the grounding zones or sub-ice-shelf cavities. For regional scale analysis, the data were extracted at a monthly scale between 1979 and 2023 using the same polygons as used to extract SIC data, which is around 100 km wide located offshore from the coastline for Enderby and Kemp Land (Fig. 4.3). The data were also extracted from a 25 × 25 km grid cell in front of individual glaciers to understand its influence on glacier terminus behaviour at a local scale, same as the sample boxes used for SIC (Fig. 4.4). Finally, the average summer mean subsurface ocean temperatures (December to February), decadal summer averages and long-term mean summer subsurface ocean temperatures (1970s-2023) were calculated for this dataset.

4.4.4 Air temperature

To investigate whether air temperature influences glacier terminus changes, monthly mean 2 m near-surface air temperature from the European Centre for Medium-Range Weather Forecasts ERA5 reanalysis were used, with a spatial resolution of 0.25 degree ($\sim$ 31 km). Previous studies have highlighted the influence of air temperature on glacier terminus behaviour.

For regional scale influence of air temperature over the two study regions, the data were extracted from the polygons with width spanning 50-100 km in both regions

(Fig. 4.5). This approach ensured that the extracted temperatures reflect near-coastal atmospheric conditions likely to affect glacier termini. This spatially averaged air temperature represents a broad, averaged regional climate signal and it minimises noise from local variability, improving the robustness of any observed correlation between temperature and glacier retreat.

While this dataset, with a spatial resolution of ∼31 km, is coarser than the width of many individual outlet glaciers in the study area (typically 3–12 km wide), it remains adequate for understanding the climatic conditions that influence changes at each glacier termini. The data were extracted for individual glaciers using square sampling boxes, where the width of each box was equal to the width of the glacier terminus. As these boxes were smaller than the dataset's grid cells, the value of the grid cell overlapping the sampling box was selected. This approach localised the temperature data as much as possible within the limits of the ERA5 resolution, ensuring the extracted climate signal is closely aligned with the position of each glacier.

Additionally, ERA5 hourly air temperature data were averaged across each day to derive daily mean temperatures. This enabled the estimation of the number of days with temperatures exceeding 0°C for each glacier and within each regional bounding polygon, facilitating comparison with the timing of glacier retreat. Finally, the average summer mean air temperatures (December to February), decadal summer averages and long-term mean summer air temperatures (1970s-2023) were calculated for this dataset. Summer mean monthly air temperature anomalies were also computed relative to the long-term summer average.

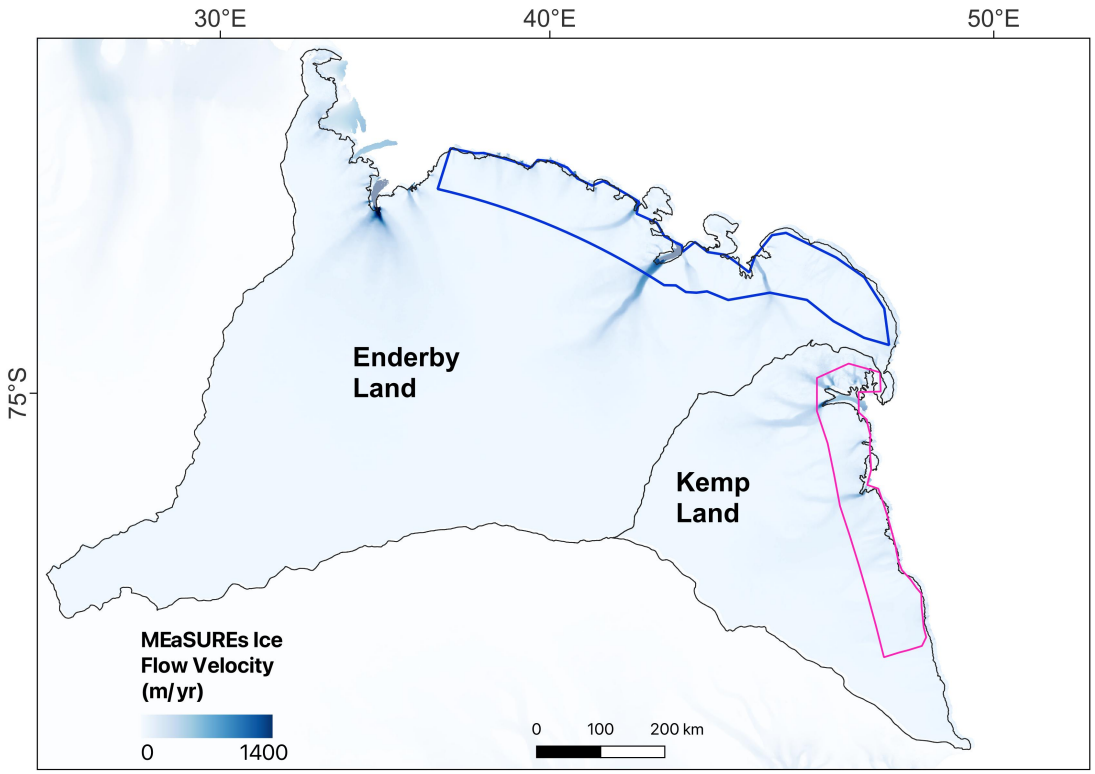

Figure 4.5: *Monthly air temperature values extracted from the blue polygon for Enderby Land and pink polygon for Kemp Land. These polygons are around 50-100 km wide.*

4.4.5 Statistical analyses

To assess how each climatic factor influences changes in glacier terminus positions during the summer months, Pearson correlation analyses at both regional and individual glacier scales was conducted. Temporal lags were incorporated to account for delayed glacier responses to antecedent atmospheric or oceanic conditions. Only the summer months have been chosen for this statistical analysis because the sea ice concentrations and sea ice extents are at their lowest and air temperatures are generally higher than winter months. Note that summer is defined as December to March for SIE and SIC and December to February for air temperature and subsurface ocean temperatures. Therefore, the summer averages for sea ice concentration, sea ice extent, air temperatures, and subsurface ocean temperatures at various depths (5-109 m, 109-446 m, and 446-967 m) were calculated. The sea ice extent was excluded for the correlation test at individual glacier scale because of the low spatial resolution of dataset. Correlations were calculated between ocean-climate variables and normalised terminus position change. The reason for choosing normalised terminus position change instead of the mean terminus position change is because glacier sizes vary ranging from 3 to 12 km. Normalisation accounts for these size differences, allowing for a more meaningful and comparable analysis across glaciers, thereby yielding more robust correlations coefficients.

The correlations were calculated from 2000 to 2023, a period with more continuous data coverage, allowing for detailed evaluation of local environmental influences. The correlations were tested at one-year (Lag 1) and two-year (Lag 2) for air temperature, sea ice concentration and sea ice extent as well as at five-year (Lag 5) lags for subsurface ocean temperatures across the three depth profiles. Here, Lag 1 refers to climatic variables measured one year prior to changes in glacier terminus positions, Lag 2 reflects an average of the two previous years, and Lag 5 represents an average of the five previous years. These lags are crucial for understanding the time-dependent nature of glacier responses to climatic variations (Boxall et al. 2024). This is because previous studies have indicated that decline in sea ice concentration prior to glacier retreat is a key factor such as at Voyeykoyev Ice Shelf (Arthur et al. 2021). Similarly,

Cook et al. (2016) suggested a response timescale of less than a decade, likely within 5–10 years, between ocean warming and noticeable glacier front retreat at Antarctic Peninsula. Therefore, in this study, a lag of 5 years was chosen to understand the influence of ocean warming on glacier retreat.

4.5 Results

Analysis of glacier terminus position changes in the study region, covering a total of 44 glaciers between the 1970s and 2023, reveals distinct trends. It is important to note that not all glaciers were mapped from the 1970s—some were first mapped in the 1980s. Figure 4.6 shows examples of how glacier ice fronts were digitised.

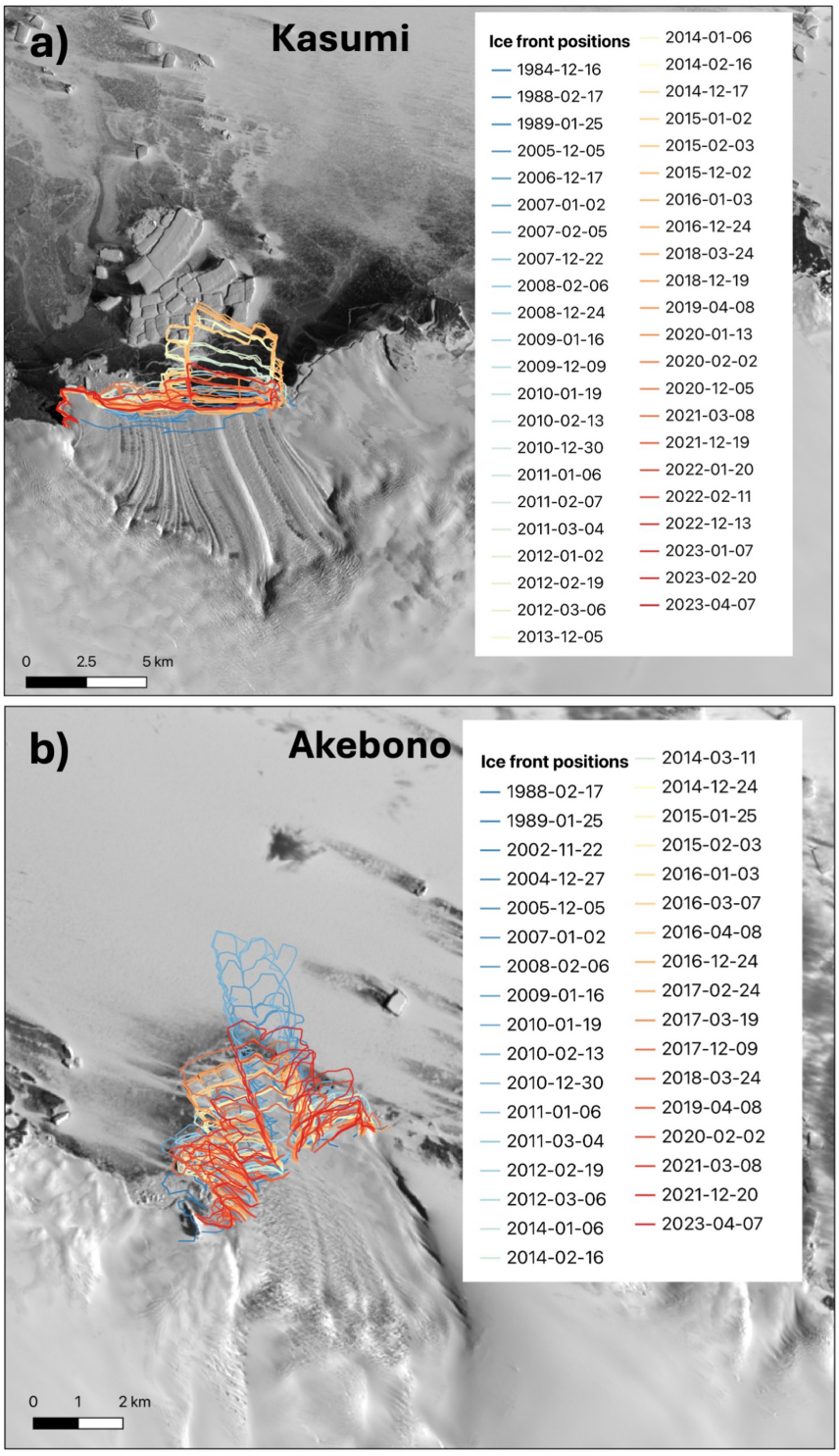

Figure 4.6: *Examples of terminus position mapping of glaciers in Enderby and Kemp Lands. Panel (a-b) shows ice front positions of Kasumi Glacier (1984-2023) and Akebono Glacier (1988-2023) in Enderby Land. The background imagery in Panel (a) is 2nd February 2020 and (b) is 9th December 2017.*

4.5.1 Long-term patterns of glacier behaviour

Figure 4.7 illustrates no consistent patterns in long-term glacier advance/retreat across the study area, instead revealing significant temporal and spatial variability in glacier termini behaviour. Some glaciers exhibit consistent trends with more steady, less dramatic changes, with limited fluctuations over time, either advancing or retreating steadily. For example, Omega and Campbell gradually retreated by $\sim$ -1.5 km and $\sim$ -1.7 km, respectively, whereas Glacier 4 has been consistently advancing, with a total advance of +4 km over the study period (1970s-2023).

In contrast, there are some glaciers that exhibit patterns of both advance and retreat, and often of high magnitude. For example, Rayner Glacier underwent multiple large retreat events between 1970s and 2023, particularly in 2005, 2016 and 2023 (Fig. 4.7; Fig. 4.8a). Cosgrove-Dover is another glacier that shows the terminus position undergoing phases of retreat and advance (Fig. 4.8b). Wilma-Robert-Downer (WRD) Glacier has been predominantly advancing between 1970s and 2023, with one substantial retreat of $\sim$ -7 km between 1990 and 1991 (labelled WRD in Fig.4.7). The consistent red colouring in Figure 4.7 between the 1991 and 2007, despite WRD advancing after the 1991 retreat event, shows that the WRD Glacier terminus had not returned to its 1990 extent during this period. (Fig. 4.5). The glacier had regained its 1990 extent in 2016 and continued to advance a further +6 km by 2023.

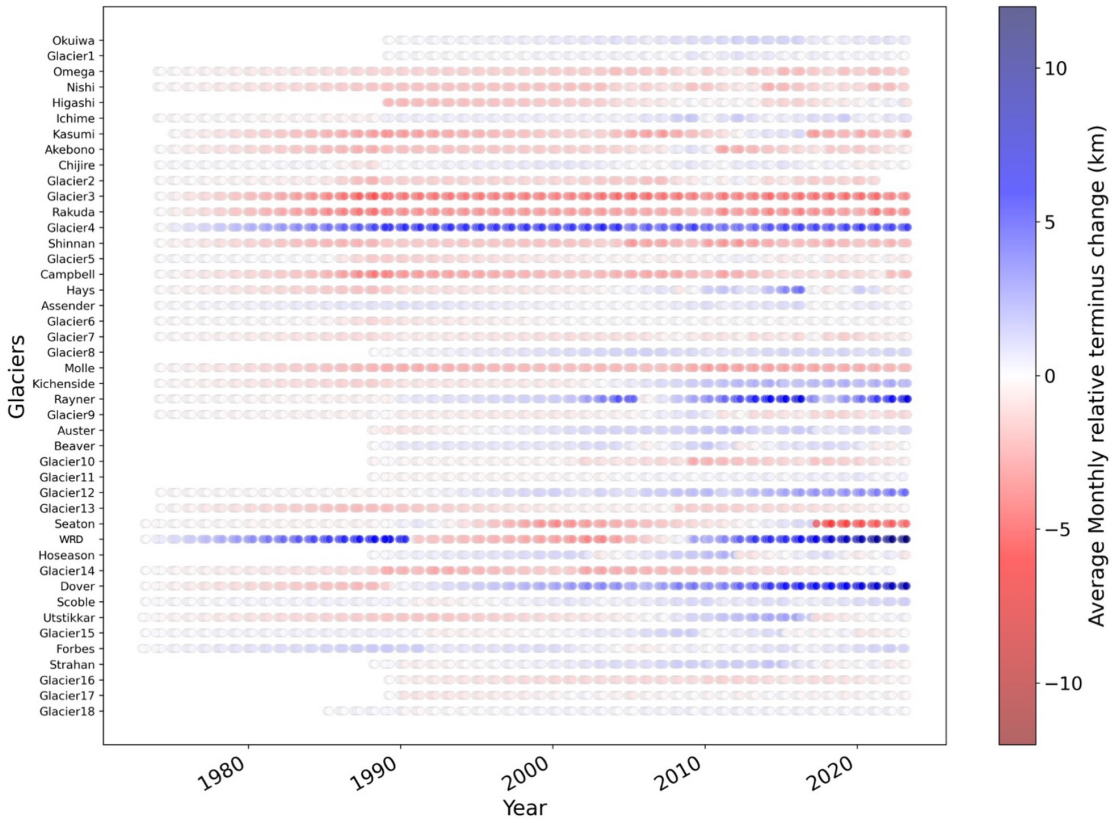

Figure 4.7: *Heatmap showing monthly average terminus change in the study region relative to the initial position for all glacier across the study region. If terminus position data were missing, linear interpolation was used for an estimated position change based on prior and subsequent positions.*

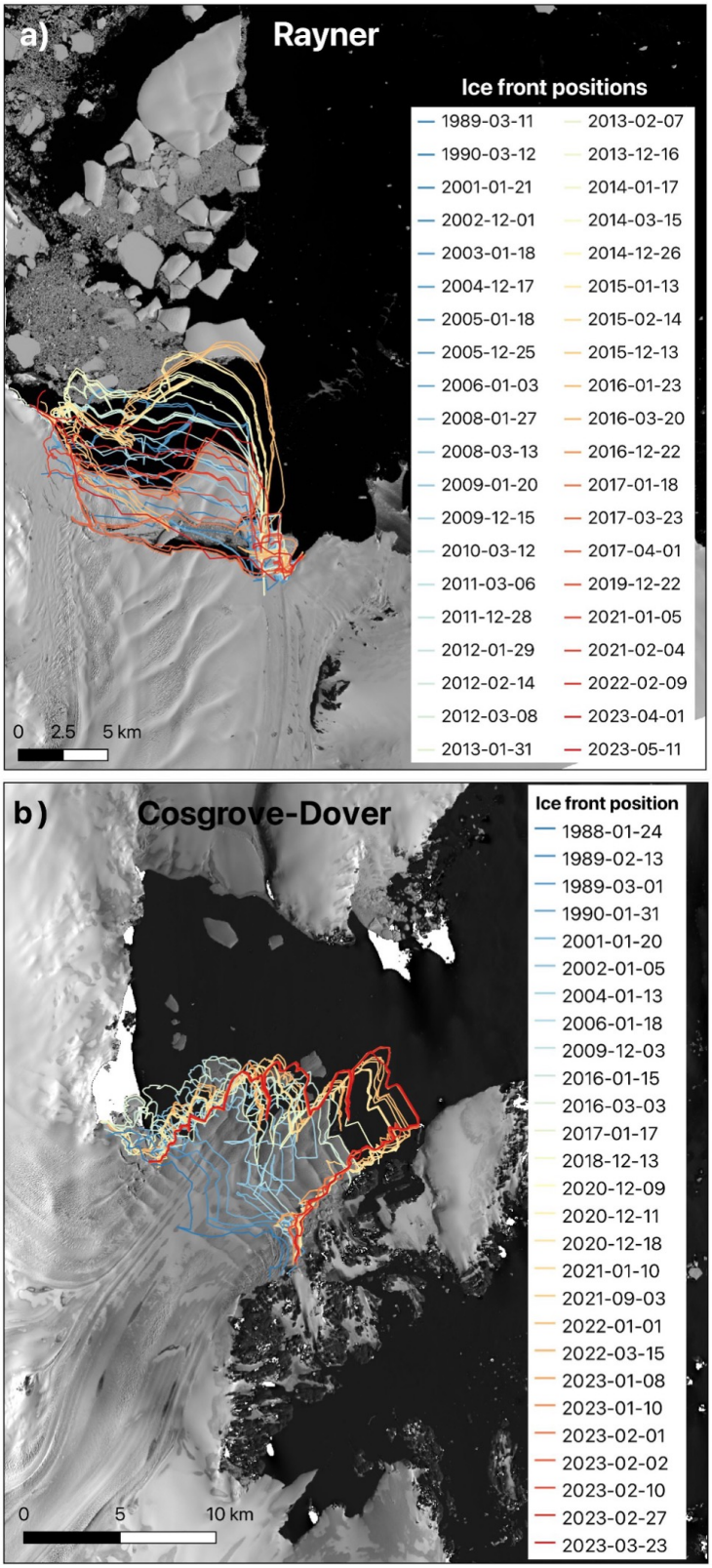

Figure 4.8: *Panel (a) illustrates Rayner Glacier, which exhibits alternating periods of advance and retreat over time. Panel (b) depicts Cosgrove-Dover Glacier, which initially retreated between 1973 and 1988, followed by a sustained phase of advance. Background imagery in Panel (a) is 20th March 2016 and (b) is 3rd March 2016.*

4.5.2 Multi-decadal variation in glacier terminus behaviour

Over the entire study period from the 1970s to 2023, 52% of glaciers retreated across the region while 48% of glaciers advanced, with a long-term median terminus change at -1.4 m yr^{-1} (Fig. 4.9a, Table 4.1). Across the epochs, from the 1970s to 1988, 61% of glaciers retreated, indicating a predominant phase of glacier recession during this period, with a median rate of –60.3 m yr^{-1} (Fig. 4.9b). Between 1988 and 2000, this pattern shifted, with 68% of glaciers advancing, marking a reversal from the previous period, with median rate of +46.7 m yr^{-1} (Fig. 4.9b). In the subsequent epochs, the majority of glaciers continued to advance from 2000 to 2010 (64%) at median rate of +2.2 m yr^{-1}. However, in the last epoch from 2010 to 2023 (57%) glaciers retreated at median rate of -4.8 m yr^{-1}. From the 1988–2000 epoch onward, the proportion of advancing glaciers steadily declined, and by the final epoch the percentage of retreating glaciers exceeded that of advancing glaciers (Fig. 4.9c–d).

At the regional scale, glacier behaviour exhibited contrasting trends between Enderby Land and Kemp Land across the study epochs, as summarized in Table 4.1. During the first epoch (1970s–1988), 71% of glaciers in Enderby Land underwent retreat, with a median rate of –86.1 m yr^{-1}, indicating a dominant period of glacier recession. In contrast, Kemp Land glaciers showed a more mixed response, with 61% advancing at a median rate of +2.4 m yr^{-1}. In the second epoch (1988–2000), the trend reversed: 77% of Enderby Land glaciers advanced at a median rate of +58.4 m yr^{-1}, while 54% of Kemp Land glaciers retreated, averaging –11.9 m yr^{-1}. The third epoch (2000–2010) saw a continuation of glacier advance in both regions, with 65% of Enderby Land and 62% of Kemp Land glaciers advancing at median rates of +18.3 m yr^{-1} and +40.3 m yr^{-1}, respectively. In the most recent epoch (2010–2023), 58% of glaciers in Enderby Land returned to retreat, at median rate of –14.7 m yr^{-1} and in Kemp Land 54% glaciers retreated at a median rate of +7.8 m yr^{-1}.

Table 4.2 further highlights the individual glacier termini behaviour. During 1970s–1988, Glacier 3 recorded the most significant retreat at –300 m yr^{-1}. In the second

epoch, the Wilma-Robert-Downer Glacier showed the highest retreat rate at –743 myr^{-1}. This glacier also exhibited the most substantial advance during 2000–2010, reaching +566.9 m yr^{-1}. In the final epoch (2010–2023), both the Wilma-Robert-Downer and Cosgrove-Dover glaciers showed exceptional advances, with rates of +593.3 m yr^{-1} and +462.5 m yr^{-1}, respectively, indicating highly dynamic and regionally variable glacier behaviour. In addition, Rayner Glacier initially retreated at -17.4 m yr^{-1}, then advanced in the next two epochs at +128.1 m yr^{-1} and +165.2 m yr^{-1} and finally retreated again in the last epoch at -151.7 m yr^{-1} (Fig. 4.8a, Table 4.2)

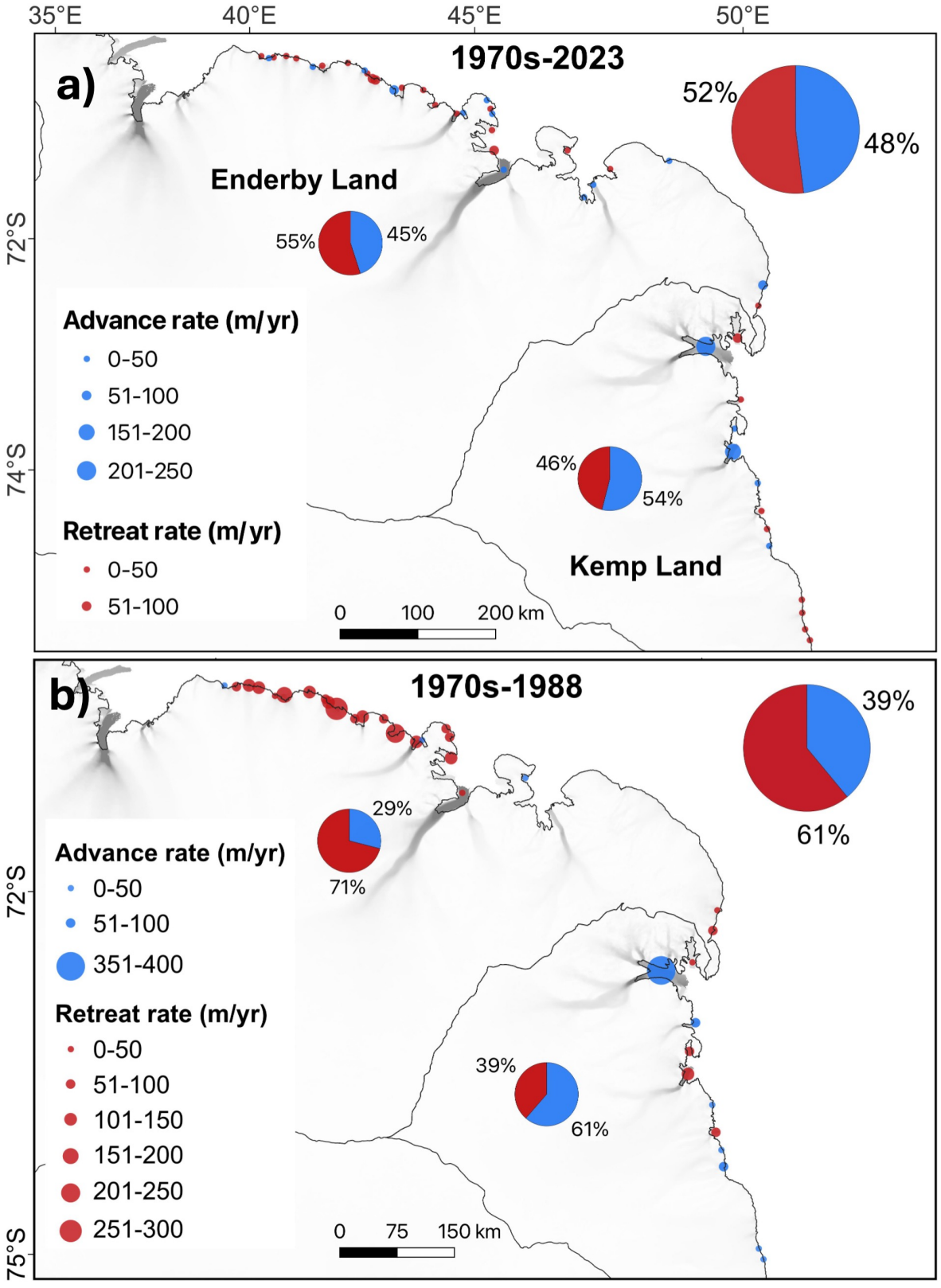
35°E
40°E
45°E
50°E
72°S
74°S
a)
1970s-2023
52%
48%
Enderby Land
55%
45%
Advance rate (m/yr)
0-50
51-100
151-200
201-250
Retreat rate (m/yr)
0-50
51-100
46%
54%
Kemp Land
0
100
200 km
b)
1970s-1988
39%
61%
29%
71%
Advance rate (m/yr)
0-50
51-100
351-400
Retreat rate (m/yr)
0-50
51-100
101-150
151-200
201-250
251-300
39%
61%
72°S
75°S
0
75
150 km

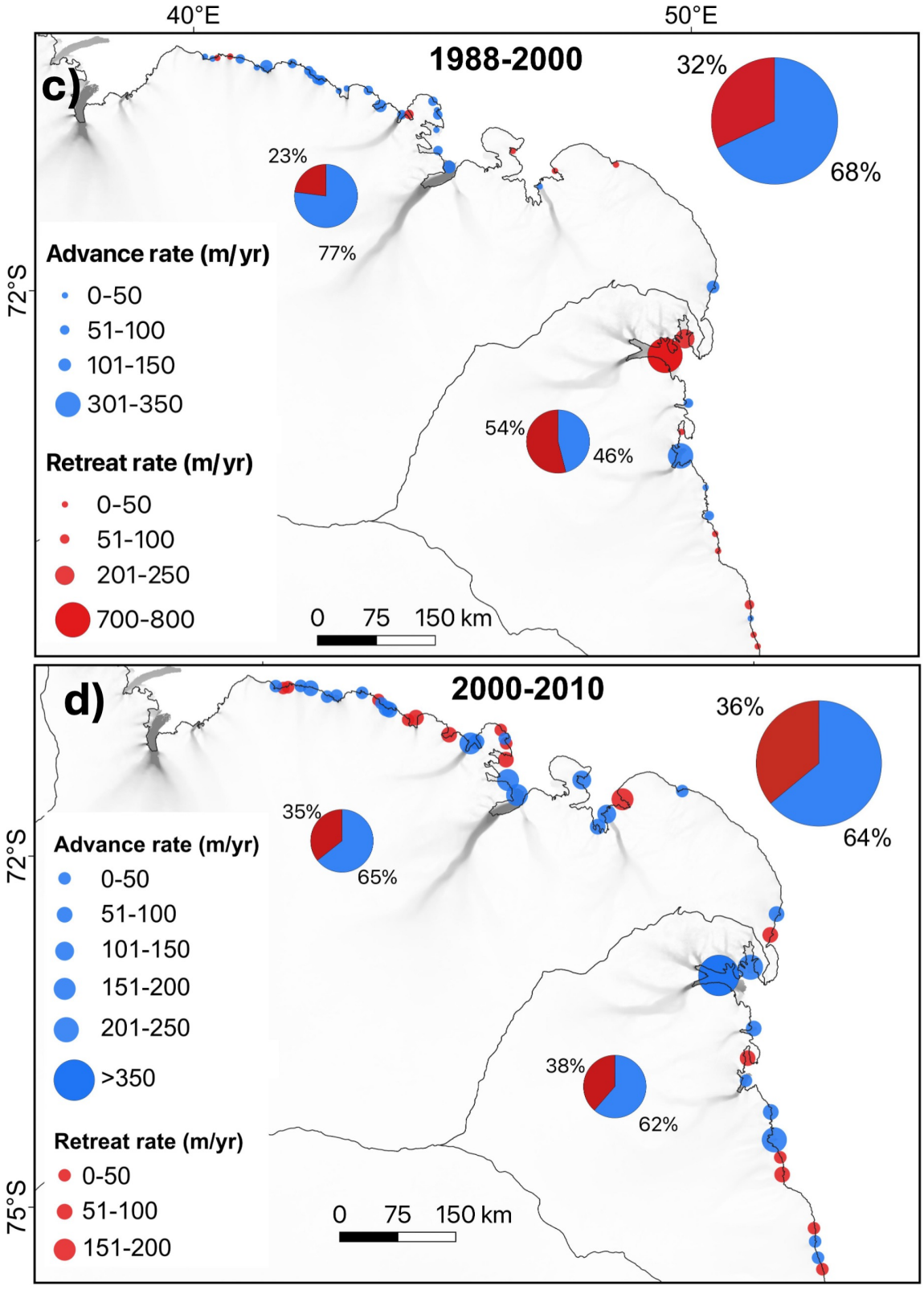
40°E
50°E
c)
1988-2000
32%
68%
23%
77%
Advance rate (m/yr)
0-50
51-100
101-150
301-350
Retreat rate (m/yr)
0-50
51-100
201-250
700-800
54%
46%
0 75 150 km
72°S
d)
2000-2010
36%
64%
35%
65%
Advance rate (m/yr)
0-50
51-100
101-150
151-200
201-250
>350
Retreat rate (m/yr)
0-50
51-100
151-200
38%
62%
0 75 150 km
72°S
75°S

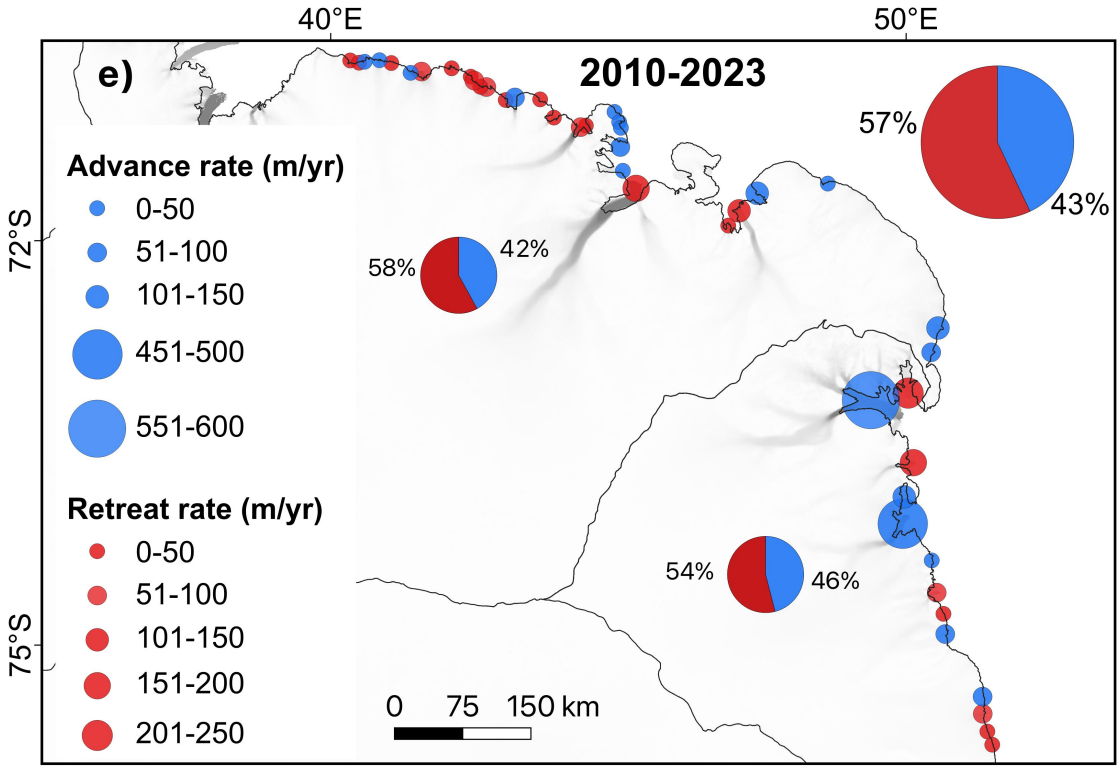

Figure 4.9: *Glacier terminus position change rates between 1970s and 2023 (a) and at decadal scales (b) 1970s-1988, (c) 1988-2000, (d) 2000-2010 and (e)2010-2023. The pie charts show the percentage of glacier in the study region with advancing and retreating termini. See Figure 4.1 for glacier names and their locations. The pie charts in the two drainage basins represents the percentage of advance and retreat in each region.*

Table 4.1: *Summary statistics of normalised glacier terminus position change (m yr^{-1}) across all glaciers, and separately for Enderby Land and Kemp Land, over different epochs.*

Summary statistics (m yr^{-1})	long-term: 1973-2023	1973-1988	1988-2000	2000-2010	2010-2023
All glaciers (n = 44)					
Mean	15.7	-61.1	21.8	40.3	11.9
Median	-1.8	-71.3	44.4	25.4	-4.9
Min.	-69.4	-300.8	-743.2	-184.3	-216.3
Max.	452.6	379.6	320.5	566.9	593.3
SD	82.7	134.2	151.0	138.6	138.9
Enderby Land (n = 31)					
Mean	10.7	-94.9	51.7	24.3	-9.8
Median	-3.5	-86.1	58.4	18.3	-14.7
Min.	-55.5	-300.8	-50.5	-184.3	-151.7
Max.	452.6	41.4	143.6	186.9	144.0
SD	85.1	125.7	80.5	95.7	76.2
Kemp Land (n = 13)					
Mean	27.8	33.0	-49.5	78.2	63.5
Median	1.4	12.4	-11.9	37.7	-1.0
Min.	-69.4	-120.5	-743.2	-82.1	-216.3
Max.	211.1	379.6	320.5	566.9	593.3
SD	78.3	131.9	243.8	196.8	233.3

4.5.3 Regional trends in glacier terminus behaviour

Analysis of normalised terminus position changes relative to 1970s positions indicates an overall retreat in Enderby Land, while Kemp Land advanced (see Fig. 4.10). However, both regions exhibited a significant retreat between 1985 and 1987 (Fig. 4.10). Following this, in Enderby Land, there is a recovery, with the mean terminus position steadily advancing from the early 1990s onward, though with some inter-

Table 4.2: *Terminus position change measurements for all outlet glaciers in DB7 and DB8.*

GLACIERS	1974–2023	1974–1988	1988–2000	2000–2010	2010–2023
Enderby Land					
Oku-iwa	18.8	35.9	35.4	41.3	-30.7
Glacier1	1.3		12.2	-6.0	-3.1
Omega	-22.0	-65.4	-15.6	-4.4	10.5
Nishi	-25.3	-106.6	-3.1	10.3	23.0
Higashi	-13.0	-115.9	53.6	97.7	-37.3
Ichime	12.1	-17.1	41.9	32.4	46.5
Kasumi	-48.9	-177.3	125.5	18.3	-91.4
Akebono	-4.6	-144.0	63.9	0.0	-50.0
Chijire	1.3	-55.1	74.3	-37.5	-14.7
Glacier2	-17.5	-141.6	89.2	48.8	-88.6
Glacier3	-55.5	-300.8	93.8	55.3	-15.5
Rakuda	-53.1	-251.1	92.4	67.3	-67.1
Glacier4	-10.1	-86.1	76.9	-14.3	-17.6
Shinnan	452.6	-128.5	27.5	-63.0	65.9
Glacier5	-4.2	-90.6	74.9	33.2	-12.7
Campbell	-35.8	-233.2	143.6	-73.2	-28.5
Hays	-2.2	-111.3	88.9	186.9	-99.5
Assender	3.6	41.4	-50.5	75.8	-40.0
Glacier6	0.3	-63.9	65.0	-14.6	15.7
Glacier7	-5.8	-62.6	10.0	3.2	34.1
Glacier8	24.6		60.7	-46.4	24.0
Molle	-32.8	-127.8	46.8	-88.9	57.9
Kitchnside	32.9	-81.4	58.4	186.2	3.5
Rayner	34.4	-17.4	128.1	165.2	-151.7
Glacier9	-15.4	12.6	-47.7	102.1	-50.0
Auster	24.2		56.3	67.0	-41.8
Beaver	2.4		37.0	104.1	-103.9
Glacier10	-8.7		-11.5	-184.3	117.9
Glacier11	8.3		-7.4	17.6	17.4
Glacier12	73.0	-8.4	120.2	61.5	144.0
Glacier13	-3.5	-77.2	63.0	-87.1	79.7
Kemp Land					
Seaton	-69.4	-14.8	-222.2	220.7	-216.3
Wilma	211.1	379.6	-743.2	566.9	593.3
Hoseason	14.2	81.8	75.9	62.6	-159.8
Glacier14	5.0	-58.2	-11.9	-50.4	143.9
Dover	174.4	-120.5	320.5	37.7	462.5
Scoble	22.5	17.4	12.6	50.1	15.5
Utstikkar	-2.5	-81.8	65.9	206.5	-82.7
Glacier15	-1.4	12.4	-24.8	-7.0	-1.0
Forbes	19.5	80.7	-44.9	-82.1	77.8
Strahan	-4.1		27.8	40.4	-67.0
Glacier16	-5.7		-78.2	-24.8	69.6
Glacier17	-3.6		-21.1	1.2	-3.7
Glacier18	1.4		-0.2	-4.8	-6.1

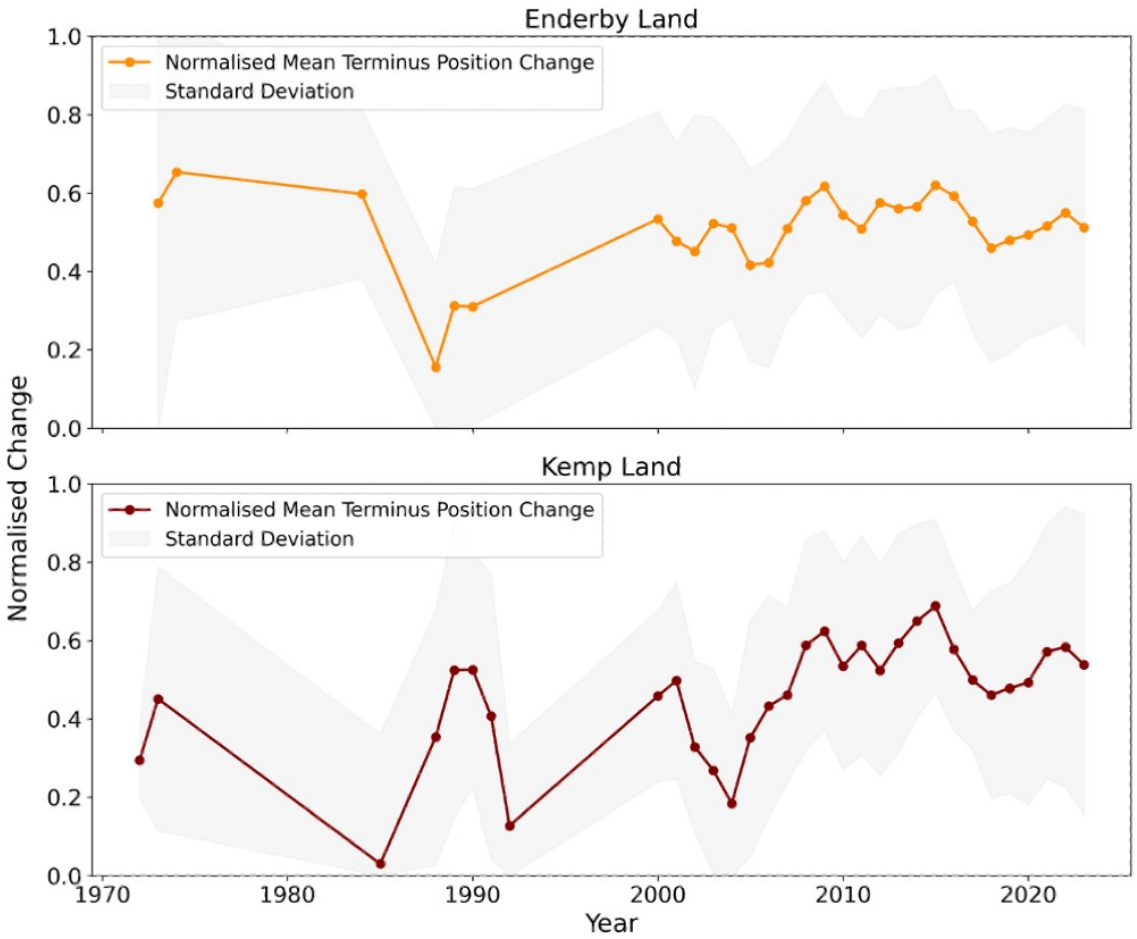

Figure 4.10: *Normalised terminus position change for (a) Enderby Land (b) Kemp Land. the shaded grey region represents the standard deviation (±2 SD). Glacier terminus position changes are normalised by scaling each glacier's observed extent between 0 and 1, where 1 represents its maximum extent and 0 its minimum. This allows glaciers of varying sizes to be compared on a consistent scale. Values are expressed relative to their 1970s positions, such that increasing values indicate terminus advance and decreasing values indicate retreat.*

annual fluctuations. In Kemp Land, there is an increase in the early 1990s, followed by a decline in the early 2000s and more variability in the later years. By 2023, Kemp Land's glaciers had advanced further than their initial position since the onset of observations, whereas Enderby Land's termini have slightly retreated since the first observation.

4.5.4 Decadal and annual variation in ocean-climate variables

4.5.4.1 Sea ice extent and sea ice concentration

Sea ice extent (SIE) reaches its annual minimum in late summer around March and climbs steadily through autumn, winter and spring to reach a peak around September or October in both Enderby and Kemp Land (Fig. 4.11a, b). Notably, Enderby Land recorded its lowest summer sea ice extents in 2016, and Kemp Land recorded in 2016 and 2024. Figure 4.11c shows that long-term summer decadal means in both regions experienced increasing sea ice extent from the first decade (1970s–1988) to the third decade (2000–2010). During the initial two epochs, sea ice extent in Kemp Land remained consistently lower than in Enderby Land. However, this disparity diminished during the third and fourth epochs. After reaching a peak during the third decade, both regions experienced a reduction in summer sea ice extent in the most recent decade (2010–2023). Overall, these trends indicate a long-term increase in summer sea ice extent until 2010, followed by a regional decline in the last decade, in both Enderby and Kemp Land.

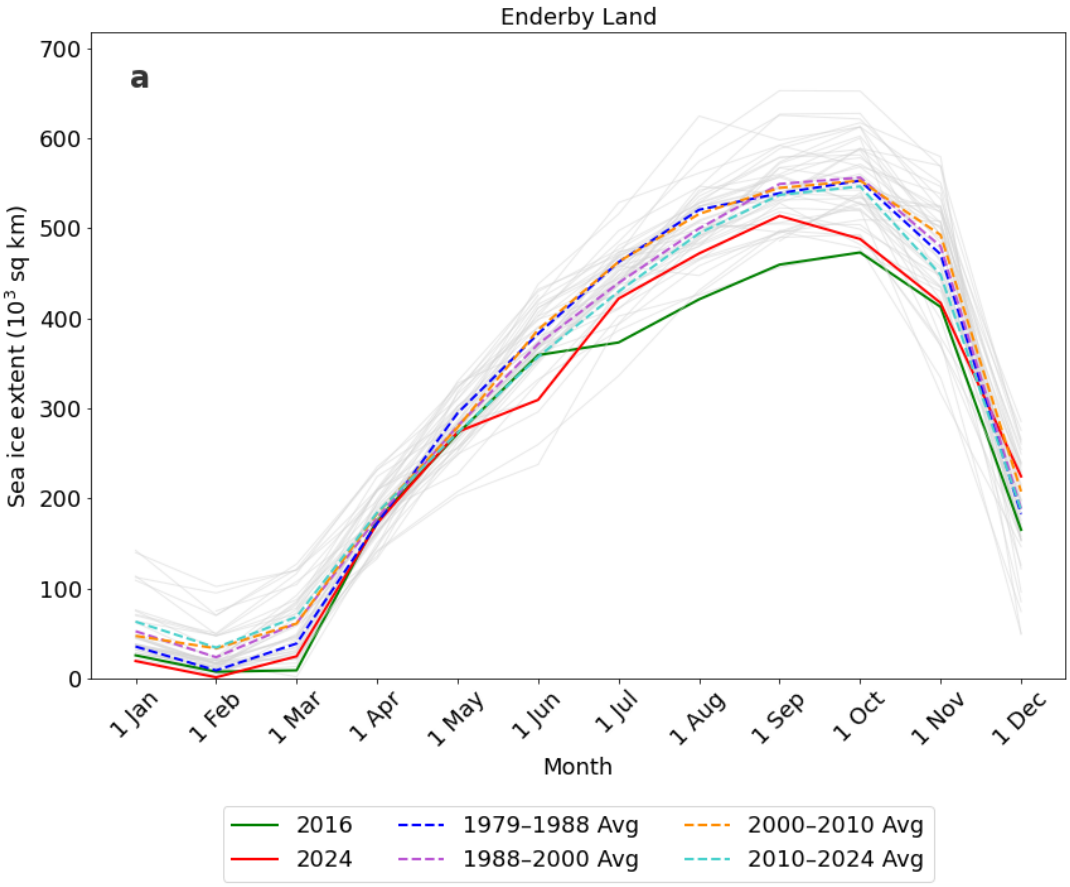
Enderby Land
a
Sea ice extent (10^3 sq km)
0
100
200
300
400
500
600
700
1 Jan
1 Feb
1 Mar
1 Apr
1 May
1 Jun
1 Jul
1 Aug
1 Sep
1 Oct
1 Nov
1 Dec
Month
2016
2024
1979–1988 Avg
1988–2000 Avg
2000–2010 Avg
2010–2024 Avg

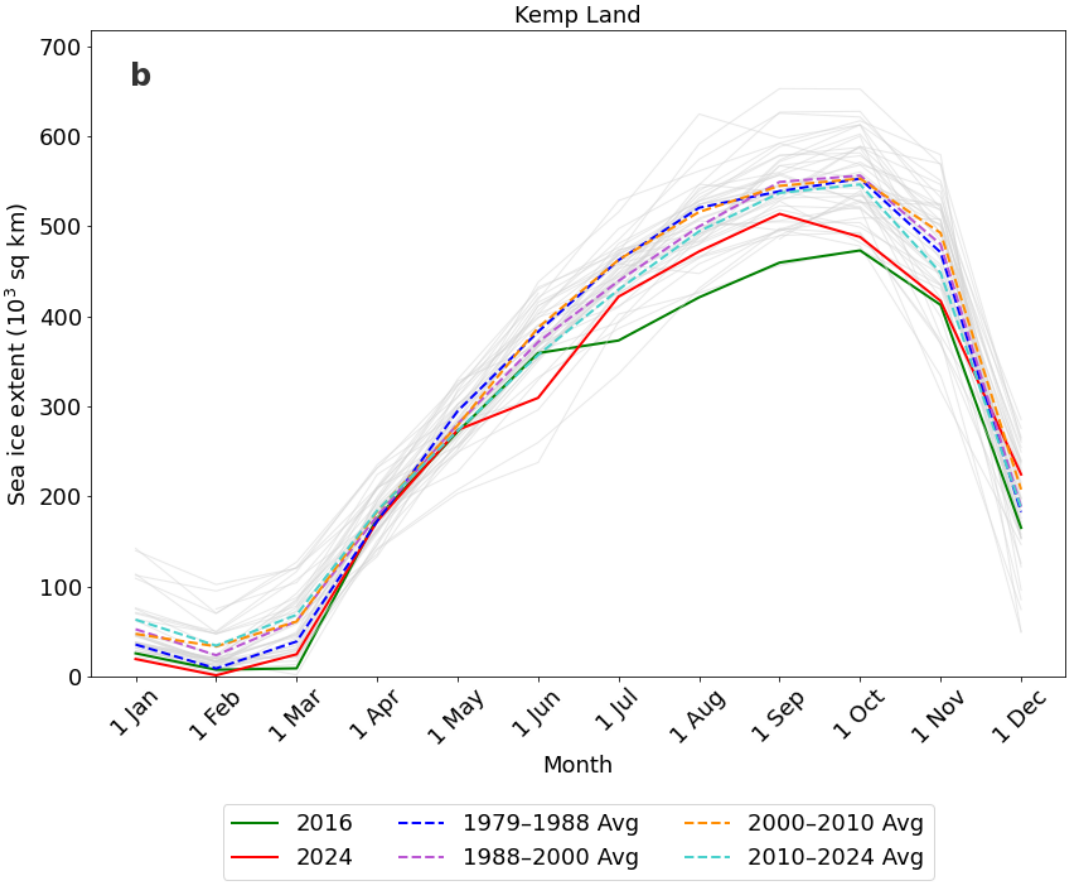
Kemp Land
b
Sea ice extent (10^3 sq km)
0
100
200
300
400
500
600
700
1 Jan
1 Feb
1 Mar
1 Apr
1 May
1 Jun
1 Jul
1 Aug
1 Sep
1 Oct
1 Nov
1 Dec
Month
2016
2024
1979–1988 Avg
1988–2000 Avg
2000–2010 Avg
2010–2024 Avg

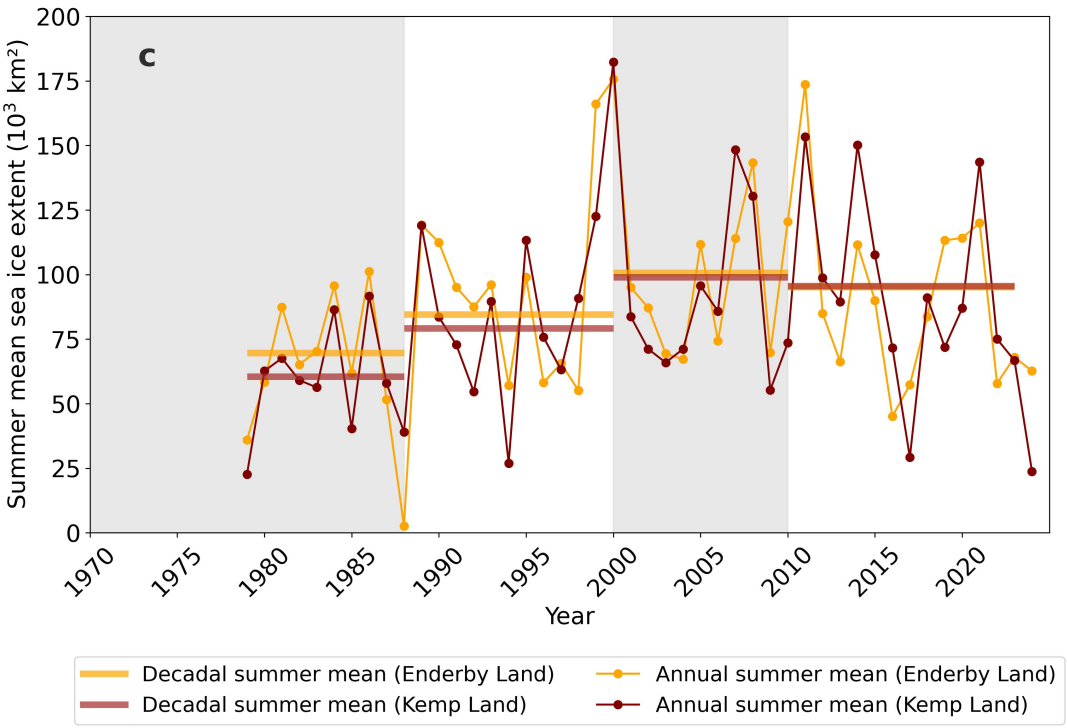

Figure 4.11: *Panels (a–b) show the summer mean (DJFM) sea ice extent between 1979 and 2023 in Enderby and Kemp Land respectively, where the AIS record low minimum years of 2017 (green) and 2023 (red) are particularly marked, with 2024 (pink) also showing quite low sea ice extent. Panel (c) shows the summer mean sea ice extent between 1979 and 2023. The grey shaded regions represent the epochs.*

Although interannual variability is pronounced, mean summer SIC exhibits an upward trend from 1979 through 2024 (Fig.11c). Enderby Land's decadal summer average remained relatively steady at 50–54%, whereas Kemp Land rose from 33% in the first decade to 45% in the third, followed by just a 2% increase in 2010–2023. Over the entire period, the regional long-term summer SIC averaged about 52% at Enderby Land and 41% at Kemp Land. SIC at Kemp Land was consistently lower than at Enderby Land and even fell below 25% in 2017.

Figure 4.12: *Summer mean (DJFM) sea ice concentration from Nimbus-7 SMMR and DMSP SSM/I-SSMIS Passive Microwave Data, Version 2 dataset between 1979 and 202. The horizontal bars represent the decadal averages for Enderby Land (orange) and Kemp Land (maroon). The grey shaded regions represent the epochs.*

Spatially, at the individual glacier scale, most glaciers along the Enderby Land coast consistently experienced relatively high summer sea ice concentrations (SIC), predominantly within the 61–80% range across all epochs. An exception to this pattern occurred during the earliest decade (1979–1988), when SIC values at several glaciers decreased to the 41–60% range (Fig. 4.13b). This decline was most pronounced along the western and central Enderby coastline. In contrast, glaciers in Kemp Land exhibited more spatial heterogeneity and generally lower SIC values. Notably, glaciers between Seaton and Cosgrove-Dover (see Figure 4.1 for location) typically showed 61-80% decadal summer SIC mean, while between Scoble and Forbes, the decadal summer mean SIC was 41-60% during 2000-2010 and 2010-2023 epochs, except during 1979-1988 when it was 21-40%. A cluster of glaciers located between

Glacier 16 and Glacier 18 (See Fig. 4.1 for location) in eastern Kemp Land recorded markedly lower summer SIC, predominantly falling within the 21–40% range for all epochs (Figs. 4.13b–d). While some isolated glaciers across both regions occasionally showed SIC values below 20% or above 80%, these extremes were rare and limited in spatial extent. Overall, Enderby Land glaciers were consistently exposed to higher and more consistent summer SIC, whereas Kemp Land glaciers experienced lower, more variable sea ice conditions, particularly in its eastern sector.

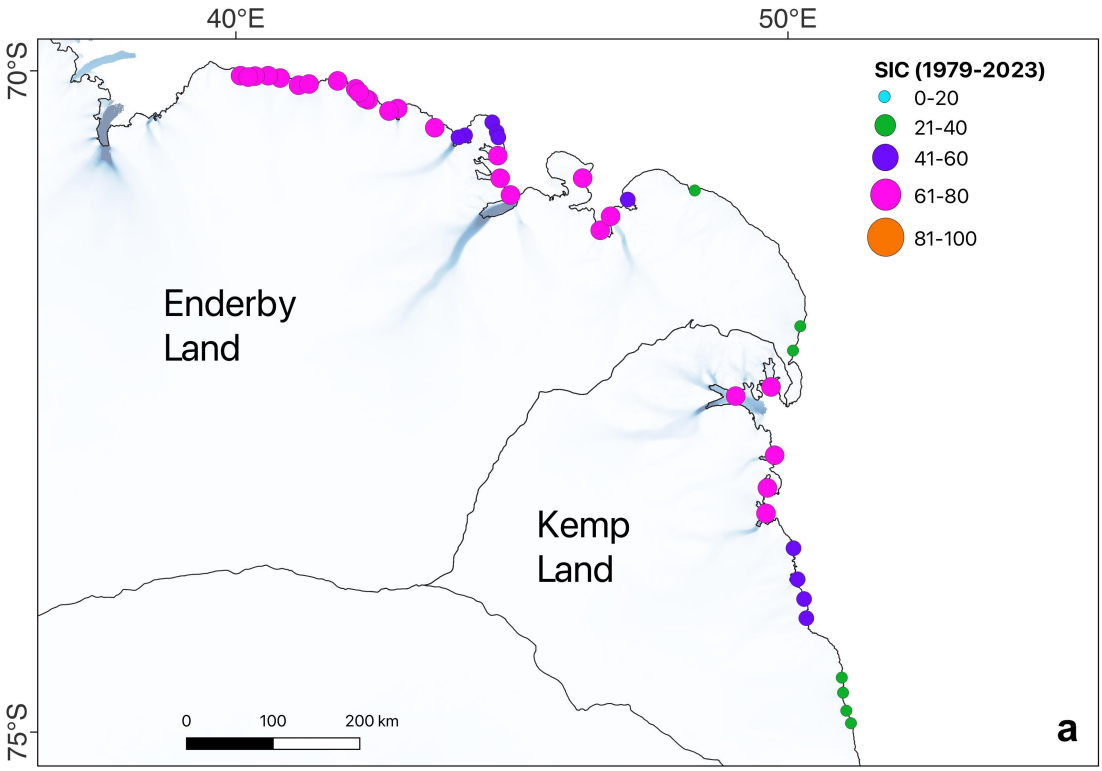

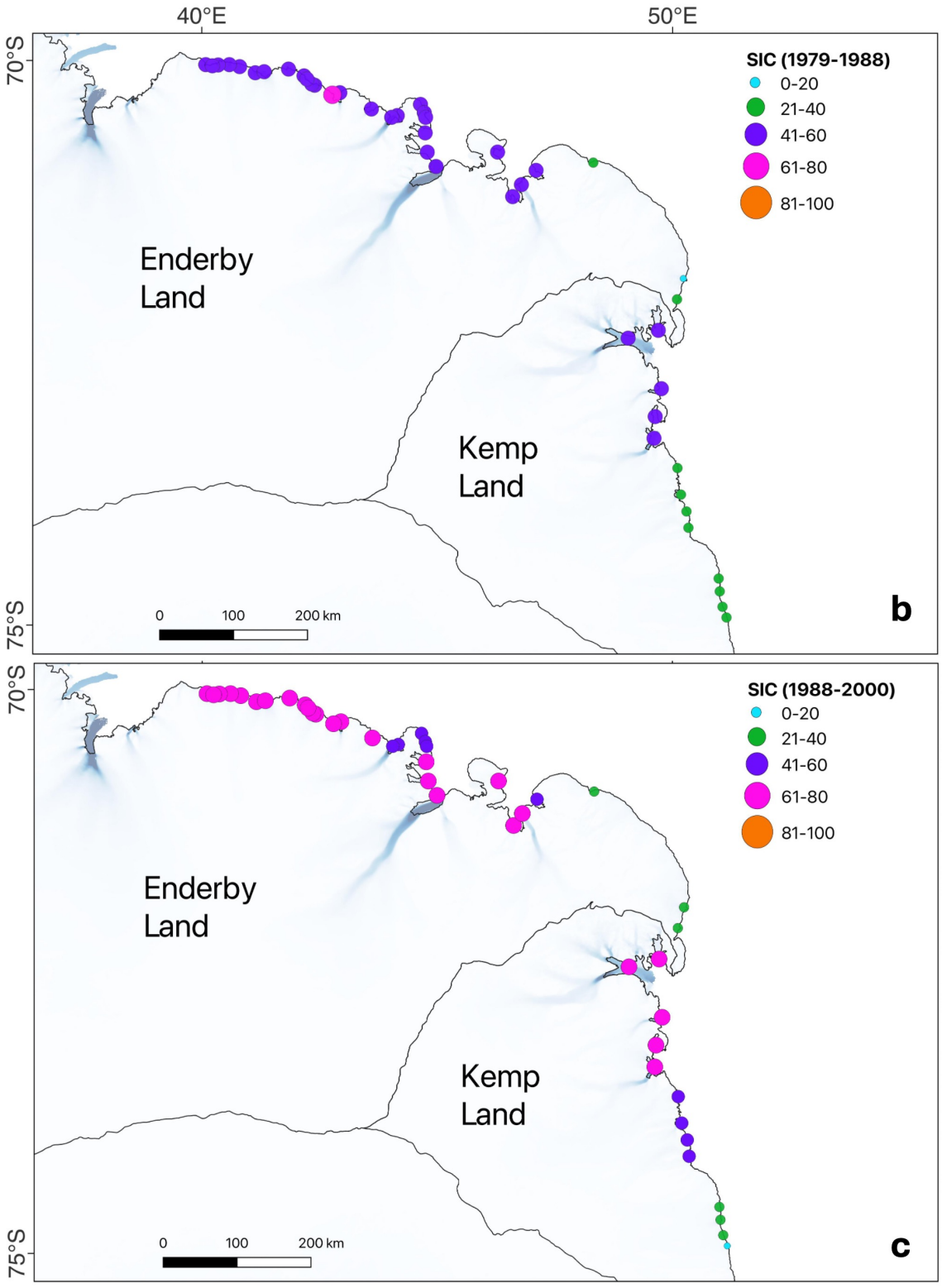
40°E
50°E
70°S
75°S
SIC (1979-1988)
0-20
21-40
41-60
61-80
81-100
Enderby Land
Kemp Land
0
100
200 km
b
SIC (1988-2000)
0-20
21-40
41-60
61-80
81-100
Enderby Land
Kemp Land
0
100
200 km
c

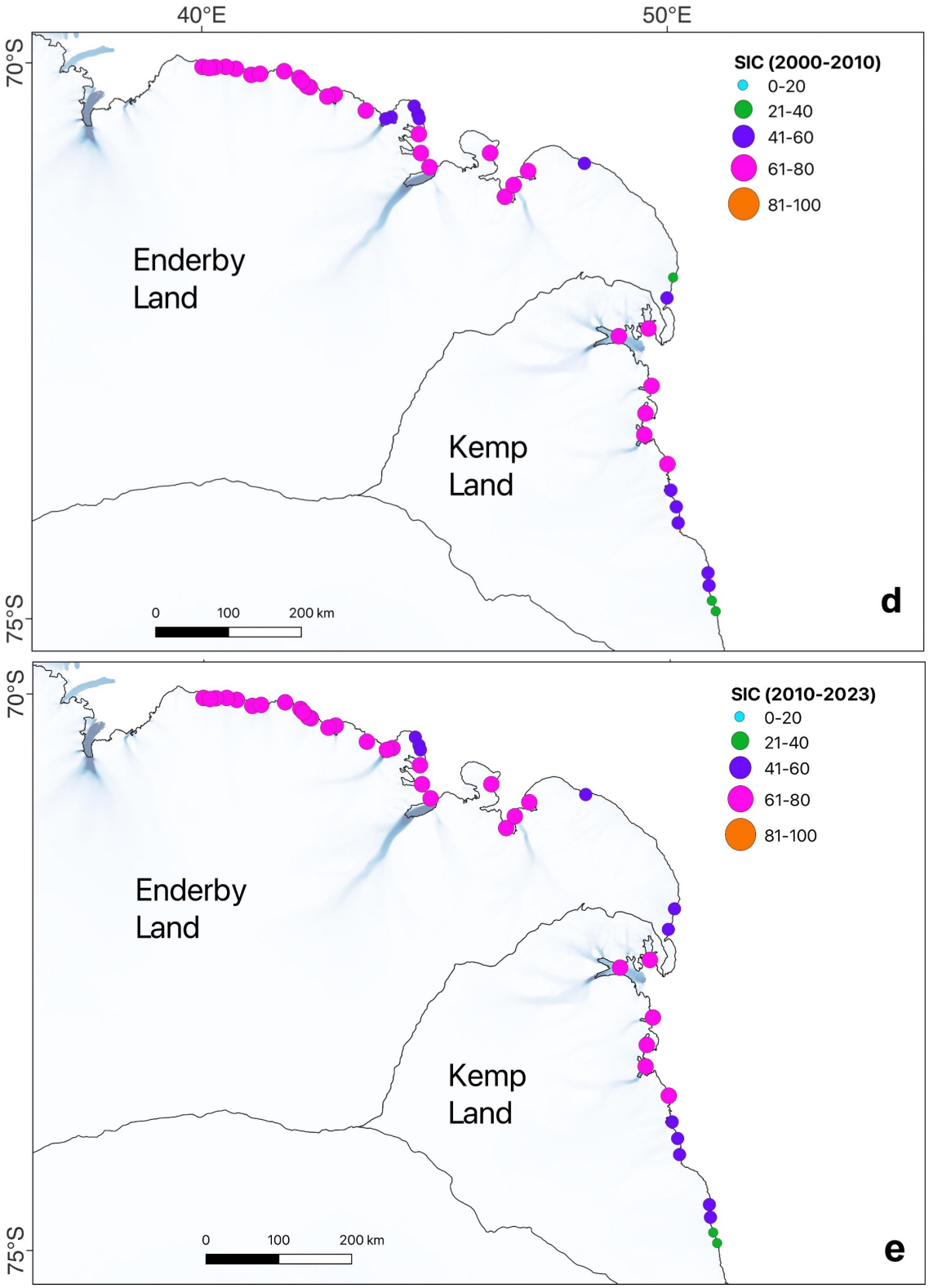

Figure 4.13: *Spatial variability in SIC over the study period and the epochs (a) 1979-2023, (b) 1979-1988, (c) 1988-2000, (d) 2000-2010 and (e) 2010-2023. See Fig for glacier names and locations.*

4.5.4.2 Air temperature

The analysis of summer air temperature trends from 1970 to 2023 (Fig. 4.14) highlights a notable difference between the two regions. Enderby Land, with an average summer temperature of -11.4°C, has consistently been much colder than Kemp Land, which averages -5.9°C. Between the first and last decade, the average summer air temperatures increased slightly by 0.1°C in Kemp Land but decreased by 0.1°C in Enderby Land. These findings indicate that while both regions remain well below freezing in summer, Kemp Land is generally warmer and has experienced a marginal warming trend over the study period, whereas Enderby Land has cooled slightly.

Figure 4.15 illustrates the interannual variability in the number of Positive Degree Days (PDDs) recorded in Kemp Land (KL) and Enderby Land (EL) during austral summer months, with generally very low values over each region during the summer period (Dec-Feb). Both regions exhibit very low PDDs (¡5 days), with sporadic occurrences across the multi-decadal record. A maximum of only 4 PDDs was recorded in KL in 1990, while EL reached just 3 PDDs in 1996. This highlights the rarity of above-freezing temperatures during summer.

At the individual glacier scale, Figure 4.16 shows the distribution of PDDs across various glaciers from 1970 to 2024 and highlights their temporal and spatial variability, with maximum of 12 days with air temperature >0°C. In Enderby Land, glaciers between Oku-iwa to Hays Glacier recorded low PDDs, indicating colder summer temperatures, whereas the glaciers between Glacier 6 and Beaver Glacier exhibited slightly higher number of PDDs over the years, particularly, between 1984 and 1996. In Kemp Land, glaciers between Hoseason Glacier and Glacier 15 (See Fig. 4.1 for location), exhibit more intense and frequent warming, with values peaking at 12–13 PDDs, in intermittent periods. These glacier-scale patterns reveal that warming events have been highly localised, with certain glaciers in Kemp Land experiencing higher PDDs compared to the colder conditions in Enderby Land.

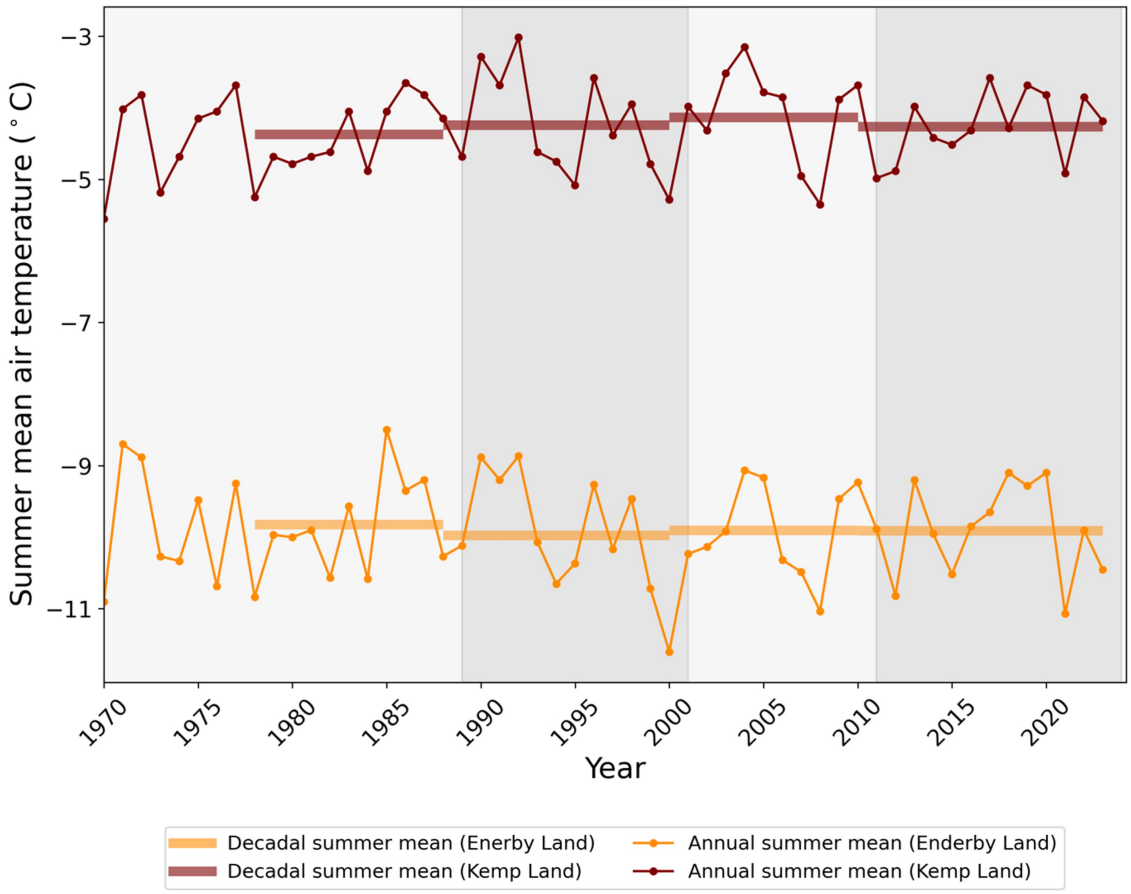

Figure 4.14: *Annual summer mean air temperature (December to February) from ERA-5 reanalysis data from European Centre for Medium-Range Weather Forecasts between 1970 and 2023. The horizontal bars represent the decadal averages of summer means for Enderby Land (orange) and Kemp Land (maroon). The grey shaded regions represent the epochs.*

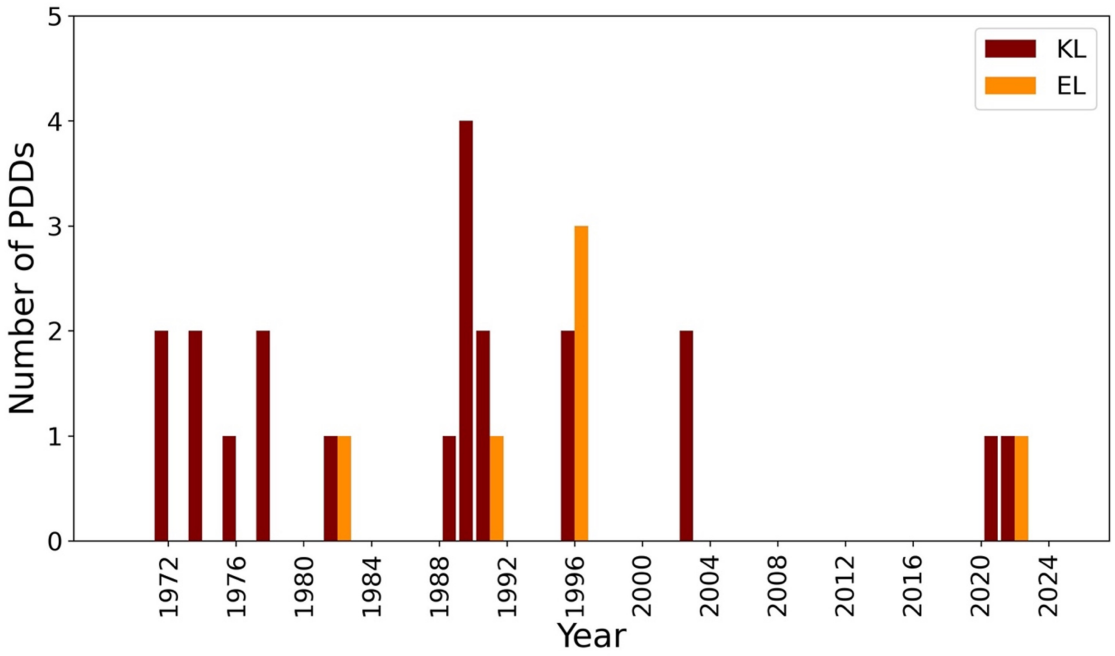

Figure 4.15: *The number of PDDs per year at a regional scale in Enderby (EL) and Kemp Land (KL).*

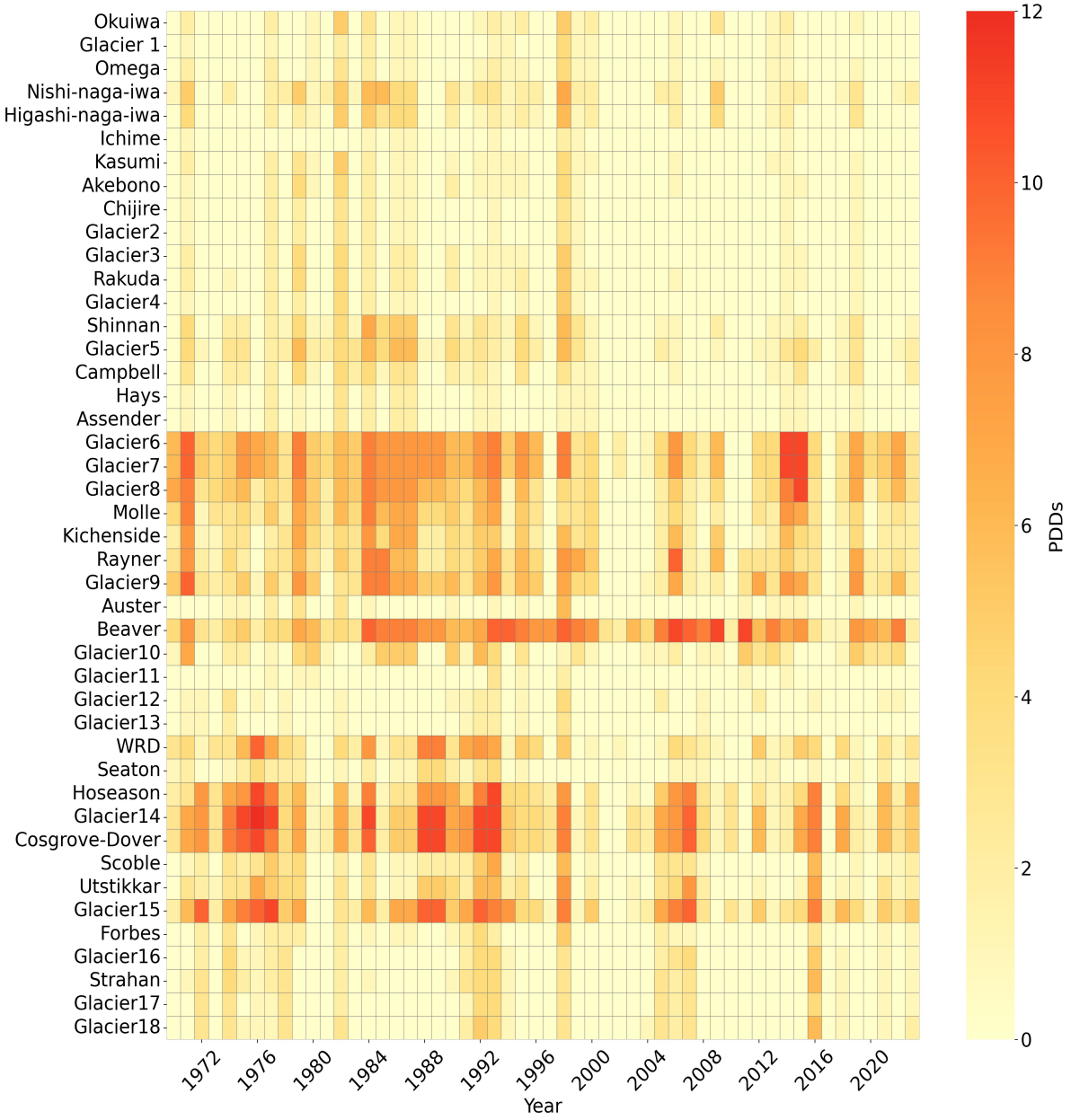

Figure 4.16: *Heatmap showing number of Positive Degree Days (PDDs) across the glaciers in Enderby and Kemp Land (see Figure 4.1 for location).*

4.5.4.3 Sub-surface ocean temperatures

Analysis of sub-surface ocean temperatures over four epochs reveal distinct regional differences between Enderby and Kemp Land (Fig. 4.17). Kemp Land consistently shows higher sub-surface ocean temperatures than Enderby Land across all depth profiles. However, by the last decade, the difference in decadal average ocean temperatures between the two regions has reduced. From 1979 to 2023, a pronounced

decadal cooling trend was also observed in each depth profile for both regions. For example, in Kemp Land, the temperature dropped from -0.9°C to -1.5°C between the first and last decade in the 5-109 depth profile. However, the temperatures started rising in the latter half of the last decade (2010-2023), which was particularly evident in the mid (109-446m) and deeper profiles (446-967m). Overall, the data show a transition from long-term cooling to more recent warming across multiple depth layers in both regions.

At 5–109 m depth, although short-lived spikes in temperatures occurred in both Enderby and Kemp Land, in the mid-1990s and early 2000s, annual and decadal trends consistently indicated a sustained long-term cooling in this depth profile at both regions (Fig. 4.17a). Decadal summer-mean temperatures declined from about –1.2°C (Enderby) and –1.0°C (Kemp) in 1978–1988 to around –1.6°C (Enderby) and –1.5°C (Kemp) in 2010–2023. The period 2000–2010 recorded both a peak warming of –0.65°C and the lowest temperatures of –1.85 °C. Thus, cooling dominates the long-term trend in the upper ocean layer. At 109–446 m depth, although a decadal long-term decrease in ocean temperatures was recorded, a strong warm anomaly was also recorded in the mid-1990s, followed by a period of pronounced cooling. Temperatures reached a minimum of –1.85°C in 2017, before rising sharply to around –0.3°C by 2023 (Fig. 4.17b). The temperature record at this depth shows alternating phases of warming and cooling, with a marked increase in the final years. At 446–967 m depth, a similar mid-1990s warm peak was observed, with subsequent cooling leading to a minimum of –0.3°C around 2012. Afterward, temperatures increased rapidly, reaching approximately +0.5°C by 2023 in both regions. Note that, in this depth profile, both regions recorded temperatures generally above 0°C and exhibited a clear increase in the final decade (Fig. 4.17c).

Overall, the subsurface ocean temperature record reflects a shift from long-term subsurface cooling—especially prominent between 1980s and 2013—to a more recent warming trend evident particularly across mid (109-446 m) and deeper (446-967 m) ocean depth layers in both regions in the post-2010 period. However, in the upper and mid-depth layers, temperatures during the most recent epoch have remained

below 0°C.

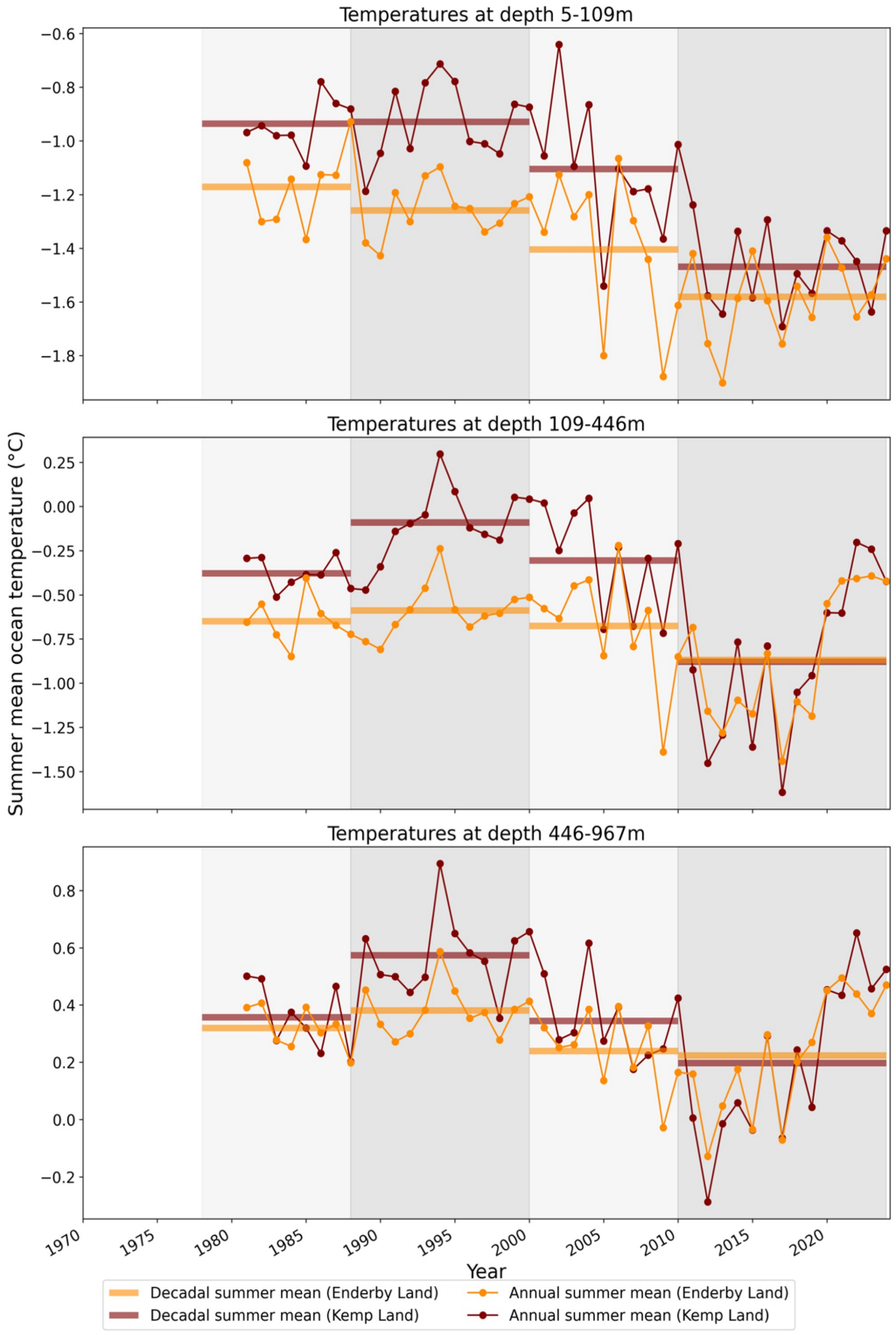

Figure 4.17: *Annual summer mean EN4 objective analysis subsurface ocean temperature (December to March) from the UK Meteorological Office Hadley Centre between 1978 and 2023 at three depth profiles (5-109 m, 109-446 m and 446-967 m). The horizontal bars represent the decadal averages of summer means for Enderby Land (orange) and Kemp Land (maroon). The grey shaded regions represent the epochs.*

Table 4.3: *Summary of mean decadal values of environmental variables such as sea ice extent and concentration, air temperature and subsurface ocean temperatures for each epoch. Note that SIC and subsurface ocean temperature data is available from 1979 onwards.*

	1970s–1988	**1988–2000**	**2000–2010**	**2010–2023**
Sea ice extent (km^2)				
EL	69725.4	84518.7	100764.8	95254.6
KL	60537.5	79258.9	98987.1	95565.2
Sea ice concentration (%)				
EL	43.9	50.7	56.5	58.5
KL	51.6	59.0	62.5	66.0
Air temperature (ºC)				
EL	-9.8	-9.9	-9.9	-9.9
KL	-4.3	-4.2	-4.1	-4.2
Sub-surface ocean Temperature (ºC)				
Depth (m)	**1970s–1988**	**1988–2000**	**2000–2010**	**2010–2023**
EL				
5–109	-0.9	-1.0	-1.1	-1.2
109–446	-0.6	-0.4	-0.6	-0.8
446–967	0.4	0.4	0.3	0.3
KL				
5–109	-0.6	-0.6	-0.7	-1.2
109–446	-0.5	0.0	-0.4	-1.0
446–967	0.3	0.6	0.3	0.1

4.5.4.4 Trends in glacier terminus behaviour and ocean-climate forcing at regional scale

The Figure 4.18 illustrates that each epoch exhibits different relationships between decadal mean terminus position and ocean-climate forcings. During the first decade (1970s-1988), the retreat phase in Enderby Land and advance phase in Kemp Land corresponds to negative summer SIC anomalies and positive sub-surface ocean temperature anomalies at 5-109 m depths (Fig. 4.18a-f). During the second decade (1988-2000), the advance in Enderby Land corresponds to positive summer SIC anomalies during the first half of the epoch positive sub-surface ocean temperature anomalies at all depths (Fig. 4.18a, c, e, g, i). In Kemp Land, glacier advanced during this epoch (1988-2000) which corresponds to negative summer SIC anomalies and positive sub-surface ocean temperature anomalies, particularly at mid-depth 109-446 m, reaching approx. +0.6°C (Fig. 4.18b, d, h).

During the third epoch (2000–2010), glaciers in Enderby Land experienced a retreat phase, coinciding with negative SIC anomalies in the early part of the decade and positive sub-surface ocean temperature anomalies, especially at mid-depth, reaching around +0.4°C (Fig. 4.18a, c, g). In contrast, glaciers in Kemp Land underwent substantial advance during this epoch, corresponding to negative summer SIC anomalies initially, followed by positive anomalies later in the decade, alongside generally negative sub-surface ocean temperature anomalies (Fig. 4.18b, d, f, j). Only mid-depth layers (109–446 m) exhibited positive anomalies, reaching approximately +0.3°C (Fig. 4.18h).

In the final epoch (2010–2023), glaciers in Enderby Land continued to retreat, associated with predominantly positive summer SIC anomalies, although some years recorded negative anomalies (Fig. 4.18a). This retreat coincided with consistently negative sub-surface ocean temperature anomalies across all depths (Fig. 4.18e, g, i). Similarly, glaciers in Kemp Land entered a retreat phase during this period, corresponding to positive summer SIC anomalies and negative sub-surface ocean temperature anomalies at all depths (Fig. 4.18f, h, j).

In addition, air temperature trends indicate that glacier retreat is generally associated with negative summer mean air temperature anomalies, while periods of advance are mostly linked to positive anomalies (Fig. 4.18k, l). Overall, the relationships between glacier terminus position and ocean–climate forcings—such as sea ice concentration (SIC), sea ice extent (SIE), sub-surface ocean temperature, and air temperature—have varied between regions and across decades. Earlier epochs showed clearer and more consistent associations, while these relationships weakened and became more inconsistent in the most recent epoch (2010–2023).

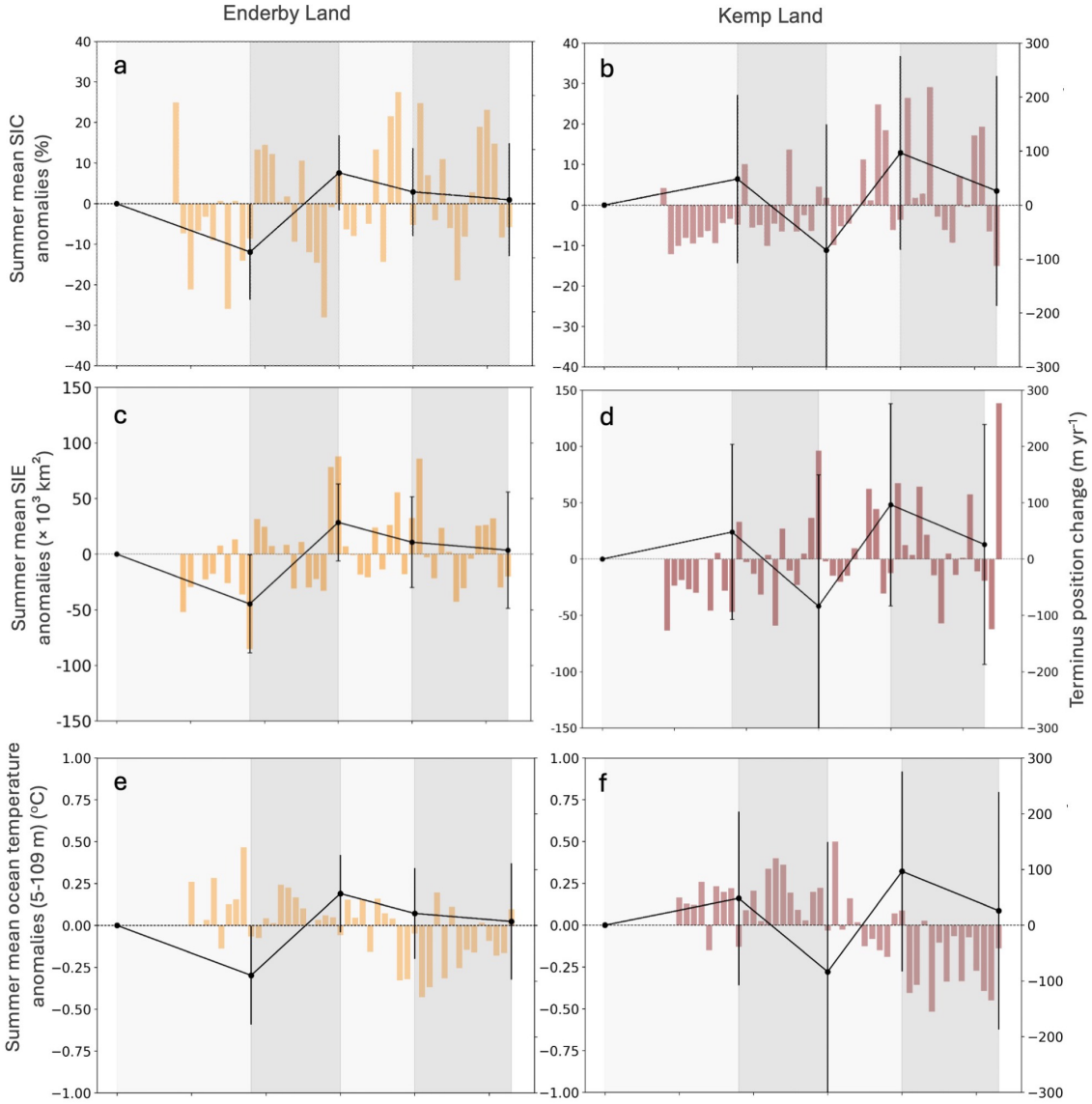

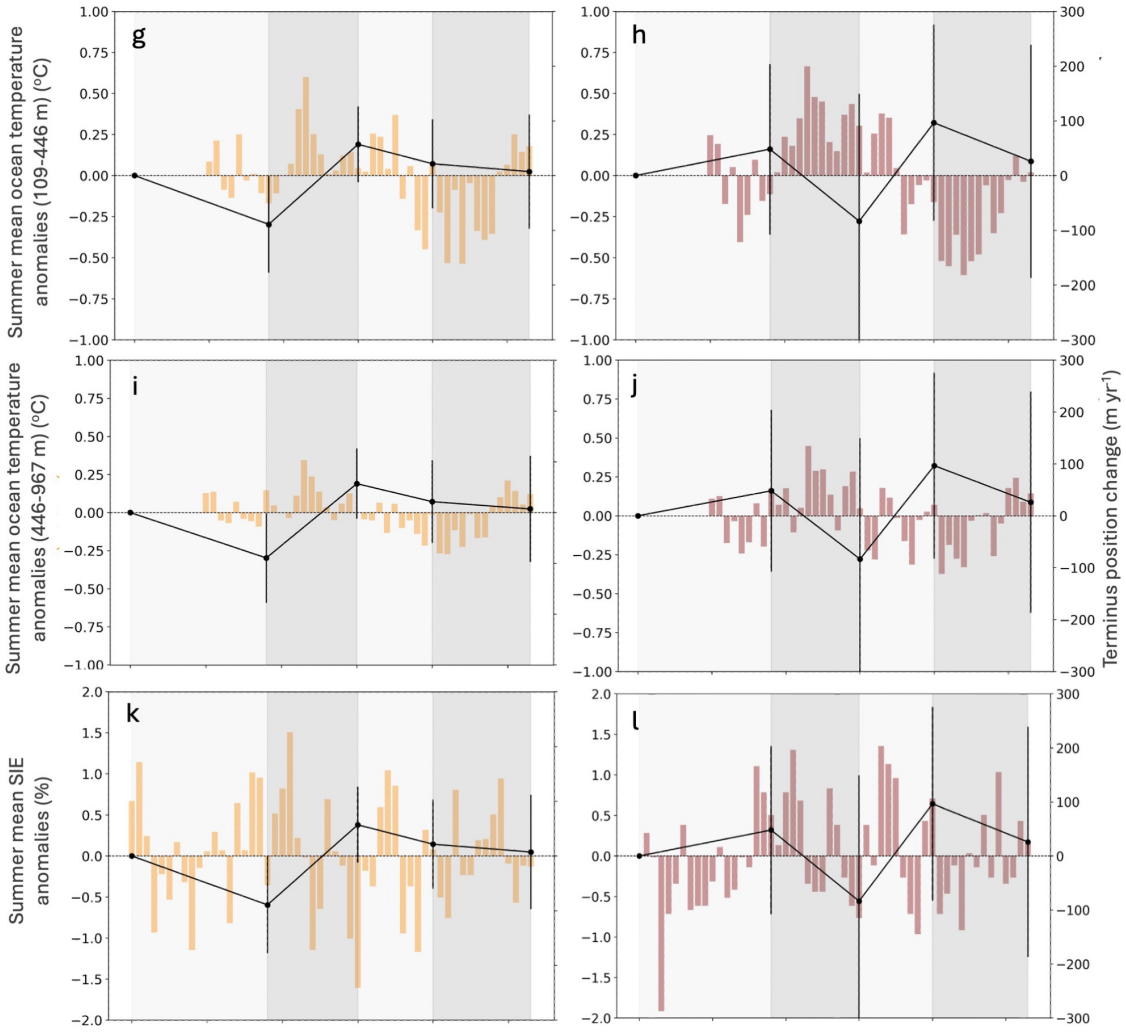

Figure 4.18: *Mean summer anomalies of (a) SIC, (c) SIE, and (e,g,i) ocean temperature at depths 5-109 m, 109-446 m and 446-967 m, respectively, (k) air temperature and mean terminus change (m yr-1) for Enderby Land (left-orange) and Kemp Land (right-maroon). Standard deviation bars for the median glacier terminus position changes. Grey shading in the background represents each epoch.*

4.5.4.5 Testing statistical correlation with ocean-climate variables at regional scale

Following the temporal patterns observed in Section 4.5.4, correlation analysis was used to assess the statistical relationships between regional glacier terminus changes and ocean–climate variables. The results show a consistent direction of correlation across both Kemp and Enderby Land, although the strength of the correlations varied depending on the specific variable and time lag. The strongest statistically significant correlations with normalised glacier terminus position changes were ob-

served for two variables: summer sea ice concentration (SIC) at a 2-year lag (r= +0.6), and subsurface ocean temperatures at 5–109 m depth at a 5-year lag (r = -0.5). This indicates that glacier advance or retreat is most strongly associated with sea ice and ocean temperature conditions occurring one to several years earlier.

In Kemp Land, the largest statistically significant correlation was found between normalised glacier terminus position and mean summer sea ice concentration (SIC). This relationship was positive with moderate strength, with correlation values of r = +0.6 at a 2-year lag (Fig. 4.19). Similarly, sea ice extent (SIE) also showed a moderate positive correlation at a 2-year lag (r = +0.4). In contrast, Enderby Land exhibited slightly weaker but still statistically significant relationships. SIC and SIE at 1- and 2-year lags exhibited moderate positive correlations (r = +0.4 to +0.5) as shown in Figure 4.19. A positive correlation between normalised terminus position and SIC or SIE indicates that higher summer SIC and SIE tends to be followed by glacier advance in subsequent years.

Statistically moderate negative correlations were observed between subsurface ocean temperatures and glacier terminus position in both regions, though the strength and depth profiles varied. In Kemp Land, statistically significant correlations of r = –0.5 and r = –0.4 were found at the 5–109 m and 109–446 m depth profiles, respectively, at a 5-year lag (Fig. 4.19). In Enderby Land, a significant negative correlation of r = –0.5 was observed only at the 5–109 m depth at the same lag (Fig. 4.19). Mid-depth (109–446 m) and deeper ocean layers (446–967 m) in Enderby Land showed weaker correlations ($\leq |0.3|$), which were not statistically significant. A negative correlation in this context indicates that warmer subsurface ocean temperatures are generally followed by glacier retreat several years later, while cooler ocean conditions tend to precede advance.

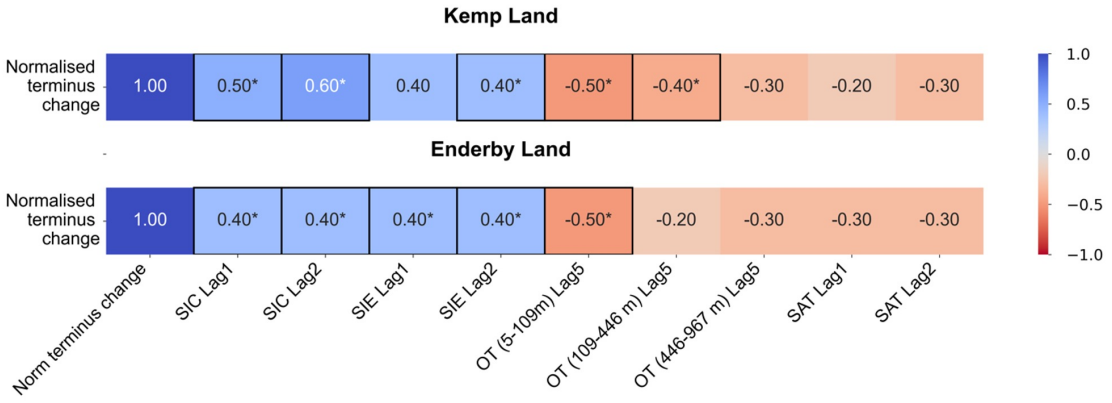

Figure 4.19: *Correlation between normalised glacier terminus position change between 1970s-2023 in (a) Enderby Land and (b) Kemp Land and analysed climate variables at lag of one and two years for sea ice concentration (SIC), sea ice extent (SIE), sub-surface ocean temperatures (OT) at dept profiles of 5-109 m, 109-446 m and 446-967 m, summer (SAT) and number of PDDs (#PDDs). The asterisks and the black outlines on the cells indicate significance levels for p = 0.05 (*).*

4.5.4.6 Testing statistical correlation with ocean-climate variables individual glaciers

The correlation coefficients between individual summer mean glacier terminus position changes and various ocean–climate variables are shown in Figure 4.20. The results reveal considerable spatial heterogeneity, with some glaciers exhibiting moderate and statistically significant relationships, while others show weaker or no meaningful correlation. Subsurface ocean temperatures and summer sea ice concentration (SIC) emerge as the most consistently correlated variables, though the direction and strength of correlation vary across the glaciers.

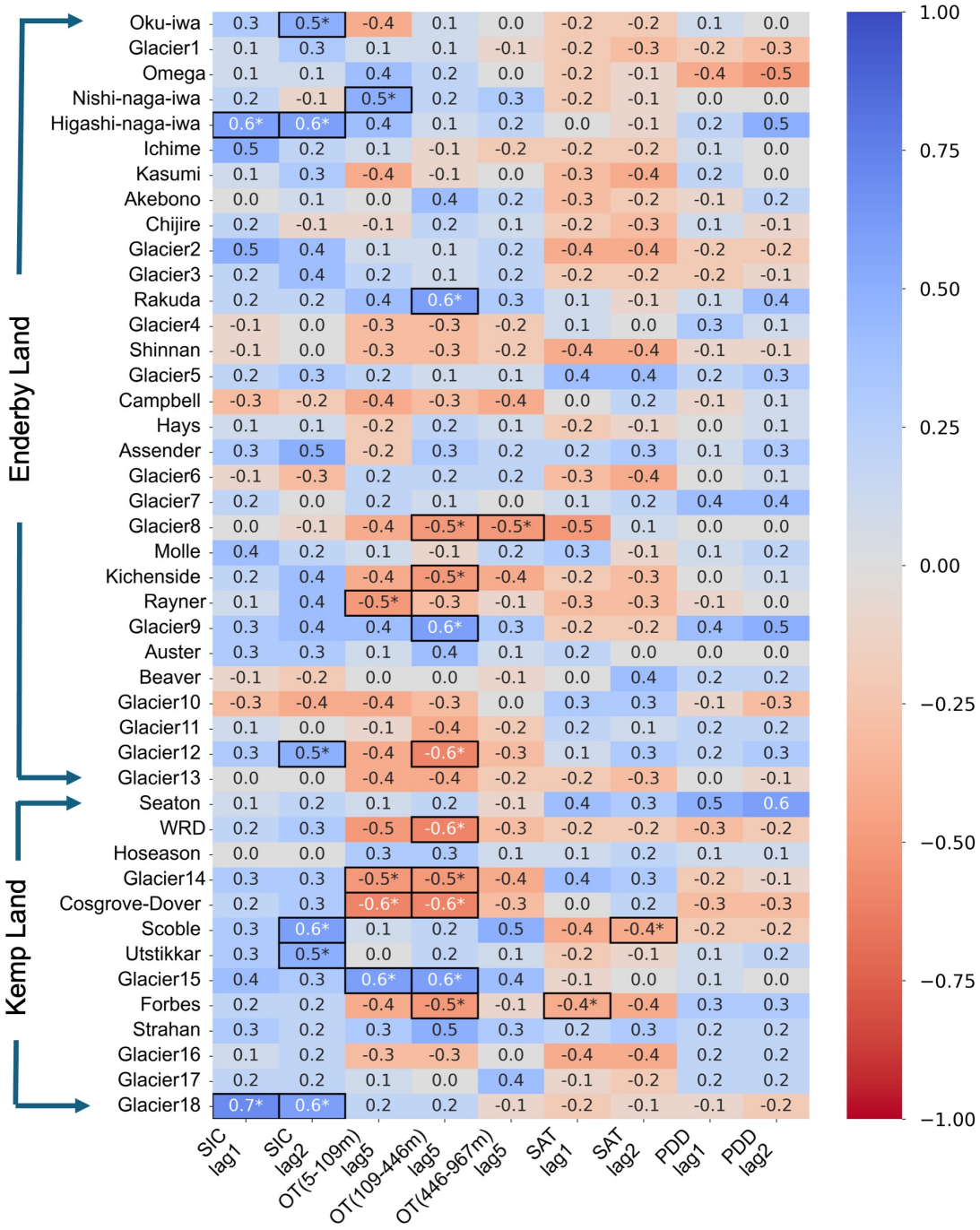

Figure 4.20: *Link between climate variables and glacier terminus change in Enderby Land and Kemp Land. The figure shows correlation coefficients for each glacier and the climate variables at lag 1 and 2 for Sea ice concentration (SIC), Summer air temperature (SAT) and lag 5 for ocean temperature (OT) at 5-109m, 109-446m and 446-967m. The highlighted cells with * shows statistically significant correlations.*

A limited subset of glaciers showed statistically significant moderate positive correlations ($r \approx +0.5$ to $+0.7$) between mean summer sea ice concentration (SIC) and normalised terminus position change, with effects appearing after 1–2 year lags.

Significant positive correlations were calculated at lag 1 only for Higashi-naga-iwa (r = +0.6) and Glacier 18 (r = +0.7). At lag 2 for Oku-iwa (r = +0.5), Higashi naga iwa (r = +0.6), Glacier 12 (r = +0.5), Scoble (r = +0.6), Utstikkar (r = +0.5), and Glacier 18 (r = +0.6). Notably, Higashi-naga-iwa and Glacier 18 exhibited statistically significant correlations between mean summer sea ice concentration (SIC) and normalised terminus position change at both lags. Many other glaciers also showed weak, statistically non-significant positive correlations ($r \approx +0.1$ to $+0.4$), weakly suggesting that higher earlier summer SIC may have preceded advance in these glaciers. In contrast, a few glaciers (e.g., Campbell, Glacier10) exhibited weak, non significant negative correlations with SIC at 1–2 year lags (r = –0.3). This relationship indicated that for a few glaciers lower summer SIC preceded advance (or higher SIC preceded retreat) there—an opposite response to the majority pattern. Overall, the results revealed that for most glaciers with significant relationships, increased summer sea ice concentration in preceding years is moderately associated with subsequent glacier advance, while a minority exhibits the reverse sensitivity. This spatial heterogeneity implies differing local controls or glacier–ocean couplings across the region.

Negative correlations were calculated at a five year lag between subsurface ocean temperature (OT) and normalised glacier terminus position predominated. In the upper layer (5–109 m), Rayner, Glacier14 and Cosgrove Dover showed statistically significant moderate negative correlations ($r \approx -0.5$ to -0.6; $p < 0.05$). In the mid layer (109–446 m), seven glaciers exhibited statistically significant moderate negative correlations ($r \approx -0.5$ to -0.6). In the deep layer (446–967 m), one glacier displayed a statistically significant moderate negative correlation. Thus, a statistically significant negative correlation with a 5 year lag means that for these glaciers, higher ocean temperatures for at least 5 years preceded terminus retreat or lower ocean temperatures for at least 5 years preceded terminus advance. Many other glaciers exhibited weaker, non-significant negative correlations ($r \lesssim -0.4$) between subsurface ocean temperature at different depths and normalised glacier terminus position. This weakly indicated that higher earlier mean summer subsurface temperatures may have preceded retreat in these glaciers. Some glaciers also showed

positive or near zero coefficients at one or more depths. For example, Glacier 15 exhibited a statistically significant positive correlation between subsurface ocean temperature (OT) at upper (5–109 m) and mid-ocean (109–446 m) depth layers and normalised glacier terminus position. This indicated that in these cases, glacier advance occurred despite sustained warm ocean conditions, or retreat occurred despite colder conditions—reflecting a lack of consistent ocean temperature–terminus response in those cases.

Correlations with summer mean air temperatures (SAT) and PDDs at a one and two-year lags were generally weak and not statistically significant. Throughout the study period, summer mean air temperatures remained well below 0°C at all glaciers, and instances of above-freezing temperatures were rare. Only a few glaciers experienced isolated days with temperatures exceeding 0°C, as shown in Fig. 4.16. As a result, the number of positive degree days was extremely low. These findings indicate that atmospheric warming and surface melt have played a minimal role in driving glacier terminus changes across all glaciers over the study period.

4.6 Discussion

4.6.1 Temporal and spatial trends in glacier terminus position change

The multi-decadal analysis revealed widespread retreat during the initial epoch between the 1970s and 1988, as approximately 61% of glaciers (n=27 of 44) retreated across the entire study area (Fig. 4.8). These findings are consistent with broader patterns across the East Antarctic Ice Sheet (EAIS). For example, Miles et al. (2016) reported that 65% of EAIS glaciers (n = 254) retreated between 1974 and 1990, and Lovell et al. (2017) observed median retreat rates of -6.7 ± 4.1 m yr^{-1} and -49.8 ± 4.1 m yr^{-1} for Oates and George V Lands, respectively, during 1972–1988. The widespread advance observed between 1988 and 2000 in this chapter aligns with EAIS-wide trends reported by Miles et al. (2016), who found that 67% of 334 glaciers advanced between 1990 and 2000, and 65% of 342 glaciers advanced between 2000

and 2012. Similarly, Lovell et al. (2017) observed a reversal to advance in Oates and George V Lands at rates of $+22.7 \pm 15.4$ m yr^{-1} and $+195.3 \pm 15.4$ m yr^{-1}, respectively, during 1988–1997. This trend of overall advance continued into the third epoch (2000–2010), although with reduced intensity, as 64% of glaciers advanced. In the most recent epoch (2010–2023) only 57% exhibiting terminus advance. Lovell et al. (2017) also reported that the subsequent epochs maintained glacier advances but at diminishing rates. This decline in advancing glacier numbers observed in this chapter and by Lovell et al. (2017) may indicate increasing heterogeneity in glacier response, potentially driven by evolving oceanic and atmospheric conditions, local glacier geometry, or other external forcings. This heterogeneity is further underscored by the marked regional differences in glacier behaviour observed across the study area.

Despite the overall patterns of terminus change across the study area, the data reveal clear regional differences in glacier behaviour between Enderby Land and Kemp Land, with marked variability across epochs (Fig. 4.10). Although 61% of glaciers across the entire study region retreated between the 1970s and 1988, this overall trend was largely driven by glaciers in Enderby Land, where 71% retreated during this period, at a mean rate of –94.9 m yr^{-1}. In contrast, 61% of glaciers in Kemp Land advanced, with a mean rate of +15.0 m yr^{-1}, highlighting a stark regional contrast. During the subsequent phase (1988–2000), glacier dynamics reversed in both regions. Enderby Land glaciers showed strong recovery with advances at +51.7 m yr^{-1}, while Kemp Land glaciers experienced net retreat, averaging –48.0 m yr^{-1}. These opposing trends illustrate the asynchronous nature of glacier response, even between neighbouring regions. The third epoch (2000–2010) saw a convergence in behaviour, with glaciers in both regions advancing (65% in Enderby Land and 62% in Kemp Land), at mean rates of +24.0 m yr^{-1} and +105.5 m yr^{-1}, respectively. However, by the most recent epoch (2010–2023), 58% of glaciers in Enderby Land retreated (–9.0 m yr^{-1}), while 54% of glaciers retreated in Kemp Land (+63.5 m yr^{-1}).

By 2023, glaciers in Kemp Land had, on average, reached their most advanced

position since the 1970s, while glaciers in Enderby Land were more extensive during the 1970s than in 2023, likely due to the retreat that occurred during 2010-2023. These contrasting patterns between Enderby Land and Kemp Land highlight the importance of regional-scale controls on glacier terminus behaviour. In fact, other studies have also documented regional differences in glacier termini behaviour across the AIS. For example, previous studies did not find a significant trend in glacier termini position changes in Victoria Land which was attributed to glacier size and local topographic settings (Fountain et al., 2017; Lovell et al., 2017; Baumhoer et al. 2021), even though the neighbouring regions of Oates and George V Land underwent decadal changes (Lovell et al. 2017). Similarly, recent work by Dømgaard et al. (2024) reported no consistent long-term trend in glacier terminus position in Kemp Land, Mac Robertson Land, or the Ingrid Christensen Coast between 1937 and 2022.

At individual glacier scale, the long-term terminus position change behaviour is asynchronous across Enderby and Kemp Land (Fig. 4.7). For example, although Glacier 4 has been advancing, Shinnan Glacier—located nearby in Enderby Land—has experienced a net retreat relative to its initial terminus position in the 1970s. This contrast highlights the differing glacier responses even between neighbouring systems (see Fig. 4.1 for locations). Similarly, in Enderby Land, Rayner Glacier underwent a series of fluctuations, with an initial slight retreat followed by a decade of advance, a brief retreat, another decade of advance, and subsequent cycles of retreat and advance (Fig. 4.8a). In contrast, its neighbouring Kichenside Glacier showed a pattern of stability to slight retreat before entering a prolonged period of advance (Fig. 4.7). Indeed, the extent of change also varies across glaciers. Such asynchronous behaviour could likely be due to local variations in oceanic and climatic forcings as well as topographic settings of the glaciers.

4.6.2 Potential drivers of regional glacier terminus behaviour

Previous studies have widely recognised the importance of sea ice in influencing glacier termini behaviour (Lucchitta and Rosanova, 1998; Miles et al., 2016; Baumhoer et al., 2021; Kondo et al., 2023). For example, Miles et al. (2016) attributed the substantial glacier termini retreat in Wilkes Land between 2000-2012 to extreme reduction in number of sea ice days. Similarly, the breakup of multi-year landfast sea ice triggered the disintegration of the Porpoise Bay Ice Shelf (Miles et al., 2016) and the Voyeykov Ice Shelf in 2007 (Arthur et al., 2022). Additionally, repeated summer fast-ice breakups have led to significant ice loss, resulting in the complete disintegration of the Parker Ice Tongue in Victoria Land in March 2020 (Gomez-Fell et al., 2022). These studies collectively demonstrate that sea ice can provide mechanical buttressing to glacier fronts, suppressing calving and inhibiting ocean-induced frontal melt. As noted by Massom et al. (2010) and Reeh et al. (2001), the presence of persistent sea ice and mélange can dampen wave-driven stresses and restrict ocean access to glacier termini.

Consistent with these earlier findings, this thesis demonstrates that sea ice conditions exert influence on glacier behaviour in both Enderby and Kemp Lands. At the regional scale, statistical analysis reveals a moderate positive significant correlation between glacier terminus position change and higher sea-ice concentration (SIC) and sea-ice extent (SIE) when introducing a two-year lag ($r = +0.4$ to $+0.6$) (Fig. 4.19). In other words, higher mean summer SIC and SIE in the preceding two years are associated with glacier advance, while lower values over the same period are linked to glacier retreat in both Kemp and Enderby Lands. This temporal relationship suggests that sea ice plays a stabilising role, buffering glacier termini from calving and frontal ablation, and potentially modulating the impact of other environmental drivers such as subsurface ocean temperatures.

In Enderby Land, during the first epoch (1970s–1988), widespread glacier retreat coincided with negative anomalies in summer SIC and SIE (Fig. 4.18a). In contrast,

the second epoch (1988–2000) saw glacier advance linked to positive SIC anomalies in the early part of the decade, despite continued subsurface ocean warming. This reversal highlights the capacity of high SIC to mitigate the effects of ocean-driven melt. However, as sea ice declined again in the late 1990s and early 2000s, the rate of glacier advance slowed markedly, suggesting a loss of this buffering effect. The most recent epoch (2010–2023) was characterised by mixed SIC anomalies and only modest glacier retreat, indicating a more complex or spatially variable influence of sea ice in recent years.

In Kemp Land, glacier response to sea ice appears more delayed or buffered. Despite negative SIC and SIE anomalies between 1979 and 1988, 61% of glaciers advanced during this period. This anomalous advance may reflect higher sea-ice concentrations prior to 1979—beyond the temporal coverage of the sea ice dataset used—or the localised presence of fast ice in fjords that provided stabilising buttressing effects. For example, the Wilma-Robert-Downer Glacier system was fronted by persistent fast ice, likely contributing to its advance and frontal stability. During the second epoch (1988–2000), sustained low SIC and SIE coincided with widespread glacier retreat, while a shift to more positive sea-ice anomalies during 2000–2010 aligned with a marked return to glacier advance. This trend continued in the most recent epoch (2010–2023), during which 54% of Kemp Land glaciers advanced in association with positive SIC/SIE anomalies.

Together, these findings underscore the importance of sea ice as a primary control on glacier terminus stability in East Antarctica. Not only do they support existing literature that highlights the mechanical role of sea ice in modulating calving and melt processes, but they also add temporal and regional resolution by demonstrating that the glacier response to sea-ice variability can differ across neighbouring regions and evolve across decades.In addition to SIC and SIE, subsurface ocean temperatures at different depth intervals plays an important role in influencing glacier termini behaviour. Prior research has shown that warmer ocean temperatures can facilitate increased basal melt rates and mass loss in glaciers (Thoma et al., 2008; Rignot et al., 2013; Dutrieux et al., 2014; Paolo et al., 2015; Wouters et al., 2015; Konrad

et al., 2018; Baumhoer et al., 2021). For example, the intrusion of warm mCDW into the cavities of Totten Glacier has resulted in enhanced basal melt rates and mass loss (REF). Similarly, the retreat of Cadman Glacier in the APIS experienced dynamic imbalance and increased ice discharge due to warm ocean water reaching the glacier (Wallis et al., 2023).

At the regional scale, statistical analysis reveals a strong negative correlation between subsurface ocean temperatures in the upper ocean layer (5–109 m depth) and normalised glacier terminus position, with the strongest relationship observed at a five-year lag (r = –0.6; Fig. 4.19). This indicates that warmer ocean temperatures are associated with glacier retreat, whereas cooler conditions are linked to glacier advance, reflecting a delayed but systematic oceanic influence on frontal stability. In Enderby Land, glacier retreat during the 1970s–1988 epoch coincided with positive temperature anomalies in the upper ocean layer (5–109 m depth), suggesting that warmer waters facilitated increased frontal ablation and contributed to terminus retreat (Fig. 4.18). Although warm ocean conditions persisted into the second epoch (1988–2000), their influence appears to have been moderated by higher SIC during the early part of the decade, allowing glaciers to advance despite the continued subsurface warming (Fig. 4.18). Nevertheless, as SIC declined in the latter half of this epoch, the continued presence of warm upper ocean waters likely limited the extent of advance during this period. In the following epoch (2000–2010), positive temperature anomalies at both upper and mid-depth layers persisted and coincided with a further reduction in the glacier advance rate, reinforcing the potential role of sustained ocean heat in inhibiting frontal stability. By the final epoch (2010–2023), negative subsurface temperature anomalies were observed and sea-ice conditions were more variable. These conditions corresponded with only a modest median rate of retreat (~ -14.7 m yr^{-1}), suggesting a potential reduction in ocean-driven melt and weaker oceanic influence during this period.

In Kemp Land, subsurface ocean temperatures at 5–109 m depth remained consistently positive across most epochs, but their influence on glacier behaviour appeared less direct. During the first epoch (1970s–1988), glacier advance occurred despite

warm upper ocean temperatures and low SIC/SIE anomalies, indicating a possible delayed response or the dominance of other stabilising controls at individual glaciers. In contrast, the second epoch (1988–2000) observed retreat at a median rate of ~ -12 m yr^{-1}, which coincided with sustained positive subsurface temperature anomalies—highlighting the potential for ocean-driven retreat when other stabilising factors are absent or diminished. During the 2000–2010 epoch, glacier advance resumed even though subsurface warming continued, implying that local controls such as bed geometry, grounding-line position, or fjord morphology may have overridden the influence of oceanic heat. In the most recent epoch (2010–2023), negative temperature anomalies were recorded across all depth intervals and coincided with continued glacier advance, supporting the idea that cooler ocean conditions reduced basal melt and promoted frontal stability in this region. Overall, these results suggest that subsurface ocean temperatures—particularly in the upper 5–109 m layer—play a key role in modulating glacier terminus change, although their influence is often mediated by sea-ice conditions and local glacier-specific factors.

Previous studies have suggested a positive correlation between air temperature and calving events—such as the collapse of the Larsen A Ice Shelf in 1995 (Rott et al., 1996), the disintegration of Larsen B in 2002 (Rack and Rott, 2004; Khazendar et al., 2007; Glasser and Scambos, 2008; Banwell et al., 2013), the breakup of the Wilkins Ice Shelf in 2008 (Braun and Humbert, 2009; Scambos et al., 2000, 2009), and the disintegration of the George VI Ice Shelf (Alison and Banwell, 2021). These events were all associated with anomalously high summer air temperatures and extensive supraglacial meltwater ponding, which in many cases triggered hydrofracturing and structural failure. However, such surface melt features are rarely observed in the study area, where summer temperatures remain well below freezing and positive degree days are limited. Consistent with this, the findings of this thesis showed no significant correlation between summer mean air temperature or the number of PDDs and normalised glacier terminus position at the regional scale. This lack of association is likely due to the consistently low summer temperatures across both regions, with PDDs rarely exceeding four days per year. On average, Enderby Land experiences colder summer temperatures (–11°C) compared to Kemp Land (–6°C),

further limiting the potential for surface melt. These conditions suggest that, unlike in the Antarctic Peninsula, air temperature plays a minimal role in driving glacier terminus change in this sector of East Antarctica.

In addition, Dømgaard et al. (2024) suggested that longer-term changes in surface mass balance may also contribute to the stabilisation of glacier termini. They found a persistent positive trend in mean annual snowfall across Kemp, MacRobertson and along the along Ingrid Christensen Coast between 1937 and 2022, with accumulation increasing by approximately 50% between 1940 and 2022. These snowfall-driven gains likely contributed to glacier thickening and frontal advance, reinforcing structural stability. The prevalence of glacier advance observed in this study—despite periods of elevated ocean temperatures—may therefore reflect the combined influence of high sea-ice concentrations and multi-decadal mass gain from snowfall.

4.6.3 Potential drivers of individual glacier termini behaviour

The limited and spatially asynchronous response of marine-terminating glaciers across Enderby and Kemp Land suggested that, overall, glacier termini has not dramatically changed during the study period (2000-2023), with terminus position variability influenced by a combination of sea ice conditions, subsurface ocean temperatures, and local glacier-specific factors, rather than by any single dominant ocean-climate forcing (Fig. 4.20). As described in Chapter 3, many glaciers in this region share key topographic and geographic features with Greenlandic outlet glaciers, such as glaciers flowing into fjords. However, unlike Greenlandic glaciers that often exhibit synchronous behaviour in response to environmental forcing (e.g., Black and Joughin, 2022), the glaciers in this sector of the EAIS showed heterogeneous responses despite experiencing broadly similar ocean–climate conditions across the regions. This heterogeneity underscores the influence of a range of glacier-specific factors operating over different timescales, including both ocean–climatic and non-climatic drivers.

A subset of glaciers displayed moderate, statistically significant positive correlations between mean summer sea-ice concentration (SIC) and normalised terminus position

change, particularly at one- and two-year lags. The presence of such lags implies that sea-ice conditions may exert a delayed control, potentially by modulating local oceanic heat fluxes. Higashi-naga-iwa Glacier exhibited statistically significant positive correlations with sea-ice concentration (SIC) at both one- and two-year lags, suggesting a robust and persistent relationship between higher SIC and subsequent terminus advance (Fig. 4.20). The Figure 4.21 shows a temporal alignment between periods of SIC and glacier terminus position change, highlighting the potential role of prolonged sea-ice coverage in stabilising the glacier front.

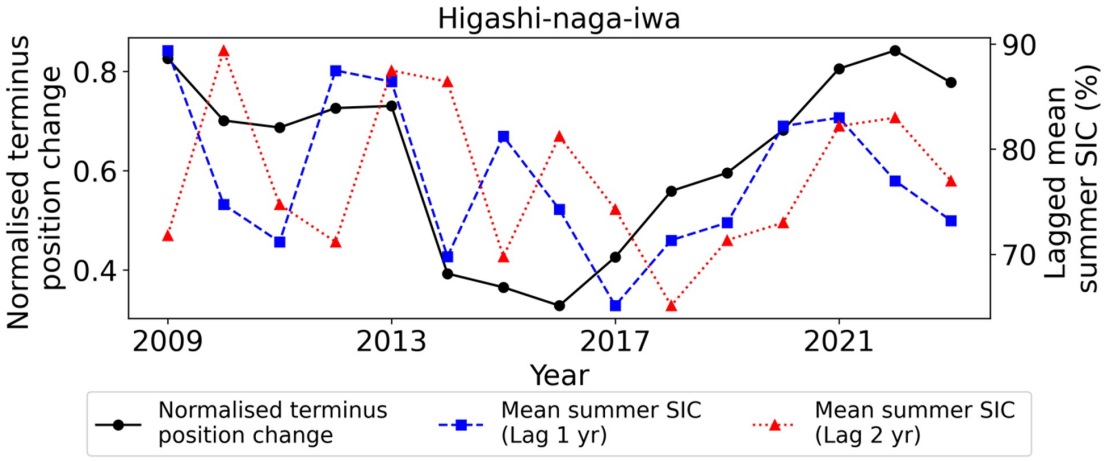

Figure 4.21: *Time series plot showing the relationship between lagged summer sea-ice concentration (SIC) and normalised terminus position change for Higashi-naga-iwa Glacier.*

This may reflect a mechanism where persistent sea-ice coverage acts as a thermal and mechanical buffer, limiting the delivery of warm ocean water to glacier termini and reducing calving or basal melt. This interpretation is consistent with earlier studies that highlight the stabilising influence of sea ice. Massom et al. (2010) showed that the presence of land-fast sea ice delayed calving at Mertz Glacier, and similar stabilisation was reported for the Voyeykov Ice Shelf prior to its disintegration following sea-ice removal (Arthur et al., 2021). More recently, Kondo and Sugiyama (2023) provided compelling evidence from Lützow-Holm Bay, East Antarctica, where five outlet glaciers exhibited synchronous frontal advance during periods of persistent sea-ice cover (2008–2015) and abrupt retreat following a major breakup event in 2016. Their analysis demonstrated that stable land-fast sea ice not only delayed

calving but also suppressed glacier flow and enhanced thickening near the grounding line through reduced stretching. Following the 2016 sea-ice breakup, all five glaciers retreated rapidly, coinciding with the most significant SIC decline in the region since 1998. Fukuda et al. (2016) also proposed that calving events at Langhovde Glacier were closely linked to local sea-ice conditions. Similarly, in Lützow-Holm Bay, the development of dense multi-year land-fast sea ice was found to be closely coupled with frontal stability, while sea-ice mobility and loss were associated with enhanced calving and ice discharge (Kondo & Sugiyama, 2023). These examples collectively underline the importance of sea-ice dynamics in modulating not only terminus position but also glacier flow regimes and thickness changes. However, this relationship is not consistent across a larger spatial scale and across timescales.

In the present study, apart from the statistically significant correlations observed across a few glaciers, majority of glaciers also exhibited weak or statistically insignificant correlations with SIC, and a few even showed slightly negative correlations (Fig. 4.22). This spatial heterogeneity suggests that while sea ice can play a stabilising role, its influence is likely modulated by local factors such as fjord geometry, bed topography, the presence or absence of ice tongues or mélange, and oceanographic settings. For instance, glaciers located in Oates and Victoria Land exhibited minimal sensitivity to SIC variations, as also noted by Lovell (2016), highlighting the complex interplay between external forcings and internal glacier dynamics. Overall, these findings underscore that while land-fast sea ice is a critical component influencing glacier terminus stability in parts of East Antarctica, its role varies considerably across the region.

Subsurface ocean temperature (OT) exhibited negative correlations with glacier terminus position change, particularly at five-year lags at upper and mid-depth layers (Fig. 4.20). These patterns suggest that sustained cooling of subsurface ocean layers could be associated with glacier terminus advance, albeit after a multi-year lag or sustained warming could precede glacier terminus retreat. This relationship is particularly apparent in a subset of glaciers where terminus advance followed pro-

longed periods of subsurface temperature decline, indicating a potential reduction in basal melt linked to reduced oceanic thermal forcing. An example is Cosgrove Glacier, which exhibited a continuous terminus advance between 2000-2023, albeit with small retreats in between (Fig. 4.21). The lagged average upper and mid-depth ocean temperatures continuously decrease between 2000-2023. The timing suggests a 5-year lagged response of the terminus to reduced subsurface heat content, consistent with the observed negative correlation. Notably, the temperatures at both ocean depth layers remained below 0°C during this period, with cooling at 109–446 m reaching nearly –1.5°C—conditions. This sustained cold phase may have allowed frontal advance. In contrast, regions such as Wilkes Land exhibit the opposite pattern, where incursions of warm modified Circumpolar Deep Water (mCDW) have been shown to enhance basal melt in marine-terminating glaciers—most notably at Totten Glacier, where variability in thermocline depth plays a key role in modulating basal melt rates (Miles et al., 2016; Hirano et al., 2023).

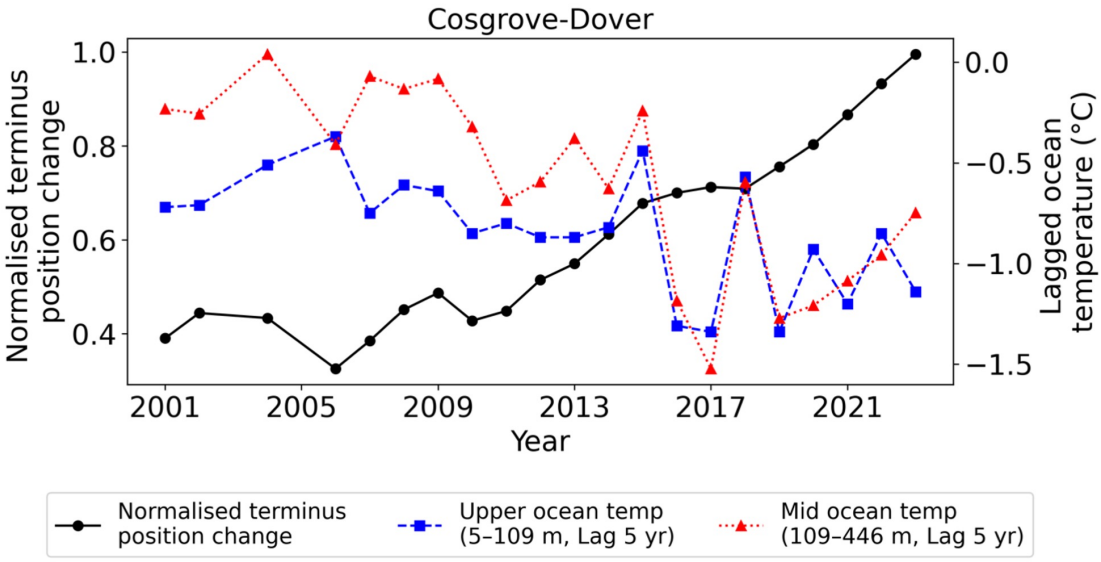

Figure 4.22: *Time series plot showing the relationship between lagged summer ocean temperatures and normalised terminus position change for Cosgrove-Dover Glacier.*

By contrast, Rayner Glacier—located within a partially confined embayment exhibited a moderate but positive correlation with SIC and a strong negative correlation with subsurface ocean temperatures. The glacier experienced episodic calving events, often preceded by rift formation, which may have been thermally precondi-

tioned by prolonged exposure to warm subsurface waters. However, post-calving, the retention of fast ice and mélange appeared to trap calved icebergs at the terminus, temporarily stabilising the ice front by reducing frontal stress. This suggests that warm ocean conditions may act not through continuous melt but by initiating rift propagation and weakening the structural integrity of the terminus over time, a mechanism observed elsewhere on the AIS (Massom et al., 2018; Miles et al., 2022). Within the same embayment, further glacier-specific variability is evident. Molle Glacier displays a significant positive correlation with subsurface temperatures across all three depth intervals, while neighbouring Rayner and Kichenside Glaciers exhibit significant negative correlations (Fig. 4.20). This implies that while Molle Glacier may respond to increased oceanic heat with terminus advance—potentially due to stress rebalancing or ice tongue extension—Rayner and Kichenside retreat under the same thermal conditions. These divergent responses within a shared oceanographic context point to a dominant role for local topography, grounding zone configuration, or basal conditions in governing glacier sensitivity.

In summary, glaciers within the same region exhibited asynchronous behaviour in response to different climatic drivers. For some, sea ice concentration was the main factor influencing retreat and advance, while others were more affected by subsurface ocean temperatures. In some glaciers, seasonal sea ice delayed calving, while consistently low sea ice often triggered earlier calving. Seasonal sea ice or mélange removal also sped up rift propagation, causing more frequent calving. Glaciers with consistent advance were often stabilized by the continuous presence of sea ice or mélange in rift cavities. Although the absence of sea ice does not directly cause calving, it weakens glacier termini, making calving more likely. These varied responses highlight the complex interactions between climatic factors and the importance of local glacier-specific and topographic conditions in shaping glacier dynamics.

4.7 Conclusion

This chapter has provided a detailed, multi-decadal assessment of terminus position changes for 44 marine-terminating glaciers in Enderby Land and Kemp Land, East

Antarctica, between the 1970s and 2023. A key finding is the overall stability and prevalent glacier advance in these regions, in notable contrast to the dynamic retreat observed in other sectors of Antarctica and Greenland.

Across the full record, glaciers showed nearly half (41%) experiencing a net advance and the remainder modest net retreat (59%). Following the epoch 1970s–1988 when retreat was predominant (61%), advance became widespread in the next epoch (1988–2000); 68% of glaciers) and persisted for many glaciers into 2000–2010. Even in the most recent epoch (2010–2023) 57% of glaciers continued to advance, and regional median rates remained low in magnitude. Individual glaciers displayed a spectrum of behaviours (e.g. steady multi-kilometre advance at Wilma–Robert–Downer; alternating phases at Rayner; persistent modest retreat at Omega and Campbell), yet these variations do not aggregate to a coherent regional retreat trend.

Upper (5–109 m) and mid depth (109–446 m) summer subsurface ocean temperatures exhibited multi decadal cooling from the late 1970s through 2010–2013, with values remaining below 0°C in the most recent epoch. Deeper (446–967 m) layers were generally slightly above 0°C but also cooled before a modest recent rise. Summertime sea ice concentration remained high in Enderby Land (decadal means = 50–59%) and increased in Kemp Land (33% to mid 40%), while summer sea ice extent increased through 2000–2010 before a modest reduction. These conditions represent a thermally conservative environment that limits oceanic heat delivery to glacier termini.

Statistically significant correlations were confined to (i) positive associations between higher summer sea ice concentration (and, regionally, extent) and subsequent (1–2 year lag) terminus advance for a subset of glaciers, and (ii) negative associations between warmer subsurface ocean temperatures—particularly at 5–109 m (5 year lag)—and subsequent retreat or reduced advance. Many glaciers showed weak or non significant correlations across all tested forcings, underscoring that external drivers exert heterogeneous influence and that no single forcing uniformly governs regional terminus behaviour.

Near surface summer air temperatures remained substantially below 0 °C (mean = –11.4°C in Enderby, –5.9°C in Kemp), with very few positive degree days recorded. Correlations between terminus change and air temperature or positive degree days were weak and not statistically significant, indicating negligible direct atmospheric melt influence on frontal positions over the study period.

Taken together, these results depict glacier systems that have operated within comparatively stable environmental envelopes over five decades. The predominance of cold subsurface waters in the upper and mid layers, combined with persistently substantial sea ice cover and a lack of appreciable surface melt, appears sufficient to maintain a slow multi-decadal advance.

This regional stability provides a useful counterpoint to rapidly evolving marine outlet systems elsewhere (e.g. WAIS, APIS, GrIS and Wilkes Land in EAIS) and highlights the importance of spatially resolved analyses: identical large-scale climatic trends do not necessitate uniform dynamic response across the Antarctic margin. The findings also illustrate the value of incorporating temporal lags when evaluating ocean–glacier linkages; immediate contemporaneous correlations would have understated the influence of antecedent ocean and sea ice states.

CHAPTER 5

The Evolution of Wilma-Robert-Downer Glacier system in East Antarctica and its potential drivers between 1970s and 2024.

Sharma, A., Stokes, C. R., & Jamieson, S. S. R. (2025). The Dynamic evolution of Wilma-Robert-Downer Glacier, East Antarctica, and its potential drivers [To be submitted]

5.1 Abstract

This chapter investigates the dynamic evolution of the Wilma-Robert-Downer (WRD) Glacier system in Kemp Land, East Antarctica, between the 1970s and 2024. Using a multi-decadal satellite record, changes in terminus position, ice velocity, surface elevation, and grounding line location are analysed to evaluate the long-term stability of the glacier system and the potential influence of oceanic, atmospheric, and glaciological drivers. The WRD glacier system experienced two major calving events (1991 and 2003) and one smaller event (2014), each associated with the progressive propagation of rifts. Despite these events, lateral pinning points provided mechanical stability, preventing significant inland retreat and enabling a sustained advance of the ice front, which reached its maximum observed extent in 2024. Post-calving advance was further supported by the presence of sea ice and mélange within rift cavities, which likely exerted a buttressing effect. Ice velocity trends show contrasting behaviour across the system: the floating ice tongue experienced a modest deceleration between 2010 and 2021, while velocities at Robert Glacier's grounding line increased by over 20% during the same period. These trends reflect the influence of combination of lateral flow constriction, structural rifting, and subglacial topographic controls. Surface elevation records ∼20 km inland from the grounding line at both Wilma and Robert Glaciers revealed prolonged thinning from the mid-1980s to the mid-2010s. This thinning was likely driven by basal melt resulting from relatively warm ocean waters, as temperatures at the mid-depth (109–446 m) and deeper-depth (446–967 m) layers frequently exceeded 0°C during this period. However, thinning slowed after 2013 at Wilma and 2016 at Robert and was accompanied by localised thickening on the floating ice tongue between 2003 and 2019, potentially linked to rift-induced flow deceleration and colder ocean temperatures. Despite these dynamic and surface changes, the grounding line positions remained stable over the multi-decadal study period, underscoring the resilience of the WRD Glacier system. These findings highlight the complex interplay between rift dynamics, oceanic conditions, and mechanical stabilisation processes, offering important insights into glacier stability and ice–ocean interactions at WRD.

5.2 Introduction

The stability and behaviour of Antarctic ice shelves and glaciers exert an important influence on the mass balance of the AIS, with direct implications for global mean sea-level rise. Over the past four decades, the AIS has been losing mass, contributing approximately 14 ± 2.0 mm to sea-level rise between 1979 and 2017, with mass loss focussed on the West Antarctic Ice Sheet (Rignot et al., 2019). Ice shelves and floating ice tongues act as critical stabilising features, buttressing the flow of grounded ice and thereby slowing its discharge into the ocean (Miles et al. 2024). When ice shelves undergo shortening or thinning, whether from calving events or thinning due to basal melting, the grounded ice behind them can accelerate—a process known as debuttressing. This increase in ice discharge can add to rates of sea-level rise, and numerical models suggest that debuttressing will be a major factor in determining the timing and magnitude of future sea-level rise from Antarctica (Golledge et al., 2015; DeConto & Pollard, 2016; Gudmundsson et al., 2019).

The retreat of ice shelves and floating ice tongues has primarily been linked to atmospheric and oceanic warming. For example, atmospheric warming, ocean swell, and surface meltwater-induced flexure and hydrofracture contributed to the collapse of Larsen B Ice Shelf in the Antarctic Peninsula (Doake & Vaughan, 1991; Scambos et al., 2003; Banwell et al., 2013, 2019; Banwell and MacAyeal, 2015). Similarly, basal melting driven by the intrusion of warm mCDW has led to substantial ice losses in the WAIS, particularly at Pine Island and Thwaites Glaciers (Shepherd et al., 2004; Joughin et al., 2014; Rignot et al., 2014; Scambos et al., 2017). In the EAIS, the loss of sea ice, influenced by increased mCDW intrusion, has contributed to substantial mass loss in Wilkes Land (Miles et al., 2016). Glaciers such as Totten and Moscow University have experienced notable ice loss and grounding line retreat, accompanied by high thinning rates and accelerated ice flow (Miles et al., 2017, 2018; Li et al., 2022; Pelle et al., 2024). Further round the East Antarctic coast, the disintegration of Porpoise Bay and Voyeykoyev Ice Shelves has similarly been linked to the loss of multi-year sea ice. In addition, structural weakening via rifting has

further exacerbated glacier retreat draining the EAIS, as seen in the retreat of the Mertz Glacier Tongue (Massom et al., 2015; Miles et al., 2020) and calving events at the Amery Ice Shelf.

In contrast, some outlet glaciers draining the EAIS have shown relative stability over recent decades evidenced by ice thickening (Smith et al., 2020), advance of glacier termini (Miles et al., 2016; Baumhoer et al., 2021) and slowdown (Miles et al., 2023). For example, Jutulstraumen in DML has maintained steady velocity and grounding line positions, even after episodes of Warm Deep Water (WDW) intrusion between 2016 and 2019 (Miles et al., 2016; Lauber et al., 2023; Sharma et al., 2025). Additionally, Shirase Glacier has shown a slowing and thickening trend, likely due to strengthened alongshore winds that limit the inflow of warm mCDW into Lützow-Holm Bay (Miles et al., 2023). Stabilising features such as ice rises and pinning points within the ice shelf can also provide vital structural support, maintaining glacier flow and grounding the floating ice tongue on stable bedrock configurations (Franke et al., 2021; Braga et al., 2023). However, Miles et al. (2024) highlighted that some of the pinning points across the AIS are reducing in size which could make the ice shelves and floating ice tongues vulnerable to calving events. Although recent studies have advanced our understanding of East Antarctic glaciers, significant knowledge gaps persist, especially at the scale of individual glaciers. Consequently, it remains unclear whether, and to what extent, climatic and non-climatic drivers influence glacier dynamics across the EAIS.

This study focuses on the Wilma-Robert-Downer (WRD) Glacier system in Kemp Land, East Antarctica—one of the relatively understudied glaciers within the EAIS. The WRD Glacier exhibits distinctive glaciological characteristics in the region and represents the largest outlet glacier system in Kemp Land. Recent work by Miles et al. (2022) suggested a potential increase in ice discharge of $\sim 6 \pm 5\%$ between 2000 and 2018 for this glacier system, although the associated uncertainty is nearly as large as the signal itself. On a broader scale, total ice discharge from Kemp Land was estimated at 17 ± 4 Gt yr^{-1} in 2008 and 18 ± 3 Gt yr^{-1} in 2015 (Gardner et al., 2018), indicating limited regional flux change over that period. The WRD

Glacier system, which includes a floating ice tongue extending into the ocean, lies in a region where the controls on glacier dynamics remain poorly understood. A range of processes—such as oceanic forcing, rift formation, and the presence of sea ice or mélange—are known to influence the behaviour of other outlet glaciers in Antarctica (Bassis et al., 2008; Durand et al., 2015; Alley et al., 2015; Miles et al., 2016, 2017; Massom et al., 2018; Arthur et al., 2021; Gomez-Fell et al., 2022; Poinelli et al., 2023; Sun et al., 2023), but their relevance to the WRD system has not been comprehensively assessed. This study aims to build upon the findings of the previous chapter by using higher-resolution spatial and temporal datasets to investigate the long-term dynamic behaviour of the Wilma-Robert-Downer (WRD) Glacier system. The focus here is on understanding the underlying oceanic, climatic, and glaciological processes that may be driving—or resisting—change at WRD glacier system. In particular, this chapter seeks to better constrain the mechanisms responsible for WRD's apparent stability. Hereafter, the term WRD is used to refer collectively to the Wilma–Robert–Downer Glacier system, including its ice front and catchment. When discussing individual glaciers within the system, they are referred to by their specific names.

To address the aim, the following research questions are addressed:

• How has the terminus position of the WRD changed over the past five decades (1970s-2024)?

- To answer this question, the terminus of the WRD will be mapped using a range of satellite imagery (e.g. Landsat) and the terminus position changes will be quantified from 1973 to 2024.

• What are the patterns and magnitudes of ice velocity variations, surface elevation and grounding line position changes in this system?

- To address this research question, ice velocity trends will be analysed using ITS_LIVE and ENVEO datasets, while surface elevation changes will be assessed using data from Schröder et al. (2019), Smith et al. (2020), and Nilsson et al. (2022). Grounding line positions will be mapped from satellite imagery, and supplemented with existing datasets to evaluate temporal changes in grounding line location.

• To what extent can observed changes be linked to atmospheric and oceanic variability, or internal glaciological processes?

- To address this question, the influence of environmental drivers—such as subsurface ocean temperature anomalies and sea ice concentration—as well as non-climatic factors, including rifting activity, will be examined. This will be achieved by analysing regional environmental datasets and comparing them with the results from the preceding research questions.

5.3 Data and methods

To investigate the dynamic behaviour of the WRD Glacier system, this chapter combines a range of remote sensing and environmental datasets to analyse changes in terminus position, ice velocity, surface elevation, and grounding line location. While the analysis of sea ice concentration, subsurface ocean temperature, and air temperature builds on the datasets introduced in Chapter 4, this chapter extends the assessment through the use of additional satellite-derived products. These include high-resolution velocity mosaics (ITS_LIVE and ENVEO), multi-mission surface elevation datasets (Schröder et al., 2019; Nilsson et al., 2022; Smith et al., 2020), and manually delineated grounding line positions from optical and DInSAR imagery. Together, these datasets support a comprehensive evaluation of glacier dynamics and potential forcing mechanisms across multi-decadal timescales.

5.3.1 Remote sensing of glacier characteristics

5.3.1.1 Ice front mapping

To investigate glacier extent from 1973 to 2024, a time series of ice-front positions were created between 1973 and 2024 using a variety of different sources: Landsat-1 imagery from 1973, Landsat-4 imagery from 1988, the RADARSAT RAMP mosaic from 1997 (Jezek et al., 2013), ASTER imagery for 2004 to 2006 and Landsat 7-8/9 imagery from 2000 to 2024, with the spatial resolution of the satellite data ranging from 15 to 250 m (Table 4.1). In each case, the ice front of WRD was

manually digitised (Fig. 5.1). The mapping approach followed the same protocol described in Chapter 4, including visual differentiation between the glacier terminus and sea ice or mélange based on texture, brightness, and outline geometry. Glacier termini typically display jagged outlines and elevated relief relative to adjacent sea ice, which was used to guide consistent delineation across the satellite images (Fig. 5.1). Errors associated with this mapping arise from manual digitisation and co-registration of satellite images, quantified as the offset between stable features in image pairs, typically estimated at 1 pixel, and the manual digitisation of the ice front estimated at 0.5 pixels (Table 4.1, Hill et al., 2018; Howat et al., 2012; Moon & Joughin, 2008).

5.3.1.2 Rift activity

To assess the evolution of the rift system, a time series of high-resolution satellite images from 1988 to 2024 was compiled. It should be noted that due to a large temporal gap in image availability between 1973 and 1988, rifts visible in the 1973 imagery were not mapped. This dataset enabled detailed mapping of rift initiation, propagation, and widening across the WRD floating ice tongue. All measurements were standardised to reflect rift conditions in February of each year; where February imagery was unavailable, images from January or March were used.

Following the methodology of Fricker et al. (2005), rift lengths were measured from a consistent initiation point at one end of the rift to its discernible tip (Fig. 6.3). The rift tip was defined as the first clearly identifiable pixel along the rift path—where the rift occupies enough of the pixel area to produce distinct contrast with the surrounding ice (Fricker et al., 2005; Walker et al., 2015; Holt & Glasser, 2022). Measurements were taken along the central axis of each rift, starting from its origin near the grounded ice at the eastern margin and extending westward to the visible rift tip.

Individual rifts were colour-coded and consistently tracked across the image sequence to document temporal changes in their geometry—such as length, width, and connectivity—as well as their evolving spatial extent in the years leading up to

major calving events. These rifts were observed to progressively lengthen and widen over time, including W6 (purple), W7 (cyan), W8 (green), W9 (yellow), W10 (dark blue), W11 (blue), W12 (orange), W13 (pink), and W14 (light blue). In addition to these principal rifts, fracture traces that extended from the rifts—identified as narrow surface features or troughs lacking a distinct opening, possibly filled with snow—were also mapped. The propagation distances and widths of the rifts were measured using georeferenced imagery in QGIS.

5.3.1.3 Ice velocity

For 2000–2018 14 annual average ice velocity mosaics from the ITS_LIVE dataset were used which cover WRD Glacier (Gardner et al., 2018). These velocity mosaics are derived from a combination of Landsat 4, -5, -7 and -8 with the use of auto-RIFT feature tracking, and with each velocity mosaic having a spatial resolution of 240 m (Gardner et al., 2019). In addition, ENVEO (ENVEO et al., 2021) velocity mosaics were also used to extract velocity between 2019 and 2021. The ENVEO velocity mosaics are derived from repeat-pass Sentinel-1 Synthetic Aperture Radar (SAR) datasets using feature-tracking and are available for each month between 2019 and 2021 at a spatial resolution of 200 m. These monthly mosaics were averaged over each 12-month period to generate annual velocity mosaics for 2019, 2020, and 2021 to compare with the ITS_LIVE annual velocity mosaics. Velocities were extracted from the four locations up-ice tongue, down-ice tongue, and the grounding lines of both Wilma and Robert Glaciers (shown in Figure 5.1) to capture spatial variations in flow dynamics across the floating tongue and near the glacier grounding zones. Following Miles et al.et al. (2018) and Picton et al.et al. (2023), the mean annual velocities were calculated by averaging all available data within each sampling box, provided that data coverage of more than 25% was available. As a result, there was limited data coverage prior to 2000. Error estimates were provided at a pixel level for both datasets (Gardner et al., 2018, 2019; ENVEO et al., 2021). The annual error values were then calculated by averaging the errors within each sample box, which range from ± 5 to ± 300 m yr^{-1}.

5.3.1.4 Grounded surface elevation changes

Grounded surface elevation change time series were extracted from the dataset presented in Schröder et al. (2019) from around 20 km inland of the grounding line (Fig. 5.1). This location was chosen because it lies near the grounded portion of the glacier, where changes in thickness are more likely to reflect upstream responses to ice flow variability and mass balance anomalies. This multi-mission dataset spans 1978 to 2017 and contains data from a variety of satellites (e.g. ERS-1/2, Geosat, Seasat, Envisat, ICESat and CrysoSat-2). Grounded ice surface elevation changes from dataset provided by Nilsson et al. (2022) were also extracted from the same location. This dataset spans 1985 to 2020. To allow a more direct comparison between the datasets, the SEC measurements from Schröder et al. (2019) were recalculated relative to December 2013, aligning with the reference year used in Nilsson et al. (2022). The two datasets were analysed from April 1992 onwards, as it was the earliest common data availability month at all four sample locations. The accompanying uncertainty estimates described in Schröder et al. (2019) and Nilsson et al. (2022) were used, which are between 0.2 and 1.7 m yr^{-1}. In addition, surface elevation changes over the floating ice tongue were assessed using the dataset provided by Smith et al. (2020), which was derived from ICESat and ICESat-2 observations spanning 2003 to 2019. This dataset has a horizontal resolution of 5 km, with associated uncertainties ranging from ± 0.03 to ± 0.6 m yr^{-1}.

Table 5.1: Satellite imagery used for glacier terminus mapping and associated error estimates.

Date	**Satellite**	**Resolution (m)**	**Co-reg. error (m)**	**Mapping error (m)**	**Total error (m yr^{-1})**
02/02/1973	Landsat-1- Band 4	60	60	30	4.5
24/01/1988	Landsat-4- Band 4	30			
15/03/1989	Landsat-4- Band 4	30	30	15	36.7
12/02/1990	Landsat-4- Band 4	30			
24/01/1991	Landsat-4- Band 4	30	30	15	35.4
23/02/1991	Landsat-4- Band 4	30			
01/02/2000	Landsat-7- Band 8	15	30	15	3.7
19/02/2001	Landsat-7- Band 8	15			
05/01/2002	Landsat-7- Band 8	15	15	7.5	19.1
16/02/2003	Landsat-7- Band 8	15			
15/01/2005	Landsat-7- Band 8	15	15	7.5	8.8
23/01/2006	Landsat-7- Band 8	15			
13/02/2007	Landsat-7- Band 8	15	15	7.5	15.9
16/02/2008	Landsat-7- Band 8	15			
06/03/2009	Landsat-7- Band 8	15	15	7.5	15.9
12/02/2010	Landsat-7- Band 8	15			
08/02/2011	Landsat-7- Band 8	15	15	7.5	17.0
14/03/2012	Landsat-7- Band 8	15			
11/02/2013	Landsat-8- Band 8	15	15	7.5	18.3
08/02/2014	Landsat-8- Band 8	15			
18/02/2015	Landsat-8- Band 8	15	15	7.5	16.3
08/03/2016	Landsat-8- Band 8	15			
16/02/2017	Landsat-8- Band 8	15	15	7.5	17.7
03/03/2018	Landsat-8- Band 8	15			
19/02/2019	Landsat-8- Band 8	15	15	7.5	17.3
09/02/2020	Landsat-8- Band 8	15			
18/02/2021	Landsat-8- Band 8	15	15	7.5	16.3
14/02/2022	Landsat-8- Band 8	15			
17/02/2023	Landsat-8- Band 8	15	15	7.5	16.6
19/02/2024	Landsat-9- Band 8	15			

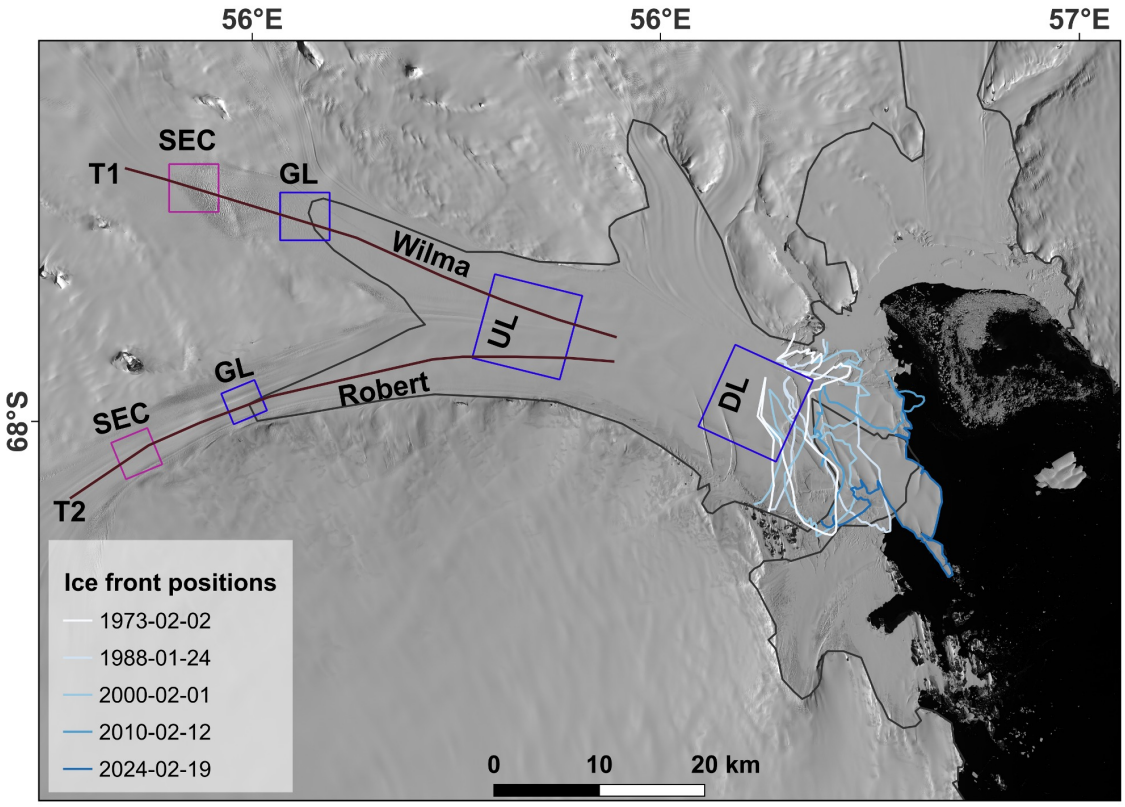

Figure 5.1: *A Landsat-9 image from February 2024 depicting the Wilma-Robert-Downer Glacier ice tongue. Ice-front positions from 1973, 1988, 2000, 2010, and 2024 are overlaid, along with transects T1 (Wilma) and T2 (Robert) used to extract ice speed and surface elevation profiles. The boxes labelled SEC indicate the areas where surface elevation change time series for Wilma and Robert are shown. Locations of velocity time series are marked as GL (grounding line), UL (up-ice tongue), and DL (down-ice tongue). The black line represents the MEaSUREs grounding line (Rignot et al. 2017).*

5.3.1.5 Grounding line position changes

Grounding line (GL) positions have been previously derived using a range of remote sensing techniques, though typically limited to discrete time periods. In this study, several previously-published GL datasets were utilised to support temporal analysis. The Antarctic Surface Accumulation and Ice Discharge (ASAID)(Bindschadler and Choi, 2011) grounding line dataset was produced through the integration of photoclinometry applied to optical satellite imagery (primarily Landsat 7 ETM+), surface elevation profiles obtained from ICESat, and manual interpretation of image features. In this dataset, the grounding line positions were digitised using Landsat 7 ETM+ imagery acquired between 1999 and 2003, based on the identification of changes in image brightness corresponding to the break-in-slope (I_b)—a commonly used proxy for the grounding line (Fig. 5.1c). The average positional uncertainty associated with the ASAID grounding line product was estimated at ±502 m (Bindschadler et al., 2011). The Mosaic of Antarctica (MOA) dataset was previously used to delineate the seaward Ib on enhanced MOA surface images (2004–2009), with an uncertainty of ±250 m (Scambos et al., 2007; Harran et al., 2005, 2014). Differential Interferometric Synthetic Aperture Radar (DInSAR) data were also used in the Making Earth Science Data Records for Use in Research Environments (MEaSUREs) Rignot et al., 2016). Similarly, the Antarctic Ice Sheet Climate Change Initiative (AIS CCI) derived flexure points (F) denoting the grounding line from DInSAR data (1996–2020). Mohajerani et al. (2021) used neural networks to delineate grounding lines for 2018, also based on DInSAR data, with an uncertainty of ±232 m.

To improve temporal resolution of GL change detection, grounding line positions were also manually delineated in this study from Landsat 4–8 imagery acquired during austral summers (October to April) between 1990 and 2022. Our approach follows the methods established by Fricker et al. (2009) and Christie et al. (2016), which apply optical image interpretation to infer GL proxies. Due to the limitations of optical sensors in directly identifying the "true" grounding line (G), proxy features were mapped such as the break-in-slope (I_b) and, where visible, the local

elevation minimum (Im)—the latter identified as a shadow-like brightness transition in the imagery (Fricker and Padman, 2006; Fricker et al., 2009; Bindschadler et al., 2011; Christie et al., 2016, 2018). These features were manually digitised using georeferenced, cloud-free Landsat scenes (see Fig. 5.11a). To quantify grounding line migration, the box method was applied (Moon and Joughin, 2008), enabling calculation of the average grounding line position change across the glacier. This method provides a robust, representative metric of grounding line change along the glacier width. Based on previous evaluations (Bindschadler et al., 2011; Christie et al., 2016), positional uncertainty was estimated for the manually-derived grounding line locations at ±100m. It was important to note that the grounding line does not always represent a sharply defined boundary but instead often spans a grounding zone, a transitional region several hundred meters wide where the ice sheet gradually loses contact with the underlying bed due to tidal flexure and hydrostatic adjustment. Within this zone, various proxies (e.g., I_b, I_m, and F) may capture different points depending on the sensor type and observation method used (Fig. 5.2).

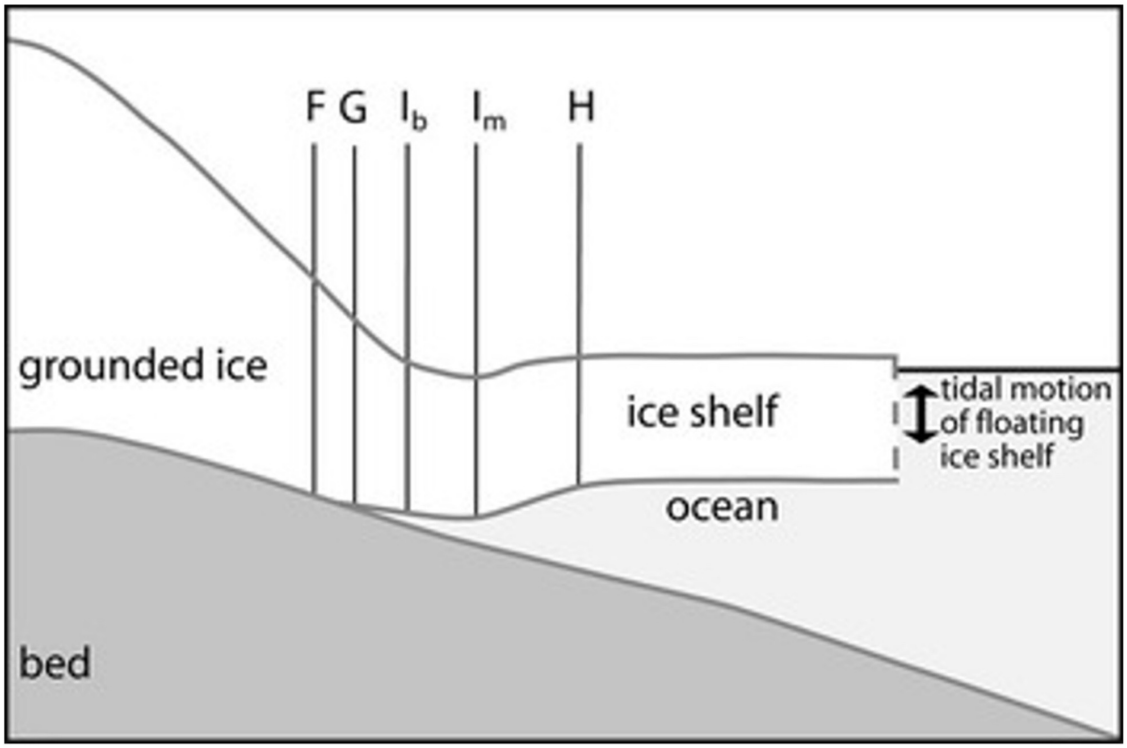

Figure 5.2: *Schematic illustrating the structure of the ice shelf grounding zone, adapted from Fricker et al. 2009. Point G denotes the true grounding line, while Point F marks the landward extent of tidal flexure. Point H represents the seaward limit of tidal flexure and the inshore boundary of hydrostatic equilibrium, and Point I indicates the location of the surface slope break.*

5.3.2 Atmospheric and oceanic data

5.3.2.1 Sea ice concentration

Monthly mean sea ice concentrations were obtained from monthly imagery from SMMR, SSM/I and SSMIS passive microwave instruments carried on the Nimbus-7 satellite between 1978 and 2023 acquired from `https://nsidc.org/data/nsidc-0051/versions/2`. The spatial resolution of the dataset was 25 km. The data were extracted from a 25×25 km grid cell located immediately offshore of the WRD Glacier terminus, similar to the method explained in section 4.3.2 and as shown in Figure 5.3. Average annual and decadal summer mean sea ice concentrations were calculated from monthly mean sea ice concentration, where summer was from December to March. This seasonal window was chosen because sea ice concentration typically reaches its minimum between end of February to March. Calculating both

annual and decadal averages enables the identification of short-term variability as well as longer-term trends in sea ice conditions that may influence grounding line and terminus behaviour at local to regional scales.

5.3.2.2 Air temperatures

To understand the potential influence of air temperatures on glacier dynamics, it was essential to assess long-term trends in near-surface atmospheric conditions. The air temperature analysis was grounded in its role as a primary driver of surface melt processes, which contribute to mass loss, firn saturation, and hydrofracture-related ice shelf weakening (Zwally et al., 2002; Joughin et al., 2008; Langley et al., 2016; Wille et al. 2019; Lai et al., 2020). While direct evidence of surface melt on the WRD Glacier is currently limited, the documented presence of supraglacial lakes in the adjacent coastal regions of Kemp Land and Enderby Land highlights the glacier's potential vulnerability under continued atmospheric warming (Stokes et al., 2019; Arthur et al., 2020; Moussavi et al., 2020). Therefore, the monthly average 2 m near-surface air temperature from the European Centre for Medium-Range Weather Forecasts ERA5 reanalysis were used, with a spatial resolution of 0.25 degree ($\sim$ 31 km). The data were extracted using a 10 x 10 km grid cell located over the WRD ice tongue. From these records, the average summer (December to February) mean air temperatures were calculated on both annual and decadal timescales.

5.3.2.3 Wind speed and direction

We use mean monthly 10-meter zonal (U) and meridional (V) wind components from the ERA5 reanalysis dataset (Hersbach et al., 2020), extracted at a spatial resolution of 30 km for the period 1979–2021. ERA5 is the European Centre for Medium-Range Weather Forecasts' fifth-generation global atmospheric reanalysis, created by assimilating a wide range of in-situ and satellite observations into a numerical weather-prediction model to produce a spatially and temporally continuous record of past climate conditions. The data are taken from a coastal region approximately 140 $\times$ 140 km in size (Box A; Fig. 5.1), offshore of WRD ice front. This area is chosen because it encapsulates the conditions that would be expected to impact

the terminus of the glacier. To derive the alongshore easterly wind component, the wind vector was calculated using an alongshore orientation of 80° from true north, following the equation:

$$A = W \cos(\theta - 80) \tag{5.1}$$

where W represents the wind speed and θ is the wind direction.

5.3.2.4 Subsurface ocean temperatures

To assess the potential influence of oceanic conditions on glacier dynamics, particularly at the ice front and beneath the floating ice tongue, the temporal variations in subsurface ocean temperature were analysed (Miles et al., 2016; Hirano et al., 2020; Adusumilli et al., 2020). These data provide insight into ocean thermal forcing which may drive basal melting. Therefore, the EN4.0.2 subsurface ocean temperature objective analysis dataset, acquired from the UK Meteorological Office Hadley Centre (`www.metoffice.gov.uk/hadobs/en4/download-en4-0-2.html`) were extracted. This dataset has a spatial resolution of 1° × 1°, with data obtained from the WOD09, GTSPP, Argo, and ASBO collections. The data consists of 28 depth layers, but the ocean temperatures for depths between 5-109 m, 109-446 m and 446-967 m were averaged because these intervals represent distinct water masses with varying thermal properties and circulation dynamics that can differently impact glacier melting rates (Miles et al. 2016). The uppermost layer (5–109 m) typically captures surface-modified waters, while the intermediate (109–446 m) and deep (446–967 m) layers correspond to subsurface and continental shelf water masses, which can include relatively warm intrusions in some regions. The data from 25x25 km grid in front of the glacier between 1980 and 2023 were extracted (Fig. 5.3).

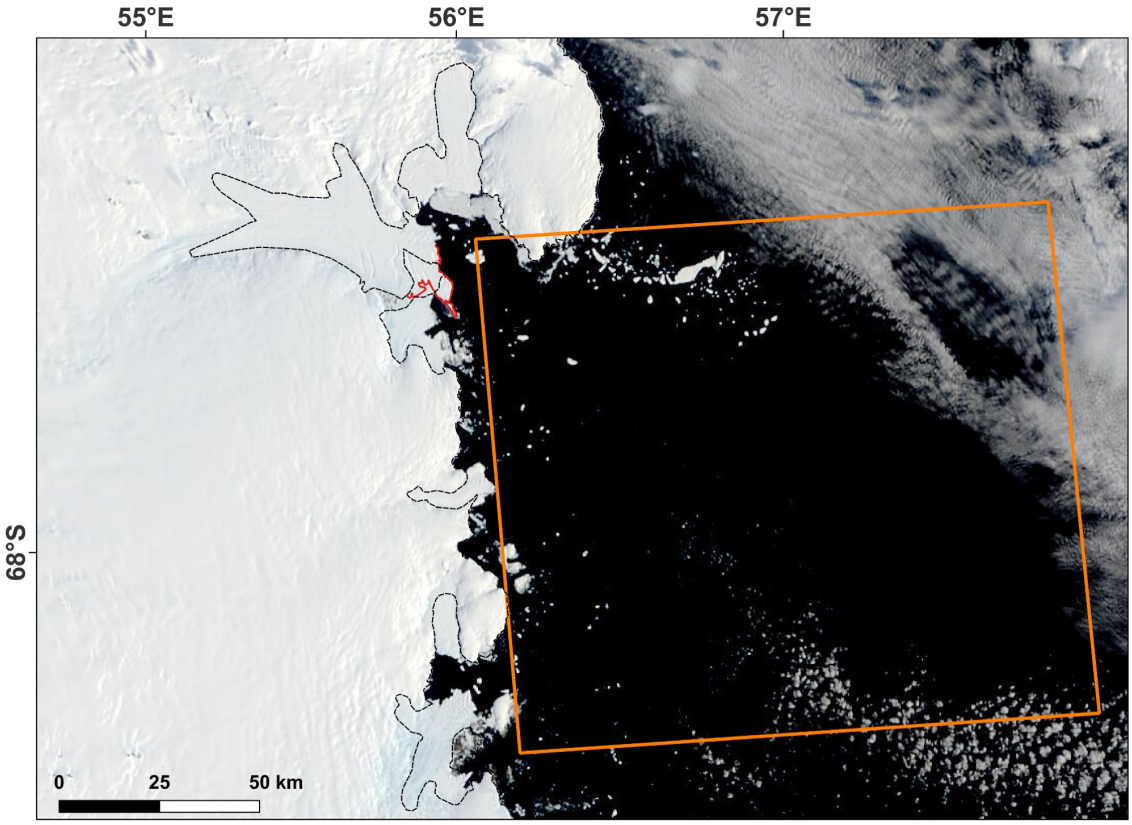

Figure 5.3: *The orange box represents the location from where sea ice concentration and ocean temperatures were extracted.*

5.4 Results

5.4.1 Ice front position change

The WRD ice tongue was mapped between 1973 and 2024 (Fig. 5.4). The ice tongue reached its maximum observed length in 2024, following a generally advancing trend over the past five decades. However, this long-term advance also included two discrete calving events. The first major calving event occurred in 1991, leading to the detachment of an iceberg measuring approximately 78 km^2 in area. This event marked the most substantial retreat of the Wilma ice tongue on record, with the ice front retreating by around 7 km, resulting in the minimum extent observed in the satellite record since 1973 (Fig. 5.4b, 5.5a). A second, smaller calving event occurred in 2003, involving the detachment of an iceberg approximately 40 km^2 in area, which caused a retreat of about 3 km at the ice front (Fig. 5.5c. 5.7, d). A

third minor calving event occurred in 2014, resulting in the loss of a small iceberg ($\sim$ 25 km^2). Despite this, the ice front experienced a near-continuous advance, with a mean rate of $\sim$ 500 m yr^{-1} between 2003 and 2024.. As of the most recent observations, the ice tongue has advanced approximately 5 km beyond its previous maximum extent in 1991 which was prior to the two calving events. Note that following the two calving events, minor calving of icebergs has occurred between 2004 and 2024 leading to a change in the shape of the ice front over the years, but not to any significant year-on-year ice front retreat. Despite episodic calving events in 1991, 2003, and 2014, the WRD ice tongue has exhibited a dominant long-term advancing trend, particularly after 2003, culminating in its maximum observed extent in 2024.

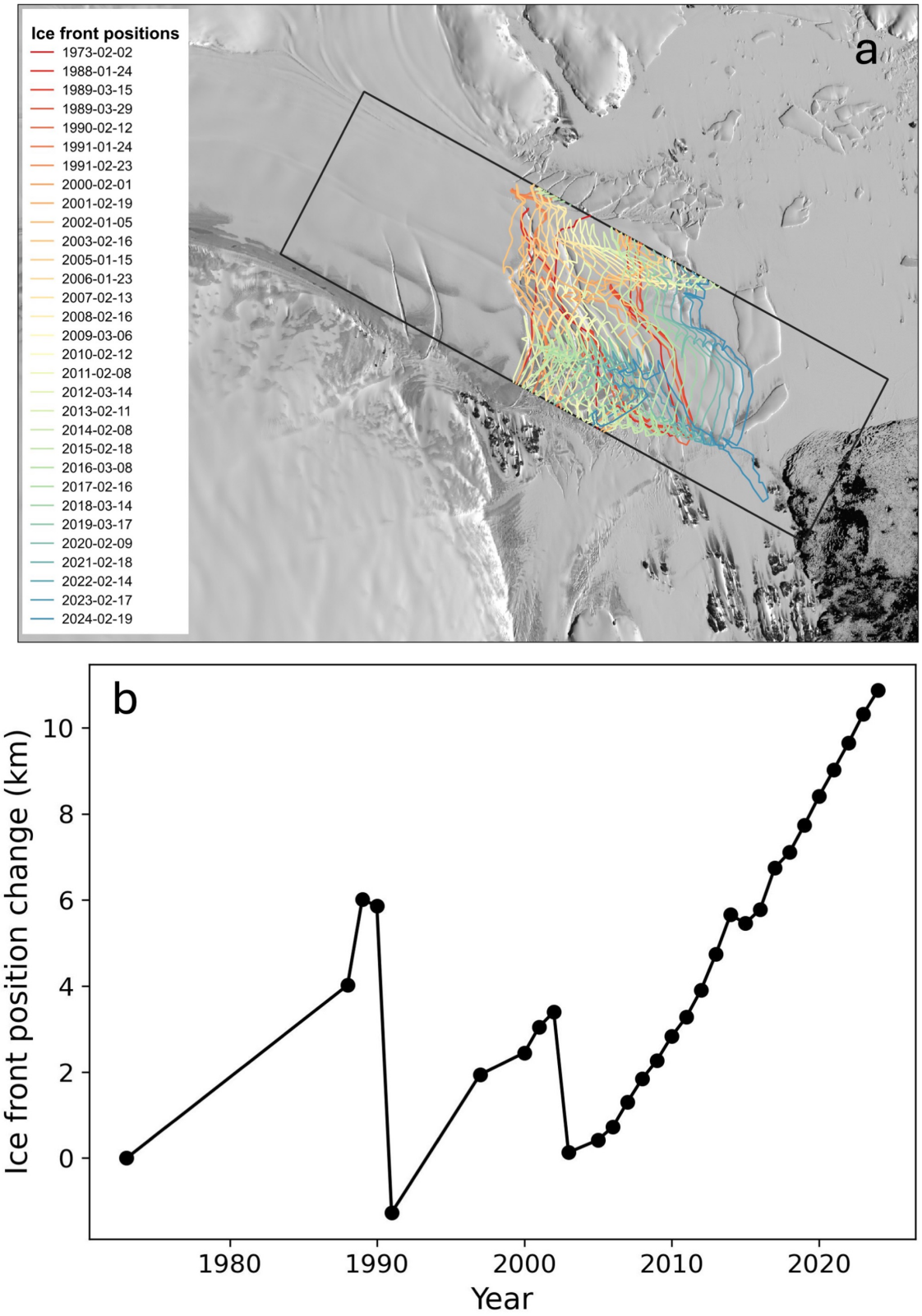

Figure 5.4: *(a) Mapped ice front position of WRD between 1973 and 2024. (b) Ice front position change of WRD during 1973–2024.*

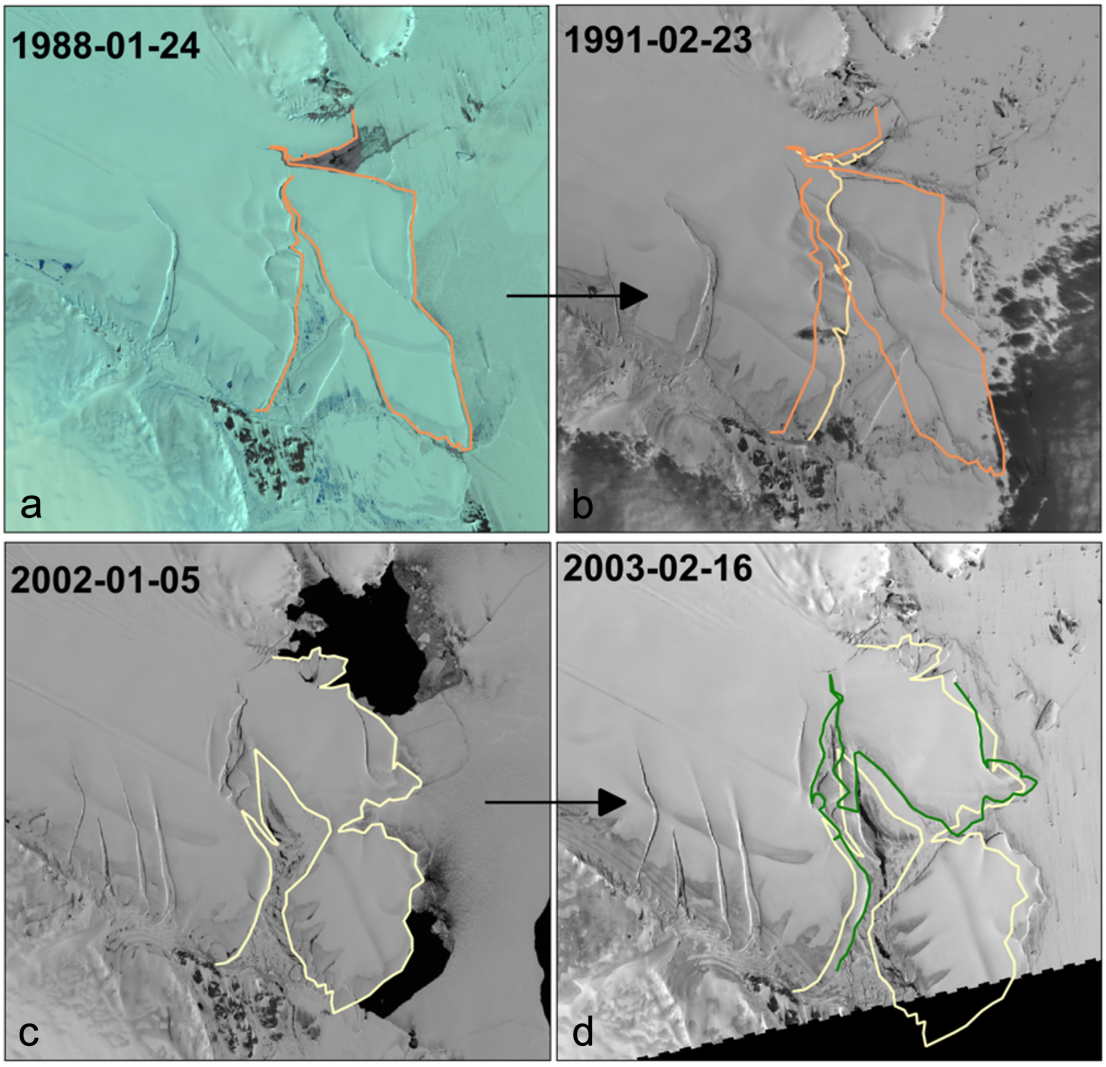

Figure 5.5: *Panels (a-b) shows the first major calving event since 1973 that occurred in 1991. Orange line represents the ice front on 24th January 1988 and yellow line represents the ice front on 23rd February 1991 after the calving occurred. Panel (c-d) shows the smaller calving event that occurred in 2003. Yellow line shows the ice front on 5th January 2002 and green line represents the ice front on 16th February 2003 when a part of the ice tongue calved off.*

5.4.2 Rifting activity

Between 1988 and 2024, the WRD ice tongue underwent progressive rift formation, propagation, and widening, with several rifts ultimately contributing to calving events (Fig.5.6). The spatial and temporal evolution of rifts highlights a pattern in which structural weakening through rift growth often preceded calving events.

Notably, three calving events—in 1991, 2003, and 2014—were each associated with the activation and expansion of specific rift systems (W1–W2, W4, W6). A notable feature of WRD rift development is the repeated formation of fractures in the same locations over multiple decades. For example, rifts W5, W11, and W12 all originated from the same zone along the eastern margin of the ice tongue. While some rifts, such as W6 and W10, showed sustained propagation and widening over time, others remained relatively stable (W8) or even declined in length (W9). The most actively evolving rift, W6, lengthened up to 14 km and widened by $\sim$ 2.3km between 2000 and 2024. Many of the rift cavities observed between 1988 and 2024 were partially or completely filled with sea ice/mélange.

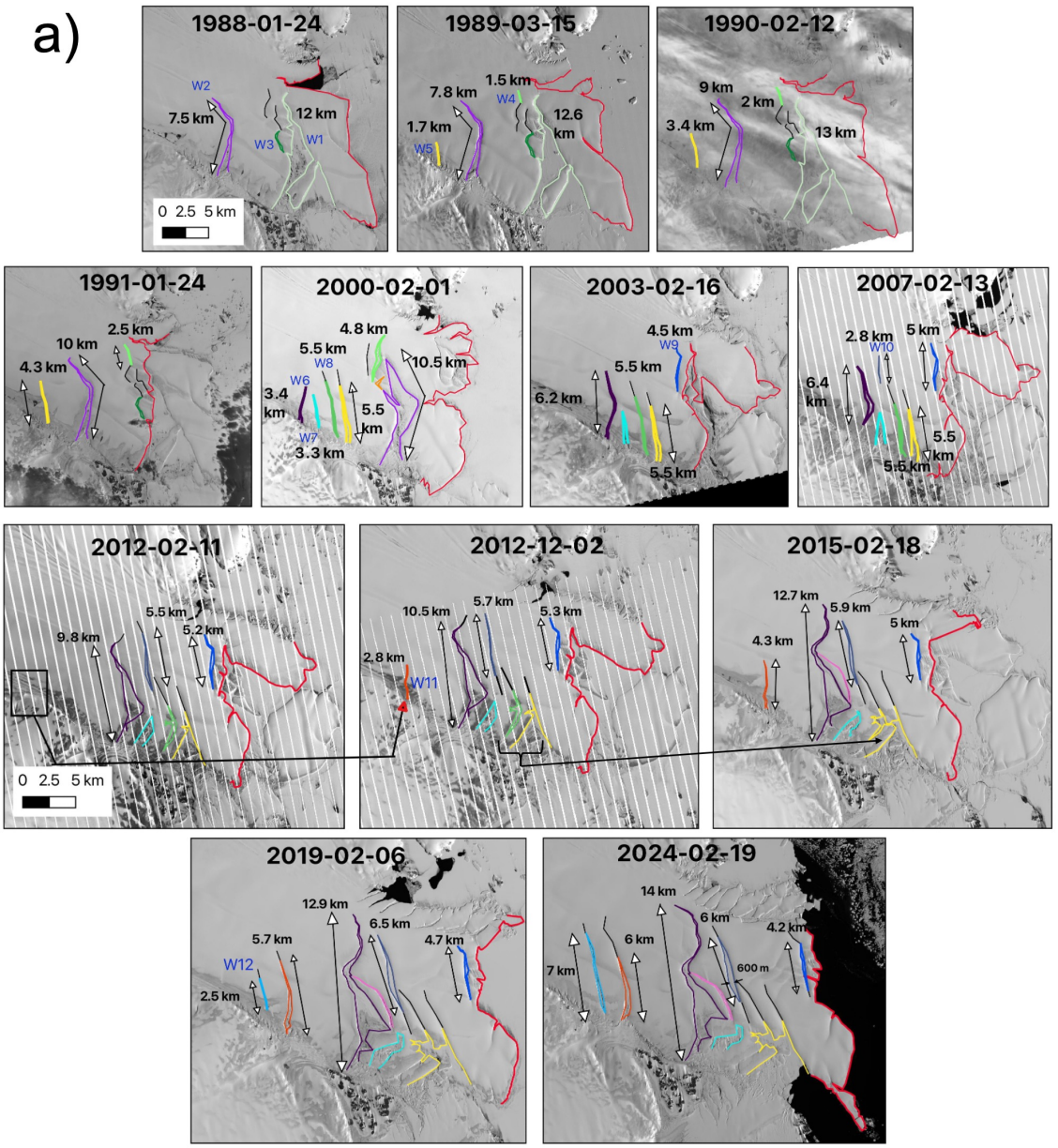
a)
1988-01-24
W2
7.5 km
12 km
W3
W1
0 2.5 5 km
1989-03-15
7.8 km
1.5 km
W4
12.6 km
1.7 km
W5
1990-02-12
9 km
2 km
3.4 km
13 km
1991-01-24
2.5 km
10 km
4.3 km
2000-02-01
4.8 km
5.5 km
W8
W6
10.5 km
3.4 km
5.5 km
W7
3.3 km
2003-02-16
4.5 km
W9
5.5 km
6.2 km
5.5 km
2007-02-13
2.8 km
W10
5 km
6.4 km
5.5 km
5.5 km
2012-02-11
5.5 km
9.8 km
5.2 km
0 2.5 5 km
2012-12-02
10.5 km
5.7 km
5.3 km
2.8 km
W11
2015-02-18
12.7 km
5.9 km
4.3 km
5 km
2019-02-06
12.9 km
6.5 km
5.7 km
4.7 km
W12
2.5 km
2024-02-19
14 km
6 km
4.2 km
6 km
7 km
600 m

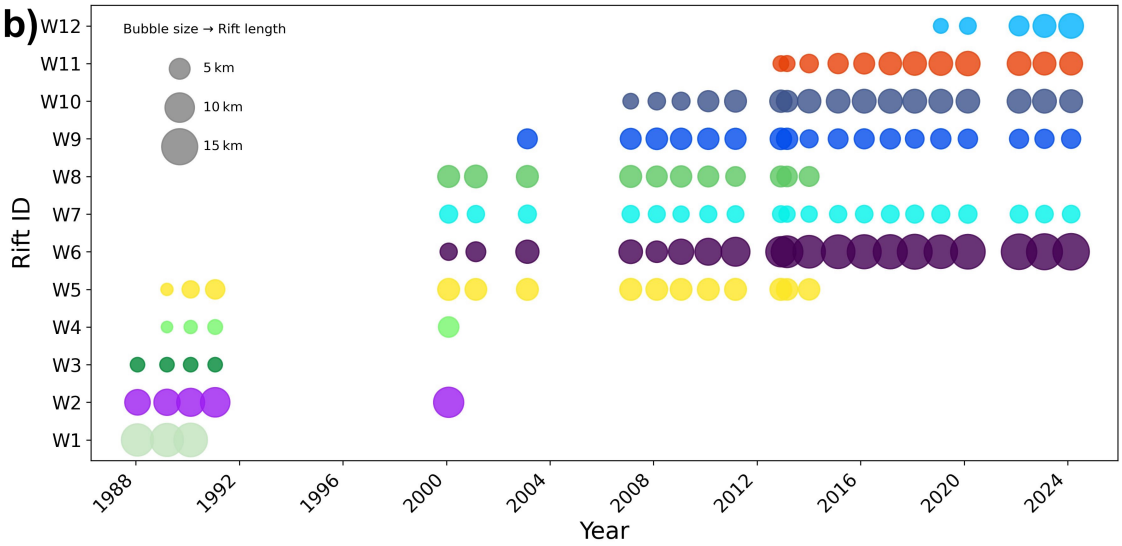

Figure 5.6: *(a) Time series of rift formation and propagation across the WRD ice tongue between 1988 and 2024, derived from high-resolution satellite imagery. Individual rifts (W1–W12) are colour-coded and tracked across years, with annotated rift lengths indicating their temporal evolution. Red lines denote the ice front position at each timestamp. Several rifts show progressive propagation and widening, with notable interactions and mergers (e.g. W2, W4, and W5) preceding major calving events. All measurements were taken from images acquired in February; where February data were unavailable, the closest available imagery from January or March was used. (b) Bubble plot showing the temporal evolution of individual rifts (W1–W12) on the WRD ice tongue from 1988 to 2024. Each bubble represents a single observation of rift length, with bubble size proportional to rift length (see legend) and colour corresponding to rift ID. Gaps in the time series reflect years with no suitable satellite imagery. The consistent tracking of rifts across multiple years highlights their initiation, propagation, and in some cases, convergence prior to calving events.*

The first major calving event in 1991 was particularly significant as it resulted in the detachment of an iceberg of approximately 78 km^2 in area and caused a notable calving of the ice front by around 7 km, the most pronounced retreat recorded in the satellite record since 1973 (Figs. 5.7a-c). This calving occurred as a result of lengthening and widening of the rift W1 between 1988 and 1991 by approximately 1 km, respectively.

The second calving event was preceded by the interaction and eventual merging of rifts W2, W4, Rift X and Y. W2 lengthened by $\sim$ 3 km at 250 m yr^{-1} and widened by 2.5 km between 1988 and 2000. Although Rift X and Y showed little

change in length, its alignment with the expanding W2 allowed the two to connect (Fig.5.7). At the same time, W4 extended by roughly 2.3 km between 1989 and 2000. The combined evolution in length and width of these rifts ultimately led to the detachment of an iceberg measuring $\sim$ 40 km^2. Although the iceberg broke off by February 2003, it remained grounded at the ice front and only began drifting after the removal of sea ice and mélange on 27 February 2015 (Fig.5.7j). Notably, the propagation pattern of Rift W6 resembles that of Rifts W1 and W2, which preceded the first and second calving events, respectively. If W6 continues advancing at its current rate of 494 m yr^{-1} and shifts its trajectory of the rift tip toward the western margin, it could eventually lead to the calving of an iceberg approximately 15 km in length.

A third, smaller calving event occurred in 2014 and was linked to the activation of W6 (Calving 3 in Fig. 5.7j–m). Following its initiation in April 2014, W6 extended further and enclosed a $\sim$ 25 km^2 ice block. Although the block detached structurally by late 2014, it remained grounded and was surrounded by mélange for over two years. It eventually drifted away in March 2017, coinciding with the clearing of mélange and compact sea ice from the rift cavity and frontal region—consistent with the delayed detachment observed in Calving 2.

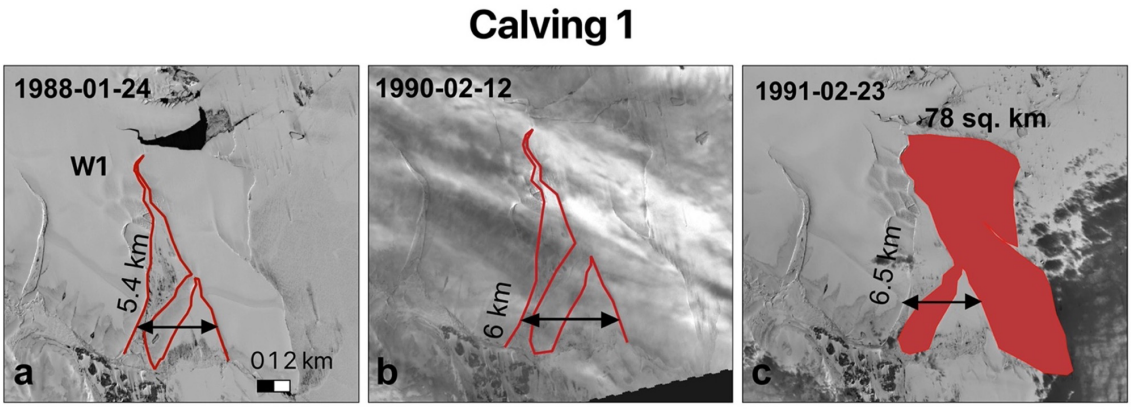

Calving 2

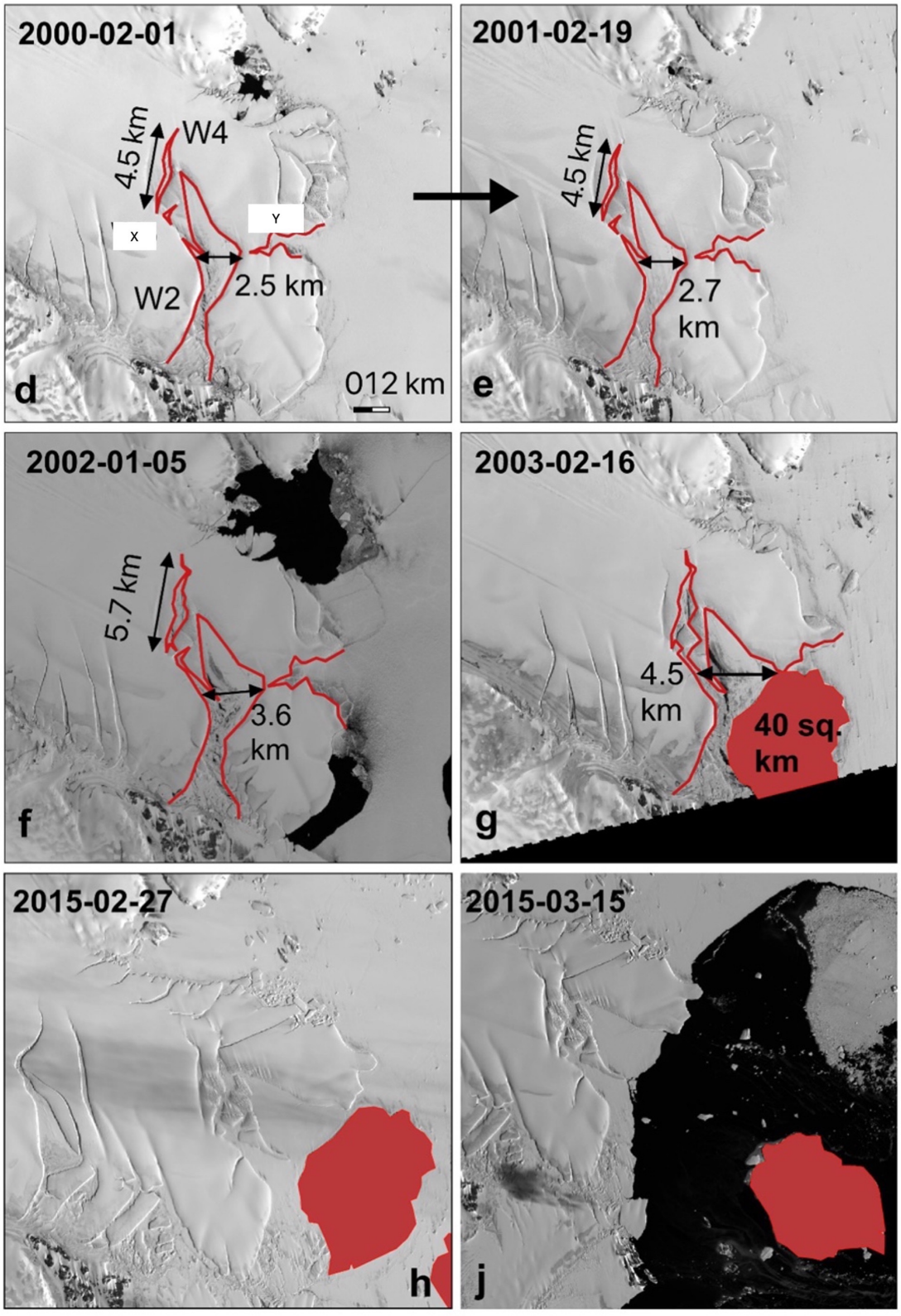
2000-02-01
4.5 km
W4
X
Y
W2
2.5 km
012 km
d
2001-02-19
4.5 km
2.7 km
e
2002-01-05
5.7 km
3.6 km
f
2003-02-16
4.5 km
40 sq. km
g
2015-02-27
h
2015-03-15
j

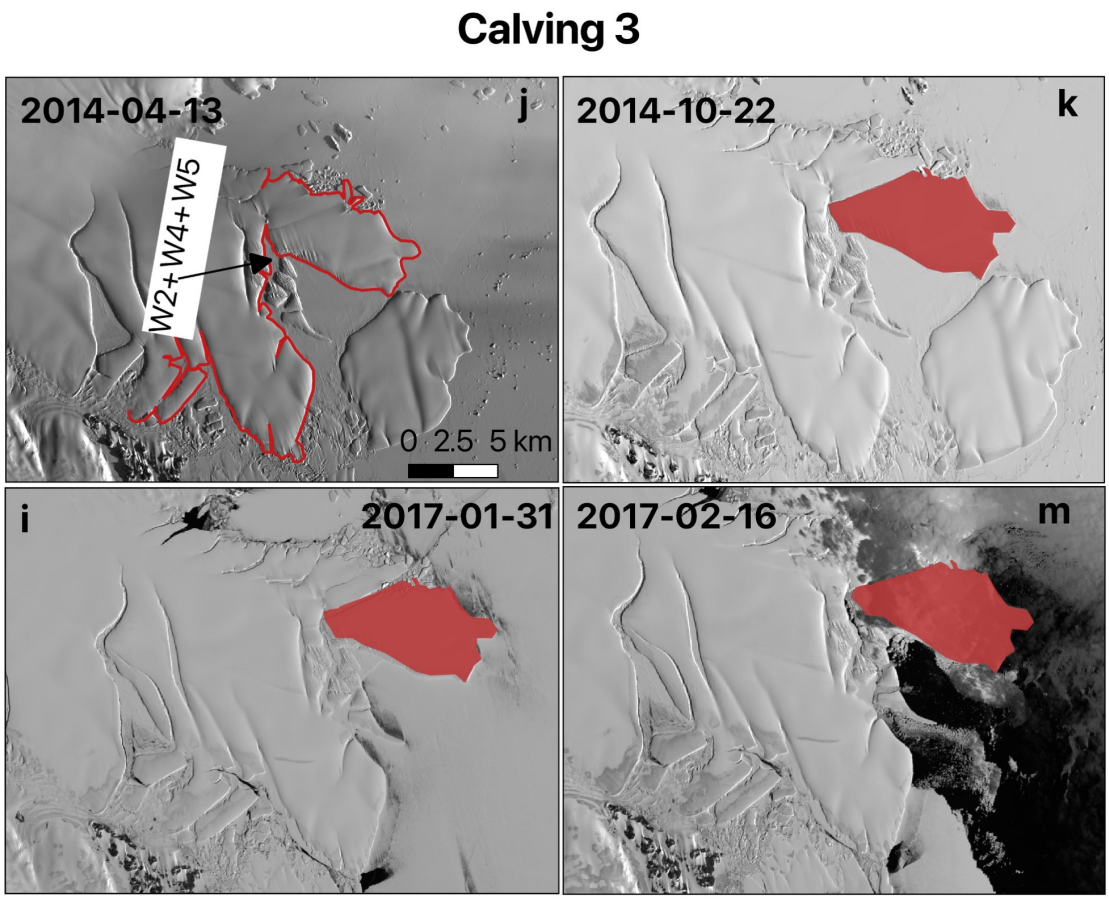

Figure 5.7: *Panels (a–c) illustrate rift propagation preceding the 1991 calving. Panels (d–g) depict the development and merging of rifts prior to the 2003 calving. Panels (h–i) indicate the timing of iceberg detachment and drift after 2003 calving event. Panels (j–n) document a minor calving event in 2014 and the subsequent iceberg drift in 2017. The red polygons in the panels represents the calved icebergs.*

5.4.3 Velocity change

Spatially, at Wilma Glacier, along transect T1, ice velocities exhibit a sharp increase near the MOA-derived grounding line, followed by a downstream decline. The peak velocity at this location, approximately 800 m yr^{-1}, was consistently lower than that observed at Robert Glacier (Fig. 5.8c). Importantly, this velocity peak at Wilma aligns closely with the position of the MOA grounding line. However, the velocity profile along transect T2 at Robert Glacier shows a distinct peak just upstream of the DInSAR-derived grounding line, with values exceeding 1000 m yr^{-1} (Fig. 5.8b). This grounding-line-related peak persists throughout the time series, and there was a minor increase in the magnitude of the peak velocity over the years (Fig. 5.8b-

c). Downstream of the DInSAR-derived grounding line position, velocities decrease gradually into the floating ice shelf before then increasing from the mid-shelf to the glacier terminus. More recent profiles also indicate a slight increase in velocity within this downstream region.

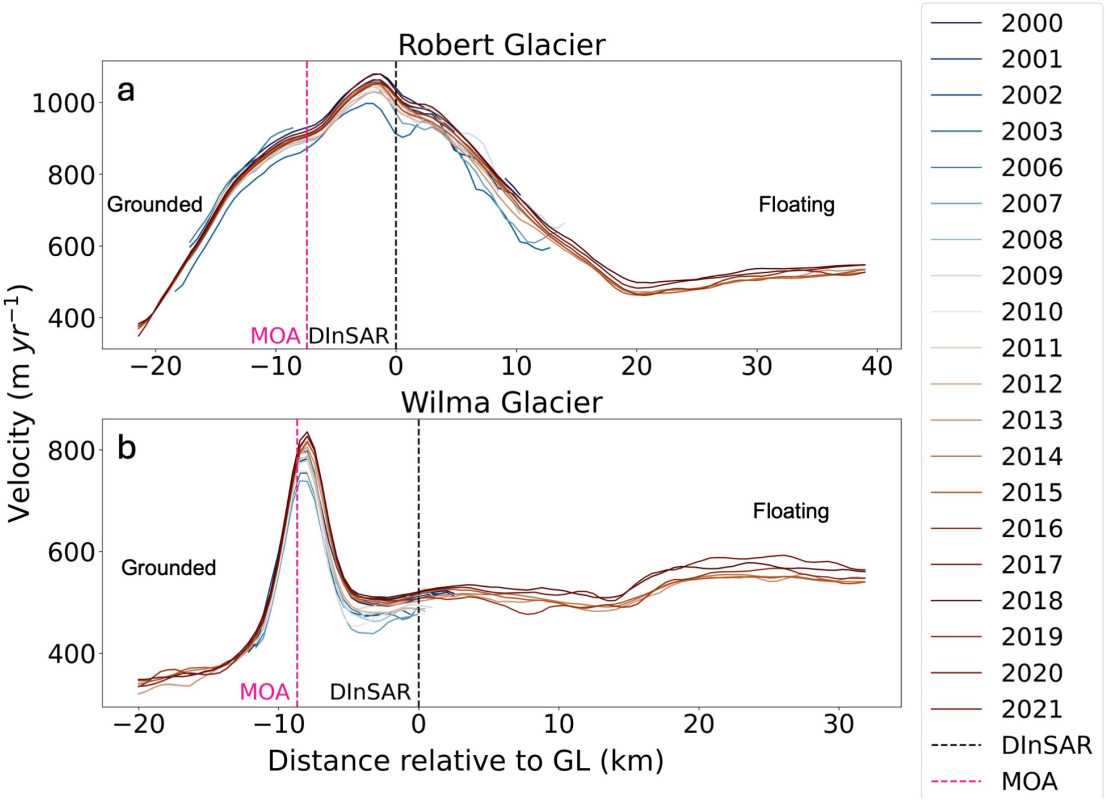

Figure 5.8: *Velocity profiles along transect T1 and T2 from 2000 to 2021. The dashed black line indicates the grounding line, the pink triangle marks the velocity at the grounding line, and the blue square marks the velocity at the up-ice tongue location.*

Velocities at the down-ice, up-ice, and grounding line locations of Wilma Glacier remained relatively consistent over time (Fig. 5.9a), although some temporal variability was observed. Robert Glacier exhibited higher velocities at its grounding line compared to Wilma Glacier, averaging approximately 958 ± 10 m yr^{-1} and 502 ± 24 m yr^{-1}, respectively (Fig. 5.9a). Between 2000 and 2021, Robert Glacier's grounding line velocity increased overall by $\sim 15 \pm 3.8\%$ (equivalent to $\sim 7.4 \pm 3.6$ m yr^{-1}). However, this trend was not uniform across the two decades: from 2000 to 2010, the velocity remained relatively constant, whereas from 2011 to 2021, it in-

creased markedly by 22±10% (approximately 20±4 m yr^{-1}). In comparison, Wilma Glacier's grounding line velocity exhibited no substantial overall change during the 2000–2021 period. Nevertheless, a slight reduction of 8±1% (∼3.6 m yr^{-1}) occurred between 2000 and 2010, followed by a modest increase of 10±3% (∼4.8±3.3 m yr^{-1}) from 2010 to 2021.

Across the WRD floating ice tongue, average velocities between 2000 and 2021 were estimated at 585 ± 28 m yr^{-1} and 523 ± 32 m yr^{-1} at the down-ice and up-ice locations, respectively. Between 2000 and 2010, the down-ice location experienced a $\sim 7 \pm 5\%$ decrease (approximately 4.4 ± 2.2 m yr^{-1}), while the up-ice location exhibited a $6 \pm 1.5\%$ increase (approximately 3.8 ± 3 m yr^{-1}). In the subsequent decade (2011–2021), both locations experienced slight velocity decreases of $3 \pm 1\%$ ($\sim 2 \pm 1$ m yr^{-1}) and 16±1% (∼7±2 m yr^{-1}) at the down-ice and up-ice locations, respectively (Fig. 5.9a).

Thus, Robert Glacier showed a marked increase in grounding line velocity after 2010, whereas Wilma Glacier remained relatively stable with only minor decadal fluctuations. Velocities across the WRD ice tongue exhibited modest changes, with slight decreases at both up-ice and down-ice locations between 2011 and 2021.

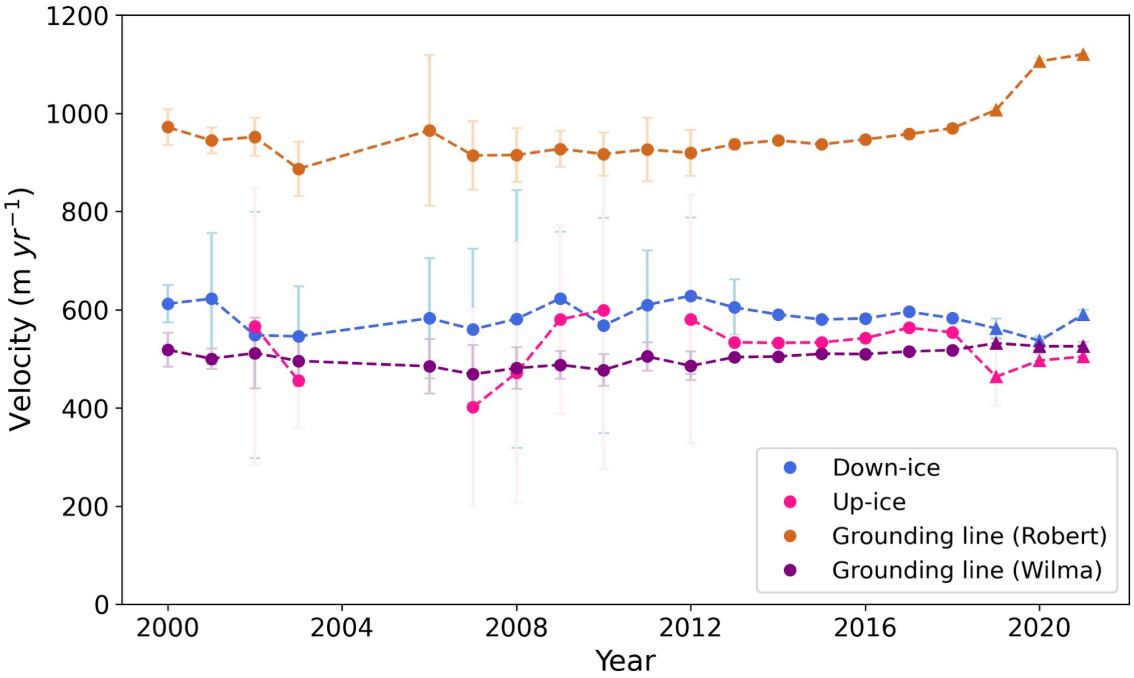

Figure 5.9: *Trends of mean annual velocity extracted from WRD Glacier at the four locations at down-ice tongue (DT), up-ice tongue (UT), grounding line (GL) and above the grounding line (AGL) (see Fig. 5.1 for location). Velocity was extracted from ITS_LIVE (circle) and ENVEO (triangle) velocity mosaics between 2000 and 2021 (Gardner et al., 2019; ENVEO et al., 2021).*

5.4.4 Grounded ice surface elevation change

Grounded ice surface elevation change observations 20 km inland of the grounding line at Wilma and Robert Glaciers reveal both thickening and thinning phases (Fig. 5.10a, b). Two independent datasets were analysed to capture these trends. Based on the dataset from Nilsson et al. (2022), the overall ice surface elevation changes between 1985 and 2020 show that Wilma Glacier experienced a very modest net thinning of -0.04 ± 0.03 m yr^{-1}, whereas Robert Glacier exhibited a slight net thickening of $+0.06 \pm 0.02$ m yr^{-1}. Although the grounded ice at both glaciers experienced thinning over the full time period, there was some variability in the rate of surface elevation change, starting with thinning and ending with thickening over time. Specifically, from 1986 to 2016, Robert Glacier exhibited thinning at a rate of -0.12 ± 0.03 m yr^{-1}, while Wilma Glacier thinned at -0.06 ± 0.02 m yr^{-1} between 1985 and 2013. However, this trend reversed in later years, with Robert Glacier exhibiting slight thickening at $+0.02 \pm 0.01$ m yr^{-1} post-2016, and Wilma

Glacier showing slight thickening post-2013 at $+0.03 \pm 0.01$ m yr^{-1}.

In comparison, ice surface elevation changes from data provided by Schröder et al. (2019) between 1988 and 2017 were estimated at $+0.05 \pm 0.06$ m yr^{-1} at Robert Glacier. However, at Wilma Glacier, it was important to note that the data from Schröder et al. (2019) are limited to the period 2010-2017 and are associated with relatively large uncertainty, with an estimated thinning rate of -0.13 ± 0.4 m yr^{-1}. At Robert Glacier, consistent thinning at -0.03 ± 0.04 m yr^{-1} was observed from 2003 to 2017. Prior to 2003, changes in grounded ice thickness at Robert alternated between periods of thinning and thickening, albeit with considerable uncertainties and missing data (Fig. 5.10b).

In addition, the surface elevation profiles along transects, T1 and T2, at Wilma and Robert Glaciers show slight changes over time. For Wilma Glacier, the MOA grounding line appears to mark the transition from grounded to floating ice (Fig. 5.10c), whereas for Robert Glacier, the DInSAR grounding line seems to indicate this transition (Fig. 5.10d).

The WRD floating ice tongue shows a clear spatial pattern in ice thickness change. The central and inland portions of the floating tongue, particularly near the grounding line, exhibit significant thinning, with maximum rates reaching up to -0.3 m yr^{-1}. This thinning was concentrated within the first 10–15 km downstream of the grounding line. In contrast, closer to the ice front, a transition to localised thickening was observed, with the highest thickening rates occurring near the terminus, reaching up to approximately +0.1 m yr^{-1}. Thus, grounded ice surface elevation at both Wilma and Robert Glaciers exhibited long-term surface elevation variability, with initial thinning trends followed by a period of reduced thinning in recent years. In contrast, the WRD floating ice tongue showed a distinct spatial pattern, with thinning downstream of the grounding line and localised thickening near the ice front.

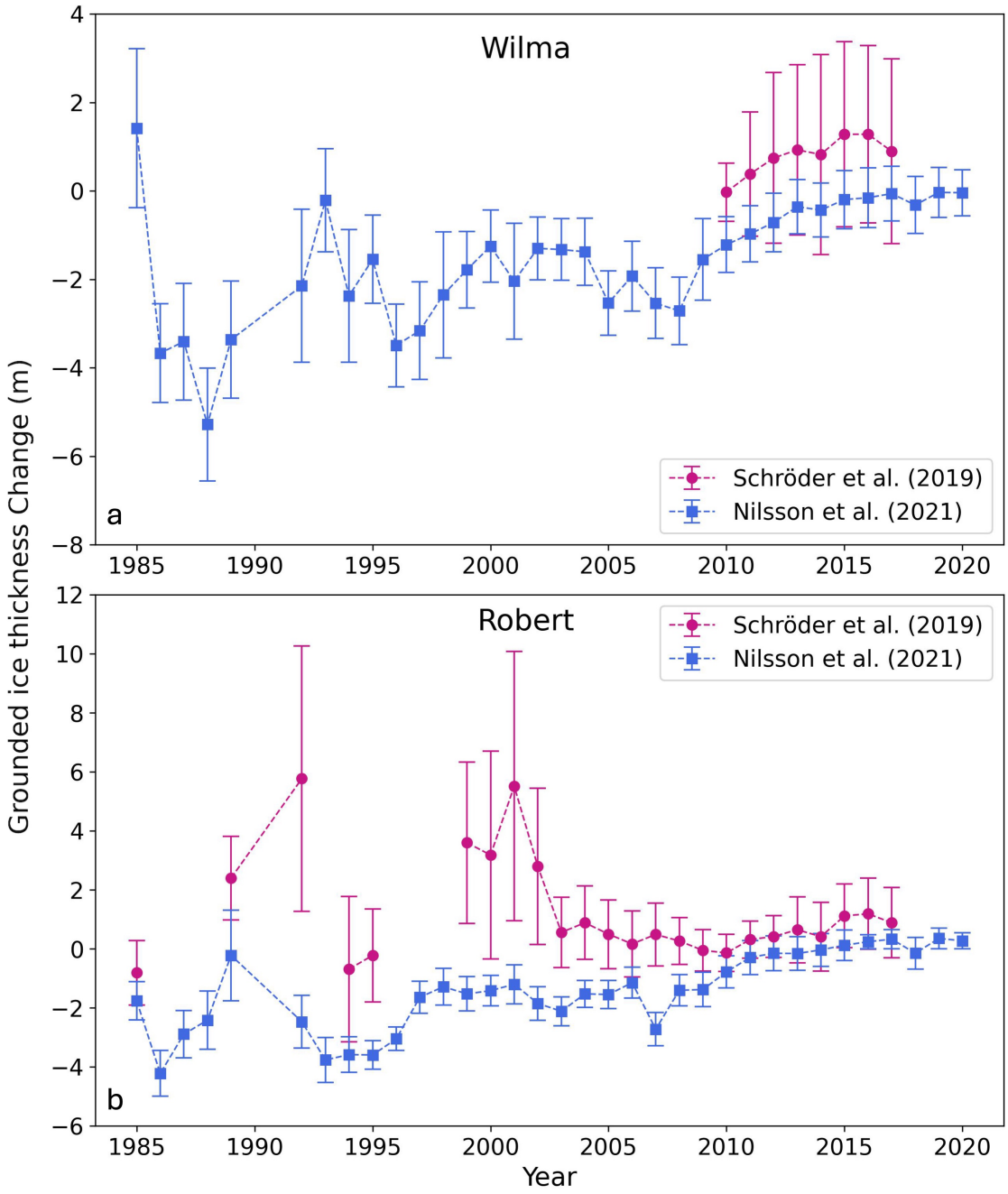
Wilma
Schröder et al. (2019)
Nilsson et al. (2021)
a
Robert
Schröder et al. (2019)
Nilsson et al. (2021)
b
Grounded ice thickness Change (m)
Year
4
2
0
−2
−4
−6
−8
12
10
8
6
4
2
0
−2
−4
−6
1985
1990
1995
2000
2005
2010
2015
2020

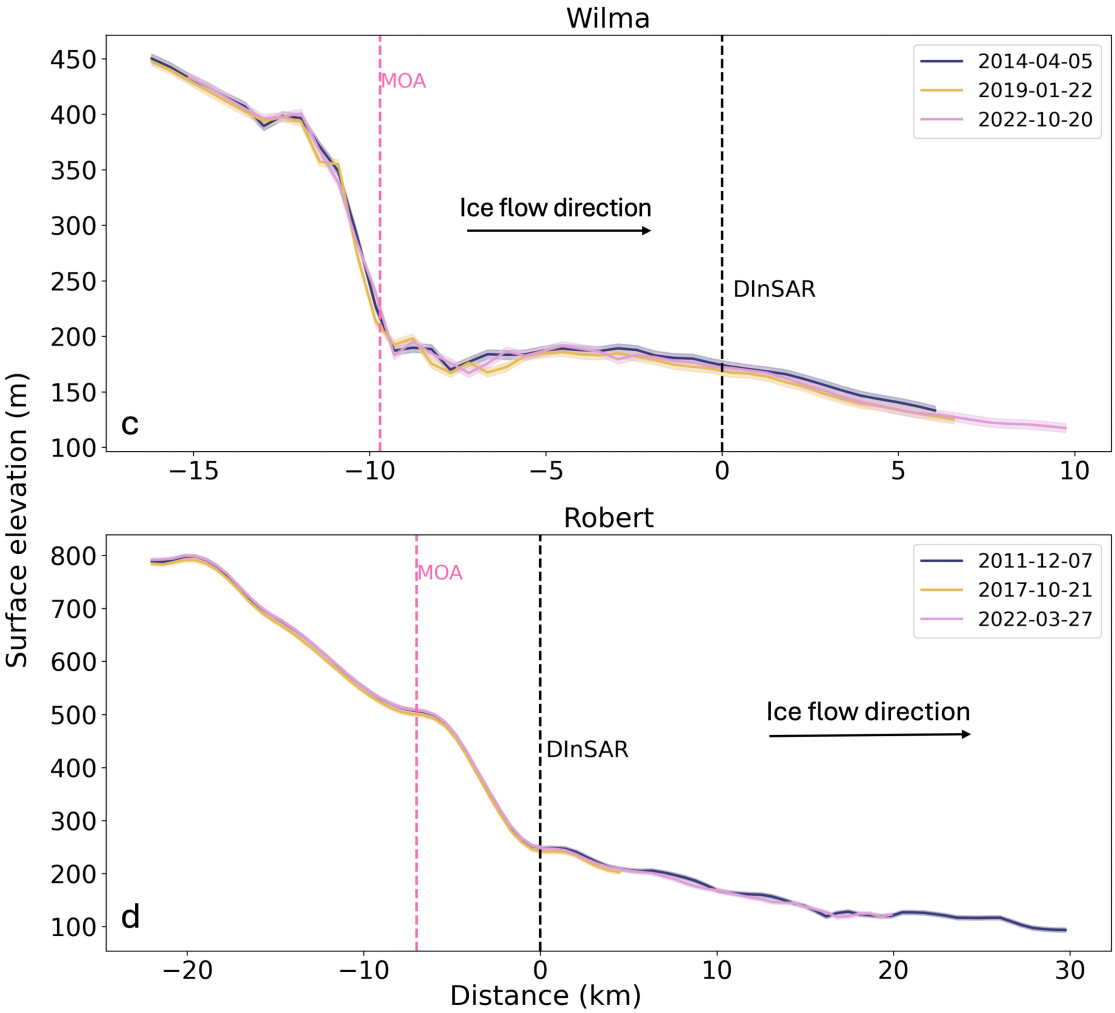
Wilma
MOA
Ice flow direction
DInSAR
2014-04-05
2019-01-22
2022-10-20
c
Robert
MOA
DInSAR
Ice flow direction
2011-12-07
2017-10-21
2022-03-27
d
Surface elevation (m)
Distance (km)

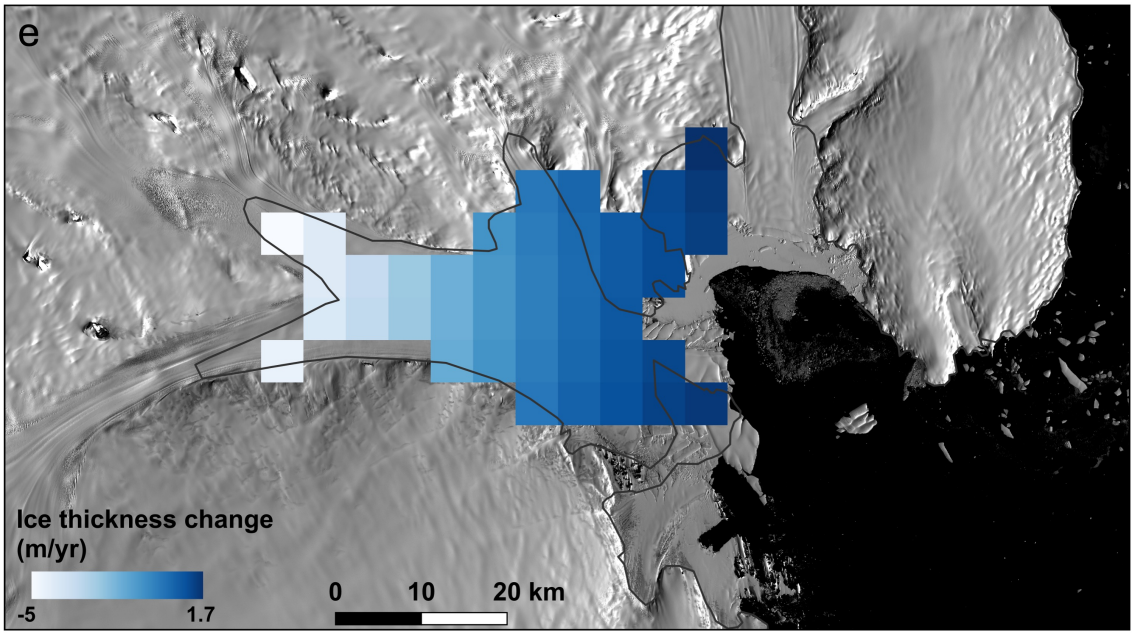

Figure 5.10: *(a-b) Annual surface elevation changes at SEC boxes (shown in Fig. 5.1) for Wilma and Robert, extracted from the Schröder et al. (2019) and Nilsson et al. (2021) datasets, where at least six data points are available per year. Error bars represent annual average errors. (c-d) Surface elevation profiles along sections of T1 and T2 at the grounding line, illustrating a seaward migration of the surface slope (e) Ice tongue thickness change between 2003 and 2019 showing thickening of the WRD ice tongue (Smith et al., 2020). Background image is Landsat-8 image from 20 March 2023.*

5.4.5 Grounded line position change

In this section, a compilation of all available grounding line positions is presented, categorised according to the two primary methodologies of measurement as detailed in section 5.2.1. Fig. 5.2 shows different features of the grounding zone used as proxy for identifying the grounding line positions using different methodologies.

DInSAR-derived grounding line positions from MEaSUREs, which identify the flexure location or hinge line (F; Fig. 5.11a; Fricker & Padman, 2006; Fricker et al., 2009; Friedl et al., 2020), are available for both Wilma and Robert Glaciers, but only for the year 2000. A more recent dataset by Mohajerani et al. (2021), which applied a fully convolutional neural network to DInSAR data, provides clusters of grounding line positions (orange) and pinning points (yellow) for 2018 at Wilma Glacier. However, no corresponding data are available for Robert Glacier from this study. Within

the most inland 2018 cluster, some grounding line positions coincide with the flexure location (F) and align well with the 2000 MEaSUREs dataset (Rignot et al., 2016), while others are located 8–10 km further downstream. These downstream points are associated with localised grounding zone features, such as pinning points (Fig. 5.11b). This indicates limited or no significant change in grounding line position at Wilma Glacier between 2000 and 2018.

Fig. 5.11b, c also shows the grounding line position determined by previously published manual delineations of the break-in slope, Ib (ASAID and MOA) and of the assumed local elevation minimum, I_m, mapped in this study. The MOA grounding line lies $\sim$ 3.5 km downstream of ASAID, both digitized in similar regions. Our results show a slight advance in grounding line position between 1988 and 2024: approximately 470 m ($\sim$ 13 m yr^{-1}) at Wilma Glacier and 320 m ($\sim$ 9 m yr^{-1}) at Robert Glacier (Figs. 5.10d, e).

Fig. 5.11d compares the manually delineated grounding line positions (ASAID, MOA, this study) with the earliest available grounding line positions derived from DInSAR (MEaSUREs). It was clear from Figure 5.11a that the DInSAR-based grounding lines, which identify the landward limit of tidal flexure (F), are consistently located much further upstream than those derived from manual interpretation of break-in slope (I_b) or elevation minimum (I_m). At Wilma Glacier, the 2000 DInSAR grounding line was $\sim$ 12 km upstream of the 2000 I_m position identified in this study. Similarly, the most landward point from the 2018 DInSAR cluster by Mohajerani et al. (2021) was $\sim$ 16 km upstream of the 2018 I_m position. At Robert Glacier, the 2000 DInSAR grounding line lies $\sim$ 15 km farther inland than the manually derived I_m position.

These results highlight that grounding line positions obtained using different methods are not directly comparable, as they represent different features within the grounding zone (Fricker and Padman, 2006; Fricker et al., 2009; Friedl et al., 2020; Picton et al., 2023). Nevertheless, the combined datasets show little evidence of significant grounding line migration at either glacier. Our manually digitized posi-

tions indicate only a modest advance of $\sim$ 470 m at Wilma and $\sim$ 320 m at Robert Glacier (Figs. 5.11b, c), within an estimated uncertainty of $\pm$100 m.

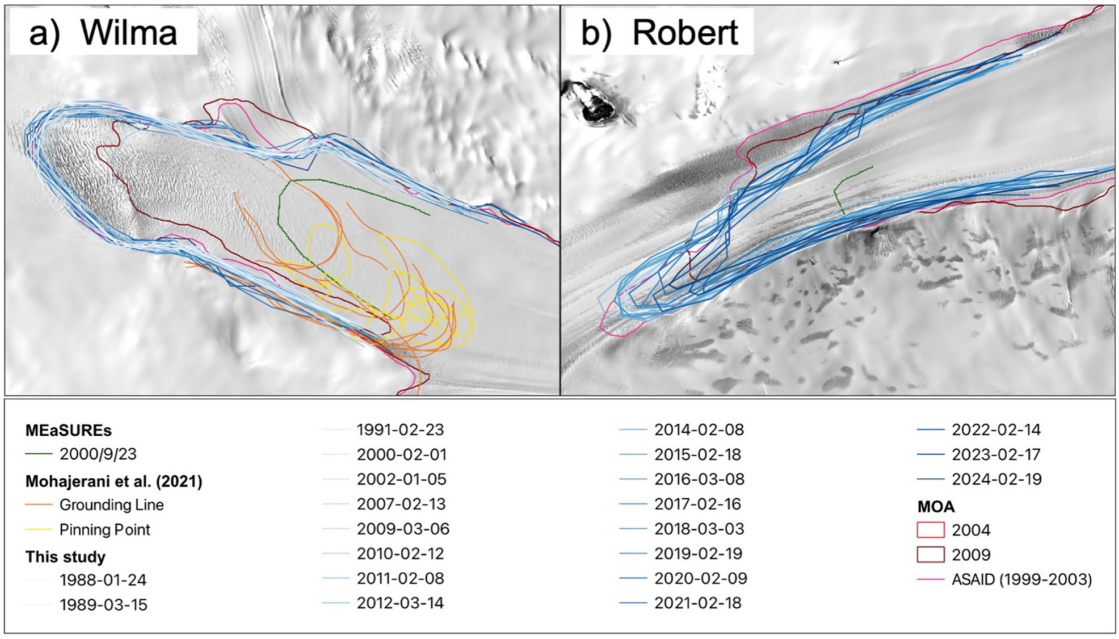

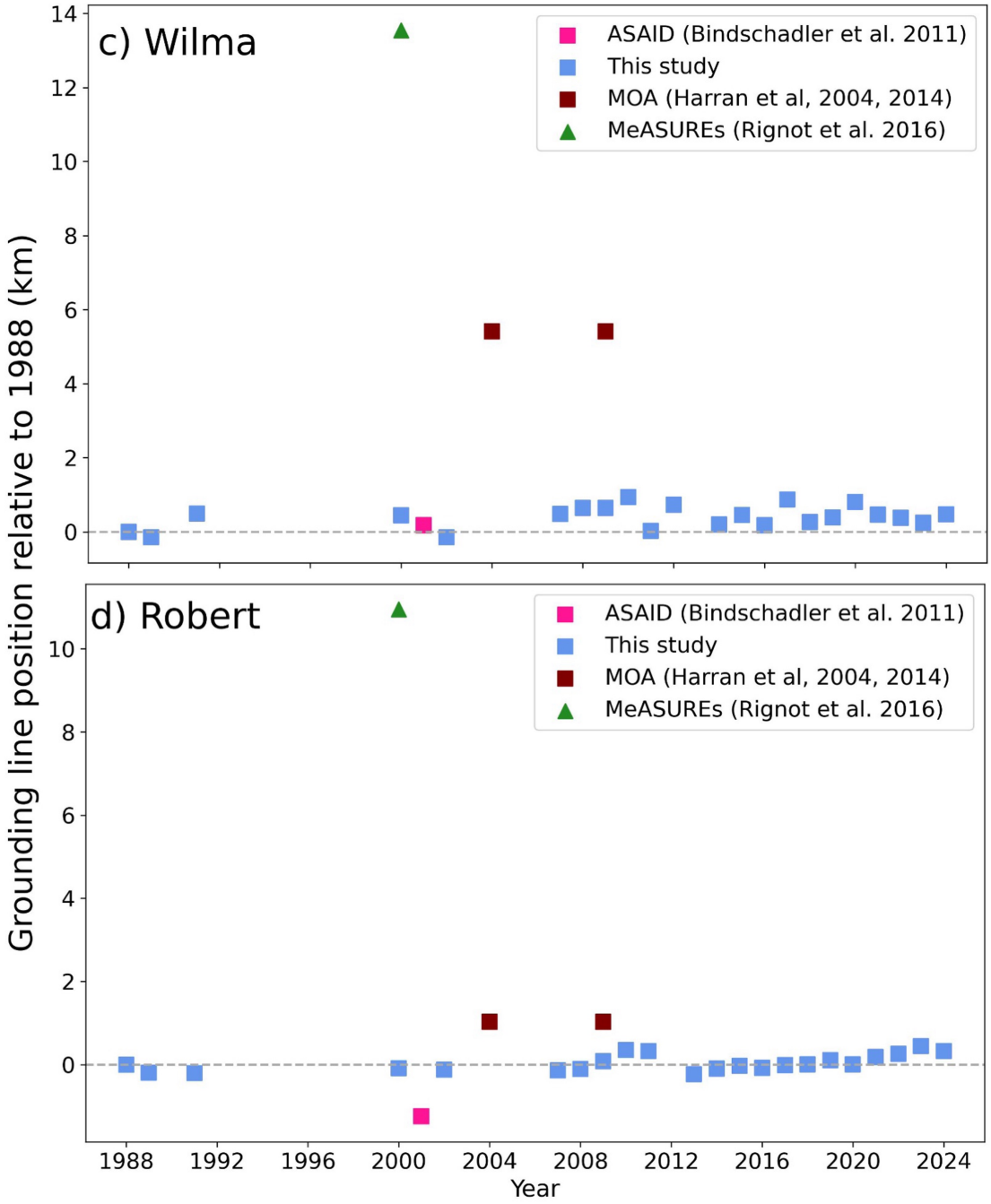

Figure 5.11: *Grounding line position of (a) Wilma and (b) Robert based on vertical motion at the floating part using DInSAR data (MEaSUREs, AIS CCI and Mohajerani et al., 2021) and manual delineation of break-in slope (ASAID, MOA, this study). Change in grounding line position relative to observed 1988 position from all datasets for (c) Wilma and (d) Robert.*

5.4.6 Atmospheric and oceanic conditions

To analyse long-term variability, the study period was divided into four distinct decadal intervals: 1970–1988, 1988–2000, 2000–2010, and 2010–2024. Analysis of the sea ice concentration over these multi-decadal intervals reveals an overall increasing trend throughout the majority of the study period. Overall, between 1980 to 2023, the mean sea ice concentration was estimated at approximately 50%. During the first decade between 1970s-1988, the sea ice concentration was estimated at 70%. In the subsequent decade (1988–2000), this average increased by 5%, reaching approximately 75%. During the third interval (2000–2010), a more modest increase of 2% was observed, bringing the average to $\sim$ 77%. This was sustained over the fourth interval (2010–2024) (see Fig. 5.12a). However, a slight decline of $\sim$ 10% occurred toward the end of this final decade, with sea ice concentration decreasing to approximately 68%.

The subsurface ocean temperature profiles across the three depth intervals reveal a long-term multi-decadal cooling trend. At the deepest depth layer (446–967 m), temperatures consistently remained below 0°C throughout the entire study period (Fig. 5.12b). Observed values ranged from approximately –1.8°C to –0.8°C, indicating persistently cold conditions at these depths over all four decadal intervals. In the mid-depth layer (105–446 m), temperatures were generally above 0°C during the first three decadal intervals, although interannual fluctuations were present. Notably, during this period, occasional declines brought temperatures down to a minimum of –0.5°C. A significant shift occurred in the fourth interval (2010–2024), when temperatures dropped consistently below –0.5°C, reaching a minimum of –1.2°C, with a corresponding decadal average of –0.6°C.

However, in the latter half of this final interval, a warming trend emerged, culminating in a maximum temperature of 0.2°C. In the uppermost layer (surface to 105 m), temperatures remained consistently above 0°C throughout the study period. Despite this, a gradual decline in decadal averages was observed, reaching an average of approximately 0.4°C in the most recent decade. Notably, within this interval,

annual average temperatures peaked at around 0.7°C, indicating episodic warming events even as the overall trend pointed toward gradual cooling (see Fig. 5.12b). Notably, in the last decade, the average annual subsurface ocean temperatures have dropped to their lowest levels since the 1970s across all the depth layers, before the temperatures peaked in the latter half of the decade.

A clear increasing trend in near-surface air temperature was observed over the multi-decadal period from 1970 to 2023. During the first decadal interval (1970–1988), the average air temperature was approximately –16°C. This value increased slightly to around –15°C in the second interval (1988–2000) and remained relatively stable during the third interval (2000–2010). In the final interval (2010–2024), a modest rise was again noted, with the decadal average reaching approximately –14.5°C. Throughout the study period, the mean decadal air temperature was approximately -15°C, with an estimated increase of 1.5°C observed from the first to the fourth decade. Despite this increase, air temperatures consistently remained well below the freezing point (0°C) across all four intervals.

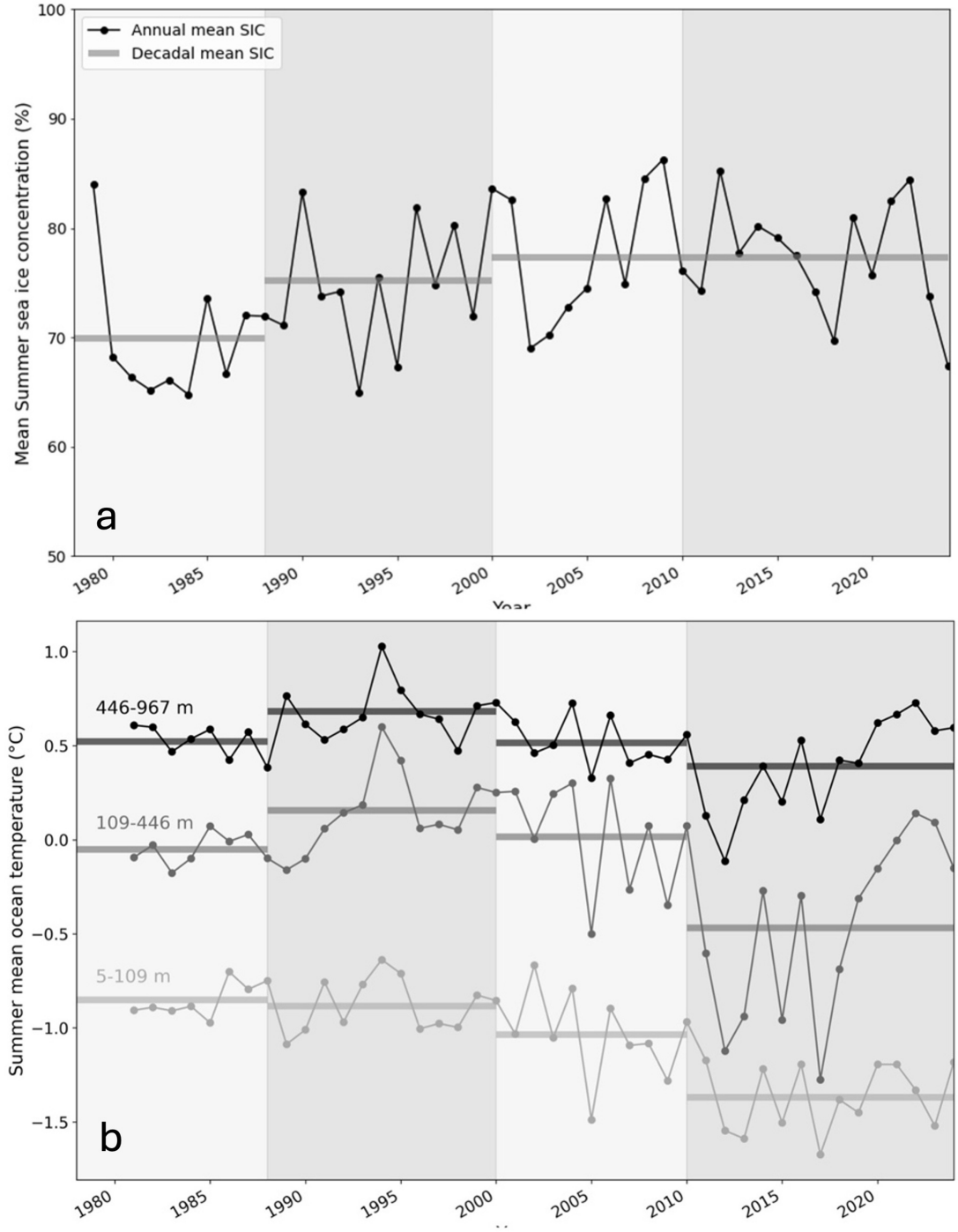
Annual mean SIC
Decadal mean SIC
Mean Summer sea ice concentration (%)
100
90
80
70
60
50
a
1980
1985
1990
1995
2000
2005
2010
2015
2020
Year
446-967 m
109-446 m
5-109 m
Summer mean ocean temperature (°C)
1.0
0.5
0.0
−0.5
−1.0
−1.5
b

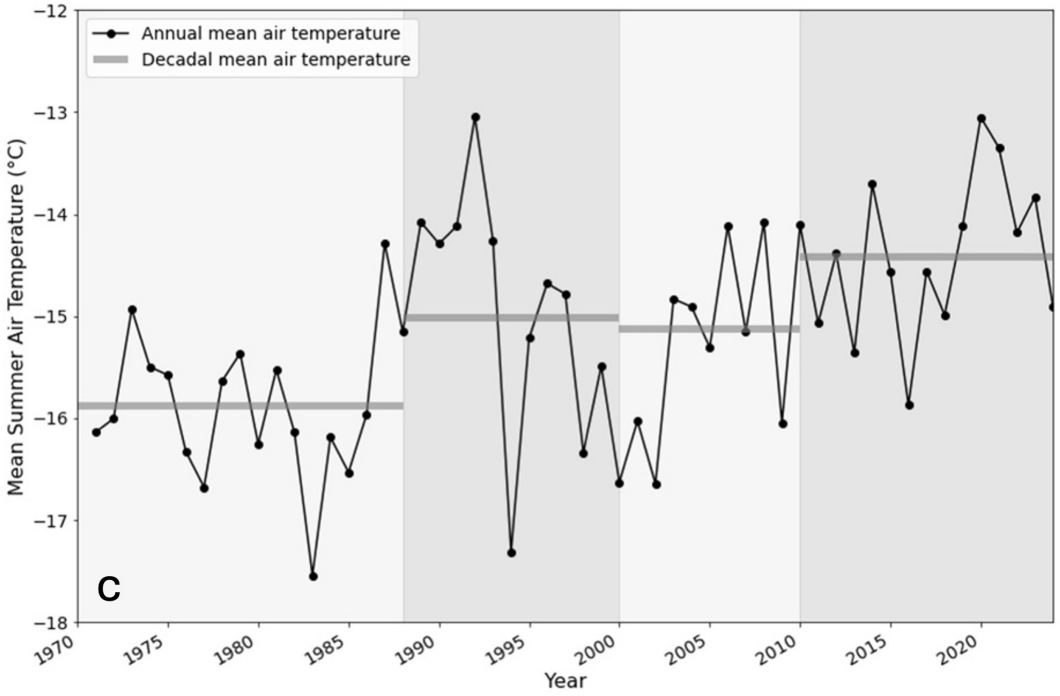

Figure 5.12: *Time series of climate variables: a) summer sea ice concentration b) summer ocean temperatures at three depth intervals (5-109 m, 109-446 m and 446-967 m). The shaded backgrounds refer to the decadal intervals and the grey bars correspond to decadal averages.*

Prior to the first calving event in 1991, satellite imagery indicates that open ocean conditions occasionally developed near the western margin of the ice tongue. For example, between late January and February 1988, few images showed persistent open ocean on the western margin of the floating ice tongue (Fig. 5.13). Although some satellite images between 1988 and 1991 are partially obscured by cloud cover. Additional images from March 1989 also show fractured sea ice approximately 19 km seaward from the ice front. On 24 January 1991, the calved iceberg is first detected, with the ice front still surrounded by sea ice and only limited open water present. However, due to the sparse availability of cloud-free imagery between 1988 and 1991, it remains difficult to pinpoint the precise timing of the calving event or to assess whether such open ocean conditions were a consistent feature during summer months (DJFM).

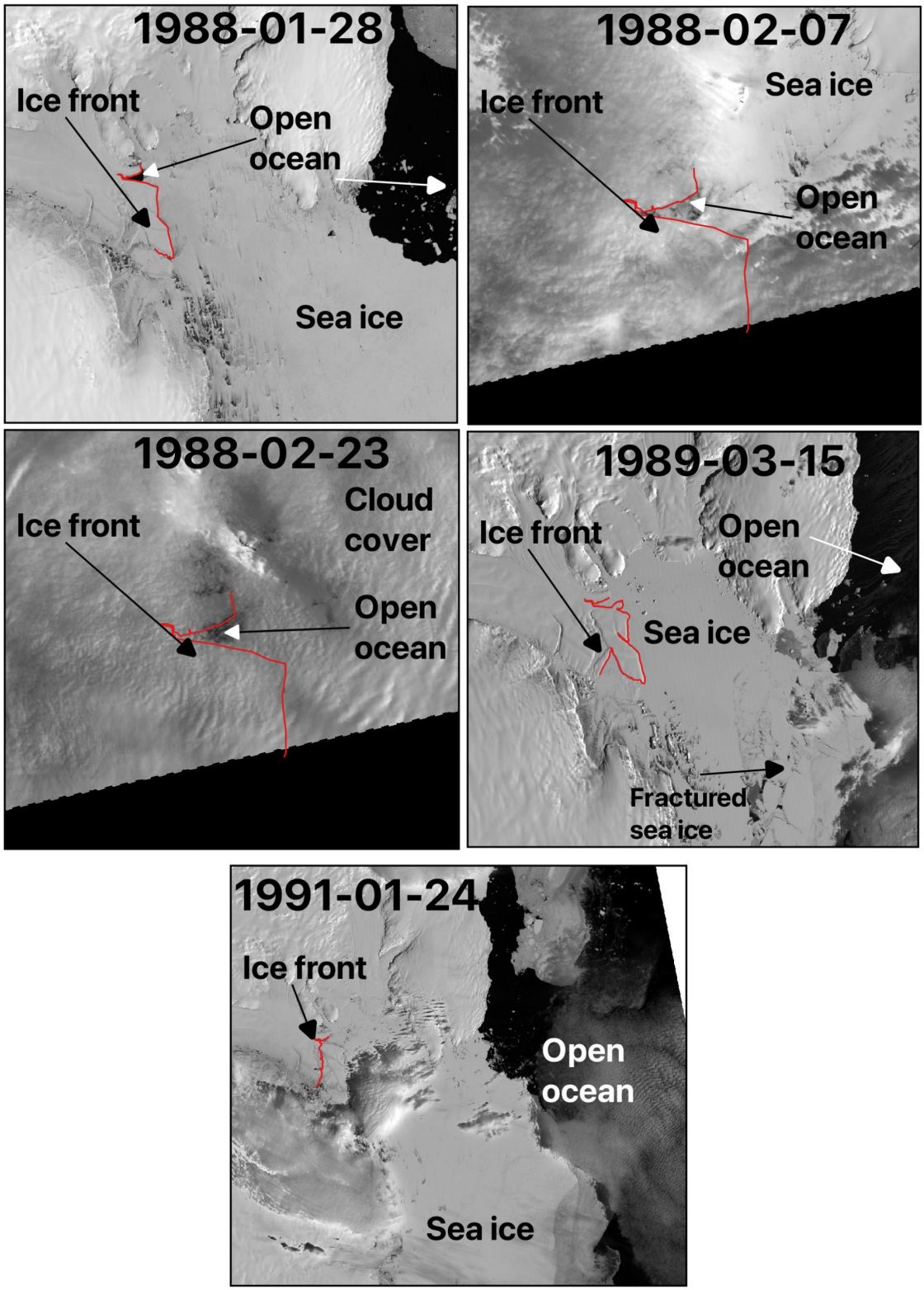

Figure 5.13: *Satellite imagery showing sea ice and open ocean conditions in front of the WRD Glacier ice tongue from 28th January 1988 until the first calved iceberg first observed on 24th January 1991.*

Satellite imagery from the period leading up to the second calving event in 2003 (Fig. 5.14) documented the progressive decline in sea ice cover and the associated detachment of an iceberg from the ice front, although the calving has been initially triggered by rift formation and evolution (Section 5.2). On 1 February 2000, a small region of open ocean first appeared along the western margin of the ice front, while most of the area remained covered by consolidated sea ice. By 19 February 2001, the extent of sea ice had visibly decreased, and sea ice started fracturing and drifting away. By December 2001, more sea ice had fractured, and widespread areas of open ocean were visible across the embayment. This trend continued into early 2002, with satellite imagery from 5 January 2002 showing larger expanses of open water and fragmented sea ice in front of the terminus. Eventually, by 16 February 2003, the iceberg that had previously remained attached to the ice front via a narrow ice bridge had fully detached.

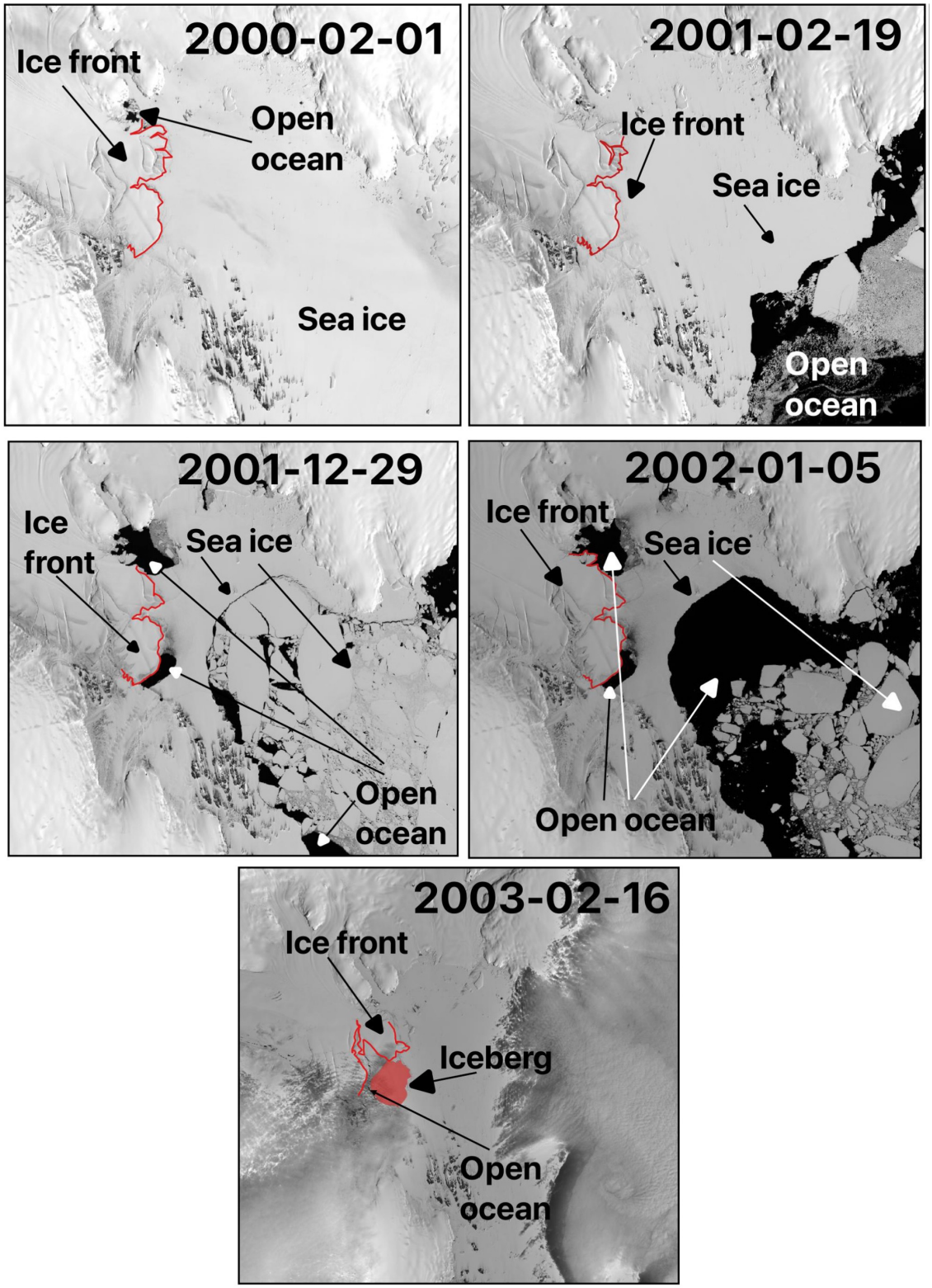

Figure 5.14: *Satellite imagery showing sea ice and open ocean conditions in front of the WRD Glacier ice tongue from 01st February 2000 until the second calving event first observed on 16th February 2003.*

Furthermore, analysis of alongshore easterly winds between 2000 and 2021 revealed a distinct period of wind strengthening offshore of the WRD ice tongue from 2007 to 2012 (Fig. 5.15). During this phase of intensification, glacier velocities at all four locations (Fig. 5.1) either increased or remained relatively stable. Specifically, velocity increased by $12 \pm 2\%$ at the Down-ice location, $44 \pm 10\%$ at the Up-ice location, $4 \pm 2\%$ at the grounding line of Wilma Glacier, and $1 \pm 0.8\%$ at the grounding line of Robert Glacier between 2007 and 2012. Following this period, from 2011 to 2021, a slight velocity reduction was observed at the Down-ice by $3 \pm 1\%$ and Up-ice locations by $16 \pm 1\%$. This slowdown of velocity coincided with the onset of weakening winds. In contrast, velocities at the grounding lines of both Wilma and Robert Glaciers showed continued increases throughout both the wind strengthening and weakening periods.

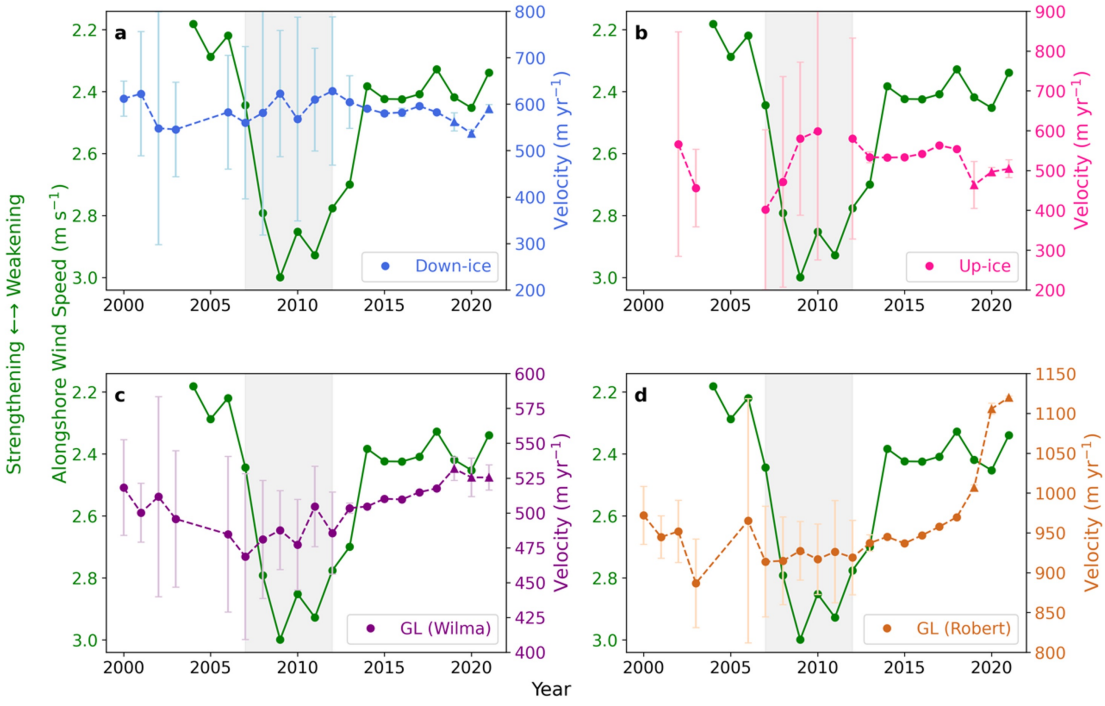

Figure 5.15: *Annually averaged ERA5-derived alongshore wind speed from Box A (see Fig. 5.1) and plotted as a 5-year rolling mean (green) and ice speed at four locations at WRD Glacier (see Fig. 5.1) plotted as a 1-year rolling mean between 2000 and 2021. Note that alongshore wind speed is plotted with an inverted axis.*

5.5 Discussion

5.5.1 Terminus position change for WRD catchment

The observations indicated that the WRD Glacier terminus has been steadily advancing, although two major calving events occurred in 1991 and 2003 and a smaller calving event occurred in 2014. By 2017, the glacier had advanced slightly beyond its maximum extent observed in 1990. By 2024, it reached its greatest recorded extent of the observation period, extending approximately 5 km beyond the 1990 maximum extent established prior to the 1991 calving event (Fig. 5.4b). This finding suggests that this glacier system has been resilient to episodic ice loss in that it has recovered in response to all the significant events that have occurred. Moreover, the lack of sustained acceleration in ice velocity further supports the interpretation that the glacier has remained largely stable and unperturbed by these events.

The analysis of rifting activity suggests that rift formation, lengthening and widening are precursors to the calving events observed at WRD ice tongue (Fig. 5.7). For instance, the progressive lengthening and widening of rift W1 preceded the 1991 calving event, highlighting the role of rift propagation in potentially weakening the structural integrity of the ice tongue (Fig. 5.7a–c). A similar process was evident before the 2003 calving event. Between 2000 and 2003, Rift W2 underwent both lengthening and widening, eventually merging with adjacent rifts (W4, W5, X, and Y), which collectively contributed to the detachment of the ~ 40 km^2 iceberg in 2003 (Figs. 5.4d-g). The widening of W2 during this period may not have been solely due to internal rift propagation. Instead, it likely reflects the gradual seaward movement of a pre-detached iceberg that remained loosely connected to the ice tongue by a narrow ice bridge, as evidenced by the progressive widening observed in satellite imagery between 2000 and 2003 (Fig. 5.7d–g). This indicated the iceberg's slow separation prior to its full detachment. Although the iceberg had calved by February 2003, it remained grounded at the terminus front and did not drift away until the complete removal of sea ice and mélange in early 2015 (Fig. 5.5h–j). Thus, historical calving events were closely preceded by rift propagation and widening, highlighting

the role of fracture evolution and iceberg pre-separation in driving major ice loss events.

Although rift formation and widening have historically preceded calving, the past decade has shown a different pattern. Despite the presence of multiple active rifts (e.g. W6–W12), no further calving events have occurred since 2014. Many of these rifts have continued to lengthen and, in some cases, widen (Fig. 5.6), yet the ice tongue has only advanced since 2015, suggesting a period of relative frontal stability. This may indicate that, while structural weakening is ongoing, the existing rifts have yet to reach a critical configuration or connectivity threshold necessary to trigger another large calving event. The lack of recent calving may also be attributed to enhanced buttressing from persistent sea-ice/mélange present in the rift openings. However, Rift W6 appears to follow a propagation pattern similar to W1 and W2, both of which were directly linked to the first (1991) and second (2003) calving events. If W6 continues to propagate inland at its current rate of approximately 494 m yr^{-1} and changes its rift tip trajectory toward the western margin of the ice tongue, it could eventually lead to the detachment of an iceberg up to 15 km in length. This suggests that, while the front has remained stable in recent years, the structural conditions for a future calving event may be actively developing.

It was likely that as the ice tongue advances, tensile stresses accumulate, particularly along its lateral margins, where pinning points exert a strong influence (De Rydt et al., 2019; Still et al., 2022; Benn et al., 2022). These stresses drive the formation of rifts, especially in areas adjacent to these anchoring points. The resulting rifts migrate forward with the flow of the ice tongue, and facilitating the recurring emergence of new fractures that migrate seaward with the glacier flow. For instance, rifts have repeatedly formed in the same stress-concentrated zones over time: Rift W5 was first observed on 15 March 1989, followed by W6 in the same region on 1 February 2000, W11 on 2 December 2012, and W12 on 6 February 2019. This persistent pattern of rifting indicates that extensional strain is a key driver of rift recurrence, with lateral pinning points playing a crucial role by localising and channelling these stresses along the edges of the glacier. A similar pattern of rift recurrence has been

observed in other glaciers, such as the Drygalski Ice Tongue (Indrigo et al., 2020), where the ice flowing out from the embayment experiences analogous stress patterns that trigger repeated rift formation. Furthermore, these lateral pinning points serve as structural anchors, resisting the ice front's retreat into the embayment. Despite two calving events caused by rift formation and propagation, the glacier consistently retreated to approximately the same position without significantly retreating into its embayment. This restrained retreat was likely due to the stabilising effect of the lateral pinning points

5.5.2 Potential drivers of ice dynamics at WRD

The observed slowdown and localized thickening of the WRD floating tongue between 2010 and 2021 appear to be influenced by a complex interplay of environmental forcings, notably oceanic thermal forcing, ice tongue confinement and structural features, and atmospheric circulation changes, rather than any single dominant driver. The slight decrease in ice velocity trends between 2010 and 2021 across the floating tongue at approximately $3\% \pm 1\%$ at the down-ice sample box and $16\% \pm 1\%$ at the up-ice sample box could be due to a consequence of enhanced lateral drag, where ice flow transitions from a broader, less-confined domain into a narrow embayment bordered by valley walls and pinning points (Adhikari & Marshall, 2012; Frank et al., 2022). The resulting shear stress and contact with lateral boundaries might have served to increase resistance, reducing ice flow and allowing for localised thickening (Benn et al., 2007; Jiskoot, 2011). Indeed, this interpretation aligns with observed slight thickening of the floating ice tongue at a rate of $+1.5 \pm 0.5$ m yr^{-1} calculated between 2003 and 2019 (Smith et al., 2020). The thickening itself could have been further enhanced by flow convergence and mechanical stabilisation from rifts and mélange occupying rift cavities, which potentially act as internal anchors, restricting flow variability, promoting mass accumulation, and reinforcing the structural integrity of the ice tongue (Amundson et al., 2020; Alley et al., 2021).

In contrast to the deceleration observed across the floating ice tongue, the region upstream of the grounding line at Robert Glacier experienced a $22 \pm 10\%$ increase in

ice velocity between 2010 and 2021 (Fig. 5.8). This acceleration likely results from a combination of topographic configuration and indirect oceanic influences. Robert Glacier overlies a deeply incised subglacial trough exceeding $\sim$ 1000 m in depth (Morgan et al., 1982), which can reduce basal resistance by lowering frictional drag at the ice–bed interface, thereby facilitating faster ice flow (Dupont & Alley, 2005; Morlighem et al., 2020).

The grounding lines of both Robert and Wilma Glaciers are positioned near 1000 m depth, a zone where incursions of relatively warm modified Circumpolar Deep Water (mCDW) are known to occur. While direct evidence of basal melt driven by ocean warming remains limited at WRD, subsurface temperatures in the region have shown a gradual rise—from ~ 0°C in 2012 to +0.8°C by 2024 (Fig. 5.9b). This slight warming may indicate an enhanced potential for basal melting. It is therefore plausible that subtle changes in oceanic heat content, combined with the glacier's topographic setting, could contribute to dynamic changes upstream of the grounding line. These observations point to a multi-faceted control on ice dynamics, shaped by bed geometry, possible basal melt processes, and evolving oceanic conditions.

The surface elevation record further supports this complex interplay. Between the late 1980s and 2015, grounded ice at both Wilma and Robert Glaciers thinned significantly, particularly $\sim$ 20 km inland of the grounding line (Fig. 5.3), with similar trends detected 10–15 km downstream (Smith et al., 2020). This thinning is consistent with a period of > 0°C subsurface ocean temperatures at mid (109-446 m) and deeper (446-967 m) depth layers (Fig. 5.8b). In recent years, however, the rate of thinning has decreased. This shift likely reflects the delayed response to a transient cooling of subsurface waters around 2012, which may have temporarily reduced basal melt potential. Additionally, increased snowfall accumulation, driven by episodic extreme precipitation and enhanced atmospheric river activity (as discussed in Section 3.3), may have contributed to surface mass gains during this period. Together, these factors suggest that the observed elevation changes reflect a lagged and modulated response to both oceanic cooling and atmospheric accumulation anomalies, rather than a direct and immediate ocean–ice interaction. Additionally, localised thicken-

ing near the terminus of the floating tongue between 2003 and 2019 (Fig. 5.10e) could be potentially linked to the presence of multi-year sea ice at the glacier front. Furthermore, the observed slowdown in ice flow on the floating tongue due to presence of rifts may have caused ice to accumulate, contributing to localised zones of thickening near the ice front.

Previous studies such as Miles et al. (2023) have linked strengthened easterly winds with reduced intrusion of modified Circumpolar Deep Water (mCDW) beneath ice tongues, a pattern associated with lower basal melt rates. This suppression of oceanic heat delivery can, in turn, lead to local ice thickening and a corresponding slowdown in glacier velocity, as documented for Shirase Glacier (Miles et al., 2023).In this study, although a deceleration was observed at both Up-ice and Down-ice sites on the WRD floating tongue, this trend only becomes apparent after 2011, subsequent to the period of pronounced wind strengthening between 2007 and 2012. Moreover, at the grounding lines of both Wilma and Robert Glaciers, velocities continue to rise irrespective of whether easterly winds are strengthening or weakening. These observations suggest that any relationship between wind patterns and glacier velocity at the WRD glacier system was inconclusive. Furthermore, the WRD floating tongue resides within a confined embayment flanked by ice rises and plateaus, complicating the potential for regional wind forcing to exert significant control on up-glacier dynamics, and perhaps providing some protection for the glacier terminus when it does not extent far from the coastline.

Despite some moderate changes in ice velocity and surface elevation across the WRD glacier system, the grounding line has remained remarkably stable throughout the study period. Grounding line positions derived in this study by identifying the elevation minimum method (I_m) following Fricker et al. (2009) and Christie et al. (2019), showed no significant inland migration between 1988 and 2024. Historical grounding line positions derived from other datasets such as the 2008 MOA data (Haran et al., 2008, 2009), which identifies the break-in slope (I_b), and the 2002 MEaSUREs dataset, which identifies the landward limit of tidal flexure (F; Fricker et al., 2009), suggest offsets of up to $\sim$ 10 km. Therefore, it was important to

recognise that these datasets are based on fundamentally different definitions and detection methodologies and are not inherently comparable in a time series context. Each method captures a different aspect of the grounding zone, which can span several kilometres from fully grounded to freely floating ice and may be influenced by spatial variability in bed geometry, hydrostatic equilibrium, and tidal forcing. For example, in Figure 5.4, the DInSAR-derived grounding line appears downstream of the velocity peak, likely underestimating the true grounding position. This misalignment suggests that the DInSAR grounding line underestimates the true grounding line position at WRD in this context.

Within rift cavities, sea ice and mélange function as mechanical adhesives, effectively binding fractured sections of the ice tongue and limiting further rift propagation. This infill helps maintain structural cohesion across weakened regions of the ice shelf or tongue, thereby delaying or even temporarily preventing calving (Fig. 5.14; Amundson et al., 2010; Larour et al., 2014; Massom et al., 2018). However, the role of sea ice in calving processes is not purely stabilising. During the second calving event in 2003, satellite imagery reveals that the formation and eventual coalescence of several rifts—particularly W2, W4, and Rift X—were the principal triggers (see Section 5.2). Yet sea ice conditions may have played a more nuanced, dual role. While persistent infill within rifts typically suppresses calving, under certain circumstances, it can instead facilitate it. For instance, once a rift has fully penetrated the ice tongue and an iceberg is nearly detached, sea ice or mélange surrounding the calving front may reduce lateral resistance and frictional contact with the terminus. Moreover, wind- or current-driven motion of sea ice can exert additional mechanical forces on a partially detached iceberg, promoting separation once the remaining connection weakens. Thus, in the 2003 event, while rift development initiated the calving, sea ice may have contributed to the final detachment by enabling the iceberg to break free and drift seaward. Following the 2003 event, sea ice and mélange remained a persistent feature within rift systems. Notably, Rift W6 was consistently infilled with sea ice and mélange throughout the 2000–2024 period (Fig. 5.6). This long-term infill likely suppressed further calving by providing structural support along rifted margins and by preventing the release of a small iceberg fragment

that remained tenuously connected to the terminus. Consequently, the structural integrity of the floating tongue was maintained over the following decade.

In addition to stabilising internal rift zones, sea ice in front of the terminus exerted a frontal buttressing effect that reduced extensional stress and likely contributed to the gradual advance of the ice front (Robel et al., 2017; Schlemm et al., 2022). Although the iceberg formed in 2003 had technically calved, it remained mechanically "glued" in place by the persistent presence of sea ice and mélange for over a decade. It was only between 27 February and 15 March 2015—when sea ice cover in front of the terminus dissipated for the first time since the 2003 calving—that the iceberg finally detached and drifted away (Fig. 5.7j, m). This sequence highlights the critical role of frontal sea ice not only in delaying iceberg movement but also in maintaining the long-term stability of the ice tongue.

This mechanism is consistent with findings by Khazender et al. (2009), who demonstrated that consolidated ice mélange exerted considerable mechanical resistance at the Brunt/Stancomb Wills Ice Shelf by physically linking otherwise separate ice shelf segments. Massom et al. (2010) also reported mechanical coupling between multiyear fast ice and the Mertz Glacier ice tongue was sufficient to delay calving along pre-existing rift systems by around 10 years. In fact at WRD, during periods when sea ice was absent in front of the terminus, the mélange within the rift cavities continued to provide mechanical cohesion. This suggests that the mélange in rift cavities could maintain ice tongue integrity and facilitate continued frontal advance.

The future stability of the ice tongue is closely tied to the continued presence of both mélange within rift systems and sea ice at the glacier front. While current SICs in front of the ice tongue remain relatively high, the overall trend in sea ice extent across the AIS is declining. Since 2016, Antarctic sea ice extent has experienced years of record-low sea ice extents across the AIS (Parkinson et al., 2019). Indeed, Figure 4.11c shows a slight reduction in decadal regional sea ice extent in Kemp Land by a approx. 10 x 103 km^2 between 2000-2010 and 2010-2024. A con-

tinued downward trend in sea ice extent would make it increasingly likely that the mechanical "glue" provided by frontal sea ice and mélange—so vital to restraining calving—could weaken or disappear altogether. Figure 5.9b indicates that subsurface ocean temperatures have begun to increase again post-2020. Should this ocean warming trend continue, the ice tongue would face increased exposure to relatively warm waters and ocean swells, especially in the absence of protective sea ice and mélange. These combined mechanical and oceanic forcings would heighten structural vulnerability, promote rapid propagation of existing rifts, and potentially destabilise the ice tongue. These conditions reflect developments at other Antarctic glaciers, such as the Pine Island Glacier, where debuttressing events led to rapid structural weakening and dynamic retreat and has been projected to retreat further inland in the future (Scambos et al., 2004; Fürst et al., 2016; Robel et al., 2017).

5.6 Conclusion

This study offers an assessment of the Wima-Robert-Downer Glacier system's evolution from the 1970s to 2024, highlighting the evolution of terminus position, ice velocity, and surface elevation changes. The glacier's terminus exhibited a general advancing trend, punctuated by two major retreat events in 1991 and 2003, primarily triggered by rift initiation and propagation (Fig. 5.7). Following these calving events, the glacier was constrained by lateral pinning points that acted as mechanical anchors, effectively limiting inland retreat and promoting terminus re-advance. The recurrence of rifting underscores the dominant role of extensional strain in driving fracture patterns, a mechanism observed in other Antarctic systems such as the Rayner and Drygalski Ice Tongues (Indrigo et al., 2021).

Since 2002, the continued advance of the ice front appears to have been supported by sustained summer sea ice concentrations and the presence of mélange within rift cavities. Together, these elements likely exerted a mechanical buttressing effect that slowed rift propagation, limited lateral deformation, and contributed to the overall stability of the terminus. Even during the brief absence of sea ice between 27 February and 15 March 2015—when a 40 km^2 iceberg calved and drifted away—the

remaining mélange within rift zones continued to support the ice tongue's structure and sustain forward motion (Fig. 5.7h, i). Over the period 2000–2021, ice velocities across the floating tongue exhibited a modest deceleration, driven by lateral constriction into a narrower flow channel and by pervasive rifting, both of which also promoted surface thickening near the terminus.

Surface elevation data from Wilma and Robert Glaciers show prolonged thinning approximately 20 km upstream and 10–15 km downstream of the grounding line, followed by a deceleration in thinning rates (2000-2021) and instances of localised thickening on the floating ice tongue (2003-2019). The thickening may stem from flow deceleration and ice accumulation, potentially facilitated by presence of rifts. Grounding line positions across WRD remained remarkably stable throughout the study period, with no significant inland retreat detected. This further supports the conclusion that the WRD system has maintained structural resilience to episodic ice loss over the past five decades, in contrast to the dynamic retreat observed in other sectors of East Antarctica.

Together, these findings suggest that the WRD Glacier system is currently in a stable configuration, sustained by a combination of mechanical, oceanic, and glaciological processes. However, the continued evolution of rift systems, coupled with potential future reductions in sea ice and oceanic warming, may increase its susceptibility to future calving and dynamic change. The results highlight the value of integrated multi-decadal assessments for understanding the stability and vulnerability of outlet glaciers in East Antarctica.

CHAPTER 6

Ice dynamics and structural evolution of Jutulstraumen, Dronning Maud Land, East Antarctica (1963-2022)

Sharma, A., Stokes, C. R., & Jamieson, S. S. R. (2025). Ice dynamics and structural evolution of Jutulstraumen, Dronning Maud Land, East Antarctica (1963–2022). Journal of Glaciology, 71, e65. https://doi.org/10.1017/jog.2025.29

6.1 Abstract

Jutulstraumen is a major outlet glacier in East Antarctica that drains into the Fimbulisen, Dronning Maud Land. This study presents the first long-term ($\sim$ 60 years) record of its behaviour using optical satellite imagery. The analysis reveals that the ice front has been steadily advancing since its last major calving event in 1967, with a consistent ice flow velocity of approximately 720 ± 66 m yr^{-1} between 2000 and 2021, accompanied by spatially variable thickening of the grounded ice at a rate of $+0.14 \pm 0.04$ m yr^{-1} from 2003 to 2020. Evidence also suggests a minor grounding line advance of $\sim$ 200 m between 1990 and 2022, although this estimate was associated with considerable uncertainty. Mapping of the major rifts on Jutulstraumen's ice tongue from 2003 to 2022 indicates a general increase in rift length, along with several minor calving events along the lateral margins. Given the current ice front advance rate of $\sim$ 740 m yr^{-1}, the ice tongue has been projected to reach its most recent maximum extent—last observed in the mid-1960s—within the next 40 years. However, extrapolation of rift lengthening trends suggests that a major calving event may occur sooner, potentially by the late 2050s. Overall, the findings indicate no evidence of dynamic imbalance, consistent with observations from other major glaciers in Dronning Maud Land.

6.2 Introduction

The Antarctic Ice Sheet (AIS) is currenly losing mass as a result of anthropogenic climate warming (Meredith et al., 2019; The IMBIE Team, 2023). Recent satellite observations show that mass loss from the AIS has accelerated over recent decades (Rignot et al., 2013, 2019; Schröder et al., 2019), with losses predominantly from the West Antarctic Ice Sheet (WAIS), which experienced an average imbalance of -82 ± 9 Gt yr^{-1} between 1972 and 2020 (The IMBIE Team, 2023). The ongoing response of the AIS to atmospheric and oceanic warming continues to raise concerns regarding its future contribution to global sea level rise (McGranahan et al., 2007; Oppenheimer et al., 2019). Palaeoclimate reconstructions (Noble et al., 2020) and ice

sheet modelling studies (Nowicki et al., 2013; DeConto & Pollard, 2016; Seroussi et al., 2020; Payne et al., 2021) have highlighted the AIS's sensitivity to past warming periods, which were often used as analogues for future mass loss under projected atmospheric warming scenarios (DeConto et al., 2021).

While mass loss from the WAIS has been evident since the early 1990s (The IMBIE Team, 2023), the East Antarctic Ice Sheet (EAIS) has been broadly in balance or slightly gaining mass, with a recent estimate of $+3 \pm 15$ Gt yr^{-1} between 1992 and 2020 (The IMBIE Team, 2023). However, spatial variability in the EAIS's response to climate forcing is evident. Notably, regions such as Dronning Maud Land (DML) have experienced mass gains, while Wilkes Land has undergone significant mass loss (Shepherd et al., 2012; Khazendar et al., 2013; Greenbaum et al., 2015; Li et al., 2016; Medley et al., 2018; Rignot et al., 2019; Brancato et al., 2020; Smith et al., 2020; Stokes et al., 2022; The IMBIE Team, 2023). The average mass balance of DML between 1992 and 2017—comprising basins 5 to 8 as defined by Zwally et al. (2012)—has been estimated at $+13.3 \pm 3.4$ Gt yr^{-1} (Shepherd et al., 2020), with the Shirase Glacier catchment contributing approximately +46 Gt ($\sim$ 1.2 Gt yr^{-1}) of mass gain between 1979 and 2017 (Rignot et al., 2019). This gain, which commenced around 2000 (Schröder et al., 2019; Smith et al., 2020), has been attributed to thickening of the floating ice tongue (Schröder et al., 2019; Smith et al., 2020) and a subsequent deceleration of ice flow upstream of the grounding line (Miles et al., 2023), influenced by the strengthening of alongshore winds that restrict the inflow of warm modified Circumpolar Deep Water (mCDW) into the Lützow-Holm Bay (Miles et al., 2023).

By contrast, Wilkes Land (basin 13 in Fig. 6.1) exhibits a negative mass balance, estimated at -8.2 ± 2.0 Gt yr^{-1} between 1992 and 2017 (Shepherd et al., 2019), with Totten Glacier losing approximately -236 Gt ($\sim$ -6.2 Gt yr^{-1}) between 1979 and 2017 (Rignot et al., 2019). This loss has been linked to the intrusion of warm mCDW into the glacier cavity through deep oceanic troughs, leading to enhanced basal melt (Miles et al., 2016; Rignot et al., 2019). The EAIS response to climate change is therefore spatially heterogeneous and basin-specific (cf. Stokes et al., 2022).

Despite recent mass gains in DML, some studies have reported increased basal melt linked to Warm Deep Water (WDW) influx (Lauber et al., 2023) and predict significant mass loss under future warming scenarios (Golledge et al., 2015, 2017; DeConto et al., 2021). Observations at Fimbulisen between December 2009 and January 2019 indicate an increased influx of WDW after 2016, resulting in elevated basal melt rates of $\sim$ 0.62 m yr^{-1} (Lauber et al., 2023). This process has been associated with a decline in sea ice concentration and intensification of subpolar westerlies (Lauber et al., 2023). Model projections further suggest that the Recovery Basin in DML may be vulnerable to future ocean warming, particularly under high-emissions scenarios (Golledge et al., 2015, 2017), with potential for substantial mass loss by 2300 following a +3°C warming scenario (DeConto et al., 2021), albeit with considerable uncertainty. Continued incursions of warm water and projected climate warming could therefore accelerate basal melt and impact ice shelf mass balance in DML earlier than anticipated.

However, there remains a significant gap in long-term, systematic observations of glacier dynamics across major outlet glaciers in this region. Without these observations, understanding of the current and future regional response of the EAIS to climate forcing remains limited.

To address this, the present study provides the first long-term, systematic assessment of Jutulstraumen—one of the largest outlet glaciers in DML—to evaluate its recent evolution from the 1960s to 2022 and to assess its potential future trajectory. This is achieved through the use of remotely sensed satellite imagery and several secondary datasets, focusing on: (1) ice front positions; (2) ice velocity (Gardner et al., 2019; ENVEO, 2021); (3) surface elevation change (Schröder et al., 2019; Smith et al., 2020; Nilsson et al., 2022); (4) grounding line position (Haran et al., 2005, 2014; Bindschadler et al., 2011; Rignot et al., 2016); and (5) structural mapping (Fricker et al., 2005; Holt et al., 2013; Walker et al., 2015).

6.3 Study area and previous work on Jutulstraumen

The Fimbulisen (FIS) is the largest ice shelf in the EAIS ($\sim$ 39,400 km^2) located between 71.5°S to 69.5°S and 3°W to 7.5°E. Jutulstraumen ('The Giant's Stream' in Norwegian) is a fast-flowing ice stream ($\sim$ 700 m yr^{-1}) that feeds the central part of the ice shelf (Figs.1, 2, Lunde, 1963; van Autenboer & Decleir, 1969; Gjessing, 1970) and has an annual ice discharge of 30 ± 2.2 Gt yr^{-1} between 2009 and 2017 (Rignot et al. , 2019). The average mass balance of Jutulstraumen has been estimated at +33 Gt between 1979 and 2018 (Rignot et al. , 2019). There has been only one major calving event recorded between the 1960s and 2022, occurring in 1967 (van Autenboer & Decleir, 1969; Vinje, 1975; Swithinbank et al. , 1977; Kim et al. , 2001) when a $\sim$ 100 km long by $\sim$ 50 km wide iceberg calved from Jutulstraumen's floating ice tongue (named 'Trolltunga') along newly formed perpendicular rifts (Vinje 1975; Humbert & Steinhage, 2011). This calved iceberg then drifted along the Weddell Sea for more than 13 years (Vinje, 1975).

Jutulstraumen is pinned by ice rises on either side of the ice tongue (Kupol Moskovskij to the east and Bløskimen and Apollo Island to the west) (Matsuoka et al. , 2015; Figs. 1,2), which may influence the flow and contribute to a stabilising effect on the current ice shelf configuration (Melvold & Rolstad, 2000; Goel et al. , 2020). The main trunk of Jutulstraumen drains a major valley that ranges between 20-200 km wide and begins $\sim$ 60 km inland of the modern grounding line and cuts through a significant coastal mountain range: the massifs Sverdrupfjella to the east and Ahlmannryggen to the west (Fig. 6.2, Humbert & Steinhage, 2011). The valley through which Jutulstraumen flows is a graben resulting from major rifting following the breakup of Gondwana (Fig. 6.1c, Decleir & van Autenboer, 1982; Wolmarans and Kent 1982; Melvold & Rolstad, 2000; Ferraccioli et al. , 2005). The depth of the Jutulstraumen trough, estimated at $\sim$ 1500 m below sea level at the deepest part (Fig. 6.1, Gjessing, 1970; Decleir & Autenboer, 1982; Melvold & Rolstad, 2000), allows the ice to drain from the EAIS interior and has the potential to make

the area susceptible to ocean warming. However, recent modelling has explored the sensitivity of Jutulstraumen to mid-Pliocene warming (Mas e Braga et al. , 2023), a period which is often used as an analogue for a near-future climate state (DeConto et al. , 2021), and their findings highlight that the ice stream thickens by around 700 m, despite its retrograde bed slope. This thickening was attributed to lateral stresses at the flux gate constricting ice drainage and thus stabilising the grounding line (Mas e Braga et al. , 2023).

Previous research suggests that recent (2010-2011) ocean conditions were relatively cold and dominated by Eastern Shelf Water in the cavity beneath the ice tongue (Hattermann et al. , 2012), with an estimated mean basal melt rate of $\sim$ 1 m yr^{-1} based on interferometric radar and GPS-derived strain rates in the central part of Fimbulisen (Langley et al. , 2014). The basal melt rate has been shown to vary between 0.4 and 2.8 m yr^{-1} based on the different methods used, such as oceanographic measurements (Nicholls et al. , 2008; Hattermann et al. , 2012), satellite altimetry and InSAR data (Shepherd et al. , 2010; Pritchard et al. , 2012; Depoorter et al. , 2013; Rignot et al. , 2013), and oceanographic modelling (Smedsrud et al. , 2006; Timmermann et al. , 2012). However, recent observations show pulses of Warm Deep Water (WDW) entering the cavity since around 2016, occasionally reaching over -1.5°C, with peak temperatures up to 0.2°C, contributed to a basal melt rate of 0.62 m yr^{-1} and which has been linked to mass loss of 15.5 Gt yr^{-1} between 2016 and 2019 (Lauber et al., 2023). These changes, driven by a positive Southern Annular Mode (SAM) resulting in stronger westerlies and reduced sea ice, could significantly impact the ice shelf's mass balance and its buttressing effect on inland ice.

In summary, the response of EAIS to climate change is complex and varies across different regions. This is influenced by factors such as presence or absence of warm ocean conditions and bed topography (Morlighem et al. , 2020). The lack of observational data for several major outlet glaciers, including Jutulstraumen, makes it even more challenging to understand how the glaciers in the EAIS were currently responding, or will respond to, changing climate. Thus, in this paper, this study

conducted a systematic observations of Jutulstraumen between the 1960s and 2022 with the aim of improving understanding of the changing ice conditions in this part of DML.

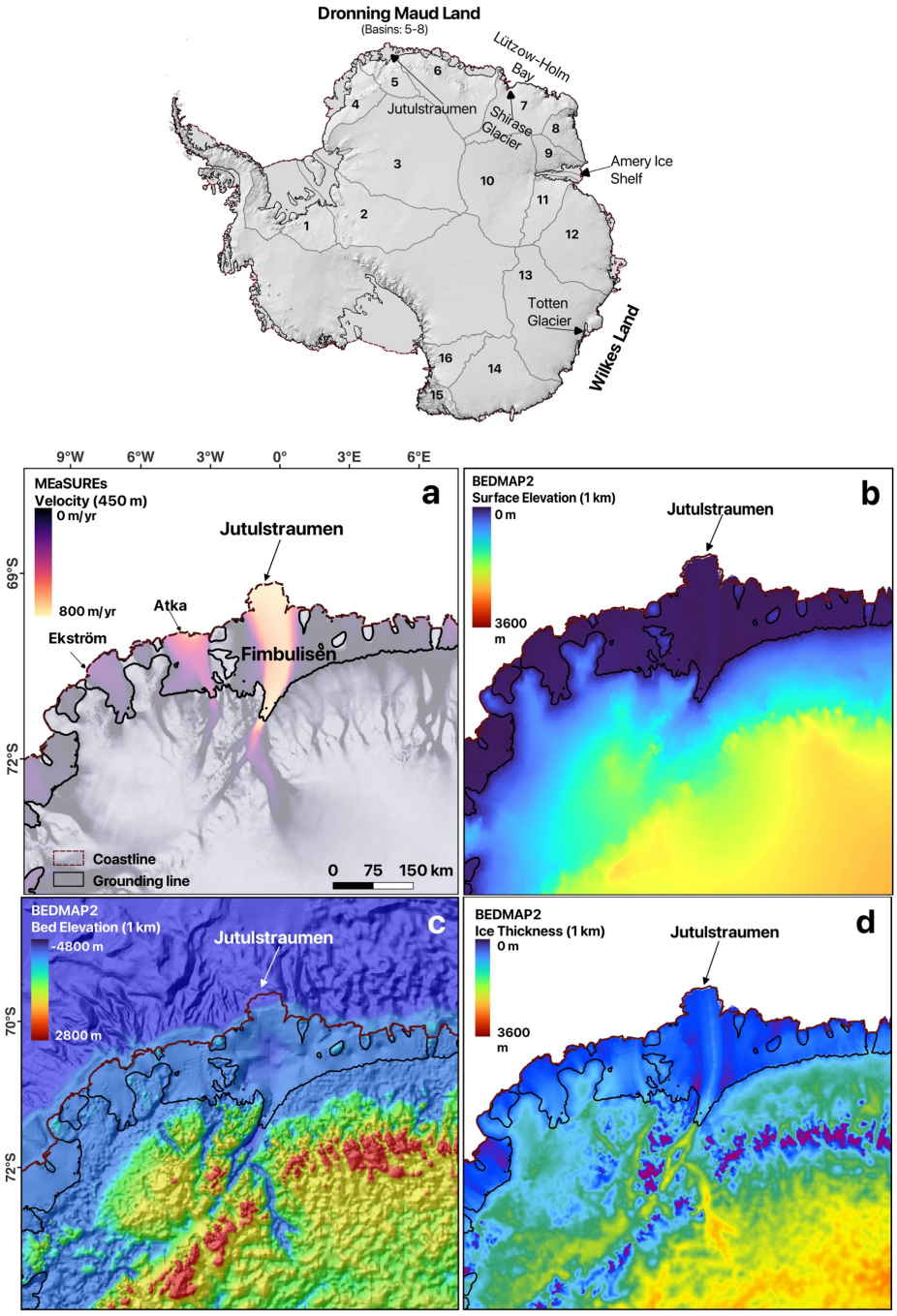

Figure 6.1: *Regional glacial and topographic setting of Jutulstraumen in DML, with numbers referring to drainage basins in the EAIS. (a) MEaSUREs (Rignot et al., 2016) ice flow speed of the study area, (b) Surface elevation of the study area using Bedmap2, (c) Bed elevation of the study area using Bedmap2, (d) Ice thickness of the study area using Bedmap2. Bedmap2 was sourced from Fretwell et al. (2013). The grounding line and coastline were from Rignot et al. (2017). Note that grid spacing in panel 'a' is 400 m and in panels 'b–d' is 1 km.*

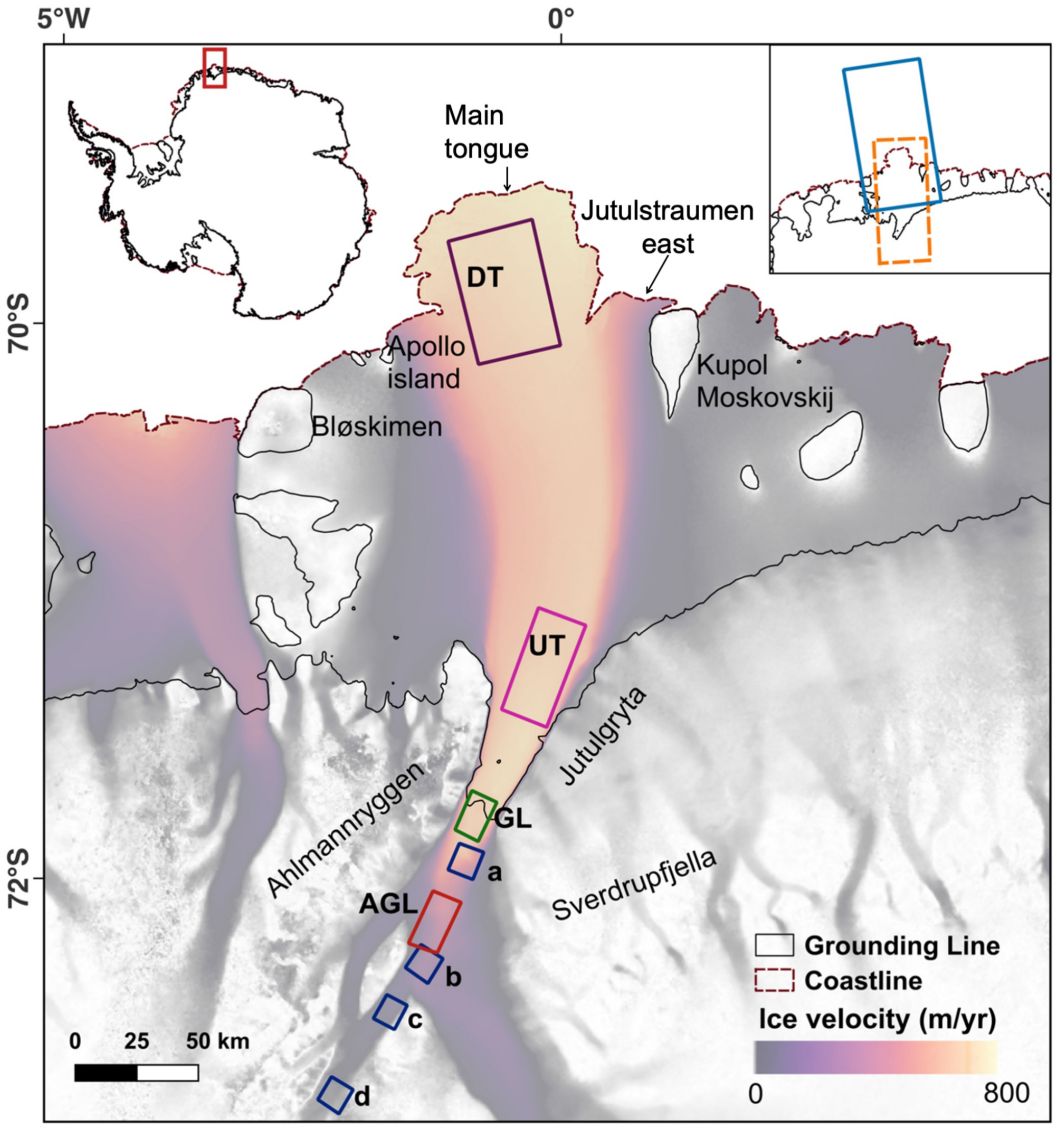

Figure 6.2: *Location map of Jutulstraumen, EAIS overlain with MEaSUREs ice velocity. Grounding line (solid black) and coastline (dashed maroon) is from MEaSUREs (Rignot et al., 2017). Velocity analysis is undertaken in each of the four boxes in the map marked as down-ice tongue (DT), up-ice tongue (UT), grounding line (GL) and above grounding line (AGL). Location of* 20×20 *km sampling boxes (navy blue) used to extract elevation change data from Schröder et al. (2019), Smith et al. (2020) and Nilsson et al. (2022). Each sample box represents a specific distance from the grounding line to understand the surface elevation change at (a) 20 km, (b) 60 km, (c) 80 km and (d) 120 km from the grounding line. Note that the sample boxes used for elevation change were different from those used for ice velocity measurements because the velocity analyses primarily focus on changes at and downstream of the grounding line, whereas the elevation change were designed to capture major changes extending further upstream into the catchment area. ERA-5 2 m air temperature data were extracted from the dashed orange box and Nimbus-7 sea ice concentration data were extracted from the solid light blue box (top right insert).*

6.4 Data and Methods

6.4.1 Ice front position change

In this study, a combination of satellite images from Landsat 1 MSS (1973-1974), Landsat TM 4 and 5 (1989-91), Landsat 7 ETM+ (1999-2013) and Landsat 8 OLI/TIRS (2013-2022) with cloud-free conditions were acquired from the USGS Earth Explorer website (https://earthexplorer.usgs.gov) to map changes in Jutulstraumen between 1963 and 2022 (Table 6.1). In addition, an orthorectified declassified ARGON satellite photograph of 1963 has been used (Kim et al., 2001). A time series of ice front position change was generated between 1963 and 2022 based on the availability of imagery during the austral summer in the broadest sense (October-April). The annual ice front positions were manually digitised using ArcGIS Pro 2.8.2. The changes in position were quantified using the well-established box method which accounts for any uneven changes along the ice front (Moon & Joughin, 2008). Given the shape and orientation of Jutulstraumen's main ice tongue (Fig. 6.4), a curvilinear box was used (Lea et al., 2014). It should be noted that, in addition to the main outlet of Jutulstraumen, there exists an ice front along the eastern margin, separated by a rift, referred to as Jutulstraumen east hereafter (Figs. 2, 4c-d). The curvilinear box method was applied separately here. The errors in the measurements arise from co-registration of the satellite images (Landsat 1-8) with a 2022 Landsat-8 base image (which is quantified as the offset between stable features in image pairs, generally estimated at 1 pixel) and the manual digitisation of the ice front estimated at 0.5 pixels (Miles et al., 2013, 2016, 2018, 2021; Black and Joughin, 2022). The error was quantified using error propagation, considering the varying spatial resolutions of the imagery and the temporal gaps between them. The estimated error ranges from ± 3 m yr^{-1} to ± 63 m yr^{-1} (Table 6.1).

Table 6.1: *Satellite images acquired during this study from 1963 to 2022 and associated error.*

Date	**Satellite**	**Resolution (m)**	**Co-reg. error (m)**	**Mapping error (m)**	**Total error (m yr^{-1})**
October, 1963	ARGON	140			
18/11/1973	Landsat-1 Band4	60	60	30	6
19/01/1985	Landsat-4 Band4	30			
19/01/1985	Landsat-4 Band4	30	30	15	12
08/10/1987	Landsat-4 Band4	30			
08/10/1987	Landsat-4 Band4	30	30	15	3
15/02/2000	Landsat-7 Band8	15			
15/02/2000	Landsat-7 Band8	15	15	7.5	9
02/12/2001	Landsat-7 Band8	15			
02/12/2001	Landsat-7 Band8	15	15	7.5	17
26/11/2002	Landsat-7 Band8	15			
26/11/2002	Landsat-7 Band8	15	15	7.5	4
02/02/2007	Landsat-7 Band8	15			
02/02/2007	Landsat-7 Band8	15	15	7.5	5
05/03/2010	Landsat-7 Band8	15			
05/03/2010	Landsat-7 Band8	15	15	7.5	17
01/03/2011	Landsat-7 Band8	15			
01/03/2011	Landsat-7 Band8	15	15	7.5	16
10/03/2012	Landsat-7 Band8	15			
10/03/2012	Landsat-7 Band8	15	15	7.5	18
18/02/2013	Landsat-8 Band8	15			
18/02/2013	Landsat-8 Band8	15	15	7.5	8
05/04/2015	Landsat-8 Band8	15			
05/04/2015	Landsat-8 Band8	15	15	7.5	19
19/02/2016	Landsat-8 Band8	15			
19/02/2016	Landsat-8 Band8	15	15	7.5	15
25/03/2017	Landsat-8 Band8	15			
25/03/2017	Landsat-8 Band8	15	15	7.5	9
06/03/2019	Landsat-8 Band8	15			
06/03/2019	Landsat-8 Band8	15	15	7.5	16
02/04/2020	Landsat-8 Band8	15			
02/04/2020	Landsat-8 Band8	15	15	7.5	11
05/10/2021	Landsat-8 Band8	15			
05/10/2021	Landsat-8 Band8	15	15	7.5	63
10/01/2022	Landsat-8 Band8	15			

6.4.2 Glacier velocity

Average annual velocities were acquired from the Inter-mission Time Series of Land Ice Velocity and Elevation (ITS_LIVE) annual velocity mosaics (Gardner et al., 2018, 2019) between 2000 and 2018. These velocity mosaics were derived from a combination of Landsat 4, -5, -7 and -8 with the use of auto-RIFT feature tracking with each velocity mosaic having a spatial resolution of 240 m (Gardner et al., 2019). In addition, ENVEO (ENVEO et al., 2021) velocity mosaics were also used to extract velocity between 2019 and 2021. The ENVEO velocity mosaics were derived from repeat-pass Sentinel-1 Synthetic Aperture Radar (SAR) datasets using feature-tracking and were provided monthly between 2019 and 2021 at spatial resolution of 200 m. The monthly ENVEO velocity mosaics were averaged over 12-months for each year between 2019 and 2021 to compare with the ITS_LIVE annual velocity mosaics.

Velocities were extracted from the four regions shown in Fig. 6.2. Following Miles et al. (2018) and Picton et al. (2023), the mean annual velocities were calculated by averaging all available data within each sampling box, provided that data coverage of more than 20% was observed. However, a scarcity of data resulted in limited coverage, especially prior to 2000 (Table 6.2). Error estimates were provided for both datasets (Gardner et al., 2018, 2019; ENVEO et al., 2021), with each pixel having its own error term. The annual error values were then calculated by applying the error propagation formula to the individual error values (grid cells) within each sample box for each ITS_LIVE annual velocity error mosaics (Gardner et al., 2018, 2019). Similarly, using error propagation, the monthly errors were calculated for the ENVEO velocity error mosaics. Subsequently, the annual velocity errors for 2019 to 2021 were computed using error propagation, accounting for the uncertainties in the monthly errors (ENVEO et al., 2021). Some of the velocity measurements were omitted from the analysis given the mean error from each sample box was more than 50% of the mean velocity magnitude (Miles et al., 2018; Picton et al., 2023) (Table 6.2). The accompanying errors associated with the velocity mosaics at DT, UT, GL and AGL ranged from ± 0.5 to ± 163 m yr^{-1}.

Table 6.2: *Percentage of velocity data coverage within each sampling box for Jutulstraumen. Missing values indicate that velocity data omitted from*

Year	**DT**	**UT**	**GL**	**AGL**
2000	-	30	47	22
2002	-	80	64	21
2003	-	31	-	-
2006	-	-	-	-
2007	22	65	64	59
2008		76	66	83
2009		86	59	28
2010	59	98	70	51
2011		88	63	24
2012	-	26	-	-
2013	85	100	100	100
2014	100	100	100	100
2015	100	100	100	100
2016	100	100	100	100
2017	100	100	100	100
2018	100	100	100	100

6.4.3 Elevation change

A range of previously published elevation change datasets were compared to understand any changes along Jutulstraumen. The elevation change measurements were extracted at four locations at 20 km, 60 km, 80 km and 120 km inland of the grounding line (Fig. 6.2). The average monthly elevation change was calculated by averaging all available data within each 20×20 sample boxes (Fig. 6.2) using datasets provided by Schröder et al., (2019), Smith et al., (2020) and Nilsson et al.,

(2022). The accompanying uncertainty estimates provided with the three datasets were use and the monthly error were calculated by applying the error propagation formula to the individual error values (grid cells) within each sample box.

The dataset provided by Schröder et al. (2019) is a combination of multiple satellite missions (e.g., ERS-1/2, Geosat, Seasat, Envisat, ICESat and CrysoSat-2) between 1978 and 2017, but referenced to September 2010. The dataset is provided with a horizontal resolution of 10 km and the associated monthly uncertainties at the sampling boxes range from ±0.1 to ±10 m yr^{-1} (Schröder et al., 2019). Nilsson et al. (2022) provided a monthly elevation change dataset that spans from 1985 to 2020, with reference to December 2013. This dataset was produced as a part of the NASA MEaSUREs ITS_LIVE project. It also combines measurements from several satellite missions (e.g., ERS-1/2, Geosat, Seasat, Envisat, CrysoSat-2, ICESat and ICESat-2) at a horizontal resolution of 1920 m. Monthly mean surface elevation change (SEC) was extracted from the same sampling boxes. The accompanying monthly uncertainties at the sample locations range from ±0.05 to ±3 m yr^{-1}. To allow a more direct comparison between the datasets, the SEC measurements from Schröder et al. (2019) were recalculated relative to December 2013, aligning with the reference year used in Nilsson et al. (2022). The two datasets were analysed from April 1992, as it is the earliest common data availability month at all four sample locations. The 5-year moving averages for the two datasets were then calculated. The errors associated with the 5-year moving average were determined from monthly errors using error propagation.

Additionally, the dataset provided by Smith et al. (2020) is derived from ICESat and ICESat- 2 missions, spanning from 2003 to 2019, with horizontal resolution of 5 km (Smith et al., 2020). The associated uncertainties range between ±0.001 to ±0.006 m yr^{-1}. To compare the three datasets, the mean rates of elevation change in each box were calculated for Schröder et al. (2019) from 2003-2017, Smith et al. (2020) from 2003-2019 and Nilsson et al. (2022) from 2003-2020 (Table 6.3).

6.4.4 Grounding line changes

Five previously published grounding line datasets spanning various dates between 1992 and 2018 were analysed, along with new grounding line positions mapped in this study using manual digitisation between 1990 and 2022 (Fricker et al., 2009; Christie et al., 2016). Together, all these datasets were derived through either manual delineation or Differential Interferometric Synthetic Aperture Radar (DInSAR) techniques. It should be noted that each dataset identifies distinct features within the grounding zone, which makes comparison of changes through time more challenging (Fig. 5.2, Fricker et al., 2009; Brunt et al., 2010). For example, the MEaSUREs grounding line dataset (Rignot et al., 2016) detects the landward limit of tidal flexure (F), ASAID dataset (Bindschadler et al., 2011) detects the break-in slope, I_b, whereas this study detects the local elevation minimum, I_m.

In this study, the grounding line positions were manually delineate using Landsat 4-8 images, during austral summers (October to April) between 1990 and 2022, following the methods outlined in Fricker et al. (2009) and Christie et al. (2016). As optical satellite imagery cannot precisely determine the "true" grounding line (G), the break-in-slope (I_b) or the local elevation minimum (I_m) (Fig. 5.2) were generally used as a proxy for G. Here, the I_m was identify as a shadow-like change in the brightness of the imagery (Fricker and Padman, 2006; Fricker et al., 2009; Bindschadler et al., 2011; Christie et al., 2016, 2018) and digitised it on the georeferenced cloud-free Landsat images. To determine whether the mapped grounding line advanced or retreated, the box method (Moon & Joughin, 2008) was used, with the box extending to the ends of the mapped grounding lines. This method was used because it provides an average grounding line position change across the glacier. A positional uncertainty of around ±100 m was also estimated, following Bindschadler et al. (2011) and Christie et al. (2016).

In addition, among the manually delineated grounding line datasets is the Antarctic Surface Accumulation and Ice Discharge (ASAID) dataset, which was created using a combination of photoclinometry applied to satellite imagery (primarily Land-

sat 7 ETM+), elevation profiles from ICESat data and visual analysis of optical satellite imagery. The grounding line was digitised on Landsat 7 ETM+ images between 1999 and 2003 by identifying changes in image brightness indicative of the break-in-slope (I_b). The average estimated positional uncertainty associated with the ASAID grounding line position for outlet glaciers is ±502 m (Bindschadler et al., 2011). Similarly, The Mosaic of Antarctica (MOA) grounding line dataset was derived by manually delineating the most seaward break-in slope (I_b) on highly contrast-enhanced MOA surface morphology images (Scambos et al., 2007) for 2004 and 2009, with an associated uncertainty of ±250 m (Harran et al., 2005, 2014). Furthermore, some grounding line positions were also derived using Differential Interferometric Synthetic Aperture Radar (DInSAR). The Making Earth Science Data Records for Use in Research Environments (MEaSUREs) dataset provides grounding line positions between 1992 and 2014, identifying the landward limit of tidal flexure (F). This dataset was derived using DInSAR from Earth Remote Sensing Satellites 1 and 2 (ERS-1 and ERS-2), RADARSAT-1, RADARSAT-2, the Advanced Land Observing System Phased Array type L-band Synthetic Aperture Radar (ALOS PALSAR), Cosmo Skymed, and Copernicus Sentinel-1 (Rignot et al., 2016). The associated uncertainty with the dataset is estimated at ±100 m (Rignot et al., 2016). The European Space Agency's Antarctic Ice Sheet Climate Change Initiative (AIS CCI) has also been derived using DInSAR from ERS-1, ERS-2 and Sentinel-1 imagery collected between 1996 and 2020, with an estimated error of ±200 m. In this dataset, the upper limit of vertical tidal motion has been used as an approximation of flexure point (F) in the grounding zone. The Mohajerani et al. (2021) dataset employs a fully convolutional neural network to automatically delineate grounding lines for 2018 by identifying the landward limit of tidal flexure (F) using DInSAR data, with associated uncertainty of ±232 m.

6.4.5 Structural glaciological mapping

To understand the structural glaciology of Jutulstraumen, some of the major surface structural features were manually mapped on selected cloud-free optical satellite imagery in 1986, 2001, 2015 and 2022 using bands with highest spatial resolution, e.g.

band 4 in Landsat 1-4 and band 8 for Landsat 7 ETM+ and Landsat 8 OLI/TIRS (Holt et al., 2013; Table 6.1). The major structural features included rifts, fractures, crevasses, longitudinal flow features (flowstripes, flow bands, streaklines), surface expressions of major basal channels, ice rises and ice rumples. The criteria used to identify these various features is same as the approach taken by Glasser et al. (2009) and Holt et al. (2013), except for the identification of basal channels which has been adapted from Alley et al. (2016).

Table 6.3: *Ice-shelf features, examples, identifying criteria and significance adapted from Glasser & Scambos (2008); Glasser et al. (2009); Humbert & Steinhage (2011); Holt et al. (2013).*

Feature	Example	Structure	Identification	Significance
Ice front	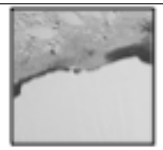	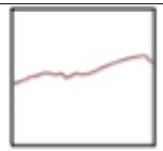	Sharp transition from ice-shelf margin to open ocean or sea ice. Sea ice is often seen as a darker shade than glacial ice in optical satellite imagery.	Indicates the maximum ice-shelf extent for a particular time period. Successive images can be used to track fluctuation of the ice front to understand ice dynamics.
Fracture		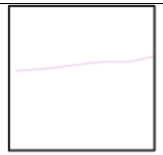	Appears as narrow, linear cracks visible as a sharp line.	Indicative of stress within the ice shelf.
Rift	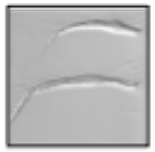		Fractures on the ice shelf with visible opening, often forming perpendicular to the flow direction. Rifts may be filled with mélange, seawater, or sea ice and penetrate the entire shelf thickness.	Indicative of ice-shelf integrity; rift tracking is a common method for estimating ice-flow velocity.
Crevasse field		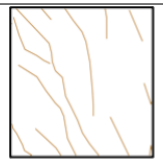	Network of surface fractures appearing as dark (open or water-filled) or bright (snow-covered) lines, often forming distinct zones.	Formed under widespread tensile stress, creating organised fracture fields perpendicular to maximum tension.
Fracture traces			Shallow troughs or surface lines similar to rifts but without clear openings, often snow-filled.	Represent structural weaknesses and influence ice-ocean mass and energy exchange; may reflect basal crevasse expression.

Table 6.3: (*continued*)

Feature	Example	Structure	Identification	Significance
Longitudinal surface structures	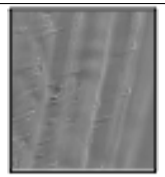	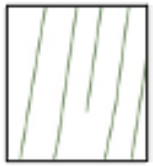	Long, linear features parallel to flow, visible as alternating dark/light lines from shaded relief.	Indicate faster flow regions and suture zones between different flow units.
Surface expression of basal channels			These features appear as surface depressions starting at the GL, displaying abrupt shifts in their path. They usually align with the ice-flow direction and gradually dissipates towards ice-edge. These features appear to deepen or widen on the ice shelf (Alley et al., 2016).	Indicates basal melt and erosion of ice-shelf base. This might lead to development of crevasse zones and potentially weaken the ice shelf (Alley et al., 2016).
Ice rises			Elevation of the surface of ice shelf that disturbs the ice flow, indicated by smooth surface.	Indicates area of ice shelf grounded by local bedrock.
Mélange zone	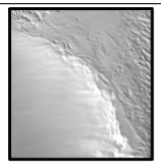		Region that appears as filled with icebergs ad sea ice, appears to have varying ice textures and wider than rift (Humbert & Steinhage, 2011).	It represents a typical shear margin.
Grounding zone			Sudden break-in slope and presence of intense crevasses. Sometimes melt water ponds tend to form at the grounding zone.	Intersection between grounded ice and floating ice (Vaughan, 1995).

To measure in more detail the rifts that propagate from the ice front into the ice tongue in more detail (Fig. 6.3), a total of 200 cloud-free images were selected. These images were collected during the austral summers between 2003 and 2022. They were obtained from the Moderate Resolution Imaging Spectroradiometer (MODIS) and have a spatial resolution of 250 m. For the purposes of this study, the austral summer is considered between October to early April (cf. Walker et al., 2015). Following the methodology in Fricker et al. (2005), the rift length was measured from a consistent point at the ocean-end of the rift to the 'rift tip' (Fig. 6.3). The 'rift tip' was identified as the first point on the glacier where the rift pixel is discernible, i.e., the point in the image where rift occupied enough of the pixel to provide a good contrast against the background (Fricker et al., 2005; Walker et al., 2015; Holt & Glasser, 2022). Since these rifts were located at the ice front, it is possible that the ocean-end of the rifts may undergo discrete minor calving events between subsequent images, potentially leading to rift shortening. In such cases, when calving leads to rift shortening, the rift is assigned a new name to reflect the updated starting point. For example, RW3 becomes RW6, after the calving event in 2011 (Fig. 6.9a). This results in a consistent start point for the rifts across all subsequent images, enabling accurate measurement of rift propagation into the ice tongue. In addition, the average annual and austral summer propagation rates were determined by applying a linear fit to the time series data of rift lengths utilising the least squares method, following methodology outlined in Walker et al. (2015). The linear regression analysis was performed to estimate slopes for each summer season for each rift (Case A, Table 6.5, 6.6). Case B represents the linear fit applied to the differences in rift lengths between the end of one summer and the start of the next summer. Case C denotes a linear fit applied to the entire dataset of rift lengths for each rift (Table 6.5, 6.6).

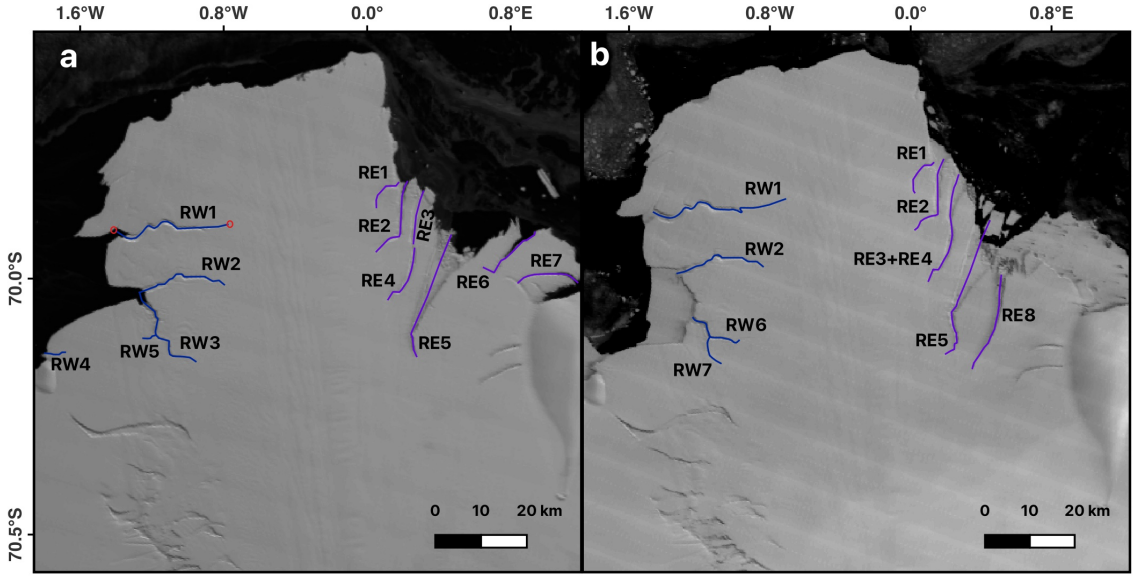

Figure 6.3: *(a-b) Rifting of the ice-shelf front monitored in this study (blue lines:western rifts (RW) and purple lines:eastern rifts (RE)) with background image: (a) MODIS images acquired on 13 March 2006 and (b) acquired on 16 December 2016. (b) shows the rifts formed later in the study period (RW6, RW7, RE8). It also shows that rift RE3 lengthened and joined RE4 (later named RE3+RE4). Note: Red circles in (a) denote start and end points for RW1, a front-initiated rift.*

6.4.6 Relationship between rift propagation and environmental variables

6.4.6.1 Air temperature

Daily mean near-surface (2 m) air temperature data were extracted for all austral summers between 2003 and 2022, which is provided at a 0.25 degree (30 km) from ERA5 reanalysis data (Hersbach et al., 2023). To understand the link between rift propagation and temperature, the positive degree-days (PDDs) were calculated using mean degree-hour method (Day, 2006). PDD is defined as the total sum of hourly averaged temperatures per day above 0°C. The PDDs were summed over each season, and the relationship between seasonal PDD and rift propagation rate was assessed to determine the presence of any significant correlation.

6.4.6.2 Sea ice concentration

Sea-ice concentration data were extracted from Nimbus-7 SMMR and DMSP SSM/I-SSMIS Passive Microwave Data V002 (DiGirolamo et al., 2022). This region includes multi-year sea ice and mélange that fills the rift openings. The spatial resolution of the sea ice concentration dataset is 25 km. As sea-ice concentration and rift lengths both have strong seasonal signals, a linear regression was performed to understand if changes in sea-ice concentration influences the propagation rate (Walker et al., 2015). To directly compare the variability in sea ice concentration with rift propagation rates, the seasonal component of sea-ice concentration was first removed.

6.5 Results

6.5.1 Ice front position

The earliest images date from 1963 and 1973 and confirm that a large calving event occurred between these dates, resulting in around 60 km of retreat (Fig. 6.4). The analyses indicate that the ice front gradually advanced between 1973 and 2022 and that it is currently around 30 km landward from its near maximum extent prior to the calving event in 1967. Furthermore, there is little evidence that the shape of the ice front has exhibited any major change between 1973 and 2022 (Fig. 6.4), suggesting no major calving events have taken place over this period. In addition, the ice front advance rate showed limited changes with an average of $\sim$ 740 m yr^{-1} between 1985 and 2022, albeit with small interannual variations in the ice front advance rate (Fig. 6.4e).

At the smaller Jutulstraumen east outlet, the ice front retreated by $\sim$ 2.3 km between 1987 and 2000, followed by a slight advance of $\sim$ 1 km between 2000 and 2002, a large retreat of $\sim$ 10 km between 2002 and 2007, and with a further re-advance of $\sim$ 6 km between 2007 and 2022 (Figs. 6.4c, d).

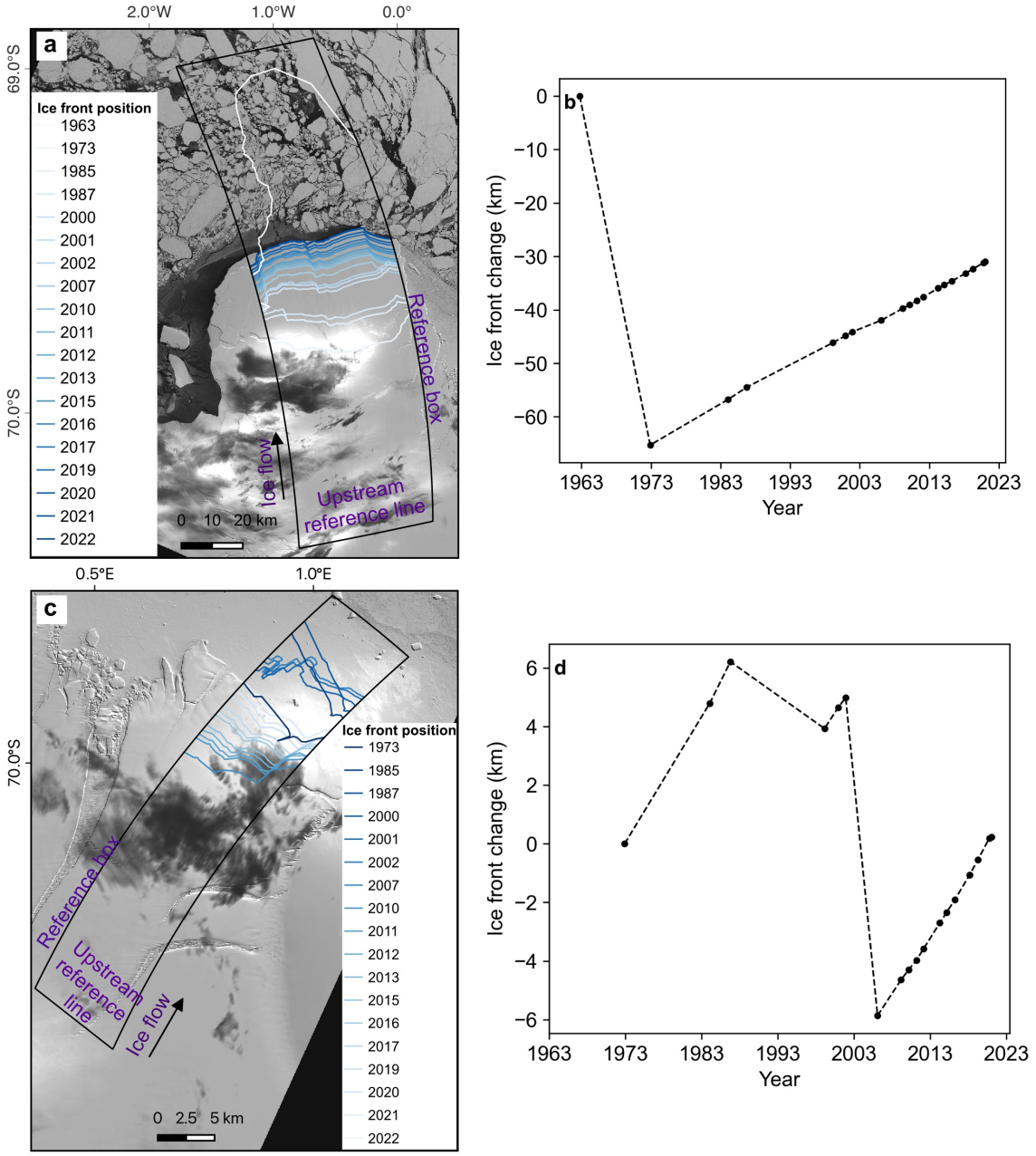
a
2.0°W
1.0°W
0.0°
69.0°S
70.0°S
Ice front position
1963
1973
1985
1987
2000
2001
2002
2007
2010
2011
2012
2013
2015
2016
2017
2019
2020
2021
2022
Reference box
Ice flow
Upstream reference line
0 10 20 km
b
Ice front change (km)
0
−10
−20
−30
−40
−50
−60
1963
1973
1983
1993
2003
2013
2023
Year
c
0.5°E
1.0°E
70.0°S
Ice front position
1973
1985
1987
2000
2001
2002
2007
2010
2011
2012
2013
2015
2016
2017
2019
2020
2021
2022
Reference box
Upstream reference line
Ice flow
0 2.5 5 km
d
Ice front change (km)
6
4
2
0
−2
−4
−6
1963
1973
1983
1993
2003
2013
2023
Year

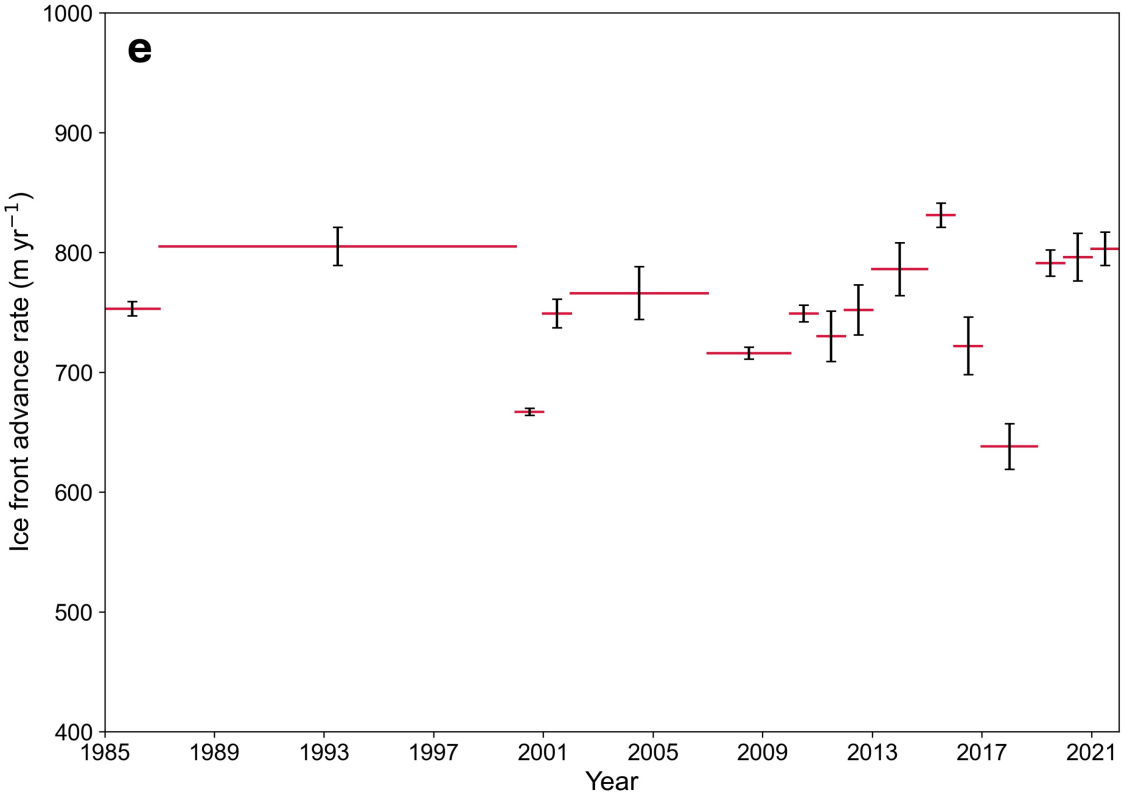

Figure 6.4: *(a) Mapped ice front position of the main tongue of Jutulstraumen between 1963 and 2022. (b) Ice front position change of Jutulstraumen's main tongue during 1963–2022 from the black curvilinear box delineated in (a). (c) Mapped ice front position of the eastern extension of Jutulstraumen between 1973 and 2022 (d) Ice front position change of eastern extension of Jutulstraumen during 1963–2022 from the black curvilinear box delineated in (c). The background image in (a) and (c) is a Landsat- 8 image from 13 October 2021. (e) Advance rate of main tongue of Jutulstraumen between 1985 and 2022. The red bars represent average advance rates over each period of measurement and black bars represent associated error (see Table 6.1).*

6.5.2 Glacier velocity

The glacier velocity trend along the floating ice tongue showed little overall change between 2000 and 2021, with only minor interannual fluctuations (Fig. 6.5). As a result, the mean annual velocity was estimated at $\sim$ 720 $\pm$ 66 m yr^{-1} across all sampling boxes over the floating ice tongue. This estimated glacier velocity is consistent with the mean rate of advance described in the previous section, which was calculate as around 740 m yr^{-1}, albeit with some minor fluctuations between 1985 and 2022 (Fig. 6.5).The mean velocity is in the same range at DT, UT and GL,

but is much less at box AGL (Figs. 6.2, 6.5). The associated uncertainties ranged from ±0.5 to ±163 m yr^{-1} (Fig. 6.5). Although a 10% increase in velocity at UT between 2011 and 2012 was observed , the absolute value of increase (55 m yr^{-1}) is smaller than the associated error (±118 m yr^{-1}). In addition, the 15% decrease in velocity at AGL between 2008 and 2009, with an absolute velocity decrease of 61 m yr^{-1} is smaller than the associated error of ±62 m yr^{-1}.

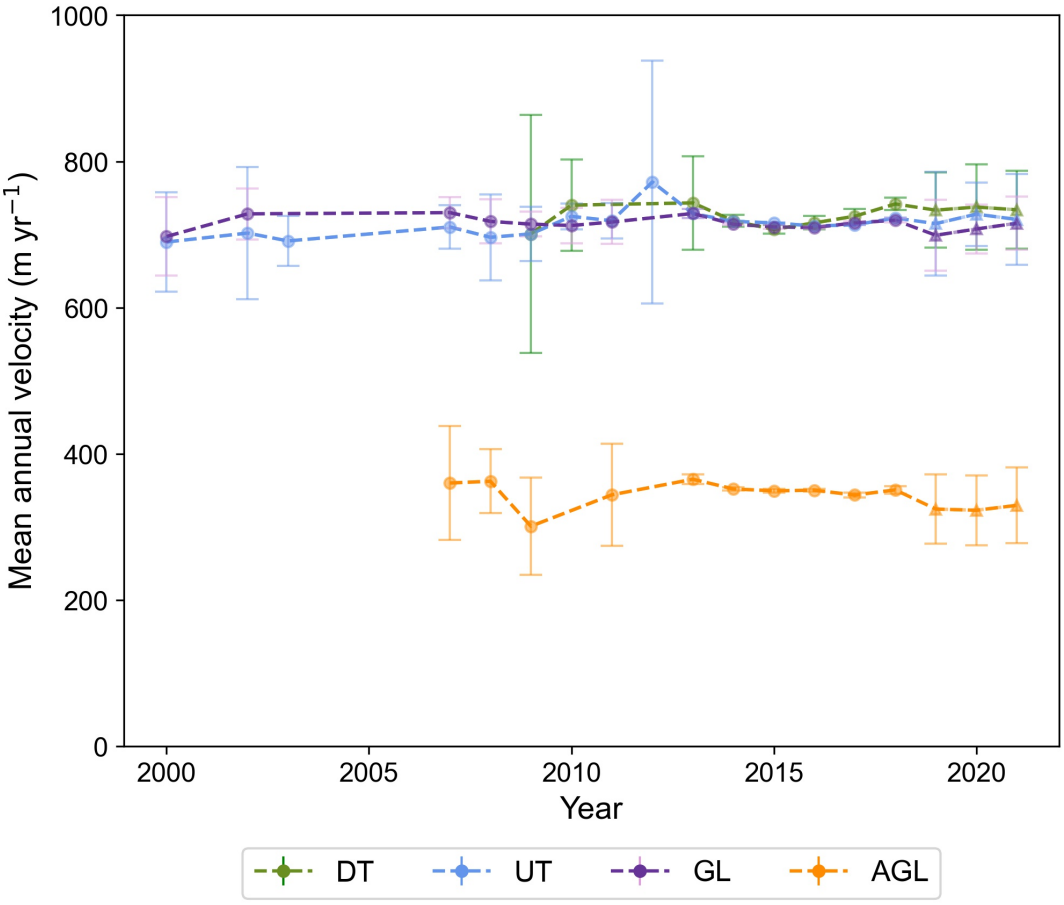

Figure 6.5: *Trends of mean annual velocity extracted from Jutulstraumen at the four locations at down-ice tongue (DT), up-ice tongue (UT), grounding line (GL) and above the grounding line (AGL) (see Fig. 6.2 for location). Velocity is extracted from ITS_LIVE (circle) and ENVEO (triangle) velocity mosaics between 2000 and 2021 (Gardner et al., 2019; ENVEO et al., 2021).*

6.5.3 Elevation change

The results indicate that elevation change trends obtained from Schröder et al. (2019) and Nilsson et al. (2022) were less comparable and associated with higher uncertainties pre-2003, with notably inconsistent trends between 1992 and 2003 at all sample locations (20, 60, 80, and 120 km inland of GL). However, a general agreement between the two datasets is observed after 2003, with a clear thickening trend of the grounded ice observed from around 2003. It is also worth noting that both datasets manifest some interannual variability (Fig. 6.6). Nonetheless, an overall thickening was observed when averaged across all sampling boxes, at a rate of $+0.11 \pm 0.1$ m yr^{-1} between 2003-2017 (Schröder et al., 2019) and $+0.14 \pm 0.04$ m yr^{-1} between 2003 and 2020 (Nilsson et al., 2022) upstream of the grounding line. Furthermore, a similar pattern of thickening of the grounded ice is also observed in the dataset provided by Smith et al. (2020) with an average rate of $+0.17 \pm 0.005$ m yr^{-1} (Table 6.3).

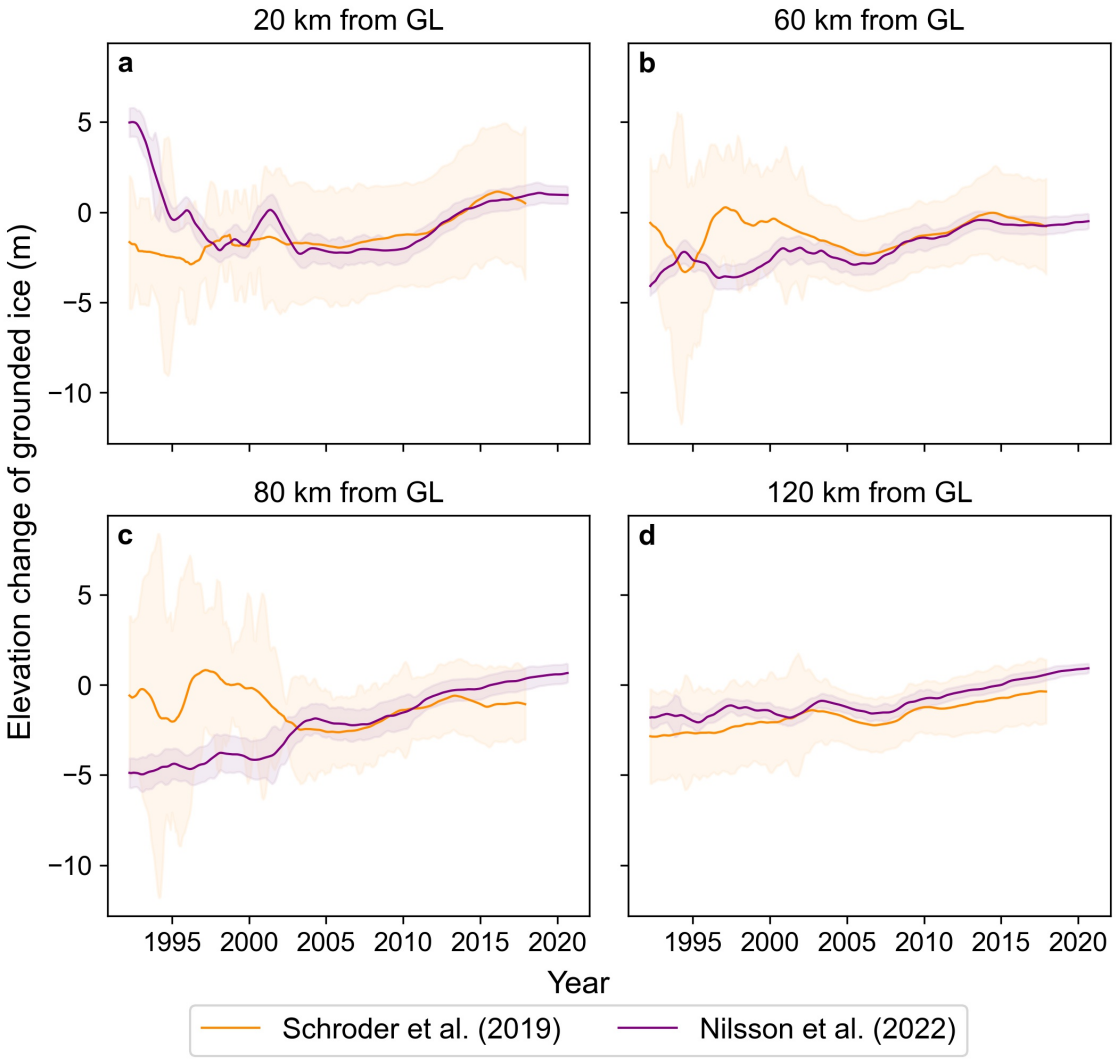

Figure 6.6: *Monthly elevation changes of the grounded ice observed at four locations, i.e., (a) 20 km, (b) 60 km, (c) 80 km and (d) 120 km inland from the grounding line (GL) at Jutulstraumen between 1992 and 2020, obtained from Schroder et al. (2019) and Nilsson et al. (2022). The solid lines represent 5-year moving averages and the shaded area represents the corresponding error propagation.*

Table 6.4: *The average rate of thinning and thickening of grounded ice observed at four locations inland of the grounding line of Jutulstraumen between 2003 and 2020 using dataset provided by Schröder et al. (2019), Nilsson et al. (2022) and Smith et al. (2020).*

Distance from GL (km)	**Schröder et al. (2019)** (2003–2017) (m yr^{-1})	**Nilsson et al. (2022)** (2003–2020) (m yr^{-1})	**Smith et al. (2020)** (2003–2019) (m yr^{-1})
20	$+0.14 \pm 0.10$	$+0.18 \pm 0.04$	$+0.15 \pm 0.004$
60	$+0.11 \pm 0.10$	$+0.10 \pm 0.03$	$+0.19 \pm 0.006$
80	$+0.10 \pm 0.10$	$+0.17 \pm 0.04$	$+0.14 \pm 0.003$
120	$+0.07 \pm 0.01$	$+0.11 \pm 0.02$	$+0.17 \pm 0.001$

6.5.4 Grounding line

In this section, a comprehensive compilation of all available grounding line positions is present, categorised according to the two primary methodologies of determining grounding line position detailed in section 6.4.4. Fig. 6.7a shows the grounding line positions acquired using DInSAR. Notably, the DInSAR-derived data for Jutulstraumen in 1994 were provided by both MEaSUREs (4/3/1994) and AIS CCI (derived from double differences of three subsequent images: (4/3/1994, 7/3/1994, 10/3/1994) coinciding on the same date. The grounding line positions from these two datasets for 1994 align closely.

More recently, the dataset provided by Mohajerani et al. (2021), which also used DInSAR data as input for a fully convolutional neural network, included clusters of grounding line positions (green) and pinning points (yellow) for 2018. Note that within the cluster that is furthest upstream, there were some grounding line positions that correspond to the flexure location or the hinge line, F (Fricker and Padman, 2006; Fricker et al., 2009; Friedl et al., 2020) and these align closely with the 1994 grounding line positions provided by MEaSUREs (Rignot et al., 2016) and the AIS

CCI (Fig. 6.7a). This overlap at the flexure location suggests a consistency between the three datasets. Meanwhile, other grounding line positions within this cluster were associated with localised features of the grounding zone such as pinning points (Fig. 6.7a). Overall, this suggests limited or no change in grounding line position over the 24-year period between 1994 and 2018.

Fig. 7b shows the grounding line position determined by previously published manual delineations of the break-in slope, I_b (ASAID and MOA) and of the assumed local elevation minimum, I_m, mapped in this study. The ASAID and MOA grounding line positions were digitised at similar locations, showing limited change over time. However, the grounding line positions obtained in this study exhibited a slow advance of $\sim$ 200 m ($\sim$ 6 m yr^{-1} on average) between 1990 and 2022 (Fig. 6.7b).

Fig. 7c compares the manually delineated grounding line positions (ASAID, MOA, this study) with the earliest available grounding line positions derived from DInSAR (MEaSUREs). It is evident from Fig. 7c that the grounding line positions obtained from MEaSUREs and AIS CCI which identifies the landward limit of the ice flexure caused by tidal movement (F), were consistently located much further up the ice tongue compared to those obtained from manual delineation of break-in slope, I_b (ASAID, MOA) and the local elevation minimum, I_m (this study). For example, the 1994 DInSAR-derived grounding line position is $\sim$ 18 km upstream from the 1993 grounding line position (I_m) identified in this study. Similarly, the furthest upstream grounding line position from the 2018 DInSAR-derived cluster provided by Mohajerani et al. (2021) is $\sim$ 16 km upstream of the 2018 grounding line position identified in this study. This clearly emphasises that grounding line positions acquired using different methods were not directly comparable as they were recording different features of the grounding zone (Fricker and Padman, 2006; Fricker et al., 2009; Friedl et al., 2020; Picton et al., 2023). However, taken together, there is little evidence for a major change in grounding line position at Jutulstraumen (Fig. 6.7c), although the manually digitised method suggests there may have been a very small ($\sim$ 200 m) advance, with approximately $\pm$100 m uncertainty associated with it (see white to blue lines in Fig. 6.7b).

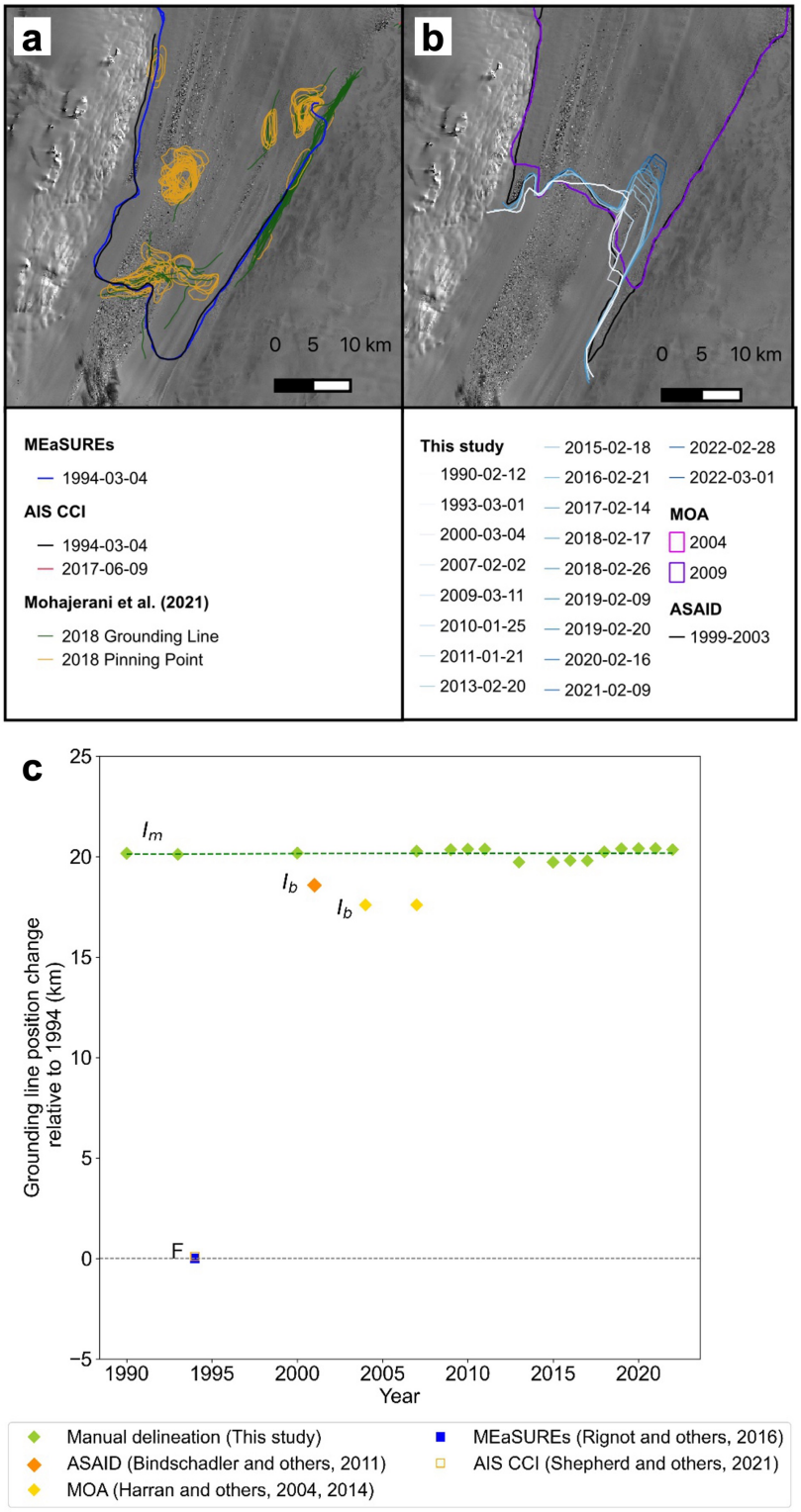

Figure 6.7: *Grounding line position change of Jutulstraumen based on different GL datasets. (a) Grounding line position based on vertical motion at the floating part using DInSAR data (MEaSUREs, AIS CCI and Mohajerani et al., 2021). (b) Grounding line position based on manual delineation of break-in slope (ASAID, MOA, this study). (c) Change in grounding line position relative to observed 1994 position from all datasets.*

6.5.5 Structural glaciology

The features on Jutulstraumen ice tongue, based on the criteria in Table 6.3, were displayed in Fig. 6.8. The western side of the ice tongue has previously been observed to be heavily rifted (cf. Humbert & Steinhage, 2011). Several distinct rifts filled with sea ice/mélange have lengthened during the observation period, predominantly on the western side, with additional rifts forming and expanding on the eastern side near Jutulgryta (Figs. 2, 8). The western side also shows a consistent area of fracture traces, with a slight increase in these features noted over the study period (Fig. 6.8). Moreover, a surface crevasse field is located near Ahlmannryggen on the western side, with a smaller crevasse field on the eastern side near Jutulgryta (Figs. 2, 8, Humbert & Steinhage, 2011). A mélange zone has been observed between the western crevassed field and Ahlmannryggen. Additionally, during the observation period (1986 to 2022), rifts at the ice front continued to propagate, leading to small calving events on both the western and eastern margins of the ice tongue (Fig. 6.9)

Although changes in all identified features (Fig. 6.8) were not quantified in this study, 15 of the largest rifts propagating inland from the ice front were recognised and quantified, as they may play an important role in future calving events.

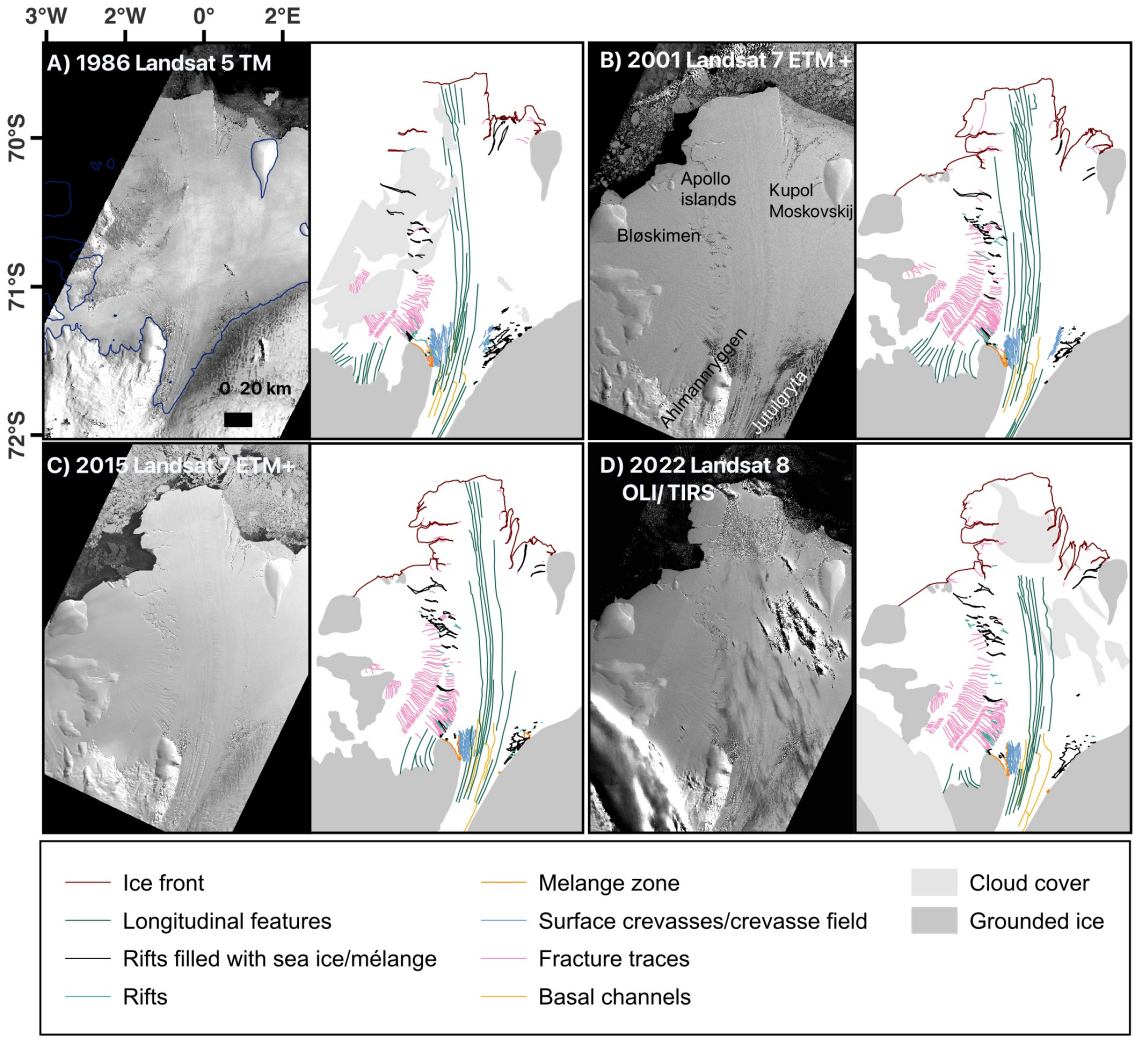

Figure 6.8: *Structural evolution of Jutulstraumen illustrating widespread rifting from 1986 to 2020. Increased rifting is apparent in the western side of the glacier. The dark blue line in the 1986 satellite image is the MEaSUREs grounding line v2 (Rignot et al., 2017).*

6.5.6 Rift propagation and links to environmental variables

We examine seven major rifts on the western and eight on the eastern margin of Jutulstraumen (Fig. 6.3) using satellite imagery (MODIS) from 2003 to 2022. Note that these rifts appear to be a consequence of the ice shelf interaction with the topography near the ice front. For example, the rifts on the west appear to be related to re-activation of pre-existing fractures as the ice pulls away from the headland. On the eastern margin, however, the rifts appear to be associated with the ice

shelf's detachment from the ice rise (Kupol Moskovskij) at the front of the glacier. Overall, during the study period, most of these rifts lengthened during the austral summer and there was minimal change during the austral winter. Furthermore, in some seasons, the rift length at the beginning of austral summer was lower than the end of previous summer. This could be due to rift 'healing', snow accumulation at the rift tip, or the presence of sea ice/mélange in the rift cavity resulting in a lower estimation of rift length. Nevertheless, the 19-year timeseries compiled from MODIS imagery shows an overall increase in the lengths of all the rifts measured at different propagation rates (Table 6.5, 6.6, Fig. 6.10). Fig. 6.10 shows seasonal variation in rift propagation superimposed on a multi-year linear trend.

All seven rifts monitored at the western side of Jutulstraumen exhibited increases in length, with periods of short-term decrease, at an overall long-term average rate of $\sim$ 2.4 m d^{-1} from 2003 to 2022. In comparison, rifts on the eastern margin propagated at a slightly slower rate of $\sim$ 0.7 m d^{-1}. As they lengthened on the eastern margin, rift widening was also observed. For example, rift RE5, which formed around 1986, widened by $\sim$ 3 km between 2003 and 2022 ($\sim$ 0.4 m d^{-1}) and consequently opened-up towards the ocean and filled with sea ice/mélange (Fig. 6.3a). On the western margin, RW4 had the fastest long-term propagation rate ($\sim$ 8 m d^{-1}) while RW2 had the slowest rate ($\sim$ 0.2 m d^{-1}; Fig. 6.10, Table 6.5). On the eastern margin, RE8 had the fastest long-term rate ($\sim$ 3.2 m d^{-1}), while RE1, RE2 and RE7 had the slowest rate ($\sim$ 0.1 m d^{-1}; Fig. 6.10, Table 6.6). The highest propagation rates have been documented in those rifts that were relatively short-lived.

Most rift propagation rates were found to decrease over time. For instance, the rates during 2003-2011 were higher than those between 2012 and 2022, specifically for RW1 (2003-2011: 3.1 m d^{-1} and 2012-2022: 0.3 m d^{-1}) and RW2 (2003-2011: 0.9 m d^{-1} and 2012-2022: 0.1 m d^{-1}). In addition, smaller rifts exhibited higher propagation rates. On the western margin, RW4 and RW5 showed propagation rates of approximately 8 m d^{-1} and 1.6 m d^{-1}, respectively, until the calving event in 2011 (Table S4), when a small part ($\sim$ 183 km^2) of the ice front calved off (Fig. 6.9a). Similarly, the rifts RE6 and RE7 propagated at $\sim$ 1.4 m d^{-1} and $\sim$ 0.1 m d^{-1} from

2003 until a calving event in 2006 (Table 6.6), when a small part ($\sim$ 128 km^2) of the ice front calved off (Fig. 6.9b).

Note that, on the western margin, RW3 (yellow) was observed until 2011 when a small part calved off and the remaining fragment of RW3 was re-named as RW6 (violet) (Fig. 10a). On the eastern margin, RE3 (green) and RE4 (light pink), which were separate until 2009, merged in the latter half of 2009 and were renamed as RE3+RE4 (brown) (Fig. 6.10b).

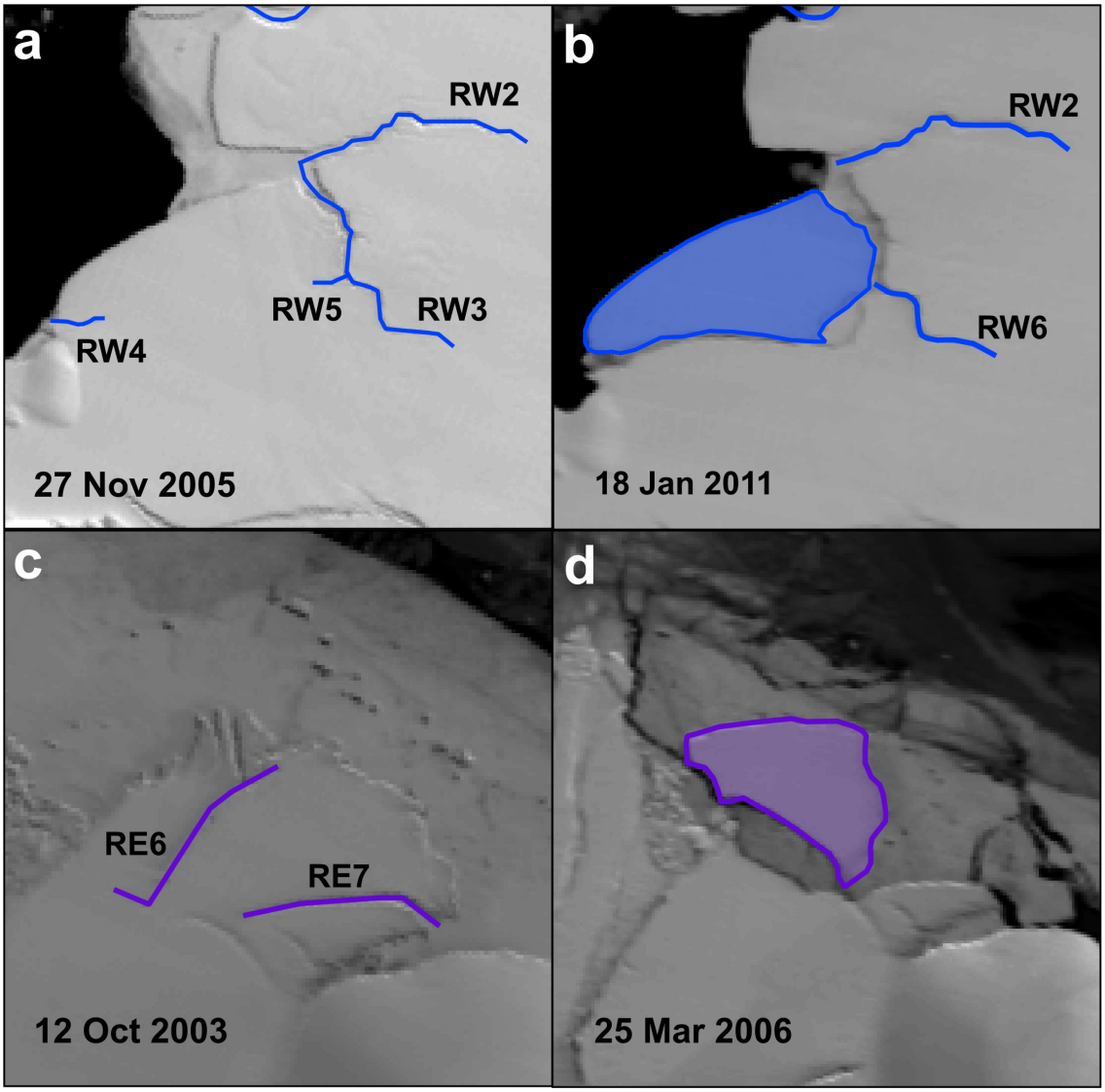

Figure 6.9: *(a) Shows the calving of a small part on the eastern margin of Jutulstraumen between 27 November 2005 and 18 Oct 2011 due to propagation of rifts RW4 and RW5. (b) Shows the calving of a small part on the western margin of Jutulstraumen between 12 October 2003 and 25 March 2006 due to propagation of rifts RE6 and RE7.*

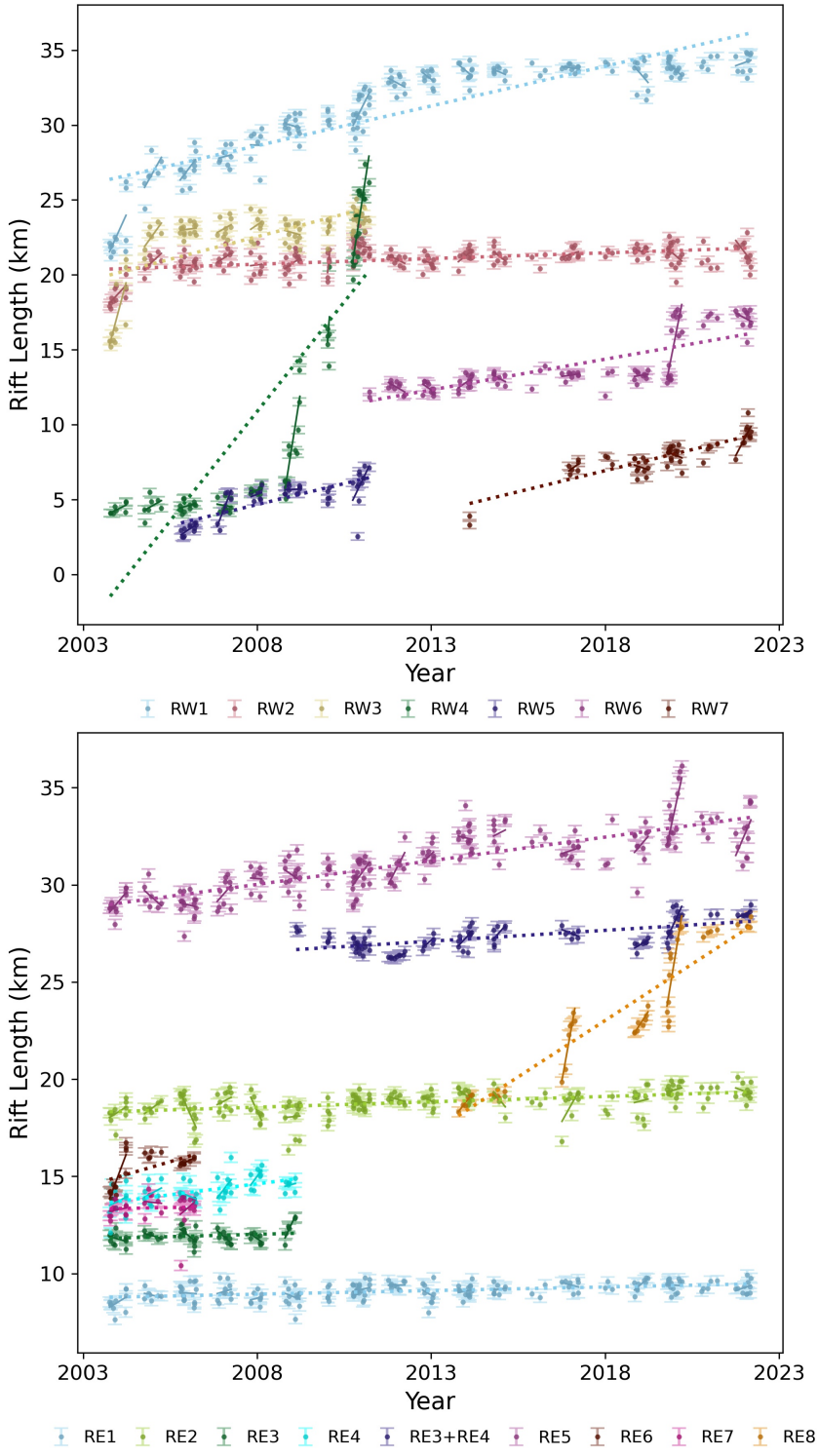

Figure 6.10: *Measured rift lengths derived from MODIS imagery between 2003 and 2022 on the (a) western side and (b) eastern side of Jutulstraumen. The error bars represent 1 pixel, where pixel size for MODIS is 250 m. MODIS times series for RW1 to RW7 and RE1 to RE8 with linear regression analysis. Solid lines show the linear regression performed to estimate slopes for each summer season for each rift (Case A, Table 6.5, 6.6)). Dashed lines denote a linear fit applied to the entire dataset of rift lengths for each rift (Case C. Table 6.5, 6.6).*

The patterns of rift propagation have been observed to be highly variable, ranging from 0 m d^{-1} to 100 m d^{-1}, within each austral summer season (Fig. 6.10). The regression analysis determined that the propagation rates for each summer season were significantly different from each other between 2003 and 2022 at 95% confidence interval (Table 6.5, 6.6). In addition, the differences between rift length at the end and beginning of austral summer were mostly less than one pixel (< 250 m), with instances of rift healing also observed, indicating minimal rift propagation during winter period (Walker et al., 2015). For Case C, the linear fit applied to the entire dataset showed variable rift propagation rates, as detailed in Tables 6.5 and 6.6. This analysis underlines the complex and variable nature of rift propagation rates.

Further analysis of factors that influence rift propagation rates reveals that the relationship between these rates and environmental conditions have no significant correlation (see Figs. 6.12-S15). The 2 m air temperature observed over the sample box, covering the fast-flowing part of the glacier (Fig. 6.2), varied during austral summer (October-early April), ranging from -35°C to 4°C. Air temperatures typically peaked soon after late December and the PDDs typically occurred between December and February (Figs. 6.11a, b). The analyses tested whether the seasons with highest propagation rate coincided with high PDD periods and vice versa but, no statistically significant correlation is detected between the two variables at 95% confidence interval (e.g. for RW1, correlation coefficient = 0.02). In fact, while some rifts exhibited a weak positive correlation with PDD, others showed a weak negative correlation (Figs. 6.12, 6.13). This observation suggested that PDDs were not a factor driving rift propagation at Jutulstraumen (Figs. 6.12, 6.13).

Similarly, no significant correlation was observed between sea ice concentration and rift propagation rates. Sea-ice concentration over each austral summer exhibit some interannual variability but the maximum sea-ice concentration was observed between October to November after which it starts to decrease to its minimum value in late January or early February (Fig. 6.11c). It was observed that rift propagation begins in late October when sea-ice concentration is close to its maximum. The analysis tested whether higher rift propagation rates tended to occur during

low sea-ice concentration seasons and vice versa (Figs. 6.14, 6.15) and find that rift propagation rate shows no significant correlation with sea-ice concentration (e.g. for RW2, correlation coefficient = 0.01). Indeed, some rifts displayed a weak positive correlation with sea ice concentration while others exhibited a weak negative correlation. Although the analysis did not identify correlations at the seasonal scale for either air temperature or sea ice concentrations, the possibility remains that such relationships may emerge at finer temporal resolutions (e.g., daily or weekly).

Table 6.5: *Propagation rates and 95% confidence intervals (m d^{-1}) derived from measured rift lengths of western margin of Jutulstraumen using MODIS imagery.*

Season	**RW1**		**RW2**		**RW3**		**RW4**		**RW5**		**RW6**		**RW7**	
	RW	CI	RW	CI	RW	CI	RW	CI	RW	CI	RW	CI	RW	CI
CASE A														
2003/04	8.4	2.2	5.7	2.3	23.1	10.9	2.1	0.3						
2004/05	4.4	1.3	7.2	3.1	13.5	6.3	3.6	2.3						
2005/06	2.2	0.7	-1.4	0.7	0.4	0.3	0.2	1.8	5.8	3.1				
2006/07	4.8	1.3	0.4	0.2	3.3	0.1	4.2	0.1	14.9	8.4				
2007/08	14.4	9.4	-4.4	1.2	-0.9	0.3	4.7	0.3	5.1	1.3				
2008/09	0.9	0.2	-1.2	0.2	1.4	0.5	51.1	12.1	-2.8	0.5				
2009/10			33.9	12.2	24.7	9.6	16.5	5.6						
2010/11	15.2	7.1	-4.8	0.8	6.8	2.4	35.5	23.2	27.1	3.3	12.5	9.3		
2011/12	2.2	0.4	-0.2	0.1							-0.1	0.4		
2012/13	-3.1	1.2	-6.1	1.3							-4.8	0.1		
2013/14	-3.1	1.3	1.4	0.06							-2.1	0.1		
2014/15	0.07	0.1	-3.7	0.2							0.4	0.2		
2015/16														
2016/17	1.5	0.2	-1.4	0.2							0.04	0.02	3.8	0.3
2017/18														
2018/19	7.3	2.5	-0.1	0.2							0.9	0.04	8.4	6.7
2019/20	2.2	0.3	-6.5	1.1							20.6	17.1	-0.3	4.3
2020/21			-3.3	0.2							0.5	0.6		
2021/22	3.9	0.2	-0.7	0.6							1.0	0.06	3.6	0.4
CASE B	0.2	0.1	0.4	0.3	0.2	0.02	0.5	0.2	0.4	0.04	0.3	0.08	0.1	0.07
CASE C	1.5	0.1	0.2	0.06	1.9	0.4	8	1.1	1.6	0.4	1.5	0.2	1.6	0.3

Table 6.6: *Propagation rates and 95% confidence intervals (m d^{-1}) derived from measured rift lengths of Eastern margin of Jutulstraumen using MODIS imagery.*

Season	**RE1**		**RE2**		**RE3**		**RE4**		**RE3+4**		**RE5**		**RE6**		**RE7**		**RE8**	
	RE	CI	RE	CI	RE	CI	RE	CI	RE	CI	RE	CI	RE	CI	RE	CI	RE	CI
CASE A																		
2003/04	2.9	0.1	3.2	0.2	-1.4	0.2	2.4	1.3			5.8	3.6	13.1	4.7	1.0	0.5		
2004/05			-1.2	0.1	3.6	3.0	-1.5	0.01	2.6	1.0	-4.4	1.2	0.9	0.4	-0.3	0.1		
2005/06	-0.4	0.2	-10.9	4.3	-3.8	3.1	-2.0	0.1			-1.4	0.3	2.4	0.9	4.2	2.1		
2006/07	1.5	0.5	2.5	0.5	-4.4	2.4	6.4	0.4	5.6	2.2								
2007/08			1.3	0.3	-10.5	8.7	-3.4	0.2	6.8	2.5	-0.4	0.2						
2008/09			-1.9	0.2			0.5	0.3	10.5		5.3	1.3	0.4		-3.4	0.2		
2009/10			6.6	0.5							5.6	2.5						
2010/11			1.2	2.0	-0.7	0.1							6.7	3.3				
2011/12	0.1	0.1	-1.5	0.1					1.7	1.0	9.5	6.1						
2012/13			-2.9	0.2	-2.0	0.2			4.2	2.4	4.7	2.7						
2013/14	1.0	0.5	-3.7	0.1					5.2	2.1	-1.2	0.6			6.4	2.2		
2014/15			0.6	0.2	-6.3	0.2			5.5	0.6	2.5	0.6						
2015/16																		
2016/17	-1.3	0.1	8.8	1.1					-2.0	0.5	1.7	0.4			27.4	10.5		
2017/18																		
2018/19	4.3	0.1	1.2	0.2					2.9	0.2	5.7	2.4			7.7	3.5		
2019/20	-0.3	0.2	1.5	1.3					10.7	5.8	22.4	10.3			29.9	15.3		
2020/21			3.5	0.2	3.3	0.2					1.5	0.6						
2021/22			1.7	1.2	-1.7	1.1			2.5	0.2	11.2	5.2			0.8	0.2		
CASE B	0.1	0.04	0.1	0.05	0.4	0.3	0.8	0.3	0.4	0.2	0.2	0.1	2.1	0.5	1.2	0.8	0.04	0.01
CASE C	0.1	0.03	0.1	0.08	0.1	0.1	0.6	0.3	0.3	0.06	0.7	0.07	1.4	0.9	0.1	0.08	3.2	0.4

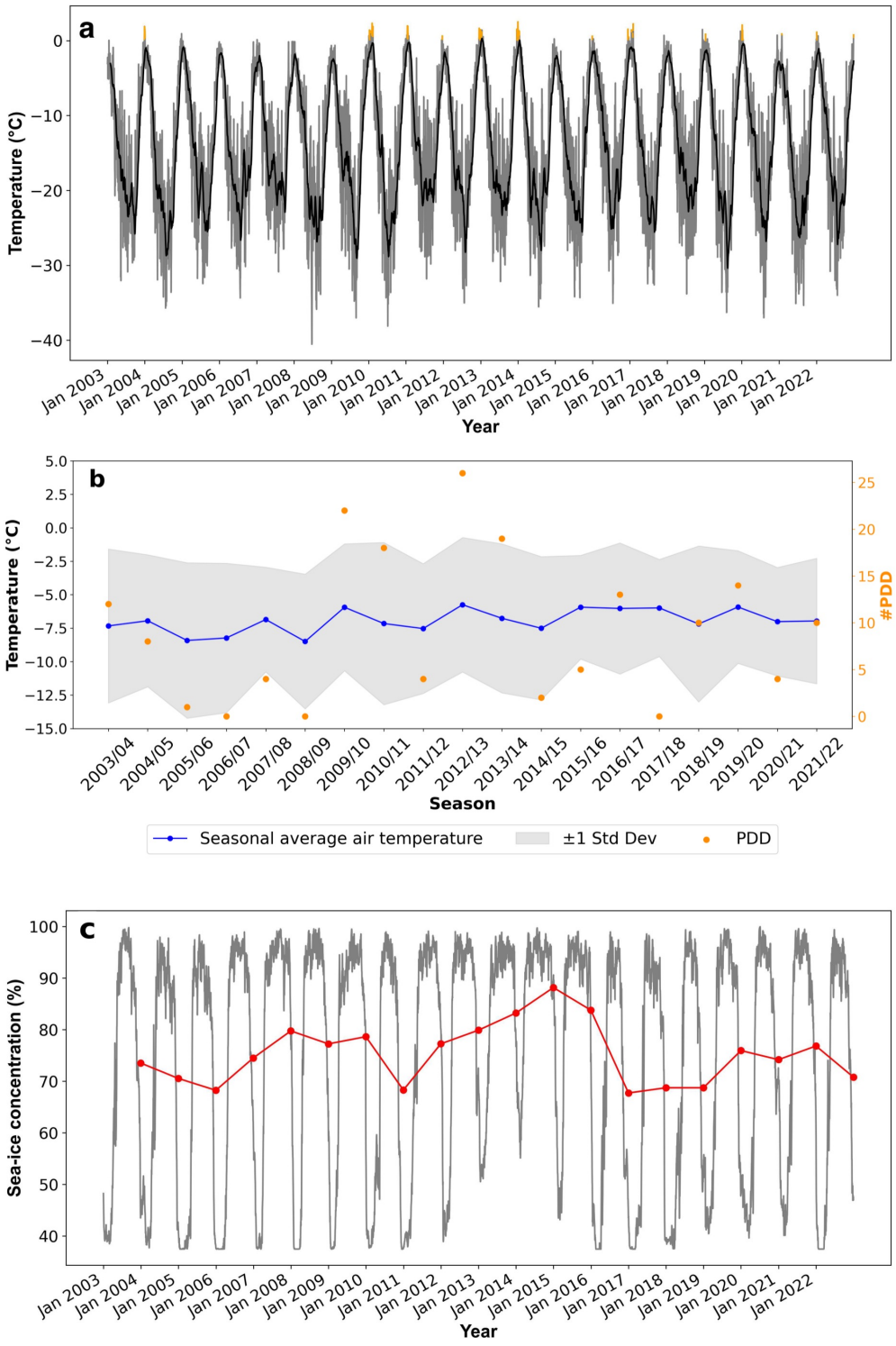

Figure 6.11: *(a) Daily averaged 2 m air temperature in grey overlaid with 6-month moving average (in black) and orange highlights denotes temperature > 0°C. (b) Average austral summer air temperatures over Jutulstraumen from 2003 to 2022 (blue). The shaded region indicates the 1 standard deviation (grey), while the orange markers represent the number of PDDs for each austral summer. (c) daily averaged sea-ice concentration in grey overlaid with summer average sea-ice concentration (%) (red).*

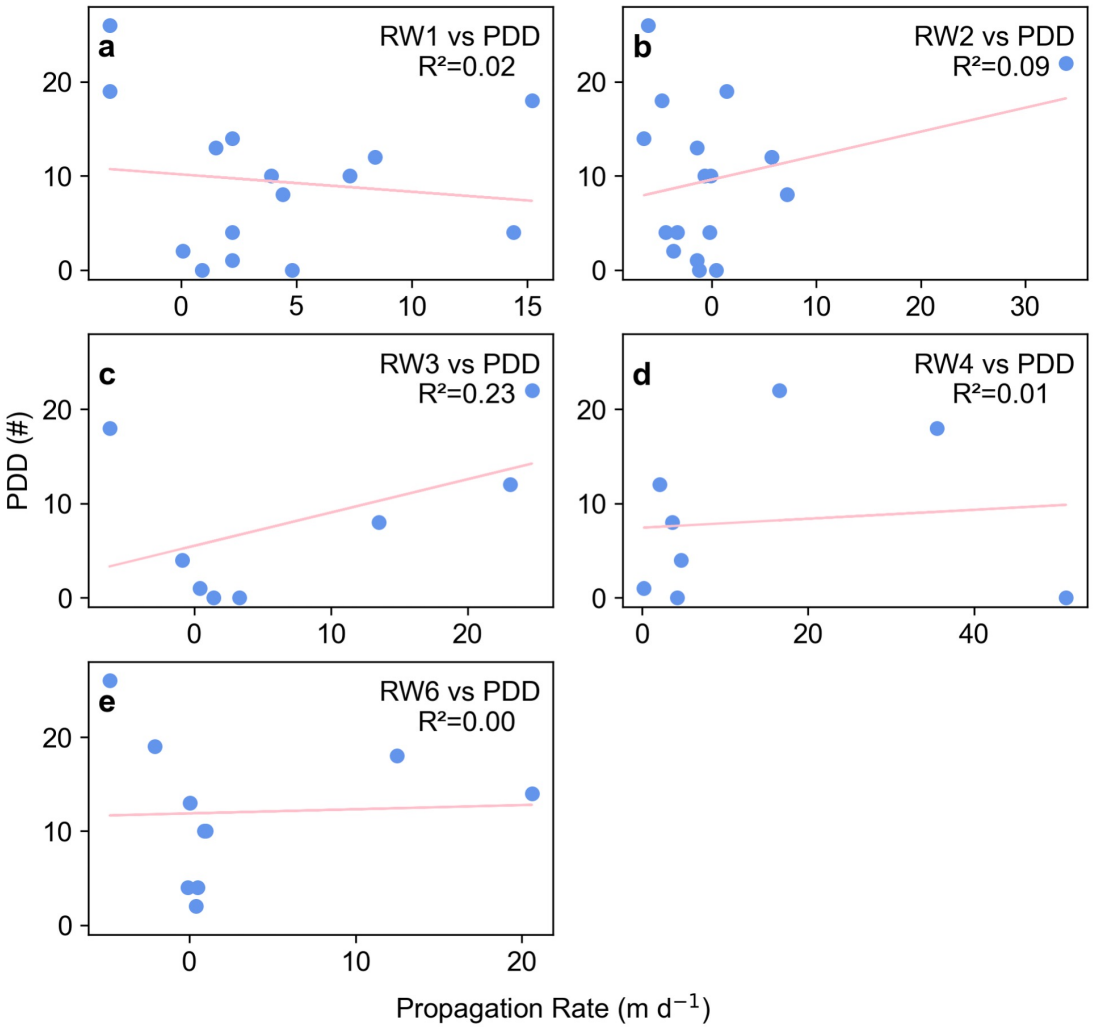

Figure 6.12: *Scatter plots illustrating the relationship between propagation rates of rifts on the western margin (RW) and positive degree days (PDD). Subplots (a) through (f) correspond to RW1, RW2, RW3, RW4, RW5, RW6 and RW7, respectively. Each subplot presents a fitted linear regression line to highlight the correlation between the propagation rate and PDD for each rift. RW5 and RW7 were omitted from the figure because each has fewer than five data points, and such small sample sizes can yield unreliable estimates.*

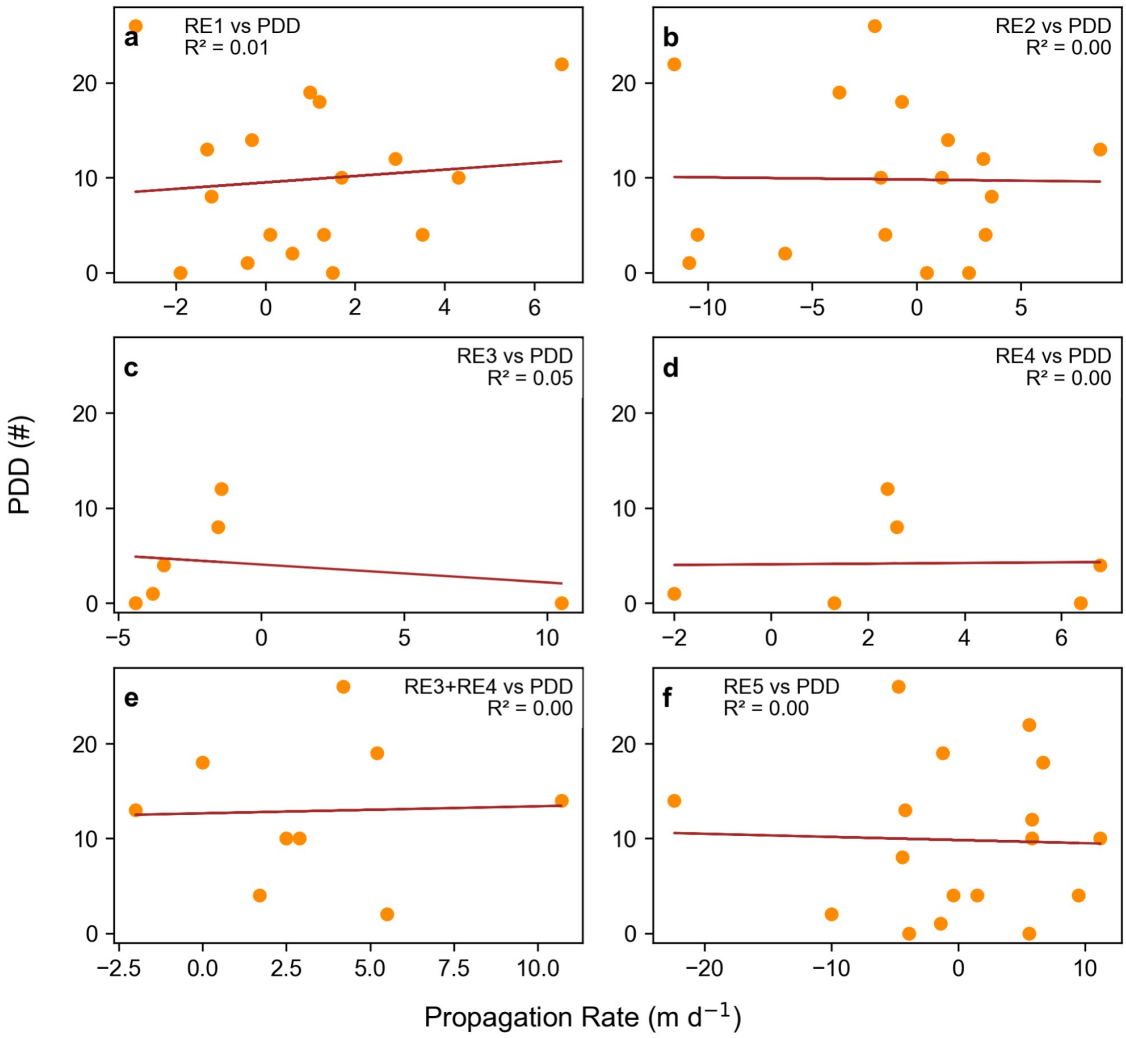

Figure 6.13: *Scatter plots illustrating the relationship between propagation rates of rifts on the eastern margin (RE) and positive degree days (PDD). Subplots (a) through (f) correspond to RE1, RE2, RE3, RE4, RE5, and RE8, respectively. Each subplot presents a fitted linear regression line to highlight the correlation between the propagation rate and PDD for each rift. The correlation coefficients were only consider for rifts that have been present for more than three summer seasons; hence, RE6, RE7 and RE8 were not included due to the limited data (less than 5 data points), which would render the correlation coefficients less reliable.*

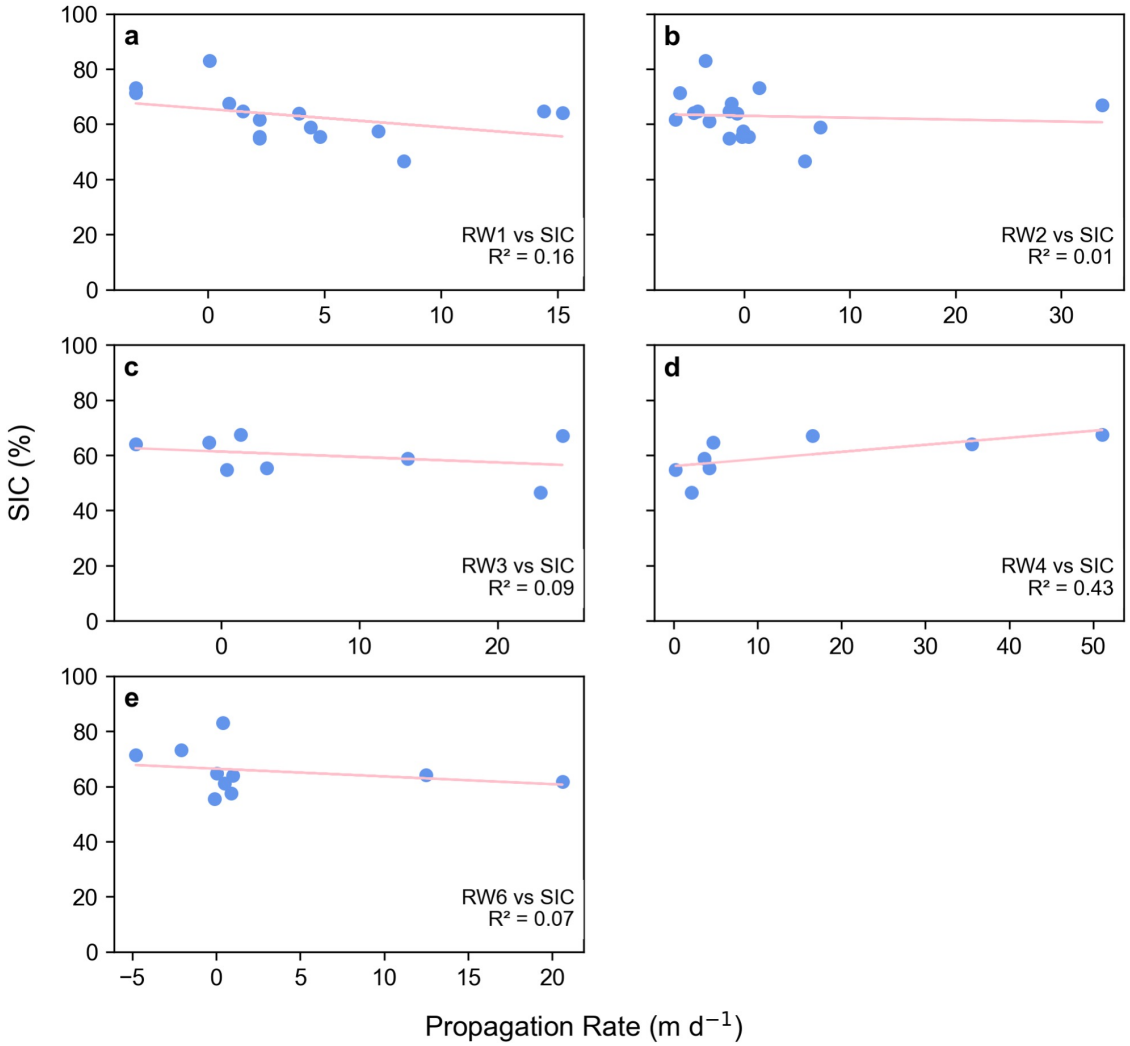

Figure 6.14: *Scatter plots illustrating the relationship between propagation rates of rifts on the western margin (RW) and summer mean sea ice concentration (%). Subplots (a) through (f) correspond to RW1, RW2, RW3, RW4, RW5, RW6 and RW7, respectively. Each subplot presents a fitted linear regression line to highlight the correlation between the propagation rate and summer mean sea ice concentration (%) for each rift. RW5 and RW7 were omitted from the figure because each has fewer than five data points, and such small sample sizes can yield unreliable estimates.*

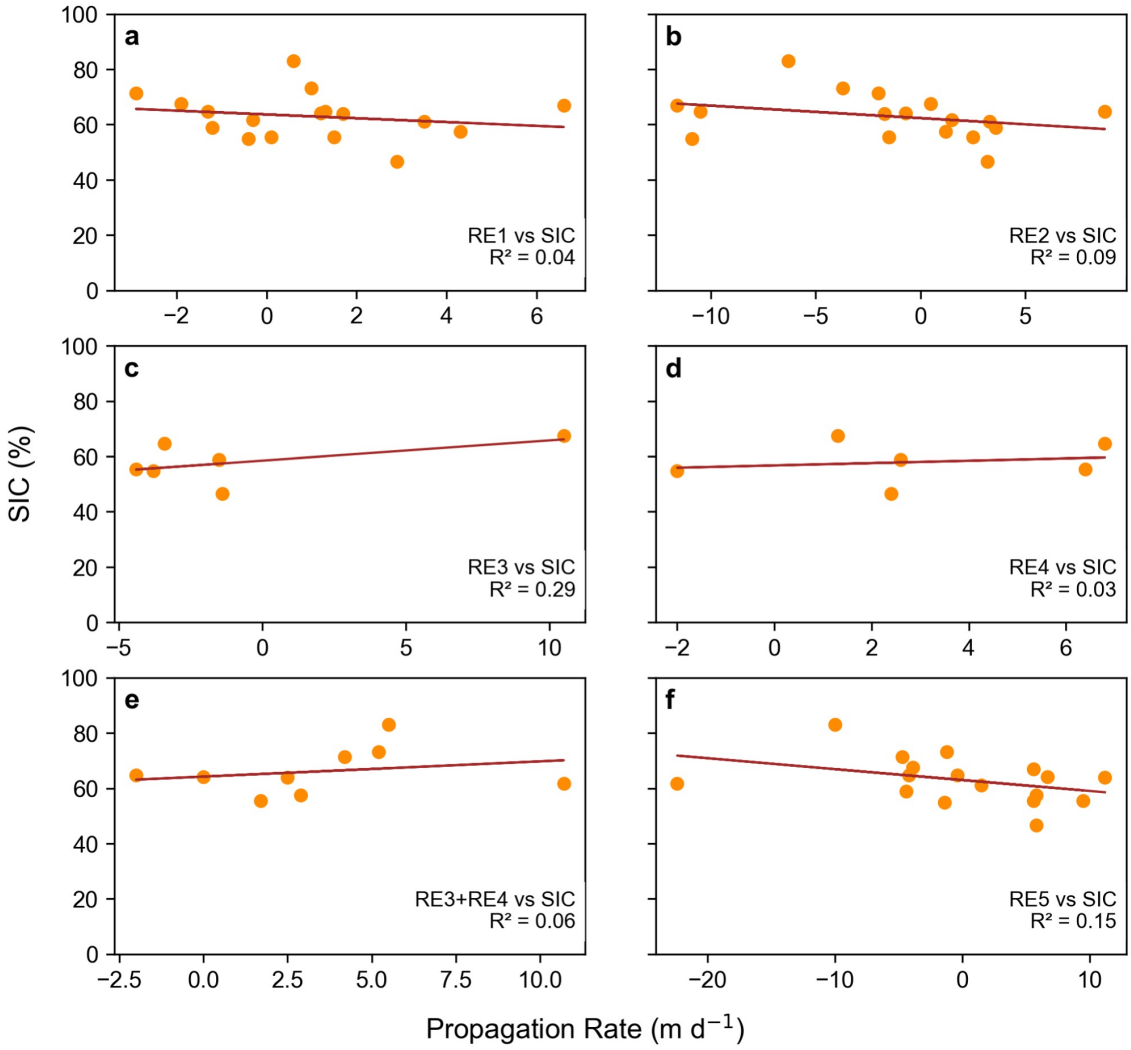

Figure 6.15: *Scatter plots illustrating the relationship between propagation rates of rifts on the eastern margin (RE) and summer mean sea ice concentration (%). Subplots (a) through (f) correspond to RE1, RE2, RE3, RE4, RE5, and RE8, respectively. Each subplot presents a fitted linear regression line to highlight the correlation between the propagation rate and summer mean sea ice concentration (%) for each rift. The correlation coefficients were only considered for rifts that have been present for more than three summer seasons; hence, RE6, RE7 and RE8 were not included due to the limited data (less than 5 data points), which would render the correlation coefficients less reliable.*

6.6 Discussion

6.6.1 Little change in ice dynamics at Jutulstraumen over the past 60 years

Taken together, the observations indicate minimal dynamic change on Jutulstraumen over the last six decades, with the key findings indicating a steady advance of the main ice tongue ($\sim$ 740 m yr^{-1}), limited change in ice velocity ($\sim 720 \pm 66$ m yr^{-1}), small average thickening of grounded ice across the catchment ($\sim +0.14 \pm 0.04$ m yr^{-1}), and no obvious change in grounding line position, other than a possible advance of around 200 m, albeit with large uncertainties ($\sim \pm 100$ m).

Between 1973 and 2022, the ice front advanced at an average rate of $\sim$ 740 m yr^{-1} with limited change in geometry. Currently, the ice front is $\sim$ 30 km behind the maximum extent of the ice front in 1960s, just before it underwent its last major calving event (Fig. 6.4a). This suggests that it will take nearly $\sim$ 40 years for the ice front to reach its previous maximum extent, considering the current ice front advance rate.

The average ice flow velocity remained consistent throughout the observation period. This could be largely influenced by the pinning points flanking Jutulstraumen coupled with high strain rates arising from the presence of the western rift system and lateral stress from the bounding mountain topography (west: Ahlmannryggen and east: Jutulgryta) near the grounding line (Fig. 6.2, Humbert & Steinhage, 2011; Mas e Braga et al., 2023), along with a cold-water regime. The steady velocity may also be partly attributed to the presence of large 'passive' frontal areas in Fimbulisen (Fürst et al., 2016). This 'passive' frontal area, also known as 'passive shelf ice' (PSI), refers to a portion of the floating ice shelf which, upon removal, is expected to have little to no dynamic impact. The PSI for the Jelbart-Fimbulisen area was estimated to be 17.1%, indicative of a 'healthy' PSI portion (Fürst et al., 2016). A higher percentage of PSI is important because any loss of this passive ice does not significantly affect ice velocity. In addition, during the study period, there

were no major changes in the configuration of the Fimbulisen. The combination of a large PSI fraction and a stable ice shelf configuration might well account for the velocity observed throughout the study period.

Additionally, analysis of elevation change of grounded ice highlights an overall pattern of thickening, particularly after 2003, with an average rate of thickening estimated at $+0.14 \pm 0.04$ m yr^{-1} between 2003 and 2020 (Nilsson et al., 2022). The observed trend could be attributed to a series of high accumulation events in DML that occurred between 2001 and 2006 (Schlosser et al., 2010) and during the winter season from 2009 to 2011 (Lenaerts et al., 2013). This event resulted in an increased mass balance of around +350 Gt along the coast of DML (Boening et al., 2012; Groh & Horwath 2021). Additionally, the 2009-2011 high precipitation event over DML has been predicted to be part of a long-term trend (Frieler et al., 2015; Medley et al., 2018), but it is important to note that the predicted rates of increase in both temperature and snowfall from climate model simulations were relatively low (Medley et al., 2018). This suggests that DML could maintain its current trend of mass gain, barring any major climatic or oceanic shifts that could alter future snowfall patterns or increase basal melt rates.

The minimal changes in ice dynamics were consistent with the grounding line positions observed in this study between 1990 and 2022, which appears to have undergone very little change or possibly a very minor advance. However, discrepancies arise when comparing different datasets and methodologies, as different methodologies capture distinct features within the several-kilometer-wide grounding zone, where the transition from fully grounded to floating ice takes place. It should be noted that for fast-flowing glaciers like Jutulstraumen, the grounding line positions acquired from manual delineation based on the most seaward observed break-in slope, Ib (ASAID, MOA) and local elevation minimum, Im (this study) were further downstream than those determined from tidal-induced vertical motion from DInSAR (MEaSUREs, AIS CCI and Mohajerani et al., 2021). For example, when examining the grounding line positions that were closest in time but acquired from different methods, the 1993 position obtained in this study using manual delineation

is around 18 km downstream from the 1994 MEaSUREs and AIS CCI grounding line position.

When the relative change in grounding line position is considered across methods, analysis of DInSAR-derived positions indicates little to no migration between the 1994 grounding line (as mapped by MEaSUREs and AIS CCI) and the most upstream position within the 2018 cluster provided by Mohajerani et al. (2021). In addition, the proximity of the grounding line positions derived from manual delineation of break-in slope provided by ASAID (1999-2003) and MOA (2004 and 2009) also suggests no major change in grounding line position during that period. The grounding line position obtained in this study from optical imagery (Landsat 4-8) between 1990 and 2022 indicated only a very minor advance of $\sim$ 200 m ($\sim$ 6 m yr^{-1}), with uncertainties of $\sim$ $\pm$100m. Interestingly, this estimated rate of advance is broadly in agreement with the rate reported by Konrad et al. (2018) at $\sim 2.4 \pm 1.9$ m yr^{-1}) between 2010 and 2016, using surface elevation from CryoSat-2 and bed elevation from Bedmap2 between 2010 and 2016. Thus, although there were major discrepancies between the different methods, each method appears to show very little change over the study period, or with only a very minor advance.

In summary, the relative stability of Jutulstraumen is likely due to the stable configuration of its floating ice tongue and Fimbulisen, which have undergone no major calving events and is associated with low basal melt rate ($\sim$ 1 m yr^{-1}) (Langley et al., 2014) linked to the presence of cold Eastern Shelf water (Hatterman et al., 2012). Additionally, the velocity could be stabilised by the suture zone on the western margin of Jutulstraumen, linked to the pining points at the ice front and lateral stress from bounding mountain topography near the flux gate (Fig. 6.2, Humbert & Steinhage, 2011; Mas e Braga et al., 2023). That said, recent observations have raised concerns about a slight increase in basal melting of around 0.62 m yr^{-1} between 2016 and 2019 (Lauber et al., 2023). This increase has been linked to the incursion of pulses of WDW resulting from reduced sea ice and stronger subpolar westerlies associated with a positive SAM (Lauber et al., 2023). Furthermore, the evidence of very slight thickening upstream of the grounding line and minor grounding line

advance suggests little sign of a dynamic imbalance in Jutulstraumen. Moreover, the limited change in ice discharge, estimated at 30 ± 2.2 Gt yr^{-1} between 2009 and 2017, along with total mass gain of +33 Gt between 1979 and 2017 as reported by Rignot et al. (2019), also suggests Jutulstraumen is currently not out of balance and may even be gaining mass slightly (The IMBIE team, 2023), which is consistent with the suite of observations.

6.6.2 Structural evolution

The analysis of the structural glaciology has identified that Jutulstraumen has several large surface features that may influence the structural stability of the glacier in the future (Fig. 6.8). Notably, the western rift system, comprising of fractures, fracture traces, rifts filled with sea ice/mélange, and crevasse fields (Fig. 6.8), primarily formed due to shear stresses generated between different flow units, specifically the fast-moving central trunk and the slow-moving lateral margin of the ice stream (Humbert & Steinhage, 2011; Fig. 6.2).The persistent presence of fracture traces in the western rift system suggests that these features have gradually developed and evolved as ice passes over an ice rumple, propagating both laterally and vertically (Humbert & Steinhage, 2011). However, the fracture traces could also represent surface expressions of basal crevasses (Fig. 6.8) as suggested by Humbert and Steinhage (2011), Luckman et al. (2012) and McGrath et al. (2012). Such fracture traces or surface expressions of basal crevasses may have facilitated the initiation and evolution of rifts further downstream towards Apollo Island (Figs. 6.2, 6.8), which could potentially weaken the structural integrity of the glacier.

The rifts measured at the ice front do not originated from the ice stream itself but appearred to propagate into it near the margin. The observed temporal pattern of rift propagation wascomplex, exhibiting large seasonal and interannual variability. The long-term rift propagation rates range from around 0.1 to 8 m d^{-1}, with differences in propagation rates on the western and eastern margins of the ice tongue. The rifts on the eastern margin tend to propagate at a slower long-term summer average rate than the rifts on the western margin. This variability in rift propagation rates may

be attributed to the direction of flow of the ice-tongue, which curves towards west. This curvature influences the formation of rifts on the eastern margin as ice detaches from the ice rise, Kupol Moskovskij, near the ice front (Figs. 2, 3). Consequently, rifts such as RE5 on the eastern margin tend to expand in width and propagate at a slower rate. It was possible that as a rift widened, the stress concentrated at the rift tip, which generally drives rift lengthening, wasredistributed across a wider area of the rift wall. This redistribution of stress at the rift tip might temporarily reduce the tensile stress driving rift lengthening (Bassis et al., 2007, 2008; Glasser et al., 2009). In contrast, the rifts on the western margin appear to be related to re-activation of pre-existing fractures as the ice pulls away from the Apollo Island (Figs. 2, 8). Therefore, the calving regime could be influenced by the adjacent flow units, defined as neighbouring sections of the glacier or ice shelf characterised by varying flow velocities. The fast-flowing ice stream in the middle interacts with the slower moving ice on either side of the ice stream, generating shear stress, which could further influence the formation and propagation of these rifts.

In addition, previous studies have suggested that sea ice concentration or ice mélange can play an important role in rift propagation. When sea ice was absent in rift openings, there was an extended period of exposure to open ocean conditions and ocean swells. This exposure potentially impacts the rate at which rifts propagate, leading to calving and eventual disintegration of ice shelves, as observed in the Larsen A, B, and Wilkins ice shelves (Massom et al., 2018; Larour et al., 2021). Prior research has also linked the disintegration of ice shelves to increasing atmospheric temperatures (Mueller et al., 2008). However, using linear regression analysis, it can be confirmed that high rift propagation rates at Jutulstraumen were not related to high air temperatures at seasonal scale (Figs. 6.12, 6.13). This finding was supported by previous studies showing that despite a warmer-than-average condition during the winter of 2007, the Amery and West Ice Shelves in East Antarctica saw a decrease in rift propagation rates, and rift activity came to a complete halt in the following austral summer in the Shackleton Ice Shelf (Walker et al., 2013). Whilst during a relatively colder winter in 2005, three rifts (rifts W2, T1 and T2) in the Amery ice shelf actively propagated, indicating a complex, non-linear link between

temperatures and rift activity on these shelves (Walker et al., 2013).

Similarly, the correlation between rift propagation rate and sea-ice concentration at Jutulstraumen was also not statistically significant at 95% confidence level, indicating that lower sea-ice concentration does not necessarily lead to higher rift propagation rates. This finding aligns with previous research on the Amery Ice Shelf in the EAIS, where studies have consistently found no statistically significant correlation between environmental factors like air temperature or sea-ice concentration and rift propagation rates (Fricker et al., 2005; Bassis et al., 2008; Walker et al., 2015). In addition, ice shelves such as Larsen C, Ronne and Filchner, adjacent to the Weddell Sea and characterised by year-round high sea ice levels, have not exhibited decreased rift activity during periods of high sea ice concentration. This was unlike the behaviour observed in the Larsen A, B and the Wilkins ice shelves where a clear relationship between sea ice and rift propagation has been observed. These ice shelves experienced a notable increase in rift lengthening during periods with no sea ice buffer. This reduced buttressing from sea ice and prolonged exposure of the water-filled rifts to the ocean swells, led to calving and eventual disintegration of the ice shelves (Massom et al., 2018).

In summary, the rifts observed on Jutulstraumen were expected to continue to propagate regardless of the ice shelf-scale changes in environmental parameters (particularly, temperature and sea ice concentration). On a more regional scale, factors like the presence or absence of sea ice/mélange in rift openings or wind-blown snow/ice might impact rift propagation rates, although the lack of detailed sea ice data complicates this assessment (MacAyeal et al., 1998; Khazendar & Jenkins, 2003; Larour et al., 2004; Fricker et al., 2005; Walker et al., 2013). Nevertheless, the analysis showed that over the observation period the rifts propagate at a relatively steady rate (Fig. 6.10). Additional factors that may impact rift propagation rates could be arrival of tsunamis, as observed in Amery Ice Shelf between 2002 and 2012, following which large rift propagation events occurred (Walker et al., 2015). Moreover, mechanical/tidal interaction between the ocean and ice shelf, especially since these rifts open towards the ocean (Walker et al., 2013), could also contribute to rift propaga-

tion. Seasonal variations in rift propagation rates might stem from changing ocean conditions affecting the basal melting beneath the ice shelf. Lauber et al. (2023) reported intensified pulses of WDW beneath the ice shelf after 2016, leading to increased basal melt rates. This could influence the ice shelf's structural heterogeneity (e.g., through localised high melt rates in basal channels), further contributing to rift propagation. Alley et al. (2022) suggested that basal channels were crucial in determining the basal melt rate, a factor that greatly influences the stability of the ice shelves. Additionally, these channels can affect how and where fractures form and propagate, directly impacting ice-shelf calving. An example of this can be seen in the Pine Island Glacier, where the presence of a basal channel was linked to the formation of both transverse and along-channel fractures (Dow et al., 2018; Alley et al., 2022). The basal channels identified in this study originate near the grounding line, which could influence the expansion of the mélange zone, the propagation of the rifts filled with sea ice/mélange, or formation of new rifts/crevasses in the ice stream (Fig. 6.8). However, it remains unclear about their influence on the rifts at the ice front. In addition, the presence of marine ice in the suture zones could also impact the structural integrity of the ice shelf (Walker et al., 2013; Kulessa et al., 2014). Such dynamics have been observed on the Amery Ice Shelf, indicating a multifaceted interplay of environmental and oceanographic factors in rift propagation (Herraiz-Borreguero et al., 2013; Walker et al., 2013; Walker et al., 2015).

Thus, at Jutulstraumen, the advancing of the ice tongue and additional stresses may play a more important role than environmental factors in influencing rift propagation and the next calving event. Therefore, as the Jutulstraumen ice tongue was approaching its maximum extent of 1960s, it was essential to maintain continuous monitoring of these rifts, as they have the potential to influence a major calving event.

6.6.3 Future evolution of Jutulstraumen

In 2022, Jutulstraumen's ice front was $\sim$ 30 km behind its previous maximum extent of the 1960s. Given the average rate of advance, it would reach its last maximum

extent in $\sim$ 40 years. However, considering the long-term average rate of rift lengthening into the ice stream (Figure 6.10), the next calving event could occur before the ice tongue reaches its maximum extent—potentially in as little as 32 years. For instance, if both RW6 ($\sim$ 1.5 m d^{-1}) and RE3+RE4 ($\sim$ 0.3 m d^{-1}) propagate at their average rate, the two rifts will connect in around 32 years, leading to a calving event. This calving event will result in the loss of an iceberg of $\sim$ 55 km in length, $\sim$ 65 km in width and $\sim$ 3575 km^2 in area. The size of this potential iceberg would exceed the dimensions of the recently calved iceberg A-81 from the Brunt Ice Shelf in January 2023, which was approximately 1550 km^2 in size. Furthermore, the presence of a deep trough crossing the continental shelf beneath the floating part of Jutulstraumen would provide a pathway for warm water to intrude to the grounding line if ocean circulation were to change in the region (Fig. 6.1c). This indicates a possibility of connections being made between the projected warming of the Weddell Sea (Golledge et al., 2017) and Fimbulisen/Jutulstraumen. This was similar to the response predicted for the neighbouring Recovery catchment under future warming scenarios by Golledge et al. (2017). Modelling also suggests large-scale changes including significant ice surface thinning by 2300 in and around Jutulstraumen under a +3°C air temperature warming scenario (DeConto et al., 2021). Despite a relatively minor current response to changing climate and ocean conditions, it was essential to monitor changes in Jutulstraumen to identify early warnings of dynamic imbalance in the next few decades, particularly given that it drains a significant portion of East Antarctica.

6.7 Conclusion

This study has shown that Jutulstraumen has exhibited limited change in ice dynamics over the observation period between 1960s and 2022, with no signs of any dynamic imbalance. Following the significant calving event in 1967 (see van Autenboer & Decleir, 1969; Vinje, 1975; Swithinbank et al., 1977; Kim et al., 2001), the ice front has advanced steadily at $\sim$ 740 m yr^{-1} (1973-2022). The velocity has been largely consistent between 2000 and 2021 at $\sim$ 720$\pm$66 m yr^{-1} with minimal thicken-

ing of the grounded ice at $\sim +0.14 \pm 0.04$ m yr^{-1} across the catchment (2003-2020). The grounding line has shown no obvious change and may have slowly advanced between 1990 and 2022 ($\sim$ 6 m yr^{-1}) based on manual delineation in this study. Taken together, the observations were consistent with the notion that the large ice shelf (Fimbulisen) was modulating the steady ice velocity and stable grounding line location, largely influenced by the drag imposed by lateral pinning points either side of the main ice stream. Such behaviour was also consistent with characteristics of outlet glaciers in cold-water shelf regime, with minimal ice shelf thinning. However, recent observations highlighted the incursion of pulses of WDW beneath the ice shelf, leading to a higher basal melt rate (Lauber et al., 2023). Should such events persist or become more frequent, they could potentially influence the ice dynamics at Jutulstraumen.

The 19-year time series of rift lengths between 2003 and 2022 have indicated that the rifts have been increasing in length and some rifts (RW4 and RW5; RE6 and RE7) have triggered small calving events during the observation period (Fig. 6.9). The average propagation rates differed for each rift with most exhibiting a seasonal signal of lengthening, but with marked interannual variability. Comparison of rift propagation rates with air temperature and sea-ice concentration suggested that these phenomena were not linked to rift propagation rates at seasonal scale (Figs. 6.12-6.15). Rather, rift lengthening was likely resulting from the continued generation of shear stresses at the lateral margin as the floating ice tongue continues to advance. If the current rate of ice front advance was maintained then the next calving event was likely to occur in around 40 years, based on its position just prior to its last calving event in the late 1960s. However, if the long-term rate of rift lengthening was maintained, then it could take place much sooner and in around 32 years.

CHAPTER 7

Discussion

This chapter revisits the research questions posed in Chapter 1 and draws together key findings from the preceding chapters to evaluate how understanding of this coastline has evolved. These discoveries are then situated within the broader literature to assess their implications for the stability of the EAIS. The chapter also examines the challenges encountered during the study and outlines possibility for future research.

7.1 Summary of key findings

7.1.1 RQ1: How does the terminus behaviour of marine-terminating glaciers in Enderby, Kemp Land vary over multi-decadal and interannual timescales?

Glacier terminus behaviour in Enderby and Kemp Land has undergone pronounced temporal variability over the past five decades, marked by alternating phases of retreat and advance (Chapter 4). The earliest epoch (1970s–1988) was characterised by widespread retreat, with 74% of glaciers (32 out of 44) exhibiting terminus retreat. At a broader ice sheet scale, Miles et al. (2016) also identified this retreat pattern between 1974-1990, where all drainage basins, with the exception of Victoria Land (DB16), in the EAIS retreated. They attributed this retreat to warmer conditions linked to a negative phase of the Southern Annular Mode (SAM), which is associated with reduced sea ice conditions and increased air temperatures. Supporting this interpretation, Chapter 4 showed that summer sea-ice extent across the study region fell below 30×10^3 km^2 in several years during this period (e.g. 1979, 1985, 1988; Fig. 4.11), suggesting reduced buttressing from sea ice may have contributed to widespread glacier retreat.

In contrast, this study found a reversal in trend to glacier advance during the second epoch (1988-2000), with 68% of glaciers in Enderby and Kemp Land advanced. This coincided with a shift to a positive SAM phase that typically enhances sea ice extent and brings colder atmospheric conditions. This regional trend mirrors that reported by Miles et al. (2016), who documented widespread glacier advance across most of

the EAIS during this period. The advancing trend persisted into the following epoch (2000–2010), with 64% of glaciers continuing to advance. At the pan–ice sheet scale, Miles et al. (2016) also documented continued advance through to 2012, although they noted significant retreat in Wilkes Land, where $\sim$ 74% of glaciers retreated. These findings suggest that Enderby and Kemp Land followed the dominant EAIS-wide pattern of advance during the 1990s and early 2000s, likely driven by favourable large-scale atmospheric and sea-ice conditions associated with a prolonged positive SAM phase.

Since 2010, glacier behaviour has become increasingly heterogeneous. During the most recent epoch (2010–2023), 57% of glaciers in Enderby and Kemp Land advanced, marking a modest decline from the previous decade (64% advancing between 2000 and 2010). This reduction occurred despite the persistence of a positive SAM phase (Fig. 7.3), suggesting that SAM may no longer be the dominant driver of glacier behaviour in this region.

Despite the variability described above, an overarching long-term pattern of regional advance was identified, which is a key finding of this work. The magnitude of terminus change varied widely across glaciers, ranging from less than 1 km to nearly 10 km of net advance or retreat between the 1970s and 2023. While some glaciers, such as the Wilma-Robert-Downer (WRD) Glacier system, experienced a net advance of approximately 10 km, neighbouring glaciers like Seaton Glacier underwent a net retreat of around 3 km during the same period. The first major retreat of the WRD Glacier system occurred in 1991, marked by a $\sim$ 7 km retreat, while Seaton Glacier's significant retreat occurred in 2000 with a $\sim$ 3 km loss. In contrast, several smaller glaciers, including Glacier17 and Glacier18, showed limited variability and only minor net change ($<$ 1 km) throughout the observation period. These examples illustrate the degree of interannual and inter-glacier variability, even within a relatively confined region. The contrasting glacier terminus behaviour between Enderby and Kemp Land suggests spatial heterogeneity in environmental forcing and glacier sensitivity which is described in Section 7.1.2. Nevertheless, when aggregated, the regional tendency towards modest long-term advance remains a key outcome of this

analysis.

7.1.2 RQ2: What spatial patterns exist in glacier terminus change across Enderby, Kemp and Dronning Maud Lands, and how do these differ between the regions and individual glaciers?

As highlighted throughout this thesis, the behaviours of glaciers in Enderby and Kemp Lands often differed markedly from those in Dronning Maud Land, warranting a region-by-region discussion of key trends. The majority of glaciers in Enderby and Kemp Lands shared broadly similar glaciological settings and are geographically adjacent, however, both regions exhibit opposite glacier terminus behaviour. Enderby and Kemp Lands showed contrasting regional trends in glacier terminus change despite similar settings. While Enderby Land experienced widespread retreat between the 1970s and 1988, with 71% of glaciers retreating, Kemp Land displayed the opposite trend, with the majority of glaciers ($\sim$ 61%) advancing. A similar offset persisted into the subsequent decades. During the epoch when the overall trend across the entire study area indicated a phase of glacier advance (1988–2000), Enderby Land exhibited a more pronounced and widespread advance than Kemp Land, with 77% of glaciers advancing. In the most recent epoch (2010–2023), this regional difference continued. Enderby Land returned to a retreat-dominant state (61% of glaciers), while Kemp Land maintained a net advance (54% of glaciers). These asynchronous trends suggest that despite being located next to each other, internal glacier dynamics along with regional and local environmental forcings (e.g. sea ice conditions, ocean temperatures) lead to markedly different outcomes across both regions. These drivers are explored in more detail in section 7.1.3. Glacier terminus change behaviour differs markedly between Enderby and Kemp Lands, with contrasting trends despite similar glaciological settings, likely due to complex interactions between local and regional drivers.

Dømgaard et al. (2024) found no regional long-term trend in the frontal positions of

the studied glaciers in Kemp Land, Mac Robertson Land, and along Ingrid Christensen Coast between 1937 and 2022. While their study area partially overlaps with the one in this thesis, it also extends further east to include two neighboring regions beyond Kemp Land. Consistent with the findings presented in this thesis, they observed that glacier termini exhibited episodic advances and retreats, with variability in both magnitude (ranging from <0.1 km to 13.5 km) and temporal scale (spanning 3 to 50 years). This pattern of dynamic but non-directional change suggests that some regions of the EAIS may be characterised by natural fluctuations in glacier behaviour, rather than any persistent long-term trend in frontal position.

Beyond regional contrasts, glacier terminus behaviour also varied considerably among individual glaciers, even within the same region over the study period. Chapters 4 to 6 revealed that marine-terminating glaciers in the EAIS exhibit highly localised terminus behaviour, with pronounced variability both between and within regions. While some glaciers experienced episodic calving of varying magnitude, others underwent gradual disintegration, while several displayed oscillatory patterns marked by irregular cycles of advance and retreat. As illustrated in Chapter 4 (Fig. 4.7), no two glaciers behaved identically, even when located next to each other. While some glaciers such as Wilma–Robert–Downer (WRD) have advanced steadily since the early 2000s, neighbouring glaciers like Seaton and Hoseason have undergone intermittent retreat events during the same period. Similar intra-regional variability was reported by Dømgaard et al. (2024), who observed that Mulebreen Glacier advanced continuously from the late 1980s to 2022, while Brunvoll Glacier (Fig. 2 in Dømgaard et al., 2024) retreated and Hoseason Glacier remained stable before transitioning into a phase of fluctuating advance and retreat (See Fig. 4.1 for location of Hoseason Glacier). They proposed that enhanced snowfall, with estimated increases in precipitation of up to 50%, might have contributed to sustained glacier advance by increasing surface mass balance. The contrasting terminus behaviours observed in across Enderby and Kemp Land in this study (Chapter 4), despite broadly similar climatic exposures, emphasises the dominant role of local controls such as glacier geometry, bed topography, embayment configuration, near-terminus sea ice and subsurface ocean temperature conditions. In particular, the

differing sizes and frequencies of calving events across glaciers underscore the complex and often non-linear nature of glacier front dynamics in Enderby and Kemp Lands. Together, these findings highlight that individual glacier response is shaped by a combination of local topographic controls and spatial variability in climatic inputs, such as snowfall and mass balance.

The spatial variability in glacier terminus behaviour across Enderby, Kemp, and Dronning Maud Lands reflects the influence of both climatic and non-climatic drivers that operate at different scales. Climatic factors—such as variations in mean summer ocean temperatures and sea ice conditions—can modulate basal and frontal melting, influencing the likelihood of calving. Non-climatic controls, including glacier bed topography, the presence or absence of floating ice tongues, and internal ice stress dynamics, further modulate glacier response. These interacting mechanisms create a highly dynamic and spatially heterogeneous calving environment, helping explain why neighbouring glaciers or those within the same region can exhibit starkly different behaviours. For instance, the development and propagation of rifts—such as those observed at Glacier 1, Oku-iwa, and Rayner Glacier (Fig. 4.1) in Enderby Land—can reduce frontal stability and trigger sudden disintegration, while other glaciers remain intact. As glacier front structure and geometry evolve over time, susceptibility to calving can also change, contributing to episodic or irregular terminus change. Ultimately, each glacier responds to a unique combination of environmental and internal forcings, which helps explain the diversity of spatial patterns observed across the study area. This complexity underscores why spatial differences in terminus behaviour cannot be attributed to any single driver, but rather to a glacier-specific interplay of multiple processes.

In contrast to the heterogeneous patterns seen in Enderby and Kemp Lands, glacier terminus behaviour in Dronning Maud Land (DML) has been more consistent and dominated by long-term advance, particularly after the early 2000s. While this study (Chapter 6) focused primarily on one glacier in DML—Jutulstraumen—its systematic analysis provides valuable insight into broader regional patterns. Chapter 6 presented the first systematic, multi-decadal analysis of Jutulstraumen Glacier,

revealing continuous ice front advance ($\sim$ 740 m yr^{-1}) since its last major calving event in 1967. No significant retreats or large calving events have been recorded during the 60-year observational period, aside from small discrete calving events at the lateral margins. The glacier's ice front remains $\sim$ 30 km landward of its 1960s maximum extent, suggesting it has not yet re-attained its former limits. Jutulstraumen Glacier has advanced steadily for over five decades, exhibiting one of the most stable frontal positions in the study area.

This gradual ice front advance observed at Jutulstraumen is consistent with region-wide patterns reported across DML in previous studies. Miles et al. (2016) documented more of a balanced phase in DML between 1974 and 1990, with 53% of glaciers retreating (n=15). The trend then shifted to a drastically advancing phase in the subsequent decades between 1990-2000 and 2000-2012 with 77% (n=18) and 80% (n=20) of glaciers advancing. Goel et al. (2020) reported that 95% of glacier termini advanced between 2009 and 2014, and Baumhoer et al. (2021) noted widespread advance between 1997 and 2018 in DML. Shirase Glacier provides another example of sustained advance in DML, having advanced approximately 30 km since reaching its minimum extent in 1988 (Miles et al., 2023; Kondo et al., 2023). Shirase Glaciers' advance has been mainly attributed to climatic forcings such as strengthening of alongshore winds, which enhance upwelling processes and reduce basal melting by cooling surface waters (Miles et al., 2023). However, at Jutulstraumen it has been a combination of both. For instance, Jutulstraumen's long-term stability and net advance is the occurrence of anomalous snowfall events (Schlosser and others, 2010; Lenaerts and others, 2013) that may have enhanced surface mass balance (Boening and others, 2012; Groh and Horwath, 2021) across Dronning Maud Land. In addition, topographic features such as pinning points along with presence of ice shelves provide buttressing to the ice tongue, helping to maintain its integrity and suppress dynamic thinning or acceleration. Thus, widespread frontal advance in DML has been driven by both climatic (e.g. enhanced snowfall, ocean cooling) and topographic (e.g. pinning points, shelf buttressing) factors, promoting long-term glacier stability.

Climatic influences particularly included fluctuations in mean summer ocean temperatures and sea ice conditions which can alter basal melting as well as melting at the ice front. Non-climatic forcings such as glacier bed topography, constrained or unconstrained floating ice tongue and internal ice stress dynamics, likely plays a role in modulating ice front behaviour. Together, these interacting mechanisms create a highly variable and dynamic calving environment, emphasising the need for integrated observational and modelling approaches to fully understand the processes at play. Additionally, the structural integrity and geometry of the glacier fronts themselves seem to evolve over time, leading to disintegration events of varying magnitude. For example, the development and propagation of rifts can weaken the ice front, making it more susceptible to sudden break-up as observed in the case of most glaciers in Enderby and Kemp Lands such as Glacier 1, Oku-iwa, Rayner Glacier (see Fig. 4.1 for location). This underscores that changes in glacier termini are influenced by a complex interplay of factors operating across multiple spatial scales. Each glacier is affected by a unique combination of drivers—ranging from broader margin-wide influences on regional environmental conditions and down to highly localised controls. As a result, no two glaciers responded to the exact same set of forcings, and response was of different intensity.

7.1.3 RQ3: What are the primary factors influencing the terminus behaviour of marine-terminating glaciers across Enderby, Kemp and Dronning Maud Land?

RQ4: How do the dynamics and structural characteristics of glaciers evolve over time, and what impact do these changes have on their overall behaviour?

Chapters 4 to 6 examined both ocean–climatic and non-climatic controls on glacier terminus change across Enderby, Kemp and Dronning Maud Land. In regions such as Enderby and Kemp Land, glacier response is rarely linear or attributable to a single dominant forcing. Instead, it appears to be shaped by a nested hierarchy of

influences, operating across spatial scales—from large-scale atmospheric and oceanic variability (e.g. SAM phase, snowfall anomalies, sea-surface temperatures), to regional sea-ice trends, down to highly localised factors like topography, bathymetry or glaciological setting. Each glacier, therefore, likely responds to a distinct and complex interplay of forcings, which explains the high degree of spatial and temporal heterogeneity observed. By contrast, glacier behaviour in Dronning Maud Land (DML) appears more spatially coherent, with widespread advance over recent decades. This may reflect the influence of more consistently stabilising factors, such as the widespread presence of ice shelves, which provide buttressing to the glaciers (Fürst et al. 2016). In addition, snowfall anomalies (Lanaerts et al. 2013) and relatively cold shelf water conditions may have further supported mass gain and frontal advance. However, recent years have seen shifts in cold shelf water conditions and observed influx of WDW into the ice shelves (Lauber et al. 2023).

This stands in contrast to the more regionally synchronous behaviour documented for marine-terminating glaciers in the Greenland Ice Sheet (GrIS), even though glaciological setting of these glaciers is quite similar to those in Enderby and Kemp Land. In GrIS, neighbouring glaciers across the North-West, North-East, South-West, and South-East sectors have exhibited relatively linear retreat trends since the mid-1990s and a more consistent response to ocean–climate forcing (Fahrner et al., 2021; Black & Joughin, 2022). In the EAIS, the glacier terminus behaviour is considerably more staggered and variable, reflecting the complex interplay of both climatic and non-climatic controls. Below, we explore some of the controls on terminus behaviour across the study region.

7.1.3.1 Non-Climatic Drivers Influencing the Terminus Behaviour

Glacier stability in the EAIS is strongly influenced by the presence or absence of ice shelves, the configuration of pinning points, the geometry of glacier termini and development and propagation of rifts (Chapter 5, 6). In regions where large ice shelves are present such as Dronning Maud Land (DML) these features play a crucial role in buttressing inland ice flow. For example, Jutulstraumen Glacier, which

flows into the Fimbulisen Ice Shelf, is stabilised by multiple grounded ice rises that act as pinning points, anchoring the shelf and limiting dynamic thinning. Its narrow flux gate and convergent flow regime further restrict lateral expansion, promoting long-term terminus stability despite draining a deep trough (Chapter 6). Remarkably, Jutulstraumen has remained stable even during past warm periods (e.g. the mid-Pliocene), suggesting that stabilising feedbacks from ice rises and fjord geometry can potentially override oceanic forcing (Mas e Braga et al., 2023) even under climatic conditions that are thought to have been similar to, or slightly warmer than present. A similar stabilising configuration is observed at Shirase Glacier. The glacier is anchored by both lateral embayment walls and frontal pinning points, which have contributed to its $\sim$ 30 km frontal advance since its minimum extent in the late 1980s (Kondo et al., 2023; Miles et al., 2023). Shirase Glaciers' advance has been mainly attributed to climatic forcings such as strengthening of alongshore winds, which enhance upwelling processes and reduce basal melting by cooling surface waters (Miles et al., 2023). In contrast, many glaciers in Enderby and Kemp Land lack extensive ice shelves. Yet, some glaciers such as Wilma–Robert–Downer (WRD) Glacier and Rayner Glacier have remained relatively stable due to topographic confinement within narrow fjords or embayments. This enhances lateral drag and provides a degree of mechanical support. Chapter 5 found that WRD Glacier has advanced overall, despite experiencing episodic calving events. Similarly, Rayner Glacier exhibited alternating periods of advance and retreat, with major calving events occurring approximately every decade (e.g., 2005, 2016, 2024). In these cases, confined geometry helped moderated terminus variability in the absence of large ice shelves.

Calving events were observed across all study regions, but the scale, frequency, and glaciological impact of these events varied considerably between and within regions. In Enderby and Kemp Lands, calving often occurred as intermittent, moderate-scale events, typically following the gradual propagation of rifts and weakening of frontal integrity (Chapter 4). For instance, the WRD system experienced multiple calving events (e.g. 1991, 2003, 2014), with the largest involving the detachment of a $\sim$ 70 km^2 iceberg (Chapter 4, 5). These events, however, did not initiate sustained

retreat; rather, glaciers like WRD subsequently advanced beyond their pre-calving extent. In contrast, several unconfined glaciers, e.g. Omega Glacier (see Fig. 4.1 for location), showed more irregular, episodic retreats, often without full re-advance to pre-calving extent. By comparison, Jutulstraumen Glacier in DML, for example, has advanced by ∼30 km steadily since its last major calving event in 1967 (Chapter 6). These contrasting calving histories underscore the highly glacier-specific nature of terminus response, with confined glaciers often demonstrating recovery or advance following calving, while unconfined systems tend to experience more prolonged or irreversible retreat.

A key driver of calving in regions with either presence or absence of ice shelves is the formation and propagation of rifts. Both Jutulstraumen and WRD glaciers exhibit rift systems, though their dynamics differ. At WRD, rifts formed in response to extensional stress as the floating tongue advanced, with fracture initiation typically localised along lateral shear margins and near frontal pinning points. These structurally anchored zones consistently produced new rifts, often reoccurring in the same spatial locations following each calving event (e.g., W1, W2, and W6). This cyclical pattern of rift initiation, propagation, calving, and subsequent reformation was evident during the major calving events of 1991 and 2003, where rift W1 was responsible for the 1991 event and W2 for the 2003 event. The most recent rift, W6—developing in the same region as its predecessors—has yet to trigger a calving event, likely due to the continued presence of mélange within the rift cavity, which may be acting to suppress further propagation. As shown in Chapter 5, mélange acted as a stabilising agent, filling rift systems even during summer (DJF) and likely suppressing further propagation.

By contrast, rifts at Jutulstraumen Glacier have remained remarkably persistent since the 1970s, with little formation of new rifts across the main ice tongue (Figure 6.3). Only one additional rift, located on the eastern side of the tongue, developed following a minor calving event. Chapter 6 highlighted that in Jutulstraumen, rift propagation is more influenced by glaciological stress fields. On the floating ice tongue, rifts primarily formed due to extensional and shear stresses arising from dif-

ferential flow across the shelf (Chapter 6). These stresses were concentrated along shear margins and at transitions in ice velocity or structural integrity, such as near pinning points and embayment walls. As the shelf advanced, these zones experienced repeated fracturing, leading to the formation of persistent rift systems aligned with flow direction and structural weaknesses.. The absence of suture zones in Jutulstraumen likely facilitates steady rift propagation, while cold ocean conditions help maintain ice tongue integrity. Chapter 6 suggested that any future calving events may be triggered by rift propagation focused at the rift tip (Bassis et al., 2007), similar to the major 1967 calving event (Kim et al., 2001). Similar processes of rift-driven calving have been observed in other Enderby and Kemp Land glaciers (Chapter 4).

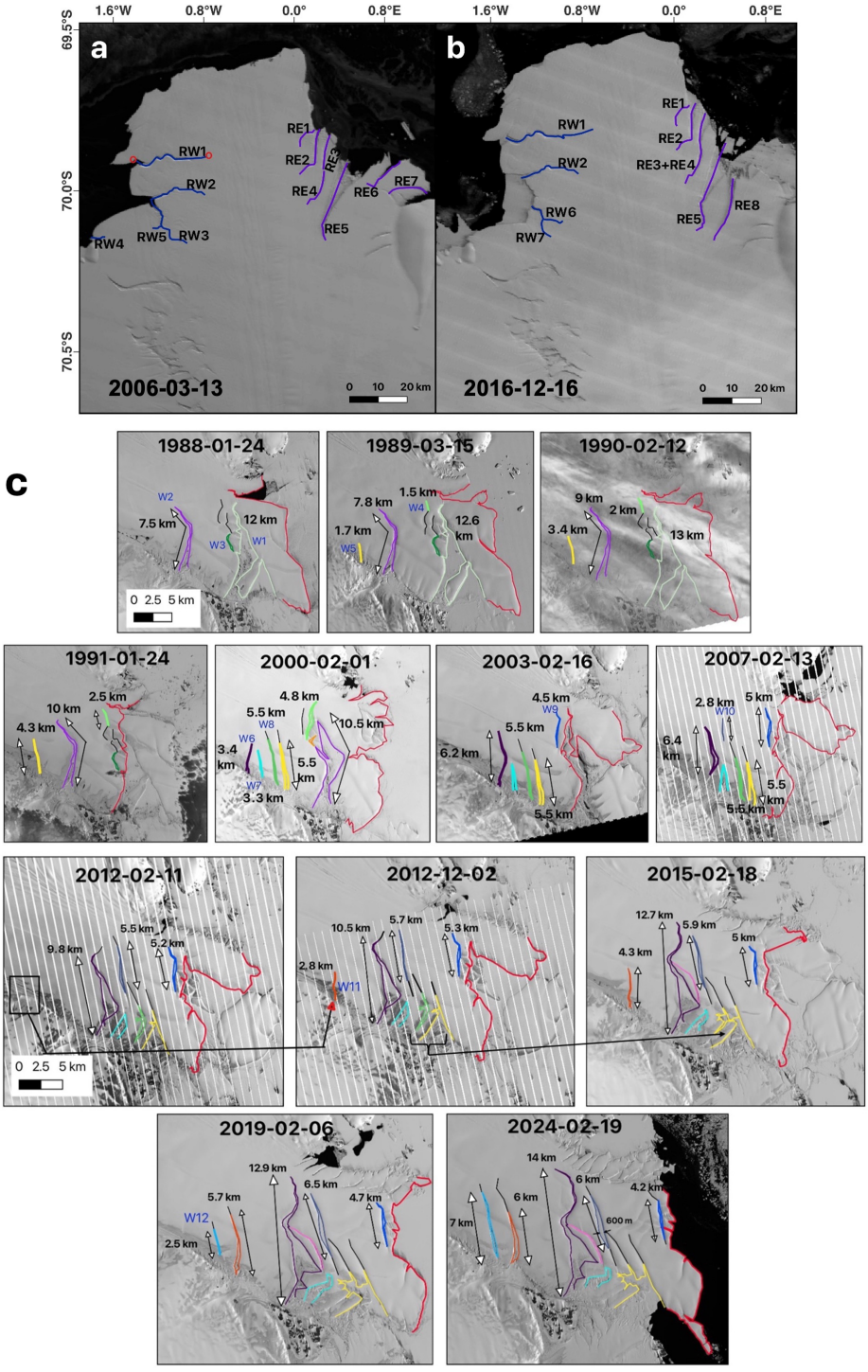

Figure 7.1: *Rifts on Jutulstraumen and WRD. Overview of location of rifts on (a) 13th Mar 2006 and (b) 16th Dec 2016 on Jutulstraumen Glacier, respectively, with major rifts on the western branch (RW1–RW7, blue) and eastern branch (RE1–RE8, purple) labeled.(c) Time series of selected Landsat/ASTER/WorldView snapshots from 1988 through 2024, illustrating the initiation, propagation, and calving of individual rifts (W1–W12, colored lines) on the WRD tongue. Bidirectional arrows with distance annotations (km) denote the cumulative extent of each rift at each date; pre- and post-calving termini are outlined in light green and red, respectively. Dates (YYYY-MM-DD) are shown above each subpanel.*

However, the long-term stability of these glaciers (e.g. Jutulstraumen, WRD) are increasingly at risk due to the ongoing reduction in the extent of pinning points across the Antarctic Ice Sheet. A recent study by Miles et al. (2024) found that these buttressing features have been steadily shrinking, particularly in Wilkes Land in the EAIS. While Miles et al. (2024) documented widespread pinning-point loss in regions such as Wilkes Land, they found no such decline in Enderby and Kemp Land, instead, pinning points in the Wilma–Robert–Downer Embayment actually increased in extent between 2000 and 2022. This is likely because there are fewer pinning points in this region to begin with, reflecting a fundamentally different bathymetric setting that offers limited potential for widespread unpinning. This trend raises concern over the unanchoring of ice shelves, which can lead to abrupt and large-scale calving events. The collapse of the Conger–Glenzer Ice Shelf exemplifies this process: the loss of a critical pinning point led to a 10% reduction in ice shelf area within a single year. This final collapse phase was driven by calving along pre-existing rifts, progressive thinning of mélange, and structural failure due to rift interconnection. Similar mechanisms have been implicated at WRD Glacier , where repeated calving events—including those in 1991 and 2003—were preceded by the gradual widening and merging of persistent rifts in zones of concentrated stress near lateral margins and pinning points. These parallels underscore the importance of structural precursors and local buttressing in controlling ice-shelf stability (Chapter 5). Likewise, the collapse of the Larsen A Ice Shelf in the mid-1990s removed mechanical support from Drygalski Glacier, causing ice velocity near the grounding line to triple.

7.1.3.2 Sea ice conditions and subsurface ocean temperatures influences on glacier terminus behaviour

Chapter 4 showed that oceanic conditions—particularly sea-ice concentration and subsurface ocean temperature are key external controls on glacier terminus change across Enderby and Kemp Land. In contrast, Chapter 6 indicated that oceanic influences on Jutulstraumen in Dronning Maud Land have been historically limited, with relatively cold shelf waters and persistent ice shelf buttressing supporting long-

term frontal stability. However, recent observations suggest that warm modified Circumpolar Deep Water (mCDW) has begun intruding into the Fimbulisen cavity since 2016 (Lauber et al. 2023), raising concerns about increased basal melt and future destabilisation. At the regional scale, normalised terminus positions were found to be moderately and positively correlated with summer sea-ice concentration, and strongly and negatively correlated with mean subsurface ocean temperatures (5–109 m depth), with respective time lags of 2 and 5 years. This suggests that glacier advance in these regions is more likely to occur during periods of higher summer sea-ice cover—which limits ocean swell and thermal erosion—and cooler subsurface conditions. Notably, retreat events were often preceded by 5-year mean ocean temperatures exceeding ~ 1.2°C, particularly in glaciers lacking protective fjord geometries or floating tongues. These findings align with previous work on ice–ocean interactions in East Antarctica, highlighting the role of reduced sea-ice days and warm water intrusions in promoting frontal instability (e.g. Miles et al., 2016; Baumhoer et al., 2021).

At the individual glacier scale, the majority of glaciers also showed statistically significant negative correlations with subsurface ocean temperatures at the 5–109 m depth interval, typically with a lag of five years, reinforcing the influence of delayed oceanic forcing on terminus behaviour. This finding aligns with previous studies across the EAIS. For example, Miles et al. (2016) attributed widespread retreat in Wilkes Land during 2000–2012 to a reduction in sea-ice days, which increased terminus exposure to wave action and oceanic heat. Similarly, Baumhoer et al. (2021) found that retreat during 2009–2018 in the same region was linked to the upwelling of warm Circumpolar Deep Water (CDW), which enhanced basal melting and weakened glacier termini. Together, these findings imply that both sea-ice concentration and subsurface ocean temperature are critical, spatially consistent drivers of glacier frontal change across East Antarctica, acting over multi-year timescales.

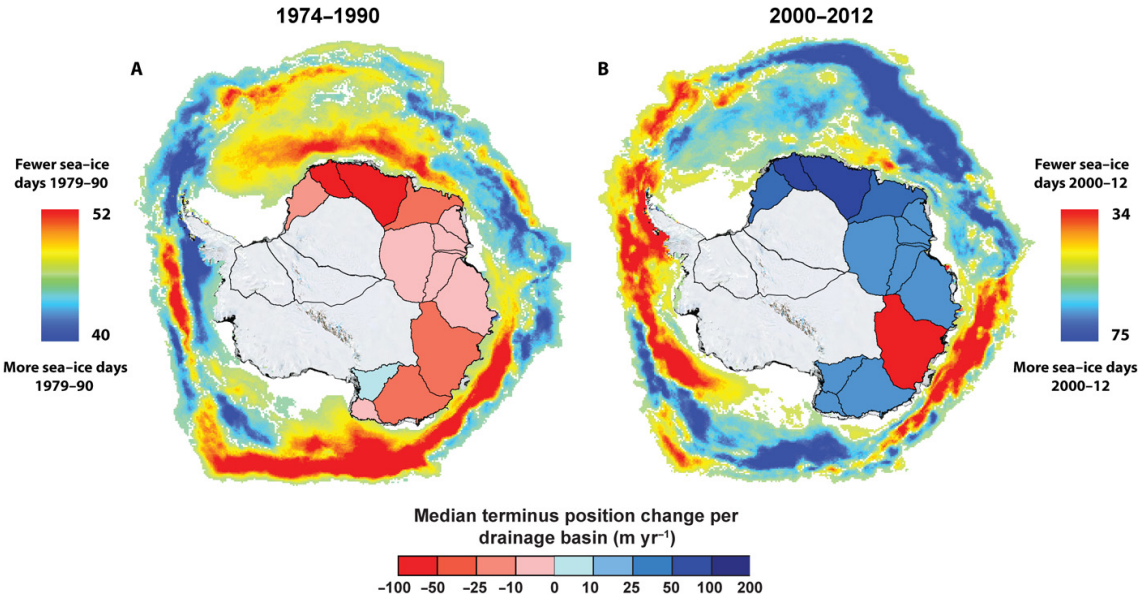

Figure 7.2: *Seasonal sea-ice changes and glacier terminus trends from Miles et al. (2016). (a, b) Difference in April–October sea-ice days relative to 1990–2000 for (a) 1974–1990 and (b) 2000–2012. Red shading indicates a reduction in seasonal sea-ice days; blue shading shows an increase. Superimposed drainage basins are coloured by their median terminus change (m yr^{-1}), with red tones for retreat and blue tones for advance*

Chapter 5 highlighted the critical role of persistent sea ice cover in regulating the dynamic stability of the WRD Glacier. Landfast sea ice anchored at the glacier terminus exerts a direct buttressing effect, suppressing frontal velocity and calving rates. This stabilising influence can persist over multiyear periods, as demonstrated by the iceberg calved in 2003, which remained grounded at the glacier front until 2015—a delay attributed to the sustained presence of sea ice impeding iceberg drift and frontal retreat. In addition to this external buttressing, sea ice and mélange retained within rift networks along the floating ice tongue appear to exert a secondary internal stabilisation mechanism. These mélange-filled rifts likely contribute to the observed suppression of calving and deceleration in flow near the glacier front, enhancing resistance to dynamic thinning (Chapter 5). Notably, this internal buttressing persists even during episodes when frontal sea ice cover is reduced or absent, suggesting that mélange confined within fjord-like geometries can maintain structural cohesion and stability independently of transient sea ice fluctuations. Collectively, these findings demonstrate that both externally anchored and internally embedded sea ice and mélange play critical roles in modulating calving dynamics

and sustaining frontal stability. This is consistent with similar observations at other Antarctic margins. For example, the Mertz Glacier tongue remained intact for years prior to its 2010 calving, partly due to sea ice and mélange consolidation (Massom et al., 2010).

Chapter 6 highlighted that Jutulstraumen Glacier, which flows into the Fimbulisen Ice Shelf, is stabilised through a combination of topographic pinning, ice rises, and sea ice or mélange-filled rift systems. This configuration effectively suppresses dynamic thinning and limits calving. Periods of persistent sea ice appear to enhance the buttressing effect, particularly when mélange accumulates within rifts, reducing their potential for propagation. However, the work presented here shows that in the absence of sea ice, the ice tongue becomes more exposed to ocean swells and warm-water intrusions. Chapter 5 also highlighted that in WRD Glacier floating ice tongue when rift tips begin to align or propagate toward one another, ocean swells may serve as mechanical triggers, potentially initiating calving even without anomalously warm conditions. While no statistically significant relationship was found between sea-ice concentration or ocean temperature and rift propagation at Jutulstraumen, calving is likely governed by a combination of oceanic exposure, internal stress fields, and rift geometry. Of particular concern is the recent detection of warm modified Circumpolar Deep Water (mCDW) in the Fimbulisen cavity (2016–2019), which has led to increased basal melt rates (~ 0.62 m yr^{-1}) and mass loss (~ 15.5 Gt yr^{-1}; Lauber et al., 2023). The intrusion of mCDW into what has majorly been a cold-shelf environment (Hatterman et al. 2014) raises concerns about the long-term stability of this formerly stable system.

By contrast, glaciers that terminate in open-ocean environments and lack both ice shelves and fjord confinement are significantly more vulnerable to oceanic forcing. Chapter 4 identified several such glaciers—Oku-iwa, Nishi-naga-iwa, and Glacier 17—which experienced short-lived advances followed by abrupt and irregular retreat episodes. These events commonly coincided with low summer sea-ice conditions and elevated subsurface ocean temperatures, leaving the termini exposed to wave action and thermal erosion. Without the protective influence of shelf ice, mélange or

landfast sea ice, these glaciers are prone to disintegration during warm years. This is supported by more recent studies highlighting that sea ice break-up can lead to disintegration of ice shelves such as Voyeykoyev Ice Shelves (Arthur et al. 2021) and Porpoise Bay (Miles et al. 2017).

7.1.3.3 Atmospheric drivers influencing glacier terminus behaviour

Chapters 4-6 explored the extent to which atmospheric variability—particularly changes in the near-surface air temperatures—modulates glacier terminus dynamics across the study area. While atmospheric drivers are widely acknowledged to influence terminus behaviour elsewhere in the AIS (Rott et al., 2011; Boening et al., 2012; Lenaerts et al., 2013; Miles et al., 2016), their effects on terminus behaviour in Enderby and Kemp Lands appear to be less direct.

Chapter 4 showed that for glaciers across the Enderby and Kemp Lands, direct statistical correlations between mean summer air temperature and observed changes in glacier terminus position were found to be generally weak or non-significant as mean summer (December-January-February) air temperatures consistently remained below 0°C at the regional scale. For individual glaciers, only a limited number of positive degree days (PDDs) were recorded across a few glaciers during the study period. Additionally, isolated meltwater ponds were only intermittently detected in satellite imagery, and their occurrences were inconsistent and none progressed to hydrofracturing (Stokes et al. 2019). Previous studies have also highlighted that even in localised regions where summer air temperatures have increased by more than 1°C since the early 1980s—such as at Mariner and Tucker Glaciers—no significant retreat in glacier front position was observed that coincided with this increase in temperature. This is likely because mean summer air temperatures in these regions remain well below freezing, limiting the potential for surface melt to directly influence terminus retreat (Baumhoer et al., 2021). Moreover, Lovell et al. (2017) found no clear relationship between air temperature and glacier terminus change in Oates Land, noting that three glaciers with substantial meltwater ponding actually advanced between 1972 and 2013. This suggests that surface warming alone

does not provide a sufficient destabilising mechanism in terms of calving. Similarly, continued advance of the Lazarev and Filchner Ice Shelves has been documented despite recent atmospheric warming trends (Baumhoer et al., 2021), further reinforcing the interpretation that present-day temperature increases are insufficient to induce substantial meltwater production or calving via surface weakening processes. In addition, Chapter 6 showed that rift propagation does not exhibit a statistical correlation with air temperature, indicating that periods of rift lengthening were not directly driven by warmer atmospheric conditions.

Although no statistically significant correlation was found between mean summer air temperatures and glacier terminus change in Enderby and Kemp Lands, the Southern Annular Mode (SAM) may nonetheless exert an indirect influence on glacier behaviour. Chapter 4 reported that 74% of monitored glacier termini retreated between the early 1970s and 1988—a period characterised by a sustained negative SAM phase (Fig. 7.3). This pattern aligns with the findings of Miles et al. (2016), who attributed the widespread retreat across the EAIS between 1974 and 1990 to the influence of negative SAM, which is typically associated with reduced sea-ice extent and warmer atmospheric conditions. In contrast, the shift to a predominantly positive SAM phase beginning around 1988 coincided with cooler, more stable conditions and a reversal towards glacier advance in both regions (Fig. 7.3). Chapter 5 extended this analysis through to 2023, confirming the persistence of a positive SAM polarity in recent decades and its consistency with the continued advance or stability of many glacier termini.

In DML, Enderby and Kemp Lands, snowfall anomalies have played a key role in modulating surface mass balance and glacier stability (Shepherd et al., 2019; Lenaerts et al., 2013; Dømgaard et al. 2024). These regions thickened by up to a decimeter per year over 25 years (1992 and 2017) (Schröder et al. 2019). DML experienced mass gains of $+3.2 \pm 0.6$ Gt yr^{-1}, with a mean accumulation of 21 cm yr^{-1} and snowfall variability of 4.3 cm yr^{-1}. Rignot et al., 2019 estimated that Jutulstraumen in DML has experienced mass gains of +33 Gt between 1979 and 2018. Chapter 6 further examined the case of Jutulstraumen Glacier, which experienced a

major calving event in the late 1960s during a negative SAM phase. While this event has been attributed to rift propagation, it remains uncertain whether unusually low sea-ice conditions—potentially linked to negative SAM—contributed to the timing or magnitude of calving (Fig. 7.3). In the decades that followed, Jutulstraumen has exhibited sustained advance, which appears to be supported by episodic snowfall anomalies. Notably, between 2009 and 2011, persistent atmospheric blocking and poleward moisture transport produced snowfall totals five to six times above the regional average (Boening et al., 2012).

Enderby and Kemp Lands similarly experienced net mass gains of $+3.3 \pm 0.9$ Gt yr^{-1} and $+2.7 \pm 0.5$ Gt yr^{-1}, respectively, during 1992–2017 (Schröder et al., 2019), driven by mean accumulation rates of 18 cm and 23 cm per year. These trends were also confirmed by Rignot et al. (2019), who reported mass balance at Enderby Land between 1979 and 2017. Evidence from other regions—such as the Amery Ice Shelf and outlet glaciers in Wilkes Land—suggests that anomalously high accumulation may exert a stabilising effect on glacier termini, primarily through thickening (Rendfrey et al., 2024), though this operates on longer timescales than dynamic calving processes.

Dømgaard et al. (2024) reported long-term thickening across Kemp, MacRobertson Land, and Ingrid Christensen Coast, superimposed by periods of decadal-scale thinning. Their results showed that surface elevation increases since 1937–1960 were greatest at Hoseason ($+0.23 \pm 0.07$ m yr^{-1}) and Taylor ($+0.11 \pm 0.05$ m yr^{-1}) Glaciers.

Taken together, these observations highlight the broader role of snowfall variability and moisture advection in modulating ice sheet mass balance and outlet glacier behaviour in East Antarctica. While accumulation alone does not directly control calving, it may support long-term stability through enhanced surface mass balance and glacier thickening, offsetting dynamic losses in some regions.

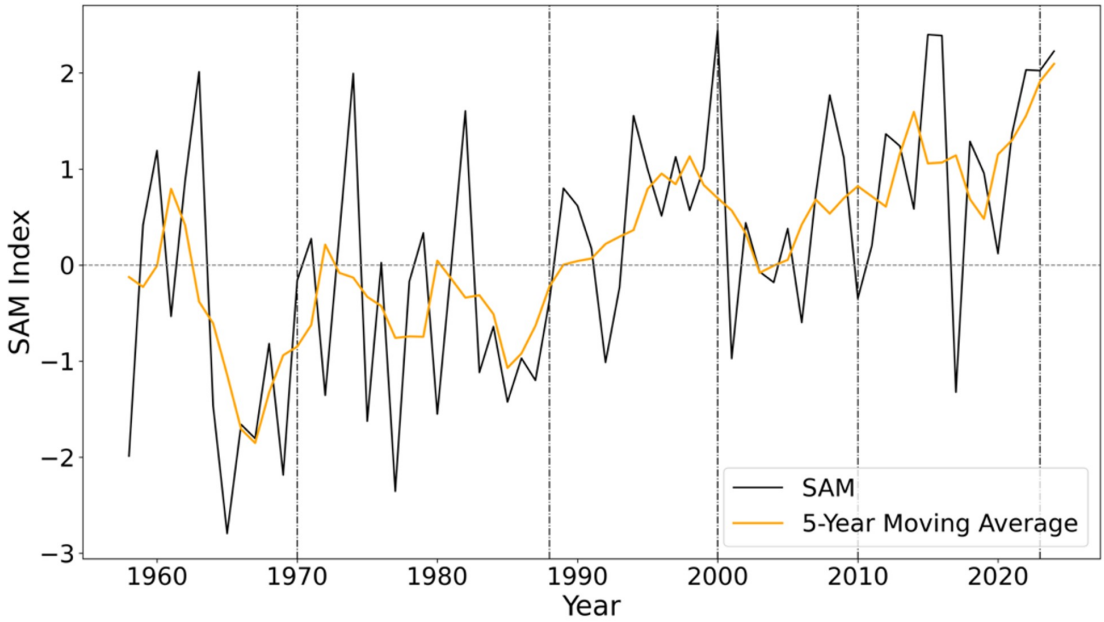

Figure 7.3: *The SAM index from 1957-2024 using the Marshall et al. (2003) observational based index.*

However, not all glaciers in these regions show signs of mass gain. Within Enderby and Kemp Lands, Rayner Glacier lost mass at ~ 0.7 Gt yr^{-1} (Rignot et al., 2019), and the Wilma–Robert–Downer (WRD) system showed modest acceleration between 2008 and 2016. Consistent with this, Miles et al. (2022) reported increases in ice discharge of $4 \pm 2\%$ at Rayner and $6 \pm 5\%$ at WRD between 2005 and 2016. At Rayner, discharge declined between 2005 and 2014 during a period of frontal advance, but increased again after a major calving event in 2014–2016, which caused 10km of retreat. This was followed by re-advance and reduced discharge. Chapter 4 further shows that Rayner underwent another calving event in 2023, retreating $\sim$ 6 km likely resulting in another short-term increase in discharge.

In contrast, the dynamic changes at WRD were more subdued. The increase in ice discharge at Wilma-Robert-Downer, however, remains relatively low and within the uncertainty range, suggesting limited dynamic change. Based on the findings presented in Chapter 5, it is estimated that between 2006 and 2017, the velocity near the ice front (UT location in Figure 5.1a) increased by only $2 \pm 0.7\%$. The reason for the slight increase estimates in ice discharge and velocity highlighted in

all the studies (Rignot et al. 2019; Miles et al. 2022; Chapter 5) between 2005 and 2017 could be linked to the calving events that occurred in 2015 and 2017 (Fig. 5.4 in Chapter 5). However, the 2015 event coincided with the presence of persistent sea ice in front of the ice tongue, which likely exerted a buttressing effect, limiting dynamic glacier retreat or acceleration. In contrast, the subsequent calving event in 2017 occurred under markedly different conditions—there was no sea ice in front of the glacier. The absence of sea ice likely removed the resistive back-stress normally provided by consolidated sea ice or mélange, allowing the glacier to respond more freely to calving-induced changes and potentially increasing ice discharge. This highlights the role of frontal conditions in modulating glacier dynamics.

This suggests that it is not only one driver that alone contributes to terminus position changes. Infact, local dynamic processes such as rifting, calving, and changes in buttressing provided by sea ice conditions continue to drive variability at the glacier scale. The glacier-by-glacier analysis presented in this thesis builds on and adds spatial extent to existing satellite-based mass balance assessments by documenting how individual outlet glaciers have evolved over multi-decadal periods in response to both climatic and dynamic forcings. Overall, the findings from Chapters 4 to 6 show that oceanic and atmospheric effects on glacier terminus changes in the EAIS are complex and shaped by multiple factors. While the SAM could have regional influence terminus stability and calving dynamics, its impact depends on other conditions like sea ice conditions, snowfall, local topography, and surface mass balance. In most cases, air temperature on its own, without enough melt to trigger hydrofracturing or weaken the ice surface, is not enough to explain changes in glacier termini positions. Similarly, although ice shelves and sea ice (in regions lacking ice shelves) can provide buttressing to glacier termini, the majority of calving events appear to have been initiated by internal glacier dynamics, such as development of rifts and their propagation. That said, the absence of sea ice likely reduces frontal buttressing, and increase in subsurface ocean temperatures may further promotee basal melting and structural weakening, thereby facilitating calving. Despite some observed terminus changes and calving events, the analysis revealed no consistent large-scale regional or sub-regional trend throughout the study period. This suggests

that glacier responses in this sector of Antarctica are more sporadic and locally driven. It is also important to note that the magnitude of observed changes in the EAIS remains relatively moderate compared to the dynamic ice loss occurring in regions like GrIS and WAIS. Nonetheless, individual glaciers in the EAIS can exhibit notable sensitivity to even minor shifts in ocean conditions, sea ice extent, and atmospheric forcing. These findings underscore the importance of integrating both regional climate patterns and fine-scale environmental variability when assessing the future behaviour of East Antarctic glaciers under climate change.

7.1.4 Opportunities for Future Research

7.1.4.1 Limitations

The limited spatial resolution of environmental datasets introduces additional uncertainty into the assessments. For example, satellite-derived sea ice concentration products typically have spatial resolutions of $\sim$ 20 km, whereas many EAIS outlet glaciers have terminus widths of less than $\sim$ 12 km. This meant that local scale changes that may have impacted particular parts of the termini or the glaciers in the study area may have been hidden within the spatial scale of the sea ice concentration data. The scarcity of in situ oceanographic observations—particularly within sub-ice shelf cavities and near grounding lines—limits our capacity to accurately quantify basal melt rates or detect early signs of destabilisation. While subsurface ocean temperature such as those observed through moored instruments or reanalysis products provide a useful proxy for upper-ocean heat content and variability, they remain an indirect indicator of the processes acting at the ice–ocean interface. This is not helped by the lack of measurements of the continental shelf bathymetry which is not well resolved around much of this area because the presence of sea ice prevents direct measurement by ship. The lack of direct measurements of basal melt rates beneath ice tongues limits the ability to quantify the actual magnitude and spatial heterogeneity of ocean-induced melting. This is particularly critical in grounding line regions, where ocean-driven basal melting can modulate ice shelf thinning and influence grounding line retreat. In the absence of high-resolution in situ observa-

tions or sophisticated inverse modelling, it remains difficult to establish definitive causal relationships between ocean temperature variability and glacier terminus behaviour at fine spatial scales.

7.1.4.2 Future Research

Given the limitations above, and the complex and often asynchronous responses of glacier termini to a range of climatic and non-climatic drivers, it is increasingly clear that predicting future changes in the East Antarctic Ice Sheet (EAIS) requires a shift toward glacier-specific monitoring and modelling, rather than relying solely on regional or continental-scale assessments. Chapters 5 and 6 have undertaken such glacier-specific analyses, revealing how individual glacier dynamics have evolved over recent decades although we note that earlier in our observation period there is less image availability compared to present day. This is increasingly possible with the increasing availability of satellite data but is still hampered by the lack of direct observation of climate and ocean conditions. This is increasingly possible with the increasing availability of satellite data but is still hampered by the lack of direct observation of climate and ocean conditions. To better understand causal mechanisms and forecast future change, it is critical to integrate observational data with numerical modelling, particularly models that incorporate ice–ocean–atmosphere interactions. As highlighted in recent work by Jordan et al. (2020), such models can be used to test hypotheses around specific forcing mechanisms and evaluate their capacity to trigger observed glacier changes—such as those inferred for the Wilma–Robert–Downer or Jutulstraumen systems. Modelling can also help identify nonlinear thresholds, feedbacks, and time lags that are not immediately apparent from satellite-derived correlations. This approach is especially critical in light of recent events, such as the gradual but ultimately destabilizing changes that preceded the collapse of the Conger-Glenzer Ice Shelf (Walker et al. 2024). Continuous, glacier-specific observation is therefore vital for detecting early signs of instability. To support this, several key observational priorities are suggested:

• High-resolution satellite monitoring of glacier termini, grounding lines, rift prop-

agation, and mélange/sea-ice conditions. Optical and SAR datasets can be used to track terminus migration and frontal stress regimes at seasonal to annual scales. Importantly, by not just mapping the terminus change, but by mapping sea ice conditions and structural evolution, a better understanding of glacier evolution can be developed.

• Deployment of autonomous oceanographic instruments to measure water temperature, salinity, and circulation directly in front of glacier termini and within ice shelf cavities. This would enable the causal relationships between ocean water and glacier change to be tested, and for the presence or absence of warm water intrusions to be established.

• Basal melt estimates, ideally derived from repeat altimetry or ice-penetrating radar, would help constrain the response of glacier tongues to ocean heat flux – especially when used in tandem with the desired direct observations of water conditions suggested above.

• Integrated climate data assimilation, such as the inclusion of SAM indices, snowfall anomalies, and surface energy balance, to resolve the role of atmospheric variability in modulating ocean and glacier response. To aid this, direct measurements of climate (air temperature, snowfall, radiation fluxes) at individual glaciers would be potentially important, especially given the different responses that individual glaciers appear to have in the region studied in this thesis.

• Developing glacier sensitivity indices across EAIS by creating a comparative framework to rank outlet glaciers by sensitivity to external forcing. Such indices could incorporate factors such as terminus width, ocean access, sea-ice persistence, bed slope, and surface mass balance trends. These could then be used to prioritize monitoring and model validation in regions of emerging dynamic instability.

A systematic approach that combines remote sensing, in situ measurements, and model–data integration is essential to move beyond case-specific insights toward a broader, process-based understanding of EAIS glacier stability. With such a frame-

work we would have the potential to constrain the thresholds and feedbacks that may drive future change.

CHAPTER 8

Conclusion

The primary aim of this thesis was to investigate the sensitivity of marine-terminating glaciers to oceanic, atmospheric, and non-climatic drivers across Enderby Land, Kemp Land, and Dronning Maud Land (DML) in East Antarctica between the 1970s and 2023. By combining a 50-year satellite record with a suite of environmental datasets, including sea-ice concentration, sea-ice extent, subsurface ocean temperature, and air temperature, this study provides new insights into the evolution of outlet glaciers in this relatively underexamined sector of the East Antarctic Ice Sheet (EAIS). The results significantly contribute to a more nuanced understanding of glaciological variability across East Antarctica, especially in regions where long-term change has remained poorly documented.

Across the study area, the majority of marine-terminating glaciers in Enderby and Kemp Lands exhibited a net advance over the past five decades, a behaviour that contrasts sharply with the widespread retreat observed in other regions such as the West Antarctic Ice Sheet (WAIS), the Antarctic Peninsula Ice Sheet (APIS), and the Greenland Ice Sheet (GrIS). Despite this overarching pattern of advance, glacier termini exhibited clear decadal-scale fluctuations. A widespread retreat was observed between the 1970s and 1988, associated with a negative phase of the Southern Annular Mode (SAM), warmer subsurface ocean temperatures, and reduced sea-ice extent. This was followed by a sustained period of advance between 1988 and 2010, coinciding with a positive SAM phase and cooler ocean conditions. Since 2010, however, the proportion of advancing glaciers has declined, suggesting a weakening of these broader ocean–climate linkages and an increasing role for localised and glacier-specific controls.

Marked regional differences were also evident. Enderby and Kemp Lands exhibited opposing trends throughout the study period. During the first epoch (1970s–1988), most Enderby glaciers retreated, while those in Kemp Land advanced. This pattern reversed in the second epoch (1988–2000), when glaciers in Enderby advanced and those in Kemp Land retreated. Both regions experienced a general advance during the third epoch (2000–2010), but diverged again in the final epoch (2010–2023), as Enderby glaciers returned to retreat while Kemp Land glaciers largely continued to

advance. Meanwhile, in DML, Jutulstraumen Glacier has advanced steadily by over 30 km since the 1967 calving event, with no evidence of substantial retreat. These regional contrasts underscore the inadequacy of relying solely on large-scale climate indices and highlight the modulating influence of local oceanographic conditions, topography, and ice shelf configuration.

At the glacier scale, behaviour was often asynchronous, even among neighbouring systems. Glaciers such as the Wilma–Robert–Downer (WRD) system exhibited long-term advance despite episodic calving events (e.g. 1991, 2003, 2014), owing to stabilising structural features such as lateral pinning points, topographic confinement, and persistent rift-infill by sea ice or mélange. In contrast, unconfined systems like Oku-iwa and Omega were more susceptible to episodic retreat. These divergent behaviours illustrate the importance of glacier-specific settings in mediating stability and suggest that individual glacier dynamics may not always reflect regional climatic signals.

Rift dynamics and structural controls emerged as critical mediators of glacier terminus stability. Calving events were recorded across all study regions, but their magnitude and consequences varied. In Enderby and Kemp Lands, moderate-scale calving was frequently followed by re-advance in structurally supported glaciers like WRD. Unconfined glaciers were less stable, often failing to recover after retreat. In DML, Jutulstraumen Glacier exhibited slowly propagating rifts across its ice tongue but has maintained continuous advance, supported by grounded ice rises, a narrow flux gate, and low basal melt. These findings emphasise that fjord confinement, ice rise pinning, and mélange-filled rift systems are critical in moderating the glaciological impact of rifting and calving.

Environmental drivers, particularly sea ice and ocean temperature, played a key role in shaping terminus behaviour. Statistical correlation analyses revealed that some glacier advance was associated with higher sea ice conditions and reduced subsurface ocean temperatures. Across the study area, sea ice and mélange acted as important stabilising agents: persistent landfast sea ice inhibited frontal re-

treat, while mélange-filled rifts restricted fracture propagation. For example, at the Wilma–Robert–Downer (WRD) system, long-term advance occurred despite presence of multiple rifts over the study period, facilitated by persistent mélange within rift cavities and in front of the terminus. The influence of atmospheric warming across glaciers of Enderby and Kemp Land was limited due to sustained sub-zero summer air temperatures.

Importantly, this study highlights that ocean-climate drivers alone are insufficient to explain observed glacier behaviour. Even adjacent glaciers subject to similar environmental forcing often responded differently, pointing to the critical role of glacier-specific factors such as grounding line geometry, fjord confinement, subglacial topography, and internal ice dynamics. The pronounced heterogeneity and asynchrony in glacier behaviour observed across the study region underscores the need for glacier-specific monitoring frameworks and high-resolution modelling capable of capturing the fine-scale processes that govern ice-sheet evolution.

Taken together, these findings demonstrate that EAIS outlet glacier stability is governed by a confluence of large-scale climate variability and highly localised glaciological controls. No single variable can reliably predict glacier change across space or time. As Antarctica continues to experience the compounding effects of atmospheric warming and increased ocean heat intrusion, future sea-level contributions from the EAIS will likely depend on both the magnitude and timing of regional climate events and the capacity of local glacier systems to buffer against them. High-resolution, glacier-specific observations and targeted numerical modelling will be essential for detecting early signals of instability, improving future projections, and refining our understanding of East Antarctica's potential sea-level contributions in a warming world.

References

Adhikari, S., Ivins, E. R., Larour, E., Seroussi, H., Morlighem, M., and Nowicki, S. M. J. (2014). Future Antarctic bed topography and its implications for ice sheet dynamics. *Solid Earth*, 5(2), 569–584.

Adusumilli, S., Fricker, H. A., Medley, B., Padman, L., and Siegfried, M. R. (2020). Interannual variations in meltwater input to the Southern Ocean from Antarctic ice shelves. *Nature geoscience*, 13(9), 616–620.

Alley, R. B., Clark, P. U., Huybrechts, P., and Joughin, I. (2005). Ice-sheet and sea-level changes. *Science*, 310(5747), 456–460.

Alley, R. B., Horgan, H. J., Joughin, I., Cuffey, K. M., Dupont, T. K., Parizek, B. R., Anandakrishnan, S. and Bassis, J. (2008). A simple law for ice-shelf calving. *Science*, 322, 1344–1344.

Alley, R. B. et al. (2014). Oceanic forcing of ice-sheet retreat: West Antarctica and more. *Annual Review of Earth and Planetary Sciences*, 43(1), 1–25.

Alley K. E., Scambos T. A., Siegfried M. R. and Fricker H. A. (2016) Impacts of warm water on Antarctic ice shelf stability through basal channel formation.

Nature Geoscience, 9(4), 290–293.

Alley, K. E., Scambos, T. A., Anderson, R. S., Rajaram, H., Pope, A., and Haran, T. M. (2018). Continent-wide estimates of Antarctic strain rates from Landsat 8-derived velocity grids. *Journal of Glaciology*, 64(244), 321–332.

Alley, K. E., Wild, C. T., Luckman, A., Scambos, T. A., Truffer, M., Pettit, E. C., et al. (2021). Two decades of dynamic change and progressive destabilization on the Thwaites Eastern Ice Shelf, *The Cryosphere*, 15, 5187–5203.

Alley K. E., Scambos T. A., Alley R. B. (2022). The role of channelized basal melt in ice-shelf stability: recent progress and future priorities. *Annals of Glaciology*, 63(87-89),18-22.

Alley, K. E.(2024). Ice-shelf disintegration in East Antarctica. *Nature Geoscience*, 17, 1193–1194.

Allison, I., Frew, R. and Knight, I. (1982). Bedrock and ice surface topography of the coastal regions of Antarctica between 48°E and 64°E. *Polar Record*, 21(132), 241–252.

Amundson, J. M., Fahnestock, M., Truffer, M., Brown, J., Lüthi, M. P. and Motyka, R. J. (2010). Ice mélange dynamics and implications for terminus stability, Jakobshavn Isbræ, Greenland, *Journal of Geophysical Research*, 115, F01005.

Amundson, J. M., Kienholz, C., Hager, A. O., Jackson, R. H., Motyka, R. J., Nash, J. D. and Sutherland, D. A. (2020). Formation, flow and break-up of ephemeral ice mélange at LeConte Glacier and Bay, Alaska. *Journal of Glaciology*, 66(258), 577–590.

Hogg, A. E., Gilbert, L., Shepherd, A., Muir, A. S., McMillan, M. (2021). Extending the record of Antarctic ice shelf thickness change, from 1992 to 2017. *Advances in Space Research*, 68 (2), 724-731.

Aoki, S., Katsumata, K., Hamaguchi, M., Noda, A., Kitade, Y., Shimada, K. et al. (2020). Freshening of Antarctic bottom water off Cape Darnley, East Antarctica. *Journal of Geophysical Research: Oceans*, 125, e2020J. C.016374.

Arthur, J. F., Stokes, C. R., Jamieson, S. S. R., Carr, J. R., and Leeson, A. A. (2020). Distribution and seasonal evolution of supraglacial lakes on Shackleton Ice Shelf, East Antarctica. *The Cryosphere*, 14, 4103–4120.

Arthur, J. F., Stokes, C. R., Jamieson, S. S. R., Miles, B. W. J., Carr, J. R., and Leeson, A. A. (2021). The triggers of the disaggregation of Voyeykov Ice Shelf (2007), Wilkes Land, East Antarctica, and its subsequent evolution. *Journal of Glaciology*, 67(265), 933–951.

Arthur, J. F., Stokes, C. R., Jamieson, S. S. R. et al. (2022). Large interannual variability in supraglacial lakes around East Antarctica. *Nat Commun 13*, 1711.

Ayres, H. C., Ferreira, D., Park, W., Kjellsson, J. and Ödalen, M. (2024) A comparison of the atmospheric response to the Weddell Sea Polynya in atmospheric general circulation models (A. G. C. M.s) of varying resolutions. *Weather and Climate Dynamics*, 5, 805–820.

Baiman, R., Winters, A. C., Lenaerts, J. and Shields, C. A. (2023). Synoptic drivers of atmospheric river induced precipitation near Dronning Maud Land, Antarctica. *Journal of Geophysical Research: Atmospheres*, 128, e2022J. D.037859.

Baines, P. G.(2009). A model for the structure of the Antarctic Slope Front. *Deep-Sea Research*, Pt II, 56, 859–873.

Bamber, J. L. and Aspinall, W. P. (2013). An expert judgement assessment of future sea level rise from the ice sheets. *Nature Climate Change*, 3(4), 424–427.

Banwell, A. F., MacAyeal, D. R. and Sergienko, O. V. (2013). Breakup of the Larsen B Ice Shelf triggered by chain reaction drainage of supraglacial lakes.

Geophysical Research Letters, 40, 5872–5876.

Banwell, A. F. and MacAyeal, D. R. (2015). Ice-shelf fracture due to viscoelastic flexure stress induced by fill/drain cycles of supraglacial lakes. *Antarctic Science*, 27(6), 587–597.

Banwell A. F., MacAyeal D. R. and Larter, R. (2021). Observations of meltwater lakes and drainage on the George V. I.. I.ce Shelf. *The Cryosphere*, 15, 633–646.

Barletta, V. R., Bevis, M., Smith, B. E., Wilson, T., Brown, A., Bordoni, A., Willis, M., Khan, S. A., Rovira-Navarro, M., Dalziel, I., Smalley, R., Jr, Kendrick, E., Konfal, S., Caccamise, D. J., 2nd, Aster, R. C., Nyblade, A., and Wiens, D. A. (2018). Observed rapid bedrock uplift in Amundsen Sea Embayment promotes ice-sheet stability. *Science*, 360(6395), 1335–1339.

Bassis, J. N. et al. (2007). Seismicity and deformation associated with ice-shelf rift propagation. *Journal of Glaciology*, 53(183), 523–536.

Bassis, J. N., Fricker, H. A., Coleman, R. and Minster, J. B. (2008). An investigation into the forces that drive ice-shelf rift propagation on the amery ice shelf, East Antarctica. *Journal of Glaciology*, 54(184), 17–27.

Braun, M. and Humbert, A. (2008). Recent Retreat of Wilkins Ice Shelf Reveals New Insights in Ice Shelf Breakup Mechanisms. *IEEE Geoscience and Remote Sensing Letters*, vol. 6, no. 2, 263-267.

Crawford, A. J., Benn, D. I., Todd, J., Åström, J. A., Bassis, J. N., and Zwinger, T. (2021). Marine ice-cliff instability modeling shows mixed-mode ice-cliff failure and yields calving rate parameterization. *Nature communications*, 12(1), 2701.

Baumhoer, C. A., Dietz, A. J., Kneisel, C., Paeth, H., and Kuenzer, C. (2021): Environmental drivers of circum-Antarctic glacier and ice shelf front retreat over the last two decades. *The Cryosphere*, 15, 2357–2381.

Benn, D. I., Warren, C. R. and Mottram, R. H. (2007). Calving processes and the dynamics of calving glaciers. *Earth-Science Reviews*, 82(3–4), 143–179.

Benn, D. I., Luckman, A., Åström, J. A., Crawford, A. J., Cornford, S. L., Bevan, S. L., Zwinger, T., Gladstone, R., Alley, K., Pettit, E. and Bassis, J. (2022). Rapid fragmentation of Thwaites Eastern Ice Shelf. *The Cryosphere*, 16, 2545–2564.

Berends, C. J., Van de Wal, R. S. W. and Van den Akker, T. (2023). Compensating errors in inversions for subglacial bed roughness: same steady state, different dynamic response. *The Cryosphere*, 17, 1585–1600.

Bindschadler, R., Choi, H., Wichlacz, A., Bingham, R., Bohlander, J., Brunt, K., Corr, H., Drews, R., et al. (2011). Getting around Antarctica: new high-resolution mappings of the grounded and freely-floating boundaries of the Antarctic ice sheet created for the International Polar Year. *The Cryosphere*, 5, 569–588.

Bintanja, R. (1999). On the glaciological, meteorological and climatological significance of Antarctic blue ice areas. *Reviews of Geophysics*, 37(3), 337–359.

Black, T. E. and Joughin, I. (2022). Multi-decadal retreat of marine-terminating outlet glaciers in northwest and central-west Greenland. *The Cryosphere*, 16, 807–824.

Boening, C., Lebsock, M., Landerer, F. and Stephens, G. (2012). Snowfall-driven mass change on the East Antarctic ice sheet. *Geophysical Research Letters*, 39(21).

Bouissou, L., Jourdain, N. C., Mathiot, P., and Madec, G. (2022). Modeling basal melt of Antarctic ice shelves using a new physically-based parameterization. *Journal of Advances in Modeling Earth Systems*, 14(12), e2022M. S.003829.

Brancato, V., Rignot, E., Milillo, P., Morlighem, M., Mouginot, J., An, L., et al. (2020). Grounding line retreat of Denman Glacier, East Antarctica, measured

with C. O. S. M. O-SkyMed radar interferometry data. *Geophysical Research Letters*, 47, e2019GL086291.

Bronselaer, B., Winton, M., Griffies, S. M., Hurlin, W. J., Rodgers, K. B., Sergienko, O. V., Stouffer, R. J., and Russell, J. L. (2018). Change in future climate due to Antarctic meltwater. *Nature*, 564(7734), 53-58.

Brunt K. M., Fricker H. A., Padman L, Scambos T. A. and O'Neel S, (2010). Mapping the grounding zone of the Ross Ice Shelf, Antarctica, using ICESat laser altimetry. *Annals of Glaciology*, 51(55), 71-79.

Carsey, F. D. (1980). Microwave observation of the Weddell polynya. *Monthly Weather Review*, 108(12), 2032–2044.

Cheng, Y., Xia, M., Qiao, G., Li, Y., Hai, G., and Lv, D. (2021). Calving cycle of Ninnis Glacier over the last 60 years. *International Journal of Applied Earth Observation and Geoinformation*, 105, 102612.

Christianson, K., et al. (2016), Sensitivity of Pine Island Glacier to observed ocean forcing. *Geophysical Research Letters*, 43 (10), 817–10,825.

Christie, F. D. W, Bingham, R. G., Gourmelen, N., Tett, S. F. B and Muto, A. (2016). Four-decade record of pervasive grounding line retreat along the Bellingshausen margin of West Antarctica. *Geophysical Research Letters*, 43(11), 5741–5749.

Cook, A. J., Holland, P. R., Meredith, M. P., Murray, T., Luckman, A., and Vaughan, D. G. (2016). Ocean forcing of glacier retreat in the western Antarctic Peninsula. *Science*, 353(6296), 283–286.

King, C., Hall, B., Hillebrand, T. and Stone, J. (2020). Delayed maximum and recession of an East Antarctic outlet glacier. *Geology*, 48 (6), 630–634.

David M. H., et al. (2020). The Southern Ocean and its interaction with the Antarctic Ice Sheet. *Science*, 367, 1326-1330.

Davis, C. H., Li, Y., McConnell, J. R., Frey, M. M. and Hanna, E. (2005). Snowfall-driven growth in East Antarctic Ice Sheet mitigates recent sea-level rise. *Science*, 308(5730), 1898–1901.

Day, T. (2006). Degree days: theory and application. (CIBSE Technical Memorandum TM41) Chartered Institution of Building Services Engineers, London.

De Rydt, J., Gudmundsson, G. H., Nagler, T. and Wuite, J. (2019). Calving cycle of the Brunt Ice Shelf, Antarctica, driven by changes in ice shelf geometry. *The Cryosphere*, 13, 2771–2787.

Decleir, H. and van Autenboer, T. (1982). Gravity and magnetic anomalies across Jutulstraumen, a major geologic feature in western Dronning Maud Land, Antarctica. *Antarctic Geoscience: 3rd Symposium on Antarctic Geology and Geophysics*, 941–948.

DeConto, R. M., and Pollard, D. (2016). Contribution of Antarctica to past and future sea-level rise. *Nature*, 531(7596), 591–597.

DeConto, R. M., Pollard, D., Alley, R. B., Velicogna, I., Gasson, E., Gomez, N., Sadai, S., Condron, A., Gilford, D. M., Ashe, E. L., Kopp, R. E., Li, D. and Dutton, A. (2021). The Paris Climate Agreement and future sea-level rise from Antarctica. *Nature*, 593(7857), 83-89.

Depoorter, M. A., Bamber, J. L., Griggs, J. A., Lenaerts, J. T. M, Ligtenberg, S. R. M, van den Broeke, M. R. and Mohold, G. (2013). Calving fluxes and basal melt rates of Antarctic ice shelves. *Nature*, 502, 89–92.

Diez, A., Matsuoka, K., Ferraccioli, F., Jordan, T. A., Corr, H. F., Kohler, J., et al. (2018). Basal settings control fast ice flow in the Recovery/Slessor/Bailey

Region, East Antarctica. *Geophysical Research Letters*, 45, 2706–2715.

DiGirolamo, N., Parkinson, C. L., Cavalieri, D. J., Gloersen, P. and Zwally, H. J. (2022). Sea Ice Concentrations from Nimbus-7 SMMR and DMSP SSM/I-SSMIS Passive Microwave Data (NSIDC-0051, Version 2). [Data Set]. Boulder, Colorado USA NASA National Snow and Ice Data Center Distributed Active Archive Center.

Doake, C. S. M., and Vaughan, D. G. (1991). Rapid disintegration of the Wordie Ice Shelf in response to atmospheric warming. *Nature*, 350, 328–330.

Dow C. F. et al. (2018). Basal channels drive active surface hydrology and transverse ice shelf fracture. *Science Advances*, 4 (eaao7212).

Drews, R., Berger, S., Favier, L., Pattyn, F., Neckel, N., Helm, V., and Eisen, O. (2017). The imprint of the West Antarctic Ice Sheet retreat on the deep subglacial structure of Pine Island Glacier. *The Cryosphere*, 11(6), 2739–2753.

Dupont, T. K., and R. B. Alley, (2005), Assessment of the importance of ice-shelf buttressing to ice-sheet flow, *Geophysical Research Letters*, 32, L04503.

Durand, G. and Pattyn, F. (2015). Reducing uncertainties in projections of Antarctic ice mass loss. *The Cryosphere*, 9, 2043–2055.

Dutrieux, P., De Rydt, J., Jenkins, A., Holland, P. R., Ha, H. K., Lee, S. H., Steig, E. J., Ding, Q., Abrahamsen, E. P., and Schröder, M. (2014). Strong sensitivity of Pine Island ice-shelf melting to climatic variability. *Science*, 343(6167), 174–178.

Eisermann, H., Eagles, G., Ruppel, A., Smith, E. C., and Jokat, W. (2020). Bathymetry beneath ice shelves of western Dronning Maud Land, East Antarctica, and implications on ice shelf stability. *Geophysical Research Letters*, 47, e2019GL086724.

Enderlin, E. M., Howat, I. M., Jeong, S., Noh, M.J., van Angelen, J. H., and van den Broeke, M. R. (2014) An improved mass budget for the Greenland ice sheet, *Geophysical Research Letters*, 41, 866–872.

ENVEO, Wuite, J., Hetzenecker, M., Nagler, T., Scheiblauer, S. (2021): ESA Antarctic Ice Sheet Climate Change Initiative (Antarctic_Ice_Sheet_cci): Antarctic Ice Sheet monthly velocity from 2017 to 2020, derived from Sentinel-1, v1. NERC EDS Centre for Environmental Data Analysis.

Fahrner, D., Lea, J. M., Brough, S., Mair, D. W. F., and Abermann, J. (2021). Linear response of the Greenland ice sheet's tidewater glacier terminus positions to climate. *Journal of Glaciology*, 67(262), 193–203.

Favier, L. and F. Pattyn, (2015), Antarctic ice rise formation, evolution, and stability. *Geophysical Research Letters*, 42, 4456–4463.

Favier, L., Durand, G., Cornford, S. L., Gudmundsson, G. H., Gagliardini, O., Gillet-Chaulet, F. and Le Brocq, A. M. (2014). Retreat of Pine Island Glacier controlled by marine ice-sheet instability. *Nature Climate Change*, 4, 117–121.

Feldmann, J. and Levermann, A. (2015). Collapse of the West Antarctic Ice Sheet after local destabilization of the Amundsen Basin. *Proceedings of the National Academy of Sciences*, 112(46), 14191–14196.

Ferraccioli F, Jones P. C., Curtis M. L., Leat P. T. and Riley T. R. (2005). Tectonic and magmatic patterns in the Jutulstraumen rift (?) region, East Antarctica, as imaged by high-resolution aeromagnetic data. *Earth, Planets and Space*, 57.

Ferrigno, J. G. and Gould, W. G. (1987). Substantial changes in the coastline of Antarctica revealed by satellite imagery. *Polar Record*, 23(146), 577–583.

Ferrigno, J. G., Lucchitta, B. K., Mullins, K. F., Allison, A. L., Allen, R. J. and Gould, W. G. (1993). Velocity measurements and changes in position of Thwaites

Glacier/iceberg tongue from aerial photography, Landsat images and NOAA AVHRR. data. *Annals of Glaciology*, 17, 239–244.

Fettweis, X., Hofer, S., Krebs-Kanzow, U., et al. (2020). GrSMBMIP: intercomparison of the modelled 1980–2012 surface mass balance over the Greenland Ice Sheet. *The Cryosphere*, 14(11), 3935–3958.

Fogwill, C. J., Turney, C. S. M., Meissner, K. J., Golledge, N. R., Spence, P., Roberts, J. L., England, M. H., Jones, R. T. and Carter, L. (2014). Testing the sensitivity of the East Antarctic Ice Sheet to Southern Ocean dynamics: Past changes and future implications. *Journal of Quaternary Science*, 29(1), 91–98.

Francis, D., Fonseca, R., Mattingly, K. S., Marsh, O. J., Lhermitte, S., and Cherif, C. (2022). Atmospheric triggers of the Brunt Ice Shelf calving in February 2021. *Journal of Geophysical Research: Atmospheres*, 127, e2021JD036424.

Frank, T., Åkesson, H., de Fleurian, B., Morlighem, M. and Nisancioglu, K. H. (2022). Geometric controls of tidewater glacier dynamics. *The Cryosphere*, 16, 581–601.

Franke, S., Eisermann, H., Jokat, W., Eagles, G., Asseng, J., Miller, H. et al. (2021). Preserved landscapes underneath the Antarctic Ice Sheet reveal the geomorphological history of Jutulstraumen Basin. *Earth Surface Processes and Landforms*, 46(13), 2728–2745.

Fraser, A. D., Massom, R. A., Ohshima, K. I., Willmes, S., Kappes, P. J., Cartwright, J., and Porter-Smith, R. (2020). High-resolution mapping of circum-Antarctic landfast sea ice distribution, 2000–2018. *Earth System Science Data*, 12, 2987–2999.

Fraser, A. D., Massom, R. A., Handcock, M. S., Reid, P., Ohshima, K. I., Raphael, M. N., Cartwright, J., Klekociuk, A. R., Wang, Z., and Porter-Smith, R.(

2021). Eighteen-year record of circum-Antarctic landfast-sea-ice distribution allows detailed baseline characterisation and reveals trends and variability. *The Cryosphere*, 15, 5061–5077.

Fretwell, P., Pritchard, H. D., Vaughan, D. G., Bamber, J. L., Barrand, N. E., Bell, R., Bianchi, C., Bingham, R. G., Blankenship, D. D., et al. (2013). Bedmap2: improved ice bed, surface and thickness datasets for Antarctica. *The Cryosphere*, 7, 375–393.

Frezzotti, M. (1997). Ice front fluctuation, iceberg calving flux and mass balance of Victoria Land glaciers. *Antarctic Science*, 9(1), 61–73.

Frezzotti M, Cimbell, A and Ferrigno J. G. (1998). Ice-front change and iceberg behaviour along Oates and George V Coasts, Antarctica, 1912-96. *Annals of Glaciology*, 27, 643–650.

Fricker, H. A., Young, N. W., Coleman, R., Bassis, J. N. and Minster, J.B. (2005). Multi-year monitoring of rift propagation on the Amery Ice Shelf, East Antarctica, *Geophysical Research Letters*, 32, L02502.

Fricker, H. A. and Padman, L. (2006). Ice shelf grounding zone structure from ICESat laser altimetry, *Geophysical Research Letters*, 33, L15502.

Fricker, H. A., Coleman, R., Padman, L., Scambos, T. A., Bohlander, J., and Brunt, K. M. (2009). Mapping the grounding zone of the Amery Ice Shelf, East Antarctica using InSAR, MODIS and ICESat Antarctic *Science*, 21(5), 515–532.

Friedl, P., Weiser, F., Fluhrer, A. and Braun M. H. (2020). Remote sensing of glacier and ice sheet grounding lines: A review. *Earth-Science Reviews*, 201.

Frieler, K. et al. (2015). Consistent evidence of increasing Antarctic accumulation with warming. *Nature Climate Change*, 5, 348–352.

Fürst, J. J., Durand, G., Gillet-Chaulet, F., Tavard, L., Rankl, M., Braun, M., and Gagliardini, O. (2016). The safety band of Antarctic ice shelves. *Nature Climate Change*, 6(5), 479–482.

Gardner A. S., Fahnestock M. A. and Scambos T. A. (2019). ITS_LIVE Regional Glacier and Ice Sheet Surface Velocities, National Snow and Ice Data Center [data set].

Gardner, A. S., Moholdt, G., Scambos, T., Fahnstock, M., Ligtenberg, S., van den Broeke, M., and Nilsson, J. (2018). Increased West Antarctic and unchanged East Antarctic ice discharge over the last 7 years. *The Cryosphere*, 12, 521–547.

Gasson, E., DeConto, R. M., Pollard, D., and Levy, R. H. (2016). Dynamic Antarctic ice sheet during the early to mid-Miocene. *Proceedings of the National Academy of Sciences*, 113(13), 3459–3464.

Gill, A. E. (1973). Circulation and bottom water production in the Weddell Sea. *Deep Sea Research and Oceanographic Abstracts*, 20(2), 111–140.

Giovinetto, M. B., Zwally, H. J., Li, J., Bentley, C. R., and Thompson, D. T. (2011). Spatial distribution of net surface mass accumulation on the Antarctic ice sheet. *Annals of Glaciology*, 33, 171–178.

Gjessing Y. T. (1970). Mass transport of Jutulstraumen ice stream in Dronning Maud Land. Årbok. Norsk Polar Institute, Oslo, 227–228.

Glasser, N. F., and Scambos, T. A. (2008). A structural glaciological analysis of the 2002 Larsen B ice-shelf collapse. *Journal of Glaciology*, 54(184), 3–16.

Glasser N. F. et al. (2009). Surface structure and stability of the Larsen C ice shelf, Antarctic Peninsula. *Journal of Glaciology*, 55(191), 400-410.

Goel V, Matsuoka K, Berger C. D., Lee I, Dall J, Forsberg R, (2020) Character-

istics of ice rises and ice rumples in Dronning Maud Land and Enderby Land, Antarctica. *Journal of Glaciology*, 66(260), 1064–1078.

Golledge, N. R., Kowalewski, D. E., Naish, T. R., Levy, R. H., Fogwill, C. J. and Gasson, E. G. W. (2015). The multi-millennial Antarctic commitment to future sea-level rise. *Nature*, 526(7573), 421–425.

Golledge, N. R., Levy, R. H., McKay, R. M. and Naish, T. R. (2017). East Antarctic ice sheet most vulnerable to Weddell Sea warming, *Geophysical Research Letters*, 44, 2343–2351,

Gomez-Fell, R., Rack, W., Purdie, H., and Marsh, O. (2022). Parker Ice Tongue collapse, Antarctica, triggered by loss of stabilizing land-fast sea ice. *Geophysical Research Letters*, 49, e2021GL096156.

Good, S. A., Martin, M. J. and Rayner, N. A. (2013). EN4: Quality controlled ocean temperature and salinity profiles and monthly objective analyses with uncertainty estimates. *Journal of Geophysical Research: Oceans*, 118, 6704–6716.

Gorodetskaya, I. V., Tsukernik, M. Claes, K., Ralph, M. F., Neff, W. D. and Van Lipzig, N. P. M. (2014). The role of atmospheric rivers in anomalous snow accumulation in East Antarctica, *Geophysical Research Letters*, 41, 6199–6206.

Greenbaum, J., Blankenship, D., Young, D. et al. (2015). Ocean access to a cavity beneath Totten Glacier in East Antarctica. *Nature Geosci*, 8, 294–298.

Greene, C. A., Blankenship, D. D., Gwyther, D. E., Silvano, A., and van Wijk, E. (2017). Wind causes Totten Ice Shelf melt and acceleration. *Science Advances*, 3(11), e1701681.

Groh, A. and Horwath, M. (2021). Antarctic Ice Mass Change Products from GRACE/GRACE-FO using tailored sensitivity kernels. *Remote Sensing*, 13(9), 1736.

Gudmundsson, G. H., Paolo, F. S., Adusumilli, S. and Fricker, H. A. (2016). Instantaneous Antarctic ice-shelf mass loss driven by thinning and ice dynamics. *Geophysical Research Letters*, 43(22), 11760–11770.

Gwyther, D. E., Galton-Fenzi, B. K., Hunter, J. R., and Roberts, J. L. (2014). Simulated melt rates for the Totten and Dalton ice shelves. *Ocean Science*, 10(2), 267–279.

Gwyther, D. E., Kusahara, K., Galton-Fenzi, B. K., Roberts, J. L., and Blankenship, D. D. (2023). Antarctic ice shelf basal melt rates controlled by ocean heat transport. *The Cryosphere*, 17, 4549–4569.

Hanna, E., Cappelen, J., Fettweis, X., Mernild, S. H., Mote, T. L., and Steffen, K. (2021). Greenland surface air temperature changes from 1981 to 2019 and implications for ice-sheet melt and mass-balance change. *International Journal of Climatology*, 41(S1), E1337–E1356.

Hanson, S., Nicholls, R., Ranger, N., Hallegatte, S., Corfee-Morlot, J., Herweijer, C., and Chateau, J. (2011). A global ranking of port cities with high exposure to climate extremes. *Climatic Change*, 104(1), 89–111.

Haran T., Bohlander J., Scambos T., Painter T. and Fahnestock M. (2005) MODIS Mosaic of Antarctica 2003–2004 (MOA 2004) ImageMap, Version 1. NASA National Snow and Ice Data Center Distributed Active Archive Center [data set].

Haran T., Bohlander J., Scambos T., Painter T. and Fahnestock M. (2014). MODIS Mosaic of Antarctica 2008–2009 (MOA2009) ImageMap, Version 1. NASA National Snowand Ice Data Center Distributed Active Archive Center [data set].

Haran, T., Linger, M., Bohlander, J., Fahnestock, M., Painter, T., and Scambos, T. (2018). MEaSUREs MODIS Mosaic of Antarctica 2013– 2014 (MOA2014)

Image Map, Version 1. NASA National Snow and Ice Data Center Distributed Active Archive Center [data set].

Hattermann, T., Nost, O., Lilly, J. and Smedsrud, L. (2012). Two years of oceanic observations below the Fimbulisen, Antarctica. *Geophysical Research Letters*, 39, 12605.

Hattermann, T. (2018). Antarctic thermocline dynamics along a narrow shelf with easterly winds. *Journal of Physical Oceanography*, 48(10), 2419–2443.

Herraiz-Borreguero, L., Allison, I., Craven, M., Nicholls, K. W. and Rosenberg, M. A. (2013). Ice shelf/ocean interactions under the Amery Ice Shelf: Seasonal variability and its effect on marine ice formation. *Journal of Geophysical Research Oceans*, 118, 7117–7131.

Herraiz-Borreguero, L. and Coleman, R. (2015). Circulation of modified Circumpolar Deep Water and basal melt beneath the Amery Ice Shelf, East Antarctica. *Journal of Geophysical Research Oceans*, 120(4), 3098–3112.

Hersbach, H., Bell, B., Berrisford, P., et al. (2020). The ERA5 global reanalysis. *Quarterly Journal of the Royal Meteorological Society*, 146, 1999–2049.

Hersbach, H., Bell, B., Berrisford, P., Biavati, G., Horányi, A., Muñoz Sabater, J. et al. (2023). ERA5 hourly data on single levels from 1940 to present. Copernicus Climate Change Service (C3S) Climate Data Store (CDS)

HeywoodK, J., et al. (2014). Ocean processes at the Antarctic continental slope. *Philosophical Transactions of the Royal Society A*, 372, 20130047.

Hill, E., Carr, R., Stokes, C. R. and Gudmundsson, H. G. (2018). Dynamic changes in outlet glaciers in northern Greenland from 1948 to 2015. *The Cryosphere*, 12(10), 3243–3263.

Hirano, D., Tamura, T., Kusahara, K. et al. (2023). On-shelf circulation of warm water toward the Totten Ice Shelf in East Antarctica. *Nature Commununications*, 14, 4955.

Hirano, D., Tamura, T., Kusahara, K. et al. (2020). Strong ice-ocean interaction beneath Shirase Glacier Tongue in East Antarctica. *Nature Commununications*, 11, 4221.

Hofer, S., Tedstone, A. J., Fettweis, X., and Bamber, J. L. (2017). Decreasing cloud cover drives the recent mass loss on the Greenland Ice Sheet. *Science Advances*, 3(6) e1700584.

Hoffman, M. J., Branecky Begeman, C., Asay-Davis, X. S., Comeau, D., Barthel, A., Price, S. F., and Wolfe, J. D. (2024). Ice-shelf freshwater triggers for the Filchner–Ronne Ice Shelf melt tipping point in a global ocean–sea-ice model. *The Cryosphere*, 18, 2917–2937.

Hogg, A. E., Shepherd, A., and Cornford, S. L. (2017). Increased ice flow in Western Palmer Land linked to ocean melting. *Geophysical Research Letters*, 44(9), 4159–4167.

Holt, T. O., Glasser, N. F., Quincey D. J. and Siegfried M. R. (2013). Speedup and fracturing of George V. I.. I.ce Shelf, Antarctic Peninsula. *The Cryosphere*, 7(3), 797–816.

Holt, T. O. and Glasser, N. F. (2022). Changes in area, flow speed and structure of southwest Antarctic Peninsula ice shelves in the 21st century. *Journal of Glaciology*, 68(271), 927-945.

Howat, I. M., Jezek, K., Studinger, M., MacGregor, J. A., Paden, J., Floricioiu, D., Russell, R., Linkswiler M. and Dominguez, R. T.(2012). Rift in Antarctic Glacier: A Unique Chance to Study Ice Shelf Retreat. *Eos Trans. AGU*, 93(8),

77.

Humbert, A. and Steinhage, D. (2011). The evolution of the western rift area of the Fimbulisen, Antarctica. *The Cryosphere*, 5(4), 931–944.

Hutchinson, D. K., Menviel, L., Meissner, K. J. et al. (2024) East Antarctic warming forced by ice loss during the Last Interglacial. *Nature Communications*, 15, 1026.

Indrigo, C., Dow, C. F., Greenbaum, J. S., and Morlighem, M. (2021). Drygalski Ice Tongue stability influenced by rift formation and ice morphology. *Journal of Glaciology*, 67(262), 243–252.

IPCC (2019). IPCC Special Report on the Ocean and Cryosphere in a Changing Climate [H.-O. Pörtner, D.C. Roberts, V. Masson-Delmotte, P. Zhai, M. Tignor, E. Poloczanska, K. Mintenbeck, A. Alegría, M. Nicolai, A. Okem, J. Petzold, B. Rama, N.M. Weyer (eds.)]

Jones, T. R., et al. (2021). Greenland ice sheet climate response inferred from firn core isotopes. *Nature Communications*, 12 (1450).

Jordan, J. R., Miles, B. W. J., Gudmundsson, G. H. et al. (2023). Increased warm water intrusions could cause mass loss in East Antarctica during the next 200 years. *Nature Communications*, 14 (1825).

Josey, S. A., Meijers, A. J. S., Blaker, A. T. et al. (2024). Record-low Antarctic sea ice in 2023 increased ocean heat loss and storms. *Nature 636*, 635–639.

Joughin, I., Alley, R. B. and Holland, D. M. (2012). Ice-sheet response to oceanic forcing. *Science*, 338(6111), 1172–1176.

Joughin, I., et al. (2023). Extensive and anomalous grounding line retreat at Vanderford Glacier, Vincennes Bay, Wilkes Land, East Antarctica. *The Cryosphere*, 17, 3593–3612.

Joughin, I., Smith, B. E. and Medley, B. (2014). Marine ice sheet collapse potentially under way for the Thwaites Glacier Basin, West Antarctica. *Science*, 344(6185), 735–738.

Kamenev E. N. (1972). Geological structure of Enderby Land. In: Antarctic geology and geophysics. *International Union of Geological Sciences (IUGS)*, 579–583.

Khazendar, A. and Jenkins, A. (2003). A model of marine ice formation within Antarctic ice shelf rifts. *Geophysical Research Letters*, 108 (C7).

Khazendar, A., Rignot, E., and Larour, E. (2007). Larsen B Ice Shelf rheology preceeding its disintegration inferred by a control method. *Geophysical Research Letters*, 34, L19503.

Khazendar, A., Schodlok, M., Fenty, I. et al. (2013). Observed thinning of Totten Glacier is linked to coastal polynya variability. *Nature Communications*, 4 (2857).

Kim, K. T., Jezek, K. C. and Sohn, H. G. (2001). Ice shelf advance and retreat rates along the coast of Queen Maud Land, Antarctica, *Geophysical Research Letters*, 106(C4), 7097–7106.

Kim, K., Jezek, K. C., and Liu, H. (2007). Orthorectified image mosaic of Antarctica from 1963 Argon satellite photography: image processing and glaciological applications. *International Journal of Remote Sensing*, 28(23), 5357–5373.

King, M. A., Bingham, R. J., Moore, P., Whitehouse, P. L., Bentley, M. J., and Milne, G. A. (2012). Lower satellite-gravimetry estimates of Antarctic sea-level contribution. *Nature*, 491(7425), 586–589.

Kingslake, J., Ely, J., Das, I. et al. (2017). Widespread movement of meltwater onto and across Antarctic ice shelves. *Nature 544*, 349–352.

Kingslake, J., Scherer, R. P., Albrecht, T. et al. (2018). Extensive retreat and re-advance of the West Antarctic Ice Sheet during the Holocene. *Nature 558*, 430–434.

Klose, A. K., Coulon, V., Pattyn, F. and Winkelmann, R. (2024). The long-term sea-level commitment from Antarctica. *The Cryosphere*, 18, 4463–4492.

Koch, I. , Drews, R. , Jansen, D. , Franke, S. , Schannwell, C. , Visnjevic, V. , Streng, K. , Eisen, O. , Helm, V. and Pattyn, F. (2020). Ice shelf internal reflection horizons reveal past dynamics and oceanic melt. FRISP 2020 - 34th Forum for Research into Ice Shelf Processes.

Kondo, K. and Sugiyama, S. (2023). Calving, ice flow, and thickness of outlet glaciers controlled by land-fast sea ice in Lützow-Holm Bay, East Antarctica. *Journal of Glaciology*, 69(278), 1751–1763.

Konrad, H., Shepherd, A., Gilbert, L. et al. (2018). Net retreat of Antarctic glacier grounding lines. *Nature Geoscience*, 11, 258–262.

Kopp, R. E., DeConto, R. M., Bader, D. A., Hay, C. C., et al. (2017). Evolving Understanding of Antarctic Ice-Sheet Physics and Ambiguity in Probabilistic Sea-Level Projections. *Earth's Future*, 5, 1217-1233.

Kulessa, B., Jansen, D., Luckman, A., King, E. C. and Sammonds, P. R. (2014). Marine ice regulates the future stability of a large Antarctic ice shelf. *Nature Communications*, 5 (3707).

Kulp, S. A., and Strauss, B. H. (2019) New elevation data triple estimates of global vulnerability to sea-level rise and coastal flooding. *Nature Communications*, 10, 4844

Langley, K., Kohler, J., Sinisalo, A., et al. (2014). Low melt rates with seasonal variability at the base of Fimbul Ice Shelf, East Antarctica, revealed by in

situ interferometric radar measurements. *Geophysical Research Letters*, 41(22), 8138–8146.

Larour, E., Rignot, E. and Aubry, D. (2004). Modelling of rift propagation on Ronne Ice Shelf, Antarctica, and sensitivity to climate change, *Geophysical Research Letters*, 31, L16404.

Larour E., Rignot E., Joughin I. and Aubry D. (2005). Rheology of the Ronne Ice Shelf, Antarctica, inferred from satellite radar interferometry data using an inverse control method, *Geophysical Research Letters*, 32(L05503).

Larour, E., Khazendar A., Borstad C. P., Seroussi H., Morlighem M. and Rignot, E. (2014). Representation of sharp rifts and faults mechanics in modeling ice shelf flow dynamics: Application to Brunt/Stancomb-Wills Ice Shelf, Antarctica. *Journal Geophysical Research Earth Surface*, 119, 1918–1935.

Larour, E., Rignot, E., Poinelli, M. an Scheuchl, B. (2021). Physical processes controlling the rifting of Larsen C Ice Shelf, Antarctica, prior to the calving of iceberg A68. *Proceedings of the National Academy of Sciences of the United States of America*, 118(40), e2105080118.

Lauber, J., Hattermann, T., de Steur, L. et al. (2023). Warming beneath an East Antarctic ice shelf due to increased subpolar westerlies and reduced sea ice. *Nature Geosciences*, 16, 877–885.

Lea, J. M., Mair, D. W. F and Rea, B. R. (2014) Instruments and Methods: Evaluation of existing and new methods of tracking glacier terminus change. *Journal of Glaciology*, 60(220), 323–332.

Leeson, A. A., Forster, E., Rice, A., Gourmelen, N., and van Wessem, J. M. (2020). Evolution of supraglacial lakes on the Larsen B ice shelf in the decades before it collapsed. *Geophysical Research Letters*, 47, e2019GL085591.

Leeson, A. A., Shepherd, A., Briggs, K. H., et al. (2015). Supraglacial lakes on the Greenland ice sheet advance inland under warming climate. *Nature Climate Change*, 5, 51–55.

Lenaerts, J. T. M., van Meijgaard, E., van den Broeke, M. R., Ligtenberg, S. R. M, Horwath, M. and Isaksson. E. (2013). Recent snowfall anomalies in Dronning Maud Land, East Antarctica, in a historical and future climate perspective. *Geophysical Research Letters 40*, 2684–2688.

Levermann, A., Winkelmann, R., Albrecht, T., et al. (2020). Projecting Antarctica's contribution to future sea level rise from basal ice shelf melt using linear response functions of 16 ice sheet models (LARMIP-2). *Earth System Dynamics*, 11, 35–76.

Li, T., Dawson, G. J., Chuter, S. J., and Bamber, J. L. (2023). Grounding line retreat and tide-modulated ocean channels at Moscow University and Totten Glacier ice shelves, East Antarctica. *The Cryosphere*, 17(3), 1003–1022.

Li, X., Rignot, E., Mouginot, J. and Scheuchl, B. (2016), Ice flow dynamics and mass loss of Totten Glacier, East Antarctica, from 1989 to 2015, *Geophysical Research Letters*, 43, 6366–6373.

Li, X., Rignot, E., Mouginot, J. and Scheuchl, B. (2015) Grounding line retreat of Totten Glacier, East Antarctica, 1996 to 2013, *Geophysical Research Letters*, 42, 8049–8056.

Lovell, A. M., Stokes, C. R., and Jamieson, S. S. R. (2017) Sub-decadal variations in outlet glacier terminus positions in Victoria Land, Oates Land and George V. L.and, East Antarctica (1972–2013). *Antarctic Science*, 29(5), 468–483.

Lowther, A., von Quillfeldt, C., Assmy, P. et al. (2022). A review of the scientific knowledge of the seascape off Dronning Maud Land, Antarctica. *Polar Biol*, 45,

1313–1349.

Lucchitta, B. K., and Rosanova, C. E. (1998). Retreat of northern Larsen Ice Shelf, Antarctica, revealed by space imagery. *Annals of Glaciology*, 27, 76–82.

Lunde, T. (1963). On the firn temperatures and glacier flow in Dronning Maud Land. Årbok. Norsk Polar Institute, Oslo, 7-24.

MacAyeal, D. R., Rignot, E. and Hulbe, C. L. (1998). Ice-shelf dynamics near the front of the Filchner-Ronne Ice Shelf, Antarctica, revealed by S. A. R interferometry: Model/interferogram comparison. *Journal of Glaciology*, 44, 419–428.

Mae, S. and Naruse, R. (1978). Possible causes of ice sheet thinning in the Mizuho Plateau. *Nature*, 273, 291–292.

Mas e Braga, M., Jones, R. S., Bernales, J. et al. (2023). A thicker Antarctic ice stream during the mid-Pliocene warm period. *Communication Earth and Environment*, 4, 321.

Massom, R. A., Scambos, T. A., Bennetts, L. G., Reid, P., Squire, V. A. and Stammerjohn, S. E. (2018). Antarctic ice shelf disintegration triggered by sea ice loss and ocean swell. *Nature*, 558, 383–389.

Massom, R. A. (2003). Recent iceberg calving events in the Ninnis Glacier region, East Antarctica. *Antarctic Science*, 15(2), 303–313.

Massom, R. A., Giles, A. B., Fricker, H. A., et al. (2010). Examining the interaction between multi-year landfast sea ice and the Mertz Glacier Tongue, East Antarctica: Another factor in ice sheet stability? *Journal of Geophysical Research*, 115, C12027.

Massom, R. A., Giles, A. B., Fricker, H. A., et al. (2015). External influences on the Mertz Glacier Tongue (East Antarctica) in the decade leading up to its calving

in 2010. *Journal of Geophysical Research Earth Surface*, 120, 490–506.

Matsuoka, K., Hindmarsh, R. C. A., Moholdt, G., et al. (2015). Antarctic ice rises and rumples: Their properties and significance for ice-sheet dynamics and evolution. *EarthScience Reviews*, 150, 724–745.

McGranahan, G., Balk, D. and Anderson, B. (2007). The rising tide: assessing the risks of climate change and human settlements in low elevation coastal zones. *Environment and Urbanization*, 19(1), 17-37.

McGrath, D., Steffen, K., Scambos, T., Rajaram, H., Casassa, G. and Rodriguez Lagos, J. L. (2012). Basal crevasses and associated surface crevassing on the Larsen C ice shelf, Antarctica, and their role in ice-shelf instability. *Annals of Glaciology*, 53(60), 10-18.

Medley, B., McConnell, J. R., Neumann, T. A., Reijmer, C. H., Chellman, N., Sigl, M., and Kipfstuhl, S. (2018). Temperature and snowfall in western Queen Maud Land increasing faster than climate model projections. *Geophysical Research Letters*, 45, 1472–1480.

Medley, B., Thomas, E. R. (2019). Increased snowfall over the Antarctic Ice Sheet mitigated twentieth-century sea-level rise. *Nature Climate Change*, 9, 34–39.

Melvold, K. and Rolstad, C. E. (2000). Subglacial topography of Jutulstraumen outlet glacier, East Antarctica, mapped from ground-penetrating radar, optical and interferometric synthetic aperture radar satellite data. *Norsk Geografisk Tidsskrift*, 54(4), 169-181.

Melvold, K., Hagen, J. O., Pinglot, J. F. and Gundestrup, N. (1998). Large spatial variation in accumulation rate in Jutulstraumen ice stream, Dronning Maud Land, Antarctica. *Annals of Glaciology*, 27, 231–238.

Meredith, M., Sommerkorn, M., Cassotta, S., et al. (2019). Polar Regions. In:

IPCC Special Report on the Ocean and Cryosphere in a Changing Climate [H.-O. Pörtner, D.C. Roberts, V. Masson-Delmotte, P. Zhai, M. Tignor, E. Poloczanska, K. Mintenbeck, A. Alegría, M. Nicolai, A. Okem, J. Petzold, B. Rama, N.M. Weyer (eds.)]

Miles, B. W. J., Stokes, C. R., Vieli, A. and Cox, N. J. (2013). Rapid, climate-driven changes in outlet glaciers on the Pacific coast of East Antarctica. *Nature*, 500(7464), 563–566.

Miles, B. W., Stokes, C. R. and Jamieson, S. S. R. (2016). Pan-ice-sheet glacier terminus change in East Antarctica reveals sensitivity of Wilkes Land to sea-ice changes. *Science advances*, 2(5), e1501350.

Miles, B. W. J, Stokes, C. R. and Jamieson, S. S. R. (2018). Velocity increases at Cook Glacier, East Antarctica, linked to ice shelf loss and a subglacial flood event. *The Cryosphere*, 12(10), 3123–3136.

Miles, B. W. J, Jordan, J. R., Stokes, C. R., Jamieson, S. S. R, Gudmundsson, G. H. and Jenkins, A. (2021). Recent acceleration of Denman Glacier (1972–2017), East Antarctica, driven by grounding line retreat and changes in ice tongue configuration. *The Cryosphere*, 15, 663–676.

Miles, B. W. J., Stokes, C. R., Jenkins, A., Jordan, J. R., Jamieson, S. S. R. and Gudmundsson, G. H. (2023). Slowdown of Shirase Glacier, East Antarctica, caused by strengthening alongshore winds. *The Cryosphere*, 17, 445–456,

Mohajerani, Y., Jeong, S., Scheuchl, B., Velicogna, I., Rignot, E. and Milillo, P. (2021) Automatic delineation of glacier grounding lines in differential interferometric synthetic-aperture radar data using deep learning. *Scientific Reports*, 11(1).

Moon, T. and Joughin, I. (2008). Changes in ice front position on Greenland's outlet

glaciers from 1992 to 2007. *Journal of Geophysical Research*, 113, F02022.

Morgan, V. I., Jacka, T. H., Akerman, G. J., and Clarke, A. L. (1982). Outlet Glacier and Mass-Budget Studies in Enderby, Kemp, and Mac. Robertson Lands, Antarctica. *Annals of Glaciology*, 3, 204–210.

Morlighem, M. et al. (2020). Deep glacial troughs and stabilizing ridges unveiled beneath the margins of the Antarctic ice sheet. *Nature Geoscience*, 13, 132–137.

Yu, H., Rignot, E., Seroussi, H. and Morlighem, M. (2018). Retreat of Thwaites Glacier, West Antarctica, over the next 100 years using various ice flow models, ice shelf melt scenarios and basal friction laws. *The Cryosphere*, 12, 3861–3876.

Morlighem, M., Williams, C. N., Rignot, E., et al. (2017) BedMachine v3: Complete bed topography and ocean bathymetry mapping of Greenland from multibeam echo sounding combined with mass conservation. *Geophysical Research Letters*, 44(21), 11051–11061.

Mutton, H. and Andrews, T. (2025). Biases in climate model global warming trends related to deficiencies in southern ocean sea ice evolution over recent decades. *Geophysical Research Letters*, 52, e2025GL115657.

Naruse, R. (1979). Thinning of the Ice Sheet in Mizuho Plateau, East Antarctica. *Journal of Glaciology*, 24, 45–52.

Nicholls, K. W., Abrahamsen, E. P., Heywood, K. J., Stansfield, K. and Østerhus, S. (2008). High-latitude oceanography using autosub autonomous underwater vehicle. *Limnology and Oceanography*, 53(5), 2309–2320.

Nilsson J, Gardner A. S. and Paolo F. S. (2022). Elevation Change of the Antarctic Ice Sheet: 1985 to 2020. *Earth System Science Data*, 14, 1-26.

Noble, T., et al. (2020). The sensitivity of the Antarctic Ice Sheet to a changing

climate: Past, present, and future. *Reviews of Geophysics*, 58, e2019RG000663.

Noone, D., Turner, J. and Mulvaney, R. (1999). Atmospheric signals and characteristics of accumulation in Dronning Maud Land, Antarctica. *Journal of Geophysical Research*, 104(D16), 19191–19211.

Nowicki, S., et al. (2013). Insights into spatial sensitivities of ice mass response to environmental change from the SeaRISE ice sheet modeling project I: Antarctica. *Journal of Geophysical Research: Earth Surface*, 118(2), 1002–1024.

Massom, R. A., Scambos, T. A., Bennetts, L. G. et al. (2018) Antarctic ice shelf disintegration triggered by sea ice loss and ocean swell. *Nature*, 558, 383–389.

Oppenheimer, M., et al. (2019). Sea Level Rise and Implications for Low-Lying Islands, Coasts and Communities. In Sea Level Rise and Implications for Low-Lying Islands, Coasts and Communities. In: *IPCC Special Report on the Ocean and Cryosphere in a Changing Climate*, 321–446.

Otosaka, I. N., Shepherd, A., Ivins, E. R., et al. (2023). Mass balance of the Greenland and Antarctic ice sheets from 1992 to 2020. *Earth System Science Data*, 15(4), 1597–1616.

Paolo, F. S., Fricker, H. A., and Padman, L. (2015). Volume loss from Antarctic ice shelves is accelerating. *Science*, 348(6232), 327–331.

Paolo, F. S., Gardner, A. S., Greene, C. A., et al. (2023). Widespread slowdown in thinning rates of West Antarctic ice shelves. *The Cryosphere*, 17, 3409–3435. tc.copernicus.org/articles/17/3409/2023/

Parkinson, C. L. (2019). A 40-y record reveals gradual Antarctic sea ice increases followed by decreases at rates far exceeding the rates seen in the Arctic. *Proceedings of the National Academy of Sciences*, 116(29), 14414–14423.

Payne A. J., et al. (2021). Future Sea Level Change Under Coupled Model Intercomparison Project Phase 5 and Phase 6 Scenarios From the Greenland and Antarctic Ice Sheets. *Geophysical Research Letters*, 48(16).

Pelle, T., Greenbaum, J. S., Ehrenfeucht, S., Dow, C. F., and McCormack, F. S. (2024). Subglacial discharge accelerates dynamic retreat of aurora subglacial basin outlet glaciers, East Antarctica, over the 21st century. *Journal of Geophysical Research: Earth Surface*, 129, e2023JF007513.

Pelle, T., Morlighem, M., Nakayama, Y., and Seroussi, H. (2021). Widespread grounding line retreat of Totten Glacier, East Antarctica, over the 21st century. *Geophysical Research Letters*, 48, e2021GL093213.

Pelle, T., Morlighem, M., and McCormack, F. S. (2020). Aurora Basin, the weak underbelly of East Antarctica. *Geophysical Research Letters*, 47, e2019GL086821.

Picton H. J., Stokes C. R., Jamieson S. S. R, Floricioiu, D. and Krieger, L. (2023). Extensive and anomalous grounding line retreat at Vanderford Glacier, Vincennes Bay, Wilkes Land, East Antarctica. *The Cryosphere*, 17, 3593-3616.

Poinelli, M., Schodlok, M., Larour, E., Vizcaino, M., and Riva, R. (2023). Can rifts alter ocean dynamics beneath ice shelves? *The Cryosphere*, 17, 2261–2283.

Pollard, D., DeConto, R. M. and Alley, R. B. (2015). Potential Antarctic Ice Sheet retreat driven by hydrofracturing and ice cliff failure. *Earth and Planetary Science Letters*, 412, 112–121.

Pritchard, H. D., Ligtenberg, S. R. M, Fricker, H. A., Vaughan, D. G., van den Broeke, M. R. and Padman, L. (2012). Antarctic ice-sheet loss driven by basal melting of ice shelves. *Nature*, 484(7395), 502–505.

Pritchard, H. D. and Vaughan, D. G. (2007). Widespread acceleration of tidewater glaciers on the Antarctic Peninsula. *Journal of Geophysical Research: Earth*

Surface, 112(F3).

Pritchard, H. D., Ligtenberg, S. R., Fricker, H. A., Vaughan, D. G., van den Broeke, M. R., and Padman, L. (2012). Antarctic ice-sheet loss driven by basal melting of ice shelves. *Nature*, 484(7395), 502–505.

Purich, A. and Doddridge, E. W. (2023). Record low Antarctic sea ice coverage indicates a new sea ice state. *Communications Earth and Environment*, 4, 314.

Rack, W. and Rott, H. (2004). Pattern of retreat and disintegration of the Larsen B Ice Shelf, Antarctic Peninsula. *Annals of Glaciology*, 39, 505–510.

Reese, R., Gudmundsson, G. H., Levermann, A. et al. (2018). The far reach of ice-shelf thinning in Antarctica. *Nature Climate Change*, 8, 53–57 .

Rendfrey, T. S., Pettersen, C., Bassis, J. N. and Mateling, M. E. (2024). CloudSat observations show enhanced moisture transport events increase snowfall rate and frequency over Antarctic ice sheet basins. *Journal of Geophysical Research: Atmospheres*, 129,

Ribeiro, N., Herraiz-Borreguero, L., Rintoul, S. R., McMahon, C. R., Hindell, M., Harcourt, R., and Williams, G. (2021). Warm modified Circumpolar Deep Water intrusions drive ice shelf melt and inhibit Dense Shelf Water formation in Vincennes Bay, East Antarctica. *Journal of Geophysical Research: Oceans*, 126, e2020JC016998.

Rignot, E., Casassa, G., Gogineni, P., Krabill, W., Rivera, A. and Thomas, R. (2004). Accelerated ice discharge from the Antarctic Peninsula following the collapse of Larsen B ice shelf, *Geophysical Research Letters*, 31, L18401.

Rignot, E. and Kanagaratnam, P. (2006). Changes in the velocity structure of the Greenland Ice Sheet. *Science*, 311(5763), 986–990.

Rignot, E., Mouginot, J. and Scheuchl, B. (2011). Antarctic grounding line mapping from differential satellite radar interferometry. *Geophysical Research Letters*, 38(10).

Rignot, E., Jacobs, S., Mouginot, J. and Scheuchl, B. (2013). Ice-shelf melting around antarctica. *Science*, 341(6143), 266–270.

Rignot, E., Mouginot, J. and Scheuchl, B. (2016). MEaSUREs Antarctic Grounding Line from Differential Satellite Radar Interferometry, Version 2. NASA National Snow and Ice Data Center Distributed Active Archive Center.

Rignot, E., Mouginot, J. and Scheuchl, B. (2017). MEaSUREs Antarctic Boundaries for I. P. Y 2007-2009 from Satellite Radar, Version 2. Boulder, Colorado USA NASA National Snow and Ice Data Center Distributed Active Archive Center.

Rignot, E., Mouginot, J., Scheuchl, B., van den Broeke, M., van Wessem, M. J., and Morlighem, M. (2019). Four decades of Antarctic Ice Sheet mass balance from 1979–2017. *Proceedings of the National Academy of Sciences*, 116(4), 1095–1103.

Rintoul, S. R., Silvano, A., Peña-Molino, B., van Wijk, E., Rosenberg, M., Greenbaum, J. S. and Blankenship, D. D. (2016). Ocean heat drives rapid basal melt of the Totten Ice Shelf. *Science Advances*, 2(12), e1601610.

Robel, A. (2017). Thinning sea ice weakens buttressing force of iceberg mélange and promotes calving. *Nature Communications*, 8, 14596.

Rolstad, C., Whillans, I. M., Hagen, J. O. and Isaksson, E. (2000). Large-scale force budget of an outlet glacier: Jutulstraumen, Dronning Maud Land, East Antarctica. *Annals of Glaciology*, 30, 35–4.

Rott, H., Skvarca, P. and Nagler, T. (1996). Rapid collapse of Northern Larsen Ice Shelf, Antarctica. *Science*, 271(5250), 788–792.

Rott, H., Müller, F., Nagler, T. and Floricioiu, D. (2011). The imbalance of glaciers after disintegration of Larsen-B ice shelf, Antarctic Peninsula. *The Cryosphere*, 5(1), 125–134.

Scambos, T. A., Hulbe, C., Fahnestock, M. and Bohlander, J. (2000). The link between climate warming and break-up of ice shelves in the Antarctic Peninsula. *Journal of Glaciology*, 46(154), 516–530.

Scambos, T. A., Bohlander, J. A., Shuman, C. A. and Skvarca, P. (2004). Glacier acceleration and thinning after ice shelf collapse in the Larsen B embayment, Antarctica. *Geophysical Research Letters*, 31, L18402.

Scambos, T. A., Haran, T. M., Fahnestock, M. A., Painter, T. H. and Bohlander, J. (2007). MODIS-based Mosaic of Antarctica (MOA) data sets: Continent-wide surface morphology and snow grain size. *Remote Sensing of Environment*, 111(2–3), 242–257.

Scambos, T. A., Bell, R. E., Alley, R. B., Anandakrishnan, S., Bromwich, D. H., Brunt, K., Christianson, K., et al. (2017). How much, how fast?: A science review and outlook for research on the instability of Antarctica's Thwaites Glacier in the 21st century. *Global and Planetary Change*, 153, 16–34.

Schannwell, C., Drews, R., Ehlers, T. A., Eisen, O., Mayer, C., Malinen, M., Smith, E. C. and Eisermann, H. (2020). Quantifying the effect of ocean bed properties on ice sheet geometry over 40 000 years with a full-Stokes model. *The Cryosphere*, 14, 3917–3934,

Schlemm, T., Feldmann, J., Winkelmann, R. and Levermann, A. (2022). Stabilizing effect of mélange buttressing on the marine ice-cliff instability of the West Antarctic Ice Sheet. *The Cryosphere*, 16, 1979–1996.

Schlosser, E., Manning, K. W., Powers, J. G., Duda, M. G., Birnbaum, G. and

Fujita, K. (2010). Characteristics of high-precipitation events in Dronning Maud Land, Antarctica. *Journal of Geophysical Research*, 115.

Schmidtko, S., Heywood, K. J., Thompson, A. F. and Aoki, S. (2014). Multidecadal warming of Antarctic waters. *Science*, 346(6214), 1227–1231.

Schröder, L., Horwath, M., Dietrich, R., Helm, V., Van Den Broeke, M. R. and Ligtenberg, S. R. M. (2019). Four decades of Antarctic surface elevation changes from multi-mission satellite altimetry. *The Cryosphere*, 13(2), 427–449.

Selley, H. L., Hogg, A. E., Cornford, S. and Dutrieux, P. (2021). Widespread increase in dynamic imbalance in the Getz region of Antarctica from 1994 to 2018. *Nature Communications*, 12, 1014.

Sergienko, O. V. (2013). Basal channels on ice shelves. *Journal of Geophysical Research: Earth Surface*, 118, 1342–1355.

Sergienko, O. V. and Wingham, D. J. (2019). Grounding line stability in a regime of low driving and basal stresses. *Journal of Glaciology*, 65(253), 833–849.

Seroussi, H., Nakayama, Y., Larour, E., Menemenlis, D., Morlighem, M., Rignot, E. and Khazendar, A. (2017). Continued retreat of Thwaites Glacier, West Antarctica, controlled by bed topography and ocean circulation. *Geophysical Research Letters*, 44, 6191–6199.

Seroussi, H., Nowicki, S., Payne, A. J., Goelzer, H., Lipscomb, W. H., Abe-Ouchi, A., Agosta, C., et al. (2020). ISMIP6 Antarctica: a multi-model ensemble of the Antarctic ice sheet evolution over the 21st century. *The Cryosphere*, 14, 3033–3070.

Sharma, A., Stokes, C. R. and Jamieson, S. S. R. (2025). Ice dynamics and structural evolution of Jutulstraumen, Dronning Maud Land, East Antarctica (1963–2022). *Journal of Glaciology*, 71 (e65).

Shen, Q., Wang, H., Shum, C., Jiang, L., Hsu, H. T. and Dong, J. (2018). Recent high-resolution Antarctic ice velocity maps reveal increased mass loss in Wilkes Land, East Antarctica. *Scientific reports*, 8(1), 1–8.

Shepherd, A., Wingham, D. and Rignot, E. (2004). Warm-ocean is eroding West Antarctic Ice Sheet. *Geophysical Research Letters*, 31, L23402.

Shepherd, A., Wingham, D., Wallis, D., Giles, K., Laxon, S. and Sundal, A. V. (2010). Recent loss of floating ice and the consequent sea level contribution. *Geophysical Research Letters*, 37(L13503).

Shepherd, A., et al. (2012). A reconciled estimate of ice-sheet mass balance. *Science*, 338(6111), 1183–1189.

Shepherd, A., Gilbert, L., Muir, A. S., Konrad, H., McMillan, M., Slater, T., et al. (2019). Trends in Antarctic Ice Sheet elevation and mass. *Geophysical Research Letters*, 46, 8174–8183.

Siegfried, M. R., Fricker, H. A., Carter, S. P. and Tulaczyk, S. (2016). Episodic ice velocity fluctuations triggered by a subglacial flood in West Antarctica. *Geophysical Research Letters*, 43, 2640–2648.

Simmonds, I. and Wu, X. (1993). Cyclone behaviour response to changes in winter southern hemisphere sea-ice concentration. *Quarterly Journal of the Royal Meteorological Society*, 119, 1121-1148.

Simmonds, I. and Keay, K. (2009). Extraordinary September Arctic sea ice reductions and their relationships with storm behavior over 1979–2008. *Geophysical Research Letters*, 36, L19715,

Skvarca, P., De Angelis, H. and Rack, W. (2004). Climatic conditions, mass balance and dynamics of Larsen B ice shelf, Antarctic Peninsula, prior to collapse. *Annals of Glaciology*, 39, 557–562.

Slater, T., Shepherd, A., McMillan, M. and Leeson, A. (2021). Increased variability in Greenland Ice Sheet runoff from satellite observations. *Nature Communications*, 12, 1441.

Smedsrud, L. H., Jenkins, A., Holland, D. M. and Nøst, O. A. (2006). Modeling ocean processes below Fimbulisen, Antarctica. *Journal of Geophysical Research*, 111 (C01007).

Smith, B., Fricker, H. A., Gardner, A. S., Medley, B., Nilsson, J., Paolo, F. S., Holschuh, N., Adusumilli, S., Brunt, K., Csatho, B., Harbeck, K., Markus, T., Neumann, T., Siegfried, M. R. and Zwally, H. J. (2020). Pervasive ice sheet mass loss reflects competing ocean and atmosphere processes. *Science*, 368(6496), 1239–1242.

Smith, E. C., Hattermann, T., Kuhn, G., Gaedicke, C., Berger, S., Drews, R., et al. (2020). Detailed seismic bathymetry beneath Ekström Ice Shelf, Antarctica: Implications for glacial history and ice-ocean interaction. *Geophysical Research Letters*, 47, e2019GL086187.

Jacobs, S. S. (1991). On the nature and significance of the Antarctic Slope Front. *Marine Chemistry*, 35(1–4), 9–24.

Stokes, C.R., Bamber, J.L., Dutton, A. et al. (2025). Warming of +1.5°C is too high for polar ice sheets. *Communications earth & environment*, 6, 351.

Stokes, C. R., Abram, N. J., Bentley, M. J. et al. (2022). Response of the East Antarctic Ice Sheet to past and future climate change. *Nature*, 608, 275–286.

Stokes, C. R., Sanderson, J. E., Miles, B. W. J., et al. (2019). Widespread distribution of supraglacial lakes around the margin of the East Antarctic Ice Sheet. *Scientific Reports*, 10 (1923).

Straneo, F. and Heimbach, P. (2013). North Atlantic warming and the retreat of

Greenland's outlet glaciers. *Nature*, 504(7478), 36–43.

Stuecker, M. F., Bitz, C. M. and Armour, K. C. (2017). Conditions leading to the unprecedented low Antarctic sea ice extent during the 2016 austral spring season. *Geophysical Research Letters*, 44, 9008–9019.

Sun, S., Cornford, S. L., Gwyther, D. E., Gladstone, R. M., Galton-Fenzi, B. K., Zhao, L. and Moore, J. C. (2016). Impact of ocean forcing on the Aurora Basin in the 21st and 22nd centuries. *Annals of Glaciology*, 57(73), 79–86.

Sun, Y., Riel, B. and Minchew, B. (2023). Disintegration and buttressing effect of the landfast sea ice in the Larsen B embayment, Antarctic Peninsula. *Geophysical Research Letters*, 50 (e2023GL104066).

Sutter, J., Eisen, O., Werner, M., Grosfeld, K., Kleiner, T., and Fischer, H. (2020). Limited retreat of the Wilkes Basin ice sheet during the Last Interglacial. *Geophysical Research Letters*, 47 (e2020GL088131).

Swithinbank, C., McClain, P. and Little, P. (1977). Drift Tracks of Antarctic Icebergs. *Polar Record*, 18(116), 495–501.

The IMBIE Team (2018). Mass balance of the Antarctic Ice Sheet from 1992 to 2017. *Nature*, 558(7709), 219–222.

The IMBIE Team (2023). Mass balance of the Greenland and Antarctic ice sheets from 1992 to 2020. *Earth System Science Data*, 15, 1597–1616.

Thoma, M., Mayer, C. and Grosfeld, K. (2008). Sensitivity of subglacial Lake Vostok's flow regime on environmental parameters. *Earth and Planetary Science Letters*, 269(1–2), 242–247.

Thompson, A. F., Stewart, A. L., Spence, P. and Heywood, K. J. (2018). The Antarctic Slope Current in a changing climate. *Reviews of Geophysics*, 56(4),

741–770.

Thompson, D. W. J., Wallace, J. M., and Hegerl, G. C. (2000). Annular modes in the extratropical circulation. Part I. I.: Trends. *Journal of Climate*, 13(5), 1018–1036.

Timmermann, R., Wang, Q., Hellmer, H. H. (2012). Ice-shelf basal melting in a global finite-element sea-ice/ice-shelf/ocean model. *Annals of Glaciology*, 53(60), 303-314.

Toh, H. and Shibuya, K. (1992). Thinning rate of ice sheet on Mizuho Plateau, East Antarctica, determined by G. P. S differential positioning. *Recent progress in Antarctic earth sciences*, 579–583.

Trusel, L. D., Das, S. B., Osman, M. B., Evans, M. J., Smith, B. E., et al. (2018). Nonlinear rise in Greenland runoff in response to post-industrial Arctic warming. *Nature*, 564(7734), 104–108.

Turner, J., Lu, H., King, J. C., Carpentier, S., Lazzara, M., Phillips, T., and Wille, J. (2022). An extreme high temperature event in coastal East Antarctica associated with an atmospheric river and record summer downslope winds. *Geophysical Research Letters*, 49 (e2021GL097108).

Turner, J., Guarino, M. V., Arnatt, J., Jena, B., Marshall, G. J., Phillips, T., et al. (2020). Recent decrease of summer sea ice in the Weddell Sea, Antarctica. *Geophysical Research Letters*, 47 (e2020GL087127).

Van Achter, G., Fichefet, T., Goosse, H. and Pelletier, C. (2022). Modelling landfast sea ice and its influence on ocean–ice interactions in the area of the Totten Glacier, East Antarctica. *Ocean Modelling*, 175, 101971.

van Autenboer, T. and Decleir, H. (1969). Airborne Radio-glaciological investigation during the 1969 Belgian Antarctic expedition. *Bull. Soc. belge Géol., Paléont.,*

Hydrol., 78(2), 87-100.

van den Broek, P., Young, M., Tzeng, Y., and Linderholm, T. (1999). The Landscape model of reading: Inferences and the online construction of memory representation. In H. van Oostendorp and S. R. Goldman (Eds.). *The construction of mental representations during reading*, 71–98.

van den Broeke, M. R., Enderlin, E. M., Howat, I. M., Kuipers Munneke, P., Noël, B. P. Y., van de Berg, W. J., van Meijgaard, E., and Wouters, B. (2016). On the recent contribution of the Greenland ice sheet to sea level change. *The Cryosphere*, 10, 1933–1946.

Vinje, T. E. (1975). Drift av Trolltunga i Weddellhavet. Årbok. Norsk Polar Institute, Oslo, 213–214.

Vitousek, S., Barnard, P. L., Fletcher, C. H., Frazer, N., Erikson, L., and Storlazzi, C. D. (2017). Doubling of coastal flooding frequency within decades due to sea-level rise. *Scientific Reports*, 7, 1399.

Walker, C. C., Bassis, J. N., Fricker, H. A. and Czerwinski R. J. (2013) Structural and environmental controls on Antarctic ice shelf rift propagation inferred from satellite monitoring. J. Geophys. Res. Earth Surf., 118, 2354–2364.

Walker, C. C., Bassis, J. N., Fricker, H. A., and Czerwinski, R. J. (2015). Observations of interannual and spatial variability in rift propagation in the Amery Ice Shelf, Antarctica, 2002–14. *Journal of Glaciology*, 61(226), 243–252.

Walker, C.C. and Gardner, A.S. (2019). Evolution of ice shelf rifts: Implications for formation mechanics and morphological controls. *Earth and Planetary Science Letters*, 526 (115764).

Walker, C. C., Millstein, J. D., Miles, B. W. J. et al. (2024). Multi-decadal collapse of East Antarctica's Conger–Glenzer Ice Shelf. *Nature Geoscience*, 17,

1240–1248.

Wallis, B. J., Hogg, A. E., van Wessem, J. M. et al. (2023). Widespread seasonal speed-up of west Antarctic Peninsula glaciers from 2014 to 2021. *Nature Geoscience*, 16, 231–237.

Wild, C. T., Alley, K. E., Muto, A., Truffer, M., Scambos, T. A., and Pettit, E. C. (2022). Weakening of the pinning point buttressing Thwaites Glacier, West Antarctica. *The Cryosphere*, 16, 397–417.

Wille, J. D., Favier, V., Gorodetskaya, I. V., Agosta, C., Kittel, C., Beeman, J. C., et al. (2021). Antarctic atmospheric river climatology and precipitation impacts. *Journal of Geophysical Research: Atmospheres*, 126.

Wille, J. D., Alexander, S. P., Amory, C., Baiman, R., Barthélemy, L., Bergstrom, D. M., et al. (2024). The extraordinary March 2022 East Antarctica "heat" wave. Part I. I.: Impacts on the Antarctic Ice Sheet. *Journal of Climate*, 37(3), 779–799.

Wolmarans, L. G. and Kent, L. E. (1982). Geological investigations in western Dronning Maud Land, Antarctica—a synthesis. *South African Journal of Antarctic Research Supplement 2*, 93.

Wouters, B., Martin-Español, A., Helm, V., Flament, T., van Wessem, J. M., Ligtenberg, S. R. M. ,van den Broeke, M. R. and Bamber, J. L. (2015). Dynamic thinning of glaciers on the Southern Antarctic Peninsula. *Science*, 348, 899-903.

Xie, S., Dixon, T. H., Holland, D. M., Voytenko, D. and Vankova, I. (2019). Rapid iceberg calving following removal of tightly packed pro-glacial mélange. *Nature Communications*, 10(3250), 1–15.

Zwally, H. J., Comiso, J. C., Parkinson, C. L., Cavalieri, D. J. and Gloersen, P. (2002). Variability of Antarctic sea ice 1979–1998. *Journal of Geophysical Re-*

search, 107(C5).

Zwally, H. J. and Giovinetto, M. B. (2011). Overview and assessment of Antarctic ice-sheet mass balance estimates: 1992–2009. *Surveys in Geophysics*, 32(4–5), 351–376.

Zwally, H. J., Giovinetto, M. B., Beckley, M. A. and Saba, J. L. (2012). Antarctic and Greenland Drainage Systems. *GSFC Cryospheric Sciences Laboratory*

Zwally, H. J., Robbins, J. W., Luthcke, S. B., Loomis, B. D. and Réy, F. (2021). Mass balance of the Antarctic ice sheet 1992-2016: Reconciling results from GRACE gravimetry with ICESat, ERS1/2 and Envisat altimetry. *Journal of Glaciology*, 67(263), 533–559.